Imperial College London
Department of Electrical and Electronic Engineering

Signal Design for Wideband Multi-functional Wireless Systems

Yumeng Zhang
张宇萌

Supervised by Prof. Bruno Clerckx

Submitted in part fulfilment of the requirements for the degree of
Doctor of Philosophy of Imperial College London and
the Diploma of Imperial College London, 2024

Declaration of Originality

I hereby declare that the content of this thesis is my own research work. The main parts of this thesis have been published in related conferences and journals. Where other sources of information have been used, they have been acknowledged.

Copyright Declaration

The copyright of this thesis rests with the author. Unless otherwise indicated, its contents are licensed under a Creative Commons Attribution-Non Commercial 4.0 International Licence (CC BY-NC).

Under this licence, you may copy and redistribute the material in any medium or format. You may also create and distribute modified versions of the work. This is on the condition that: you credit the author and do not use it, or any derivative works, for a commercial purpose.

When reusing or sharing this work, ensure you make the licence terms clear to others by naming the licence and linking to the licence text. Where a work has been adapted, you should indicate that the work has been changed and describe those changes.

Please seek permission from the copyright holder for uses of this work that are not included in this licence or permitted under UK Copyright Law.

Abstract

Wideband signals have found advantages in various wireless systems, i.e., communications, sensing and wireless power transfer (WPT), as well as their integration. This thesis explores the applications of wideband signals, by accounting for realistic system properties that are often overlooked in the existing literature, and by pushing the integration further considering a multi-functional sensing, communications and powering system to achieve higher spectrum efficiency.

First, we investigate the optimal wideband signal in WPT, adaptive to the channel state information and accounting for both the high power amplifier (HPA)'s non-linearity at the transmitter and the energy harvester (EH)'s non-linearity at the receiver. The consequential optimal wideband signal achieves the highest end-to-end power harvesting efficiency in WPT, which addresses previous literature's negligence on either HPA's or EH's non-linearities.

Second, we progress to wideband signal design for dual-function radar and communications, with a particular focus on orthogonal frequency division multiplexing (OFDM) signals. To visualize the random-deterministic trade-off between communication and radar functionalities, we design the input distribution of OFDM symbols to optimize the radar performance constrained by communication achievable rates – defined as the DFRC performance region. The signal design also accounts for the practical OFDM *on-grid* range-velocity radar estimator, whose feature has been dismissed for waveform design. The proposed input distribution effectively enlarges the performance region of DFRC, compared with existing literature.

Third, we propose an integrated sensing, communication and powering (ISCAP) system, where an OFDM signal is designed and transmitted to power a sensor, communicate with an information decoder and sense a point target simultaneously. We optimize the OFDM signal's input distribution, whose performance significantly surpasses the corresponding coexisting scenario where independent signals serve their respective functionalities in a power-splitting way.

Acknowledgements

I am generally a fortunate person as my PhD journey approaches the end. I have met with wonderful people, and with their consistent support, I finally bring this thesis to fruition.

First and foremost, I would like to express my sincere thankfulness to my supervisor, Prof. Bruno Clerckx for his ongoing recognition since my MSc. I deeply appreciate all his academic guidance, as well as his profound support to enrich my research experience and continue my career.

I am immensely grateful to my colleagues, for their timely appearance, consistent encouragement, the excellent trips and the many shared/free meals that came just when I needed them most.

Finally, I am profoundly thankful to my parents, for everything they have provided, and for always being my strongest backup. Thanks to their love and support, I always have the courage for a new journey.

Yumeng Zhang

张宇萌

London, May 2024.

Abbreviations

AC Alternating Current

ADC Analogue-to-Digital Converter

ADMM Alternating Direction Method of Multipliers

AF Ambiguity Function

aISPLD average Integrated Sibelobes to Peaklobe Difference

APE Added Power Efficiency

AWGN Additive White Gaussian Noise

BPF Band Pass Filter

BPSK Binary Phase-shift keying

C-P Communication-Powering

C-S Communication-Sensing

CP Cyclic Prefix

CRB Cramer-Rao Bound

CS Communication Symbols

CSCG Circularly Symmetric Complex Gaussian

CSI Channel State Information

DAC Digital-to-Analogue Converter

DC Direct Current

DFRC Dual Functional Radar Communications

DFT Discrete Fourier Transform

DP Detection Probability

EH Energy Harvester

FAP False Alarm Probability

FFT Fast Fourier Transform

FT Fourier Transform

GD Gradient Descent

HPA High Power Amplifier

IDFT Inverse Discrete Fourier Transform

IFFT Inverse Fast Fourier Transform

i.i.d independently and identically distributed

IoT Internet of Things

IP Interior Point

ISAC Integrated Sensing and Communications

ISCAP Integrated Sensing, Communications and Powering

ISAP Integrated Sensing and Powering

KKT Karush–Kuhn–Tucker

LCQP Linearly Constrained Quadratic Programming

LHS Left-Hand Side

LPF Low Pass Filter

MIMO Multiple Input Multiple Output

MISO Multiple Input Single Output

ML Maximum Likelihood

MSE Mean Square Error

NLoS Non Line of Sight

NR Newton Raphson

OBO Output Backoff

OFDM Orthogonal Frequency-division Multiplexing

OP Outlier Probability

PAPR Peak to Average Power Ratio

PDF Probability Density Function

PE Power Efficiency

PMV Probability Mass Vector

PS Power Splitting

PSCA Parametric Successive Convex Approximation

PSK Phase Shift Keying

PTE Power Transfer Efficiency

QAM Quadrature Amplitude Modulation

QCQP Quadratic Constrained Quadratic Programming

QPSK Quadrature Phase Shift Keying

RF Radio Frequency

RHS Right-Hand Side

RIS Reconfigurable Intelligent Surfaces

RMI Radar Mutual Information

SCP Successive Convex Programming

SINR Signal to Interference and Noise Ratio

SISO Single Input Single Output

SNR Signal to Noise Ratio

SQP Sequential Quadratic Programming

SSPA Solid-State-Power Amplifier

TS Time-Splitting

UBOP Upper Bound Outlier Probability

WIPT Wireless Information and Power Transfer

WPT Wireless Power Transfer

w.r.t with respect to

Contents

Declaration of Originality **1**

Copyright Declaration **3**

Abstract **5**

Acknowledgements **7**

Abbreviations **9**

1 Introduction **25**

1.1 Background and motivations 25

1.1.1 Wideband signals for WPT and WIPT 26

1.1.2 Wideband signals for radar and ISAC 27

1.1.3 Integrated sensing, communications and WPT system 29

1.2 Outline and contributions 30

1.3 Publications 31

1.4 Notations 32

2 Preliminaries **35**

2.1 Wideband signals and their wireless propagation 35

2.1.1 Multi-sine signals and its wireless propagation 36

2.1.2 OFDM signals and its wireless propagation 37

2.2 PTE in wideband WPT 40

2.2.1 The DC-to-RF power conversion efficiency e_1 41

2.2.2 The RF-to-RF power conversion efficiency e_2 42
2.2.3 The RF-to-DC power conversion efficiency e_3 43
2.3 Wideband signal processing for radar 45
2.3.1 Radar system model 45
2.3.2 OFDM radar processing 47
2.4 Input distribution of wideband signals in communications 48
2.4.1 Constant magnitude input distribution and the communication achievable rates 49
2.4.2 Variable magnitude input distribution and the communication achievable rates 50

3 Signal Design for Wireless Power Transfer with High Power Amplifier Non-linearities 51
3.1 Introduction 52
3.2 WPT system and signal model 55
3.3 HPA and rectenna analytical models 57
3.3.1 HPA model characterization and insights 57
3.3.2 HPA non-linearity and efficiency measurement 58
3.3.3 Analytical insights into HPA and BPF outputs 60
3.3.4 Rectenna model 62
3.4 Optimizations 63
3.4.1 Problem formulation 64
3.4.2 Model I: input waveform with the same frequencies as the transmit waveform 64
3.4.3 Model II: input waveform utilizing out-of-band frequencies . . . 68
3.5 Simulations 71
3.5.1 Frequency-flat channels 72
3.5.2 Frequency-selective channels 77

3.5.3 Comparison between Model I and Model II 81
3.6 Conclusions 83
3.7 Appendix 84
3.7.1 Convexity proof of the objective function in (3.19a) 84
3.7.2 Proof of the input power constraint in (3.24b) 85
3.7.3 Convexity proof of the constraint in (3.24b) 86
3.7.4 Approximating the input signal of Model II 86

4 Signal Design for Dual-Functional Radar-Communication Systems . 88
4.1 Introduction 89
4.2 Signal model 91
4.3 Characterizing the ML estimator's OP 93
4.3.1 ML estimator 93
4.3.2 ML-based radar metric 95
4.4 Minimizing OP for constant magnitude input distributions 99
4.4.1 Problem formulation 99
4.4.2 Low complexity optimization 102
4.5 Minimizing OP for variable magnitude input distributions (Gaussian) . . 104
4.5.1 Problem formulation 105
4.5.2 Optimization 107
4.5.3 Decoupling optimization 110
4.6 Simulations 114
4.6.1 OFDM with PSK input distribution (constant magnitude) . . . 115
4.6.2 OFDM with Gaussian input distribution (variable magnitude) . 118
4.7 Conclusions 122
4.8 Appendix 123
4.8.1 Derivation of the OP in (4.11b) 123
4.8.2 Proof of the closed-form solution for (4.19b) 124

4.8.3 Proof of (4.24e) . . . 125
4.8.4 Proof of (4.33b) in the decoupling method . . . 126

5 Signal Design for Multi-Functional Integrated Sensing, Communications and Powering Systems . . . 128
5.1 Introduction . . . 129
5.2 System and signal models . . . 131
5.2.1 Transmit signal . . . 132
5.2.2 Metric for powering . . . 134
5.2.3 Metric for sensing . . . 139
5.2.4 Metric for communication . . . 141
5.3 Optimal OFDM waveform design . . . 141
5.3.1 Problem formulation . . . 142
5.3.2 Problem optimization . . . 142
5.4 Simulation results . . . 149
5.4.1 S-P region . . . 151
5.4.2 C-P region . . . 155
5.5 Conclusions . . . 157
5.6 Appendix . . . 159
5.6.1 Proof of (5.15a) - (5.15c) . . . 159
5.6.2 Proof of (5.18a) - (5.18c) . . . 160

6 Conclusions . . . 162
6.1 Conclusions . . . 162
6.2 Future directions . . . 163

References . . . 165

List of Tables

List of Figures

2.1 The OFDM structure at the transmitter. 37

2.2 The block diagram of a generic WPT system. 41

2.3 The rectenna circuit of the EH in WPT. 43

2.4 A generic OFDM radar system. 46

3.1 The system model of WPT with non-linear HPA and EH. 54

3.2 SSPA's input-output voltage characteristics. $A_s = 1$ mV; $G = 2$ and $\beta = \{1, 2, 5, 20\}$. R_1 is the linear regime (small input signal); R_2 is the non-linear regime. 58

3.3 z_{DC} with HPA's and rectenna's non-linearity and $K = 8$. Ideal refers to the maximal achievable z_{DC} with an ideal HPA. Model I/II refers to the resultant waveform optimized from Model I/II considering non-linear HPA; No-HPA in [1] is to use the optimal transmit waveform from [1] directly to HPA's input, without pre-distorted to HPA's non-linearity. PAPR is to use the waveform from [1] but with PAPR constraints. 'Linear EH' refers to the optimal pre-distorted waveform that adapts to HPA's non-linearity and the WPT channel, without considering EH's linearity. 72

3.4 The operating point of HPA that corresponds to Fig. 3.3. The red, black and blue curves represent the waveform from Model I, Model II and No-HPA in [1] respectively. 73

3.5 The waveforms from the two end-to-end optimizations that correspond to Fig. 3.3, with HPA working in small signal regime, non-linear regime and saturation regime from top to the bottom. 73

3.6 z_{DC} of different waveforms in frequency-flat channels with different levels of the input power constraints as a function of the transmit power constraints with $K=8$. 76

3.7 One frequency-selective channel realization, and the corresponding optimal waveforms with $K=8$. From top to bottom, we plot the magnitude response of this channel realization, the waveform from the three models with $P_{\mathrm{tr}}^{\max}=-5$dBW, and the waveform from the three models with $P_{\mathrm{tr}}^{\max}=5$dBW. 77

3.8 From top to bottom, the harvested power z_{DC} and the end-to-end PTE, corresponding to Fig. 3.7. 78

3.9 Average z_{DC} with different bandwidth, $P_{\mathrm{in}}^{\max}=10$ dBW, $P_{\mathrm{tr}}^{\max}=8$ dBW. The red and black bars represent the waveforms from Model I and Model II respectively. The blue bar represents the No-HPA waveform in [1]. . . 79

3.10 Average z_{DC} with different numbers of antennas M and different numbers of sub-carriers N for $P_{\mathrm{In}}^{\max}=10$ dBW, $P_{\mathrm{Tr}}^{\max}=8$ dBW. The red and black bars represent the waveforms from Model I and Model II respectively. The blue bar represents the No-HPA waveform in [1]. 80

3.11 Average z_{DC} with different numbers of sub-carriers, giving different saturation power, $P_{\mathrm{In}}^{\max}=10$, $P_{\mathrm{Tr}}^{\max}=8$ dBW. 81

3.12 Average z_{DC} as a function of HPA's smoothing parameter (β) given different number of sub-carriers, $P_{\mathrm{In}}^{\max}=10$ dBW, $P_{\mathrm{Tr}}^{\max}=8$ dBW, $G=1$, $A_s=10$ dBA, $B=10$ MHz. 82

3.13 The magnitude spectrum of the input signal from Model II (with $P_{\mathrm{tr}}^{\max}=10$ dBW for the maximal non-linearity) (top) and the power harvesting performance corresponds to Fig. 3.3 but adding an approximated input signal of Model II whose out-off band components are cut off (bottom). 87

4.1 The magnitudes of discrete AF ($|r_{n,v,v_\epsilon}|$ in (4.10e)) and the corresponding cross correlation ($|\gamma_{n,v,v_\epsilon}|$ in (4.10d) averaging over random CSs for (b) and velocities for (c)) with uniform power allocation across both OFDM subcarriers and symbols, with $K=32$, $M=16$ and $K_G=8$. The index, q, is related to delay-Doppler bin (n, v) as follows: $q=n+(v+M/2)K_G$. 96

4.2 The overall MSE, the outlier MSE and the CRB relationship for $K=32$, $K_G=8$, $M=8$. 96

4.3 The simulated and approximated OP for $K=32$, $K_G=8$, $M=8$. 98

4.4 The grey-scale map of the proposed optimal OFDM waveform for $K=1024$, $K_G=256$, $M=512$ at $P^{\max}=-15$ dBW (a low SNR region), with the red curve illuminating the total power (sum over subcarriers) at each OFDM symbol. 115

4.5 The empirical OP of delay-Doppler estimation between the proposed metric (OPT), RMI, CRB and two windowed power allocation (Hamming and Kaiser) across the OFDM symbols, with BPSK input for $K=1024$, $K_G=256$, $M=512$. The worst SNR (the farthest range bin) at the radar's receiver and the SNR at the communication's receiver respectively range from -51 dB to -41 dB and from 1.4 dB to 16.4 dB respectively. 116

4.6 The empirical range MSE, corresponding to Fig. 4.5. 117

4.7 The empirical velocity MSE, corresponding to Fig. 4.5. 117

4.8 The empirical OP given $R^c=2.12$ bits/s/Hz with $K=32$, $K_G=8$, $M=16$. The red curve refers to the optimal input distribution proposed in Algorithm 5, shortened as 'OPT'. The green curve refers to the simplified decoupling method in Algorithm 6, shortened as 'Decouple'. The cyan curve is the radar benchmark from the optimal PSK signal in Section 4.4, shortened as 'Deter'. Similarly, the purple curve refers to the 'RMI' metric and the black curve refers to the 'CRB' metric. 119

4.9 The empirical OP with Gaussian input, $K=1024$, $K_G=256$, and $M=512$. 119

4.10 The R-C region trade-off in OFDM DFRC for $P^{\max}=0$ dBW, $K=32$, $K_G=8$ and $M=16$. 120

4.11 The power ratio of the squared symbol means (deterministic components) and the symbol variance (random components) corresponding to the 'OPT' input distribution (red) in Fig. 4.10. 120

4.12 Examples of the mean power (red) and the variance power (blue) at each subcarrier (sum over OFDM symbols) in one channel realization for the 'OPT' input distribution at points 'A', 'B' and 'C' in Fig. 4.10. The sum of the mean power (red) and the variance power (blue) is the total power at the subcarrier. 121

5.1 System and OFDM Signal Model for ISCAP. 132

5.2 The average S-P region given different achievable rate constraints ($C_{\min}=$ 0, 0.12, 0.47, 0.82, 1.17 bits/s/Hz from left to right). 'OPT' (red) refers to the optimized asymmetric complex Gaussian input distribution from Section 5.3. 'Symmetric' (black) refers to the optimized symmetric complex Gaussian input distribution. 'CSCG' (blue) refers to the optimized CSCG input distribution. 'Coexist' (magenta) refers to the non-co-design signal superposed by the optimal communication and sensing signals through PS. $P(Z_{\mathrm{DC}})=0$ means that the exerted rate and aISPLD constraints are not feasible at this point. 151

5.3 Left: Magnitude response of one powering channel realization; Right: Magnitude response of one communications channel realization. 151

5.4 For the channel realizations in Fig. 5.3, the 'OPT' input distribution corresponding to points A, B, C, and D in Fig. 5.2. For each sub-carrier (numbered 1 through 8), its complex Gaussian distribution is represented by an ellipse whose center is the mean, and whose width and height correspond to the variance of the real and imaginary parts, respectively. 152

5.5 The average C-P region given $S_{\max} = -0.948$, comparing the 'OPT', 'Symmetric', 'CSCG' and 'Coexist' inputs. 155
5.6 The 'OPT' input constellation of points E, F, G and H in Fig. 5.5 corresponds to the channel realizations in Fig. 5.3. 156
5.7 S-C-P region of the 'OPT' input with 30 dBm transmit power. 158

Chapter 1

Introduction

This chapter starts with a background overview of designing wideband signals for wireless power transfer (WPT) and wireless sensing (i.e., radar), along with their integration with wireless communications in Section 1.1. The background overview motivates us to consider practical system limits and more advanced integration of wireless networks in this thesis. Following the motivations, we present the outline and contributions of this thesis in Section 1.2. Section 1.3 lists the publications and Section 1.4 lists useful notations.

1.1 Background and motivations

The background overview in this section particularly highlights the wideband signal design with practical system properties, such as non-linear components in WPT, the discrete parameter estimation in orthogonal frequency-division multiplexing (OFDM) radar, as well as their extension to integrated systems such as wireless information and power transfer (WIPT) and integrated sensing and communications (ISAC). Moreover, we provide literature insights to consider an integrated sensing, communications and powering (ISCAP) system to boost the spectrum efficiency further.

1.1.1 Wideband signals for WPT and WIPT

Thanks to the significant reduction in the power consumption of remote sensors in the Internet of Things (IoT), far-field WPT has emerged as an alternative power source substituting wired power supply or batteries, providing more sustainability, flexibility, and adaptability [1–3].

Far-field WPT generates and transmits suitable radio frequency (RF) signals that propagate over the air before being captured and rectified into direct current (DC) via rectenna circuits at the receivers. Since the discovery of WPT's promising potential to address the powering bottlenecks in IoT, scientists have been making every effort to boost the power transfer efficiency (PTE) of WPT on several fronts, namely, circuits design [4,5], RF signals design [6,7], reconfigurable intelligent surfaces (RIS) and other materials [6,8,9].

Signals and waveforms play a crucial role in the PTE of WPT. Adapting to practical energy harvester (EH) (i.e., mainly the rectenna) structures at the receiver [1, 10, 11], experimental research verifies the advantages of receiving signals featuring a high peak-to-average-power ratio (PAPR) regarding the power conversion efficiency, but without consideration of channel state information (CSI) of the wireless propagation [11, 12]. A noteworthy contribution later is in [1] where a multi-sine transmit waveform emitted at the transmitter was theoretically designed, adaptive to CSI and rectenna's non-linear characteristics, to maximize the DC current at the rectenna's output. The model in [1] gives rise to further flourishment in the field of signal design in far-field WPT [13–22]. A corresponding low-complexity algorithm was developed in [13], and the efficiency of these waveforms was validated through prototyping and experimentation in [14, 15]. Moreover, the model has been extended to general scenarios such as large-scale [16], multi-input-multi-output (MIMO) [17, 18], limited-feedback [19], multi-user [16, 20] and opportunistic/fair-scheduling [21, 22] scenarios.

In addition to pure WPT systems, literature has also extensively investigated WIPT

systems where a common signal is used to perform both communications for mobile users and WPT for power consumption sensors. The performance of WIPT is characterized by the communication-powering (C-P) region, which defines the maximal achievable harvested power given communication constraints such as the achievable rate [23, 24]. Successive efforts have been made to enlarge the C-P region in WIPT while accounting for rectenna's non-linearities [25–31] in various configurations, such as multi-user [25], MIMO [26], and wireless powered backscatter communications [27]. Particularly, with rectenna's non-linearity, [28] showed that the modulated signal (carrying information with circularly symmetric complex Gaussian (CSCG) input) superposed by the unmodulated signal (deterministic without information) can enlarge the C-P region, with the former necessary for communications and the latter beneficial for powering.

However, the above waveforms were performed without much consideration of the power conversion efficiency at the WPT/WIPT's transmitter, especially the most non-linear and power-consuming component, namely the high power amplifier (HPA). Indeed, recent research has experimentally verified and characterized the performance degradation caused by non-linear HPAs in WPT/WIPT systems [32–36]. Furthermore, although attempts have been made to design narrowband signals in WPT/WIPT [6, 37, 38] accounting for both HPA's and EH's non-linearities, these efforts cannot exploit the benefits of wideband signals for rectenna's non-linearity. Designing wideband signals that account for both HPA's and EH's non-linearities in WPT/WIPT presents significant challenges because of the inter-carrier interference and frequency leakage [6, 32]. However, a comprehensive design that incorporates these aspects is essential to thoroughly enhance the end-to-end PTE of WPT systems.

1.1.2 Wideband signals for radar and ISAC

Wideband signals also enhance radar through waveform design [39–50]. The most recognized optimization metrics for radar include: (a) the detection probability (DP)/false

alarm probability (FAP) that describes the probability of correctly/falsely detecting the existence of a target in a certain delay/Doppler/angle bin [39–41], and (b) the mean square error (MSE) of parameter estimation [42]. However, these radar metrics usually result in high complexity when adopted for waveform optimization. As a substitute, indirect metrics based on desirable properties that good sensing signals often share – such as the ambiguity function (AF) [43–47] – have also been used. Other indirect metrics include signal-to-noise-ratio (SNR) or the signal-to-interference-and-noise-ratio (SINR) as a substitute for DP/FAP [51,52]; radar mutual information (RMI) from an information theory perspective [53,54]; or the Cramer-Rao bound (CRB) as a lower bound of MSE [55,56].

ISAC has also attracted considerable interest as a solution to the problem of spectrum shortage [57–60]. ISAC systems combine sensing and communications through proper signal/architecture/protocol design to achieve mutual performance gains [61–64]. As a notable approach of ISAC, DFRC particularly uses a common signal to perform both functionalities [60,62]. A promising signal candidate for DFRC is orthogonal frequency division multiplexing (OFDM), which originates from communications to combat channel fading but has also been developed a highly efficient 2-dimensional fast Fourier transform (2D-FFT) radar estimator with satisfying precision [65–69].

Signal design plays a significant role in improving the efficiency of OFDM DFRC, where particular attention should be paid to the inherent randomness in the waveform that originates from the embedded information-bearing communication symbols (CSs). This randomness can affect radar performance [39,70–76], but has been largely overlooked in DFRC waveform design literature [43,45,48–50,52,54,56,61–64]. As an inspiration, [70] has demonstrated that the phase randomness of CSs has only a trivial effect on the OFDM waveform's AF, making a compelling case for using constant magnitude inputs, i.e., phase-coded CSs such as PSK, in OFDM waveforms for DFRC to achieve a good radar performance [71–74]. However, to support higher communication rates, CSs with varying magnitudes (e.g., 256-QAM) may need to be embedded into OFDM waveforms, and the

impact of such variable magnitude inputs on radar performance has not been explored.

Very recently, [77, 78] shed light on the sensing-communication (S-C) trade-off w.r.t. the CS randomness – characterized by the input distribution – in DFRC. The authors depicted the S-C region (the optimal achievable sensing performance given communication constraints) and examined the optimal input distributions at the two corner points on the S-C region (i.e., radar-optimal and communication-optimal respectively). The paper reveals the fundamental S-C trade-off that the radar-optimal input distribution features CSs with deterministic sample covariance (constant magnitude inputs) while the communication-optimal input distribution features CSs with zero-mean Gaussian (variable magnitude inputs). However, for the practically relevant problem in OFDM DFRC systems of on-grid delay-Doppler bin estimation of a point target, the metrics used in [77] (RMI) and [78] (CRB) may not be the most suitable. For instance, the RMI is best suited for extended targets, whereas the CRB is best suited for continuous-valued parameters rather than discrete parameters. Hence a more appropriate metric is needed.

1.1.3 Integrated sensing, communications and WPT system

Inspired by the aforementioned wideband WIPT and ISAC systems [57, 63, 79–84], a question then arises: can we achieve (a suitably-defined) better performance by realizing sensing, communications and powering using a common signal, namely integrated sensing, communications and powering – the ISCAP system? To answer this question, we need to: a) decide and design a signal that is capable of performing sensing, communications and powering simultaneously and satisfyingly, b) evaluate the performance gain of the ISCAP signal using the proposed input signal over the traditional co-existing scenarios, c) identify the rationale of the performance gain by analyzing how the optimal signal trades off between the three functions.

Recently, [85] established the first narrowband MIMO ISCAP system where the authors

optimized the transmit beam pattern for co-design and achieved a better overall performance than the power/time-splitting counterparts in the co-existing scenario [86]. However, considering the advantages of wideband signals across various wireless networks, it would be meaningful to investigate wideband OFDM signals in ISCAP, study the spectrum interaction among the three functionalities and unveil the general trends of the optimized OFDM signal for intuitive insights.

1.2 Outline and contributions

Given the above literature, in this thesis, we want to enhance the efficiency of wideband signals across various wireless systems, by (1) improving the existing waveform design accounting for disregarded practical system properties, and (2) exploring higher spectrum efficiency with enhanced integration. Particularly, a summary of each chapter that highlights the main contributions of this thesis is given as follows.

- Chapter 2 introduces the preliminaries that are essential for the future signal design across different wireless systems, including (a) wideband signals modelling involving multi-sine and OFDM signals, (b) wideband WPT systems and the power efficiency, (c) wideband radar systems and the processor, and (d) input distributions of CSs in wireless communications.

- Chapter 3 focuses on WPT, and optimizes a multi-sine waveform at the input of HPA to maximize the harvested DC power at rectenna considering both HPA's and rectenna's non-linearities. The joint consideration bridges the previous literature's gap where only rectenna's non-linearity is considered and realizes an end-to-end PTE enhancement in WPT through waveform design. As a final note, this chapter shows wideband signals with a high PAPR are advantageous in exploiting the rectenna's non-linearity at the receiver but are disadvantageous in suffering from

HPA's non-linearity at the transmitter, which yields a carefully balanced signal design for WPT.

- Chapter 4 optimizes the OFDM signal in DFRC systems and pays particular attention to some overlooked system limits. Particularly, we optimize the input distributions of the OFDM signal to account for the impact of the random CSs on radar performance in DFRC. The input distribution design is also tailored to enhance discrete delay-Doppler bin estimation, featured by practical OFDM radar processors. In the end, this chapter concludes the fundamental random-deterministic trade-off between radar and communications in DFRC, and highlights the significance of signal design across both the time and the frequency domain in favour of the joint range-velocity radar estimation.

- Chapter 5 investigates a proposed ISCAP system, where we identify the appropriateness of using OFDM signals in the novel ISCAP system, define the performance boundaries of the system, and explore the achievable boundaries by designing the input distribution of the OFDM CSs. The chapter verifies the effectiveness of such an advanced integration compared with co-existing scenarios while highlighting the significance of signal design to balance sensing, communications and WPT functionalities.

- Chapter 6 summarizes the findings and contributions of the thesis. Additionally, this chapter outlines promising future directions for multi-functional wireless systems.

1.3 Publications

1. **Zhang, Yumeng**, and Bruno Clerckx. "Waveform Design for Wireless Power Transfer with Power Amplifier and Energy Harvester Non-Linearities." IEEE Transactions on Signal Processing (2023).

2. **Zhang, Yumeng**, Sundar Aditya, and Bruno Clerckx. "Input Distribution Optimization in OFDM Dual-Function Radar-Communication Systems." arXiv preprint arXiv:2305.06635 (2023) – submitted to IEEE Transactions on Signal Processing (under major revision).

3. **Zhang, Yumeng**, Sundar Aditya, and Bruno Clerckx. "Multi-functional OFDM Signal Design for Integrated Sensing, Communications, and Power Transfer." arXiv preprint arXiv:2311.00104 (2023) – submitted to IEEE Transactions on Wireless Communications (under major revision).

4. **Zhang, Yumeng**, Xiaodan Shao, Hongyu Li, Bruno Clerckx and Rui Zhang. "Full-space Wireless Sensing Enabled by Multi-sector Intelligent Surfaces" – submitted to IEEE Transactions on Wireless Communications (under decision).

5. **Zhang, Yumeng**, and Bruno Clerckx. "Waveform optimization for wireless power transfer with power amplifier and energy harvester non-linearities." ICASSP 2022-2022 IEEE International Conference on Acoustics, Speech and Signal Processing (ICASSP). IEEE, 2022.

1.4 Notations

Matrices and vectors are respectively denoted in form of bold upper case and bold lower case. $\mathbb{R}$, $\mathbb{C}$ and $\mathbb{Z}$ denotes the set of real numbers, complex numbers and integers, respectively. For $x \in \mathbb{C}$, $\Re\{x\}$, $\Im\{x\}$, $|x|$, and $\measuredangle x$ respectively denote the real part, imaginary part, amplitude and the phase of the complex x. For $x \in \mathbb{R}$, $(x)^+ \triangleq \max(x,0)$. For integer a, $b \in \mathbb{Z}$, $(a)_b$ means a modulo b. For a vector (matrix) $\mathbf{x}$ ($\mathbf{X}$), $\|\mathbf{x}\|$ ($\|\mathbf{X}\|$) represents its l_2 (Frobenius) norm, x_n refers to the n^{th} entry of vector $\mathbf{x}$, and $\text{diag}\{\mathbf{x}\}$($\text{diag}\{\mathbf{X}\}$) represents the diagonal matrix (vector) formed by $\mathbf{x}$ (matrix $\mathbf{X}$). $|\mathbf{x}|$ denotes the element-wise magnitude of $\mathbf{x}$, i.e., $|\mathbf{x}|_k = |x_k|$. $\mathbf{I}_{N_t}$ denotes $N_t \times N_t$ an identity

matrix and $\mathbf{1}_K$ represents an all-one vector with dimension $K \times 1$ - the subscript is omitted when the dimension is clear. $(\cdot)^H$, $(\cdot)^*$ and $(\cdot)^T$ represent the Hermitian, the conjugate and the transpose operations respectively. $\propto$ means in proportion to. $\odot$ represents the element-wise (Hadamard) product, $\oslash$ represents the element-wise (Hadamard) division, $\otimes$ represents the Kronecker product. Given a set κ, $|\kappa|$ refers to the cardinality of κ. $\delta(x)$ is the delta function. $\mathbb{1}_{(\cdot)}$ is the indicator function. $Q(\cdot)$ is the Marcum-Q function, and $I_0(\cdot)$ is the modified Bessel function of the first kind with order 0. $\mathcal{F}\{x(t)\}$ conducts Fourier Transform (FT) FT on $x(t)$ and $\mathcal{F}\{x(t)\}|_{f=f_0}$ takes the spectrum at frequency f_0.

For a random variable X, $\mathbb{E}_X\{f(X)\}$ represents the expected value of the function $f(X)$ over random variable X. $\mathcal{E}\{x(t)\}$ represents taking average of $x(t)$ over time. $\mathcal{N}(\mu, \sigma^2)$ refers to the normal distribution with mean μ and variance σ^2. Let $X_R \sim \mathcal{N}(\mu_R, \sigma_R^2)$ and $X_I \sim \mathcal{N}(\mu_I, \sigma_I^2)$ denote a pair of independent real Gaussian random variables. Then, $X = X_R + jX_I$ is said to have a complex Gaussian distribution. If $\mu_R = \mu_I = \mu$ and $\sigma_R^2 = \sigma_I^2 = \sigma^2/2$, then X is said to have a symmetric complex Gaussian distribution, denoted by $\mathcal{CN}(\mu, \sigma^2)$. The special case of $\mathcal{CN}(0, \sigma^2)$ is referred to as the circularly symmetric complex Gaussian (CSCG) distribution. In all other cases, X is said to have an asymmetric complex Gaussian distribution.

For sequences, $\{x[n]\}$ represents the sequences that collect all the related $x[n]$. $\circledast_N$ represents the sequence circular convolution with length N. The discrete Fourier transform (DFT) for sequences $\{x[n]\}$/vector $\{\mathbf{x}\}$ is denoted by DFT$\{x[n]\}$/DFT$\{\mathbf{x}\}$ with its k^{th} entry being DFT$\{x[n]\}_{(k)}$/DFT$\{\mathbf{x}\}_{(k)}$, and similarly for the inverse DFT (IDFT).

For specific functions, we have the following definitions.

Definition 1 (Rectangular function)**.**

$$\text{rect}(t) = \begin{cases} 1, & 0 \le t \le 1, \\ 0, & \text{otherwise.} \end{cases} \tag{1.1}$$

Definition 2 (Sinc function)**.**

$$\mathrm{sinc}(t) = \frac{\sin(\pi t)}{\pi t}. \tag{1.2}$$

Definition 3 (K-point DFT)**.**

$$x[k] = \mathrm{DFT}\{x[n]\}_{(k)} = \frac{1}{\sqrt{K}} \sum_{n=0}^{K-1} x[n] e^{\frac{-2j\pi kn}{K}}. \tag{1.3}$$

Definition 4 (Non-negative operator)**.**

$$(x)^+ = \begin{cases} x, & x \geq 0, \\ 0, & \textit{otherwise.} \end{cases} \tag{1.4}$$

Chapter 2

Preliminaries

In this chapter, the background knowledge of this thesis is presented. Firstly, we introduce the wideband signal models in Section 2.1, including multi-sine waves and OFDM signals. In Section 2.1, we also introduce their received signals after multi-path wireless propagation, to build the foundation of communications and WPT systems. Secondly, Section 2.2 introduces the fundamental principles in WPT systems and provides details of the PTE at each stage in WPT. Thirdly, Section 2.3 introduces wireless radar systems, specifying the OFDM radar processor. Lastly, in Section 2.4, we introduce the essential stochastic property of CSs, namely the input distribution, to lay the foundation for characterizing the randomness trade-off between integrated systems in the following chapters.

2.1 Wideband signals and their wireless propagation

This section introduces two important wideband signal models that will be involved in this thesis, i.e., multi-sine signals and OFDM signals. The two signal models have different application scenarios but can result in similar intuitions due to their identical wideband inherent. Specifically, multi-sine signals are often more analytically friendly,

particularly for providing theoretical insights. In contrast, OFDM signals offer higher spectrum efficiency in practice and better platform applicability.

2.1.1 Multi-sine signals and its wireless propagation

A K-multi-sine signal refers to a composite of K evenly frequency-spaced sub-carriers. The frequency of the k^{th} ($k=0,...,K-1$) transmitted sub-carrier is $f_k=f_0+(k-1)\Delta_f$ with f_0 being the lowest sub-carrier frequency and Δ_f being the frequency spacing. On this basis, a K-multi-sine signal is often analytically expressed in the following complex form [1]

$$x(t)=|x(t)|e^{j\angle x(t)}=\sum_{k=0}^{K-1}w_k e^{j2\pi f_k t}, \tag{2.1}$$

where w_k denotes the complex weight (might be embedded with random CSs in communications) of the k^{th} sub-carrier of $x(t)$.

The transmitted signal is then radiated and propagated through the wireless channels. Assume the wireless channels have L paths, whose l^{th} ($l=1, \cdots, L$) path delays the signal by τ_l and exerts a complex amplitude degradation of α_l with phase shift of ζ_l on the signal. The complex signal received from the l^{th} path is then expressed as [1]

$$y_l(t)=\sum_{k=0}^{K-1}\alpha_l e^{j\zeta_l}x(t-\tau_l)=\sum_{k=0}^{K-1}\alpha_l w_k e^{j(2\pi f_k(t-\tau_l)+\zeta_l)}+w(t), \tag{2.2}$$

where $w(t)$ is the additive white Gaussian noise (AWGN).

Then, the received signal is the collection of signals from all paths in (2.2), which is analytically expressed in the following form by combining (2.1) and (2.2)

$$y(t)=\sum_{l=1}^{L}y_l(t)=\sum_{k=0}^{K-1}\left[\sum_{l=1}^{L}\alpha_l e^{j2\pi(-f_k\tau_l+\zeta_l)}\right]w_k e^{j2\pi f_k t}\triangleq\sum_{k=0}^{K-1}h_k w_k e^{j2\pi f_k t}, \tag{2.3}$$

where $h_k=\sum_{l=1}^{L}\alpha_l e^{j2\pi(-f_k\tau_l+\zeta_l)}$ is the equivalent complex channel gain that the k^{th}

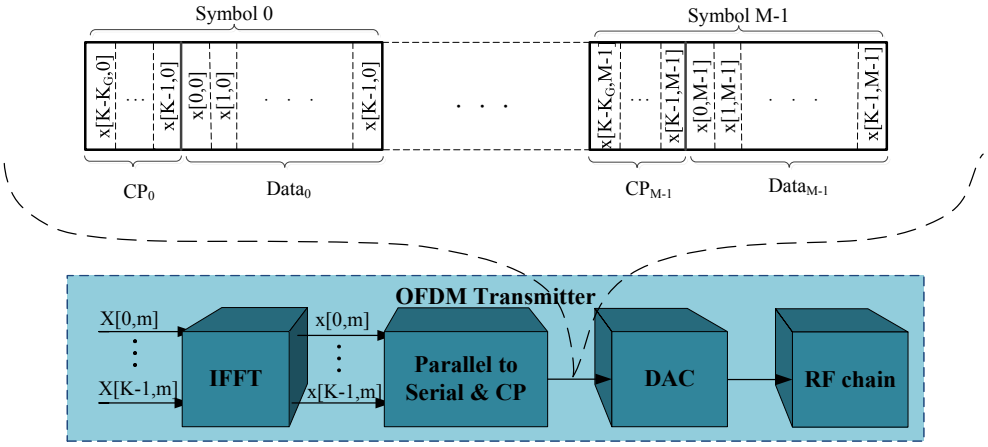

Fig. 2.1: The OFDM structure at the transmitter.

sub-carrier experiences during the multi-path wireless propagation.

2.1.2 OFDM signals and its wireless propagation

Compared with multi-sine signals, OFDM is more commonly implemented and utilized in practice. In communication literature, OFDM is often represented by multi-sine signals as their samples are identical after analogue-to-digital converters (ADCs) with perfect synchronization, leading to identicalness in scenarios where digital samples are the primary focus of analysis. However, for other functionalities such as WPT or radar where the analogue form matters, we should clarify the difference.

The structure of OFDM is shown in Fig. 2.1. The set-up employs K sub-carriers per OFDM symbol and observes M OFDM symbols within one block. At each OFDM symbol, K_G cyclic prefix (CP) is added to combat the channel fading. As shown at the initial stage in Fig. 2.1, complex data symbols are first digitally modulated in the frequency domain, i.e., $X[k, m]$ is modulated onto the k^{th} ($k=0, \cdots, K-1$) OFDM subcarrier of the m^{th} ($m=0, \cdots, M-1$) OFDM symbol. Then, IFFT is produced based on each OFDM symbol, which converts $X[k, m]$ to digital time-domain sub-pulses for transmission. The

complex time-domain sub-pulses, denoted by $x[n, m]$, are represented as [65]

$$x[n, m] = \text{IDFT}\{X[0, m], \cdots, X[K-1, m]\}_{(n)}. \tag{2.4}$$

Then, CP is added per OFDM symbol as shown in Fig. 2.1. The length of CP should be designed longer than the maximal delay of the multi-paths of the wireless channels in order to avoid inter-symbol interference, which will be explained afterwards. After adding the CP, we obtain the time-domain sub-pulses in the following form [65]

$$x_{\text{CP}}[n, m] = \begin{cases} x[K-K_{\text{G}}+n, m], & n \in \{0, \cdots, K_{\text{G}}-1\}, \\ x[n-K_{\text{G}}, m], & n \in \{K_{\text{G}}, \cdots, K_{\text{T}}-1\}, \end{cases} \tag{2.5}$$

where $K_{\text{T}} = K_{\text{G}}+K$ is the total number of sub-pulses per OFDM symbol.

The digital sub-pulses are then converted to the analogue signal for transmission through the digital-to-analogue (DAC) converter. The analogue signal is given in the following complex form [87]

$$x(t) = \sum_{n,m} x_{\text{CP}}[n, m] g(t-(n+K_{\text{T}}m)/B) \tag{2.6a}$$

$$= \sum_{q=0}^{K_{\text{T}}M-1} x_{\text{CP}}[q] g(t-q/B), \; q = mK_{\text{T}}+n, \tag{2.6b}$$

with $x_{\text{CP}}[q] = x_{\text{CP}}[n, m]$. $g(t)$ is the analogue basis for carrying sub-pulses. There are different choices of $g(t)$. For analytical ease, $g(t)$ might be assumed to be a rectangular basis, i.e., $g(t) = \text{rect}(Bt)$ with B being the bandwidth. For practical implementation, $g(t)$ might be chosen as a sinc function [87], i.e., $g(t) = \text{sinc}(Bt)$. The baseband signal is then upconverted to the central frequency f_{c} for wireless propagation.

Assume the wireless propagation environment has L paths, whose l^{th} path features delay τ_l, amplitude degradation α_l and phase shift ζ_l. The complex received signal in baseband

is given by (after down-converting and assuming the Doppler spread is small compared with the bandwidth) [87]

$$y_{\mathrm{CP}}(t)=\sum_{l,q}x_{\mathrm{CP}}[q]\alpha_l\mathrm{sinc}(Bt-B\tau_l-q)+w(t), \tag{2.7}$$

where (2.7) employs a sinc basis for the baseband sub-pulses at the DAC. Then, at the OFDM processor, the analogue signal is first sampled at the multiples of $1/B$ at ADC, whose samples are expressed as [87]

$$\begin{aligned}
y_{\mathrm{CP}}[n,\,m]\triangleq y[p]&=y_{\mathrm{CP}}(t-\tau)e^{j2\pi f_{\mathrm{D}}t}|_{t=p/B=(n+K_{\mathrm{T}}m)/B} && \text{(2.8a)}\\
&=\sum_{l,q}\alpha_l x_{\mathrm{CP}}[q]\mathrm{sinc}(p-q-\tau_l)+w[n,\,m] && \text{(2.8b)}\\
&=\sum_{t}x_{\mathrm{CP}}[p-t]\sum_{l}\alpha_l\mathrm{sinc}(t-\tau_l)+w[n,\,m] && \text{(2.8c)}\\
&=\sum_{t}x_{\mathrm{CP}}[p-t]h_t+w[n,\,m] && \text{(2.8d)}\\
&=\sum_{t}x_{\mathrm{CP}}[n-t,\,m]h_t+w[n,\,m], && \text{(2.8e)}\\
\text{with } h_t\triangleq&\sum_{l}\alpha_l\mathrm{sinc}(t-\tau_l), && \text{(2.8f)}\\
x_{\mathrm{CP}}[n-t,\,m]\triangleq&\begin{cases} x_{\mathrm{CP}}[n-t,\,m], & n\geq t,\\ x_{\mathrm{CP}}[K-n+t,\,m-1], & \text{otherwise,}\end{cases} && \text{(2.8g)}
\end{aligned}$$

where in (2.8c), $t:=p-q$. (2.8) is a discrete propagation representation for the OFDM transmission in the time domain and features a convolution in (2.8e) in the end. (2.8e) indicates that, when the maximal path delay (i.e., the largest index of non-zero h_t) is smaller than the length of the CP, $y_{\mathrm{CP}}[n,\,m]$ for $n\geq K_{\mathrm{CP}}$ is only related with the m^{th} transmit OFDM symbol from (2.8g). This enables the further operation w.r.t $y_{\mathrm{CP}}[n,\,m]$ for $n\geq K_{\mathrm{CP}}$ to avoid inter-symbol interference. Specifically, denote by $y[n,\,m]$ the complex received sub-pulse after removing the CP, which is re-written in the following

analytical form by combining (2.8) with (2.5)

$$y[n,\, m]=\sum_{l} x[n-l,\, m]h_l+w[n,\, m],\ 0\geq n\geq K, \tag{2.9}$$

Therein, $x[n-l, m]$ is an l-point circular shift version of the sequence $\{x[0,\, m],\, \cdots, x[n,\, m],\, \cdots,\, x[K-1,\, m]\}$. Then, a DFT procedure is operated to convert $y[n,\, m]$ in (2.9) back to the digital expression in the frequency domain, which is written as [87]

$$Y[k,\, m]=H_k X[k,\, m]+W[k,\, m], \tag{2.10}$$

where $H_k = \mathrm{DFT}\{h_1,\, \cdots, h_t,\, \cdots,\, h_L,\, 0,\, \cdots,\, 0\}_{(k)}$ is the frequency response of the multi-path channel (obtained by zero-padding and K-DFT w.r.t. $\{h_t\}$), and $W[k,\, m]$ is the frequency domain AWGN. Note that when there is only one non-zero entry for h_t (single path), the resultant H_k is constant across k, and the channel is frequency-flat.

2.2 PTE in wideband WPT

PTE is undoubtedly the most intuitive metric in WPT applications. A block diagram of a generic WPT system is shown in Fig. 2.2, which illuminates the components of the end-to-end PTE in WPT, including (a) the DC-to-RF power conversion efficiency at the transmitter, (b) the over-the-air RF-to-RF power conversion efficiency over wireless propagation, and (c) the RF-to-DC power conversion efficiency at the receiver [6]. Mathematically, this is written as [24]

$$e=\frac{P_{\mathrm{DC}}^{\mathrm{R}}}{P_{\mathrm{DC}}^{\mathrm{T}}}=\underbrace{\frac{P_{\mathrm{RF}}^{\mathrm{T}}}{P_{\mathrm{DC}}^{\mathrm{T}}}}_{e_1}\underbrace{\frac{P_{\mathrm{RF}}^{\mathrm{R}}}{P_{\mathrm{RF}}^{\mathrm{T}}}}_{e_2}\underbrace{\frac{P_{\mathrm{DC}}^{\mathrm{R}}}{P_{\mathrm{RF}}^{\mathrm{R}}}}_{e_3}, \tag{2.11}$$

where e_1, e_2 and e_3 refer to the DC-to-RF, the RF-to-RF and the RF-to-DC power conversion efficiency respectively. In the forthcoming sectors, we introduce the main

Fig. 2.2: The block diagram of a generic WPT system.

components/factors that affect e_1, e_2 and e_3 respectively.

2.2.1 The DC-to-RF power conversion efficiency e_1

The DC-to-RF conversion efficiency represents the ratio of the power of the radiated transmit RF signal at the transmitter's antenna against the power supply at the transmitter. This efficiency is primarily determined by the key active component at the transmitter – amplifiers. Hence, at the transmitter, the power conversion efficiency of amplifiers is our focus. Specifically, we characterize the impulse response of the non-linear HPAs at the RF chain, so that the signals can be designed to adapt to the HPA's non-linearity to enhance energy harvesting performance.

Generally, a practical HPA exerts non-linear amplitude distortion and phase shift on its input signal. The HPA's distorted effect on both amplitude and phase is normally characterized by functions w.r.t the amplitude of the input signal. Mathematically, the transfer characteristic of a practical HPA can be interpreted by [88]

$$f_{\text{HPA}}(x) = \mathcal{A}(|x|)e^{j[\measuredangle x + \phi(|x|)]}, \tag{2.12}$$

where $\mathcal{A}(|x|)$ and $\phi(|x|)$ represent the amplitude distortion of the HPA and the phase shift of the HPA, both as a function of the input signal magnitude.

In this context, we define the DC-to-RF power conversion efficiency e_1 as [89]

$$e_1 = \frac{P_{\text{RF}}^{\text{T}}}{P_{\text{DC}}^{\text{T}}} \overset{(a)}{\approx} \frac{P_{\text{out,HPA}}}{P_{\text{in,HPA}} + P_{\text{DC,HPA}}} = \frac{\mathcal{E}\left\{\left|f_{\text{HPA}}(x(t))\right|^2\right\}}{\mathcal{E}\left\{\left|x(t)\right|^2\right\} + \frac{4}{\pi}A_s\mathcal{E}\left\{\left|x(t)\right|\right\}}, \tag{2.13}$$

where the approximation in (a) only considers the main power source – HPA at the transmitter. P_{DC}^{T} is formulated since the HPA involves two types of power sources, respectively (1) the input signal power[1] $P_{\text{in,HPA}} = \mathcal{E}\left\{\Re\{x(t)\}^2\right\} = \frac{1}{2}\mathcal{E}\left\{\left|x(t)\right|^2\right\}$, and (2) the DC power supply for amplification[2] $P_{\text{DC,HPA}} = \frac{2}{\pi}A_s\mathcal{E}\left\{\left|f_{\text{HPA}}(x(t))\right|\right\}$. $P_{\text{out,HPA}} = \mathcal{E}\left\{\Re\{f_{\text{HPA}}(x(t))\}^2\right\} = \frac{1}{2}\mathcal{E}\left\{\left|f_{\text{HPA}}(x(t))\right|^2\right\}$ is the power of the radiated transmit RF signal to propagate through the wireless channels.

To make the designed signals less susceptible to HPA's non-linearity, literature has proposed methods such as PAPR reduction [1, 90], distortion power minimization [90] and out-of-band leakage power reduction [91] when designing the input signals. These papers provide initial insights that wideband signals with high peaks might be more vulnerable to HPA's non-linearities.

2.2.2 The RF-to-RF power conversion efficiency e_2

The RF-to-RF power conversion efficiency is the power ratio of the received RF signal at the receive antennas against the radiated transmit RF signal at the transmit antennas. The efficiency mainly characterizes the impulse response of the multi-path wireless propagation channels.

Based on the radiated transmit RF signal after HPA $f_{\text{HPA}}(x(t))$ in (2.12), the received RF signal after channel propagation, from (2.2), is analytically expressed in the following complex form

$$y(t) = \sum_{l=1}^{L} \alpha_l e^{j\zeta_l} f_{\text{HPA}}(x(t-\tau_l)), \tag{2.14}$$

[1]Note that the pre-defined signals, i.e., $x(t)$, are in their analytically-friendly complex forms, whose transmit/receive signals in reality being their real counterparts, i.e., $\Re\{x(t)\}$. The analytical (complex) form simplifies the transfer characteristic expression for HPA as shown in (2.12) and channel propagation as shown in (2.2). However, when analyzing their power level in WPT, we focus on their real signal transmission.

[2]We use a generalized PE approximation for all Class B HPAs (feature high PE) in [89].

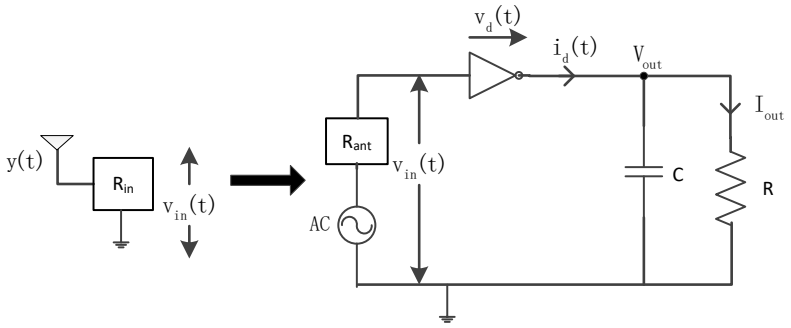

Fig. 2.3: The rectenna circuit of the EH in WPT.

which gives the RF-to-RF power conversion efficiency by

$$e_2 = \frac{P_{\mathrm{RF}}^{\mathrm{R}}}{P_{\mathrm{RF}}^{\mathrm{T}}} = \frac{\mathcal{E}\left\{\left|y(t)\right|^2\right\}}{\mathcal{E}\left\{\left|f_{\mathrm{HPA}}(x(t))\right|^2\right\}}, \tag{2.15}$$

where $P_{\mathrm{RF}}^{\mathrm{T}} = \mathcal{E}\left\{\Re\{y(t)\}^2\right\} = \frac{1}{2}\mathcal{E}\left\{\left|y(t)\right|^2\right\}$.

The RF-to-RF conversion efficiency is the earliest explored topic for wideband WPT due to its simplicity. Adapting to the channels, literature shows that the optimal solution of maximizing e_2 is to allocate all the power $P_{\mathrm{RF}}^{\mathrm{T}}$ to the sub-carrier with the strongest channel at $f_{\mathrm{HPA}}(x(t))$ [1].

2.2.3 The RF-to-DC power conversion efficiency e_3

Similarly to the DC-to-RF power conversion efficiency, the RF-to-DC power conversion efficiency e_3 is also mainly limited by the non-linear component at the receiver, i.e., the non-linear rectenna.

At the EH of WPT, the real wireless signal $\Re\{y(t)\}$ is picked up and converted into DC via a rectenna. We model the non-linear rectenna based on [1] whose equivalent circuit is depicted in Fig. 2.3. In this circuit, the receiving antenna, after picking up the RF signals, functions as a voltage source with average power $\mathcal{E}\left\{\Re\{y(t)\}^2\right\}$ and an inner impedance R_{ant}. Assume that the rectenna circuit's input impedance R_{in} matches with R_{ant}, in which

case R_{in} completely absorbs the power available from the antenna. Hence, denoting the source voltage as $v_s(t)$, we have $v_s(t)=2\Re\{y(t)\}\sqrt{R_{\text{ant}}}$, and the input voltage fed into the rectenna is $v_{\text{in}}(t)=v_s(t)/2=\Re\{y(t)\}\sqrt{R_{\text{ant}}}$, as shown on the right hand side of Fig. 2.3.

In Fig. 2.3, the rectenna is composed of a diode and a low pass filter (LPF) [3]. The transfer characteristic of the diode is written as $i_d(t)=i_s\exp\{v_d(t)/(nv_t)-1\}$ with $v_d(t)=v_{\text{in}}(t)-V_{\text{out}}$ (V_{out} is the output DC voltage of the rectenna) assuming a small signal model. To simplify the characteristic function in the optimization, the current $i_d(t)$ is approximated by Taylor expansion at point $-V_{\text{out}}$. This gives $i_d(t)=\sum_{i=0}^{\infty}k_i v_{\text{in}}^i(t)=\sum_{i=0}^{\infty}k_i' R_{\text{ant}}^{\frac{i}{2}}\Re\{y(t)\}^i$, where k_i' is the i^{th} order Taylor coefficient. Then, $i_d(t)$ passes through an LPF where its high-frequency components are filtered out before being fed into the load R. Assume that the LPF filters out all the high-frequency harmonic components in $i_d(t)$ ideally. Since the expectation of high-frequency components over time is 0, at the load R, we have $I_{\text{out}}=\mathcal{E}\{i_d(t)\}=\sum_{i=0,\text{ even}}^{i}k_i' R_{\text{ant}}^i\mathcal{E}\left\{\Re\{y(t)\}^i\right\}$ where the second equation comes from [1]. To maximize the generated power at the load R is equivalent to maximize the current at the load R, i.e., I_{out}, which, from [1], is in proportion to the following scaling term

$$z_{\text{DC}}\triangleq k_2 R_{\text{ant}}\mathcal{E}\left\{\Re\{y(t)\}^2\right\}+k_4 R_{\text{ant}}^2\mathcal{E}\left\{\Re\{y(t)\}^4\right\}, \tag{2.16}$$

with $k_2=0.0034$ and $k_4=0.3829$ [1]. (2.16) only reserves the second[4] and the fourth order terms of the Taylor approximation, which have been able to capture the non-linear properties of the rectenna.

Finally, the RF-to-DC power conversion efficiency is proportional to

$$e_3=\frac{P_{\text{DC}}^{\text{R}}}{P_{\text{RF}}^{\text{R}}}\propto\frac{z_{\text{DC}}^2 R}{\mathcal{E}\left\{\left|y(t)\right|^2\right\}}. \tag{2.17}$$

[3]We adopt the simplest resistor-capacitor LPF circuit at the EH. The LPF is assumed to be able to remove all the high-frequency harmonic components of the multi-sine signal after the non-linear diode at the rectenna.

[4]If only reserving the second order Taylor expansion term, the generated power at the load R would be a linear function of the received RF signals, i.e., the rectenna features linear impulse response.

Sufficient research has optimized the wideband signals for WPT and emphasized the non-linearity of the EH. Generally, it is shown that exploiting the EH's non-linearity boosts the energy harvesting performance, where the EH shows a particular preference for high PAPR wideband signals.

2.3 Wideband signal processing for radar

This section provides fundamental preliminaries of radar knowledge to facilitate our future model construction and derivations, with a particular focus on OFDM radar.

Radar systems can be broadly categorized into two main types: radar detection and radar estimation. In radar detection, we decide the existence/number of target(s). In radar estimation, various resources are utilized to determine specific target characteristics: (a) spatial resources to estimate the target angle, (b) bandwidth resources to estimate the target range, and (c) time-domain resources to estimate target velocity, etc. Since our paper focuses on designing wideband signals – characteristically expressed in the frequency and time domains – we will specifically concentrate on the radar range-velocity estimation in the following.

2.3.1 Radar system model

Fig. 2.4 depicts a generic mono-static radar system for range-velocity estimation, where the radar transceiver performs both the transmitting and receiving to sense a point target. Assume the radar transceiver transmits a signal $x(t)$, which is reflected by a target at a range of R with a velocity of v. Then, at the receiving antenna, the picked-up echoes are written as [66]

$$y(t) = x(t-\tau)\exp\{j\pi f_D t\}, \tag{2.18a}$$

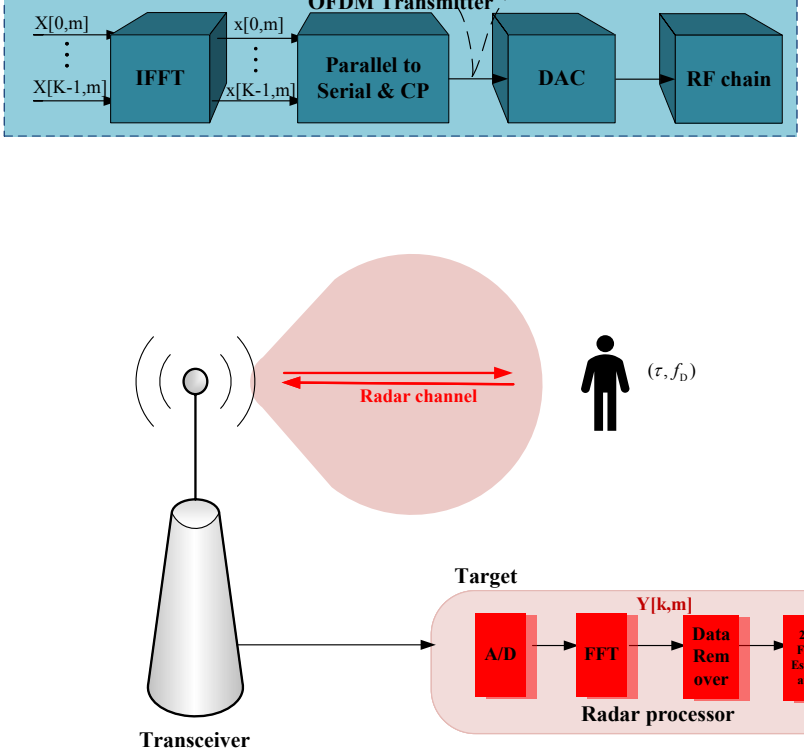

Fig. 2.4: A generic OFDM radar system.

$$\tau = \frac{2R}{c}, \text{ the round-trip delay} \tag{2.18b}$$

$$f_{\mathrm{D}} = \frac{2f_{\mathrm{c}}v}{c}, \text{ the Doppler frequency,} \tag{2.18c}$$

where c is the speed of light and f_{c} is the carrier frequency.

In practical systems with limited bandwidth and observation time, estimating τ and f_{D} leads to resolution issues, i.e., two targets are not distinguishable if their delay and Doppler shift difference are smaller than [66]

$$\Delta\tau = \frac{1}{B}, \tag{2.19a}$$

$$\Delta f_{\mathrm{D}} = \frac{B}{K_{\mathrm{T}}M}, \tag{2.19b}$$

where $K_{\mathrm{T}}M$ is the OFDM observation period per radar estimation. Hence, from (2.19), we re-express the parameters to be estimated in the following form

$$\tau = (n_0 + n_\epsilon)\Delta\tau, \tag{2.20a}$$

$$f_{\mathrm{D}} = (v + v_\epsilon)\Delta f_{\mathrm{D}}, \tag{2.20b}$$

where (n_0, v_0) represents the integer delay-Doppler bin w.r.t the well-defined resolutions in (2.19), and is often the estimation object. On the other hand, n_ϵ and v_ϵ represent the fractional delay and Doppler corresponding to the resolutions in (2.19). While n_ϵ and v_ϵ are not the estimation focus of the thesis, their effect on estimating (n_0, v_0) will be assessed.

2.3.2 OFDM radar processing

OFDM has found its potential to achieve precise range-velocity estimation with a highly efficient 2D-FFT processor. The 2D-FFT processor of OFDM radar is also shown to be the maximal-likelihood (ML) estimator fixing the resolutions of $\Delta\tau$ and Δf_{D} as in (2.19).

The conventional 2D-FFT is constructed based on the ideal assumption that the target is located exactly on the on-grid range-velocity bins, i.e., $n_\epsilon = 0$ and $v_\epsilon = 0$ from (2.20). On this basis, a single-target radar system can be viewed as a single path wireless propagation environment with delay $n_0\Delta\tau$ and Doppler shift $v_0\Delta f_{\mathrm{D}}$. Then, following (2.8), the radar return at the transceiver (after ADC) is given by [66]

$$y_{\mathrm{CP}}[n, m] = a x_{\mathrm{CP}}(t-\tau) e^{j2\pi f_{\mathrm{D}} t}|_{t=(n+K_T m)/B} \tag{2.21a}$$

$$= a x_{\mathrm{CP}}[n-n_0, m] e^{j2\pi \frac{f_{\mathrm{D}} n}{B}} e^{j2\pi \frac{v_0 m}{M}} + w[n, m] \tag{2.21b}$$

$$\approx a x_{\mathrm{CP}}[n-n_0, m] e^{j2\pi \frac{v_0 m}{M}} + w[n, m], \tag{2.21c}$$

where $a \in \mathbb{C}$ is the scattering coefficient of the target, assumed to be unchanged throughout the OFDM block. In (2.21b), the received samples after ADC lack information on the fractional n_ϵ when we assume the rectangular basis for the OFDM signal in (2.6) at DAC. Moreover, n_ϵ is often disregarded in OFDM radar literature with the assumption of perfect time synchronization at ADC to avoid inter-carrier interference. Hence, the target delay is simply assumed to be on-grid [92]. In (2.21c), we approximate $e^{j2\pi f_{\mathrm{D}} n/B} \approx 1$, since typically $f_{\mathrm{D}} \ll B$. Finally, we assume $w[n, m] \sim \mathcal{CN}(0, \sigma_{\mathrm{N}}^2)$ is the

AWGN. After removing the CP, we get the following receive sub-pulses [66]

$$y[n,\, m] \approx a x[n-n_0,\, m] e^{j2\pi \frac{v_0 m}{M}} + w[n,\, m], \tag{2.22}$$

where $x[n-n_0,\, m]$ represents a circular shift of n_0 similarly as the communication propagation in Section 2.1. After a K-point FFT, we get the frequency-domain symbol [66]

$$Y[k,\, m] = a X[k,\, m] e^{-j2\pi \frac{n_0 k}{K}} e^{j2\pi \frac{v_0 m}{M}} + W[k,\, m], \tag{2.23a}$$

$$W[k,\, m] \sim \mathcal{CN}(0,\, \sigma_{\mathrm{N}}^2). \tag{2.23b}$$

The terms that carry n_0 and v_0 in (2.23a) respectively form a typical K-DFT and M-IDFT across OFDM sub-carriers and OFDM symbols. In this context, the ML estimator of n_0 and v_0 has been proved to boil down to the following 2D-FFT processor [66, 92]

$$(\widehat{n},\, \widehat{v}) = \underbrace{\arg\, \min}_{(n,\, v)} \sum_{k,m} Y[k,m] e^{j2\pi \frac{nk}{K}} e^{-j2\pi \frac{vm}{M}}. \tag{2.24}$$

2.4 Input distribution of wideband signals in communications

While wideband signals (i.e., OFDM) have shown their appropriateness in communications, sensing and WPT, integrating these functionalities can reveal differing preferences for the input symbol $X[k,m]$. As discussed in Section 1.1, WPT and radar prefer deterministic input symbols, requiring $X[k,m]$ to align with their optimal solutions. On the contrary, for communications, $X[k,m]$ is expected to be as random as possible to carry information bits. This diversity presents a deterministic-random trade-off between communications and other functionalities.

To visualize the deterministic-random trade-off, optimizing the symbols w.r.t their input

distribution becomes a viable solution. [93] initializes the input distribution optimization of the CSs in WIPT, i.e., the symbol mean (as a counterpart of the unmodulated signals in [28]) and the symbol variance (as a counterpart of the modulated signals in [28]) of each sub-carrier assuming Gaussian distribution, and achieves a larger WIPT C-P region than [28] by assuming asymmetric Gaussian input. The optimal input distribution in [93] not only enhances the performance region in WIPT but also uncovers fundamental trade-offs between different functions, namely, powering prefers high absolute symbol means, and a further performance region gain is observed when using asymmetric non-zero mean complex Gaussian distribution.

Similar insights can be inferred in DFRC because radar also prefers constant envelopes (i.e., magnitudes) which are supported by symbol means of the input distribution. Inspired by this, this thesis classifies the CSs dependent on whether their constellations to embed the random data result in varying magnitudes or not, namely, constant magnitude input distribution and varying magnitude input distribution.

2.4.1 Constant magnitude input distribution and the communication achievable rates

Constant magnitude input distribution refers to the class of constellations where the symbol magnitude remains constant regardless of the random information, i.e., phase shift keying (PSK). For an Q-ary PSK modulation scheme, the phases of symbols take on one of Q possible values $2\pi q/Q$ for $q=0, \cdots, Q-1$, with constant magnitude across constellation points.

When it comes to designing the input distribution of a Q-ary PSK in OFDM, two parts are involved, respectively (a) the probability mass vector (PMV) of the Q constellation points – denoted by $\mathbf{p}=[p_1, \cdots, p_Q]$, and (b) the magnitude (representing the power allocation) of the constellation points across OFDM sub-carriers and OFDM symbols –

denoted by $p_{k,m}=|X[k,m]|^2$. The maximal achievable rate of an Q-ary PSK constellation is $\log Q$ bits/symbol [94], achieved by a uniform PMV.

2.4.2 Variable magnitude input distribution and the communication achievable rates

For higher communication rate requirements, a Q-ary quadrature amplitude modulation (QAM) constellation is more appropriate. A large Q (e.g., 256-QAM) makes the input distribution of QAM symbols asymptotic to a CSCG distribution, i.e., $X[k,m]\sim\mathcal{CN}\left(0,\sigma_{k,m}^2\right)$, which gives the OFDM communication capacity in the following form [87]

$$C(\sigma_{k,m}^2)=\frac{1}{KM}\sum_{k,m}\log\left(1+\frac{|h_k|^2\sigma_{k,m}^2}{B\sigma_{\mathrm{C}}^2}\right), \tag{2.25}$$

where h_k is the complex response of the communication channel at the k^{th} OFDM sub-carrier, and σ_{C}^2 is the noise power spectrum density.

However, when integrating with other functionalities such as wireless sensing and WPT, we wish to exhibit the deterministic-randomness trade-off by introducing non-zero means, and hence we generalize the input distribution to a non-zero mean asymmetric Gaussian distribution, i.e., $\Re\{X[k,m]\}\sim\mathcal{N}\left(\mu_{\mathrm{R},k,m},\sigma_{\mathrm{R},k,m}^2\right)$ and $\Re\{X[k,m]\}\sim\mathcal{N}\left(\mu_{\mathrm{I},k,m},\sigma_{\mathrm{I},k,m}^2\right)$, which gives the following communication achievable rate [93]

$$C(\sigma_{k,m}^2)=\frac{1}{2KM}\sum_{k,m}\left[\log\left(1+\frac{2K|h_k|^2\sigma_{\mathrm{R},k,m}^2}{B\sigma_{\mathrm{C}}^2}\right)+\log\left(1+\frac{2K|h_k|^2\sigma_{\mathrm{I},k,m}^2}{B\sigma_{\mathrm{C}}^2}\right)\right]. \tag{2.26}$$

Chapter 3

Signal Design for Wireless Power Transfer with High Power Amplifier Non-linearities

While the wideband signal has been designed to maximize the harvested power in WPT literature accounting for the EH's non-linearity, the non-linearity at the transmitter, particularly the active source HPA, is disregarded. This chapter optimizes a multi-sine waveform at the input of HPA to maximize the harvested DC power considering both HPA's and EH's non-linearities. Two optimization models are formulated based on whether the frequencies of the input waveform are concentrated within the transmit passband or not. Analysis and simulations show that, while EH's non-linearity boosts the power harvesting performance with multi-sine signals, HPA's non-linearity degrades the harvested power. Hence, the optimal waveform shifts from a multi-sine signal that exploits EH's non-linearity to a single-sine signal that reduces HPA's detrimental non-linear distortion as the operational regime of WPT becomes more sensitive to HPA's non-linearity and less sensitive to EH's non-linearity (and inversely). Simultaneously, operating towards HPA's non-linear regime by increasing the input signal power benefits

the harvested power since HPA's DC power supply is better exploited, whereas the end-to-end power transfer efficiency might decrease because of HPA's increasing non-linear degradation. Throughout the simulations, the proposed waveforms show significant gain over those not accounting for HPA's non-linearity, especially in frequency-flat channels. We also compare the two proposed waveforms and show that the severity of HPA's non-linearity dictates which of the two proposed waveforms is more beneficial.

3.1 Introduction

To combat HPA's non-linear effect at the waveform-design level, mainly two lines of methods have been proposed in the existing literature, namely designing signals less susceptible to HPA's non-linearity and by means of digital pre-distortion (DPD). The former method decreases the input signals' exposure to HPA's non-linear region, such as PAPR reduction [90], distortion power minimization [90] and out-of-band leakage power reduction [91]. Indeed, PAPR reduction has been introduced as a transmit waveform constraint in WPT in [1]. However, this class of methods might be less efficient in the system-level design since they dismiss HPA's transfer characteristics and the HPA's interaction with wireless channels as well as receivers [90, 91]. In contrast, DPD pre-distorts the desired input signal according to HPA's transfer characteristics to linearize the transfer function of the joint pre-distorter-and-HPA structure or, if not achievable, to minimize the non-linear effect of the HPA on system performance [95]. In the latter case, the signal is designed to adapt to the whole system's characteristics.

This chapter adopts the pre-distortion method and designs the input waveform at the HPA to boost the end-to-end power harvesting performance in wideband WPT, accounting for both HPA's and EH's non-linearities. Overall, the contributions of the chapter are summarized as follows.

(1) First, we model a practical WPT system accounting for both the transmitter's and

receiver's non-linearities as in Fig. 3.1. Specifically, the transmitter is composed of a non-linear HPA and a band pass filter (BPF). The input waveform of HPA $x^{\text{in}}(t)$ (namely the input waveform) becomes $x^{\text{HPA}}(t)$ after amplification and turns into the transmit waveform at the antenna $x^{\text{tr}}(t)$ (namely the transmit waveform) after the BPF. $x^{\text{tr}}(t)$, after propagation over the air, is picked up and transferred into DC power by a non-linear rectenna which has been modelled in Section 2.2. On this basis, we develop the relationship between the input waveform $x^{\text{in}}(t)$ and the transmit waveform $x^{\text{tr}}(t)$ at the transmitter, and maximize the generated DC power given power constraints on both $x^{\text{in}}(t)$ (the input power constraint) and $x^{\text{tr}}(t)$ (the transmit power constraint). This contrasts with all prior works on waveform optimization in [1, 6, 13, 16] that consider non-linearity at the rectenna side only.

(2) Second, we formulate and solve a first optimization model where the input waveform shares the same frequencies as those of the transmit waveform (within the transmit passband), abbreviated as Model I. The problem formulation aims for the optimal input waveform, while introducing the transmit waveform as auxiliary variables so that the harvested DC power (objective function) and the transmit power constraint are expressed in a much simpler form as a function of the transmit waveform. The relationship between the input waveform and the transmit waveform is clarified through multiple non-linear equalities. Model I realises an end-to-end optimization where the input waveform is optimized directly.

(3) Third, we formulate and solve a second optimization model where the carrier frequencies of the input waveform are not restricted by the transmit pass band of the BPF, abbreviated as Model II. The aim is to utilize the out-of-band frequencies of the BPF at the input waveform to avoid power loss at BPF. This assumption allows the input power constraint to be re-formulated as a function of the transmit waveform, making the whole optimization w.r.t the transmit waveform only. Consequently, this halves the number of variables in Model I and avoids numerous non-linear equality constraints, making the

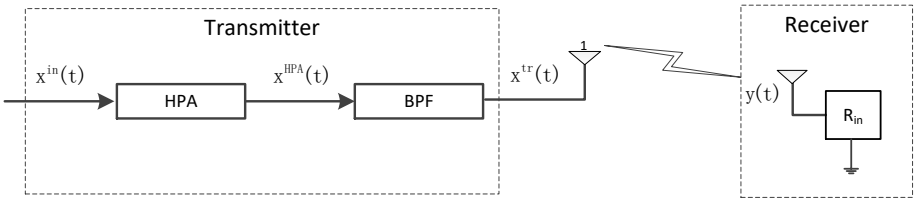

Fig. 3.1: The system model of WPT with non-linear HPA and EH.

program more stable in large-scale problems.

(4) Fourth, we provide simulation results to verify the performance gain of waveforms that consider both HPA's and EH's non-linearities over those that ignore HPA's non-linearity. We also demonstrate that HPA's non-linearity degrades the harvested power in WPT significantly, especially in frequency-flat channels. Simulations also show that operating towards the non-linear regime of HPA exploits its DC power supply more and gives larger harvested power and higher end-to-end PTE. However, if further increasing the input signal power to where the HPA saturates, the harvested power saturates and the end-to-end PTE decreases correspondingly. To compensate for the power loss from HPA's non-linearity, the proposed waveforms show a tendency to allocate power to fewer sub-carriers as the HPA experiences more non-linearity. Given this general tendency, the performance of Model I and Model II are similar in most simulations, while scenarios are also explored to make the waveform from Model I (or Model II) slightly more advantageous than the other by adapting the HPA's parameters and operating region.

Organization: Section 3.2 introduces the system model and Section 3.3 models the signal relationships after the non-linear HPA and rectenna. Section 3.4 addresses the waveform optimization given two different assumptions on the frequencies of the input signal at HPA. Section 3.5 evaluates the performance and Section 3.6 concludes the work.

3.2 WPT system and signal model

In this section, we model and define the wireless signals at each stage of a practical WPT architecture with a non-linear HPA at the transmitter and a non-linear EH at the receiver. At the transmitter, the generated multi-carrier signal is first amplified and then filtered before being transmitted. The RF signal then propagates through Rayleigh fading channels and is picked up by the EH for the purpose of power harvesting. The functioning of different building blocks will be clarified in Section 3.3.

We consider a single-user single-input-single-output (SISO) multi-carrier WPT system as depicted in Fig. 3.1. The non-linear analysis of the transmitter starts from the input of the non-linear HPA at the RF chain. For simplicity, we denote the complex input signal at the HPA as $x^{\text{in}}(t)$, the complex signal at the output of the HPA as $x^{\text{HPA}}(t)$, and the complex transmit signal as $x^{\text{tr}}(t)$. We consider a multi-carrier scenario where K evenly frequency-spaced sub-carriers are finally transmitted. The frequency of the k^{th} ($k=0, \cdots, K-1$) transmitted sub-carrier of $x^{\text{tr}}(t)$ is $f_k = f_0 + (k-1)\Delta_f$ with f_0 being the lowest sub-carrier frequency and Δ_f being the frequency spacing.

At the transmitter, the complex input signal at the HPA is expressed as [1]

$$x^{\text{in}}(t) = \sum_{k\in\kappa^{\text{in}}} w_k^{\text{in}} e^{j2\pi f_k t} \triangleq \sum_{k\in\kappa^{\text{in}}} \left(\overline{w}_k^{\text{in}} + j\widehat{w}_k^{\text{in}}\right) e^{j2\pi f_k t}, \tag{3.1}$$

where $w_k^{\text{in}} = \overline{w}_k^{\text{in}} + j\widehat{w}_k^{\text{in}}$ denotes the complex weight of the k^{th} sub-carrier of $x^{\text{in}}(t)$, with $\overline{w}_k^{\text{in}}$ and $\widehat{w}_k^{\text{in}}$ being the corresponding real and imaginary part respectively. κ^{in} is the integer set which indicates the frequency range that $x^{\text{in}}(t)$ involves [1,2].

[1] If $\kappa^{\text{in}} = [0, \cdots, K-1]$, $x^{\text{in}}(t)$ will have the same activated frequencies with the transmit signal $x^{\text{tr}}(t)$. In this case, the signal after HPA, $x^{\text{HPA}}(t)$, will incur out-of band frequencies (at the multiples of Δ_f due to the HPA's non-linearity) which are going to be filtered out by the BPF in Fig. 3.1. This corresponds to the first model (Model I) in the chapter.

[2] Otherwise, if assuming the input signal with unlimited bandwidth, i.e., $\kappa^{\text{in}} = [-f_0/\Delta_f + 1, \cdots, \infty]$, the input signal $x^{\text{in}}(t)$ can be designed to concentrate the frequency components of $x^{\text{HPA}}(t)$ within the transmit pass band. In this case, the signal after the non-linear HPA can pass the BPF in a lossless way, i.e., $x^{\text{HPA}}(t) = x^{\text{tr}}(t)$. This corresponds to the second model (Model II) in the chapter.

Similarly, the complex signal at the output of the HPA is given by

$$x^{\mathrm{HPA}}(t) = \sum_{k\in\kappa^{\mathrm{HPA}}} w_k^{\mathrm{HPA}} e^{j2\pi f_k t} = \sum_{k\in\kappa^{\mathrm{HPA}}} \left(\overline{w}_k^{\mathrm{HPA}} + j\widehat{w}_k^{\mathrm{HPA}}\right) e^{j2\pi f_k t}, \tag{3.2}$$

where $w_k^{\mathrm{HPA}} = \overline{w}_k^{\mathrm{HPA}} + j\widehat{w}_k^{\mathrm{HPA}}$ denotes the complex weight of the k^{th} sub-carrier of $x^{\mathrm{HPA}}(t)$, with $\overline{w}_k^{\mathrm{HPA}}$ and $\widehat{w}_k^{\mathrm{HPA}}$ being the corresponding real and imaginary part respectively [3]. κ^{HPA} represents the frequency set that $x^{\mathrm{HPA}}(t)$ involves.

The BPF then removes the frequencies out of the transmit passband $[f_0,\, f_0+(K-1)\Delta_f]$, which gives the complex transmit signal in the following

$$x^{\mathrm{tr}}(t) = \sum_{k=0}^{K-1} w_k^{\mathrm{tr}} e^{j2\pi f_k t} = \sum_{k=0}^{K-1} \left(\overline{w}_k^{\mathrm{tr}} + j\widehat{w}_k^{\mathrm{tr}}\right) e^{j2\pi f_k t}, \tag{3.3}$$

where $x^{\mathrm{tr}}(t)$ is the complex transmit signal. $w_k^{\mathrm{tr}} = \overline{w}_k^{\mathrm{tr}} + j\widehat{w}_k^{\mathrm{tr}}$ denotes the complex weight of the k^{th} sub-carrier of $x^{\mathrm{tr}}(t)$, with $\overline{w}_k^{\mathrm{tr}}$ and $\widehat{w}_k^{\mathrm{tr}}$ being the corresponding real and imaginary part respectively [4].

The transmitted signal $x^{\mathrm{tr}}(t)$ then propagates through a multipath channel with L paths, whose l^{th} path features amplitude suppression α_l, path delay τ_l, and phase shift ζ_l. Then the received signal is written as (from Section 2.1 [1])

$$y(t) = \sum_{k=0}^{K-1} \left[\sum_{l=1}^{L} \alpha_l e^{j2\pi(-f_k\tau_l+\zeta_l)} \right] w_k^{\mathrm{tr}} e^{j2\pi f_k t} \triangleq \sum_{k=0}^{K-1} h_k w_k^{\mathrm{tr}} e^{j2\pi f_k t}, \tag{3.4}$$

where $h_k = \sum_{l=1}^{L} \alpha_l e^{j2\pi(-f_k\tau_l+\zeta_l)}$ denotes the equivalent complex channel that the k^{th} sub-carrier experiences during transmission.

[3] $\overline{w}_k^{\mathrm{HPA}}/\widehat{w}_k^{\mathrm{HPA}}$ for $\forall\ k$ is a function of $\{\overline{w}_k^{\mathrm{in}},\, \widehat{w}_k^{\mathrm{in}}\}$, and can be viewed as a simplified form of $\overline{w}_k^{\mathrm{HPA}}\left(\{\overline{w}_k^{\mathrm{in}},\, \widehat{w}_k^{\mathrm{in}}\}\right)/\widehat{w}_k^{\mathrm{HPA}}\left(\{\overline{w}_k^{\mathrm{in}},\, \widehat{w}_k^{\mathrm{in}}\}\right)$, whose relationship is characterized later in Section 3.3.

[4] $\overline{w}_k^{\mathrm{tr}}/\widehat{w}_k^{\mathrm{tr}}$ for $\forall\ k$ is a function of $\{\overline{w}_k^{\mathrm{in}},\, \widehat{w}_k^{\mathrm{in}}\}$, and can be viewed as a simplified form of $\overline{w}_k^{\mathrm{tr}}\left(\{\overline{w}_k^{\mathrm{in}},\, \widehat{w}_k^{\mathrm{in}}\}\right)/\widehat{w}_k^{\mathrm{tr}}\left(\{\overline{w}_k^{\mathrm{in}},\, \widehat{w}_k^{\mathrm{in}}\}\right)$.

3.3 HPA and rectenna analytical models

This section characterizes the relationship between signals at different stages in Section 3.2 based on the transfer characteristics of the non-linear HPA and rectenna in Section 2.2, and characterizes the final harvested power explicitly.

3.3.1 HPA model characterization and insights

The input signal $x^{\text{in}}(t)$ is amplified and filtered before being transmitted. Deviating from our discussions in Section 2.2, we focus on a classic solid-state-power amplifier (SSPA) modelled in [88], which is defined by

$$f_{\text{HPA}}\big(x(t)\big) = \mathcal{A}\big(\big|x(t)\big|\big)e^{j[\angle x(t)+\phi(|x(t)|)]}, \tag{3.5a}$$

$$\text{with } \mathcal{A}(x) = \frac{Gx}{\left[1+\left(\frac{Gx}{A_s}\right)^{2\beta}\right]^{\frac{1}{2\beta}}}, \tag{3.5b}$$

$$\phi(x) = 0, \tag{3.5c}$$

where function $\mathcal{A}(x)$ represents the amplitude distortion of the HPA, and function $\phi(x)$ characterizes the phase shift of the HPA. G is the small-signal amplifier gain of SSPA, A_s is the saturation voltage of SSPA, and β (positive) is the smoothing parameter of SSPA. (3.5c) indicates that the SSPA does not have phase shift. Features of SSPA are clarified in Fig. 3.2, where the small signal input is offered an amplifier gain of $G=2$ approximately while the large signal input is shown to be suppressed below the saturation voltage of SSPA (A_s). The larger the smoothing parameter β, the higher the linearity SSPA exhibits below its saturation voltage.

From (3.5a), the complex signal at the output of the HPA (SSPA) becomes the following

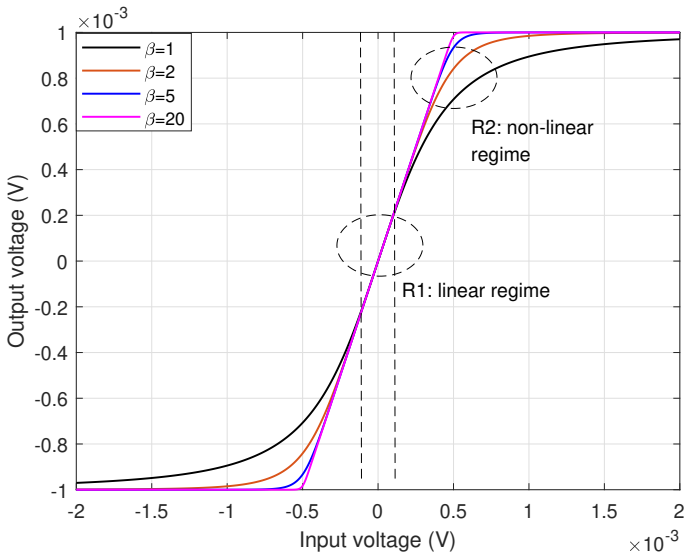

Fig. 3.2: SSPA's input-output voltage characteristics. $A_s = 1$ mV; $G = 2$ and $\beta = \{1, 2, 5, 20\}$. R_1 is the linear regime (small input signal); R_2 is the non-linear regime.

expression [88]

$$x^{\mathrm{HPA}}(t) = f_{\mathrm{HPA}}\left(x^{\mathrm{in}}(t)\right) = \frac{Gx^{\mathrm{in}}(t)}{\left[1+\left(\frac{G|x^{\mathrm{in}}(t)|}{A_s}\right)^{2\beta}\right]^{\frac{1}{2\beta}}}. \tag{3.6}$$

3.3.2 HPA non-linearity and efficiency measurement

This section introduces several important metrics to characterize HPA's operating status so that in future analysis, we can build a relationship between the severity of HPA's non-linearity and the power harvesting performance. Firstly, we evaluate HPA's non-linearity numerically. An effective measurement is the output backoff (OBO) at HPA's operating point, which is defined as the ratio of HPA's saturation power ($P_{\mathrm{s,HPA}}$) to HPA's output signal power ($P_{\mathrm{out,HPA}}$) as in the following [89]

$$\mathrm{OBO} \triangleq \frac{P_{\mathrm{s,HPA}}}{P_{\mathrm{out,HPA}}} \triangleq \frac{A_s^2}{\mathcal{E}\{|x^{\mathrm{HPA}}(t)|^2\}}. \tag{3.7}$$

Smaller OBO indicates more severe HPA's non-linearity.

Besides the severity of non-linearity, power efficiency (PE) is also an important metric to

evaluate HPA's performance, defined as the ratio of HPA's output signal power ($P_{\text{out,HPA}}$) to HPA's DC power supply ($P_{\text{DC,HPA}}$). Here, we use a generalized PE approximation for all Class B HPAs (feature high PE) in [89], which is given by

$$\text{PE} \triangleq \frac{P_{\text{out,HPA}}}{P_{\text{DC,HPA}}} \triangleq \frac{\pi}{4} \frac{\mathcal{E}\{|x^{\text{HPA}}(t)|^2\}}{A_s \mathcal{E}\{|x^{\text{HPA}}(t)|\}}. \tag{3.8}$$

From (3.8), the PE of HPA describes the efficiency of using HPA's DC power supply. Usually, higher input signal power drives more efficient use of HPA's DC power supply and produces higher output signal power, until HPA's saturation voltage is reached where the produced output power saturates.

One limitation of the PE metric in (3.8) is that it does not account for the power source from the input signal. When HPA approaches its saturation region, the output power is comparable to or even less than the input power of HPA, while the PE in (3.8) keeps increasing. In this context, a more effective metric of HPA efficiency is the added PE (APE), where the power of the input signal is also taken into consideration. APE is defined as the ratio of the produced signal power (the difference between HPA's output power and HPA's input power ($P_{\text{in,HPA}}$), i.e., $P_{\text{ADE}} \triangleq P_{\text{out,HPA}} - P_{\text{in,HPA}}$) to HPA's DC power supply, and is given by [89]

$$\text{APE} \triangleq \frac{P_{\text{ADE}}}{P_{\text{DC,HPA}}} \triangleq \frac{\pi}{4} \frac{\mathcal{E}\{|x^{\text{HPA}}(t)|^2 - |x^{\text{in}}(t)|^2\}}{A_s \mathcal{E}\{|x^{\text{HPA}}(t)|\}}. \tag{3.9}$$

APE gives us an insight into HPA's PE considering all its power sources, including the input signal power and the DC power supply. In contrast with the PE metric in (3.8) which prefers high input power, the APE in (3.9) might decrease or even become negative when the input signal power increases to HPA's highly non-linear operation regime, where the produced output power saturates regardless of the input signal power. In this condition, increasing the input signal power is not beneficial in terms of the whole system's overall PTE, and APE would then become an important measurement metric.

The PE and APE metrics are introduced to give an insight into where the performance gain of the proposed waveforms comes from when analyzing the simulations in section 3.5.

3.3.3 Analytical insights into HPA and BPF outputs

In this section, we assume that the input waveform of HPA has the same activated frequencies as those of the transmit waveform, from f_0 to f_{K-1} with frequency spacing Δ_f. In this case, due to HPA's non-linearity, $x^{\text{HPA}}(t)$ incurs distorted weights across the in-band frequencies and intermodulation leakage across the out-of band frequencies at the multiples of Δ_f. For the convenience of the following optimization formulation, we need to explicitly build the relationship between HPA's input waveform $x^{\text{in}}(t)$, HPA's output waveform $x^{\text{HPA}}(t)$ and the transmit waveform $x^{\text{tr}}(t)$.

Towards this, our main idea is to sample $x^{\text{HPA}}(t)$ in (3.6) and then conduct FT. Starting from (3.6), we first re-express $x^{\text{HPA}}(t)$ as in the following

$$\begin{aligned} x^{\text{HPA}}(t) &= f_{\text{HPA}}\left(x_B^{\text{in}}(t)e^{j2\pi f_0 t}\right) = \frac{G x_B^{\text{in}}(t)}{\left[1+\left(\frac{G|x_B^{\text{in}}(t)|}{A_s}\right)^{2\beta}\right]^{\frac{1}{2\beta}}} e^{j2\pi f_0 t} \\ &= \frac{G}{\left[1+\left(\frac{G|x_B^{\text{in}}(t)|}{A_s}\right)^{2\beta}\right]^{\frac{1}{2\beta}}} x^{\text{in}}(t) \triangleq \mathcal{A}\left(\left|x_B^{\text{in}}(t)\right|\right) x^{\text{in}}(t), \end{aligned} \tag{3.10}$$

where $x_B^{\text{in}}(t) = x^{\text{in}}(t)e^{-2j\pi f_0 t}$ is the baseband signal of $x^{\text{in}}(t)$. (3.10) indicates that the spectrum of $x^{\text{HPA}}(t)$ is the convolution between the spectrum of the baseband function $\mathcal{A}\left(\left|x_B^{\text{in}}(t)\right|\right)$ and the spectrum of $x^{\text{in}}(t)$. The latter part is easily represented by $\left\{w_k^{\text{in}}\right\}$.

Remark 1. *We avoid sampling directly on $\mathcal{A}(|x^{in}(t)|)$ since a large number of samples would be required to achieve our desired frequency resolution Δ_f given its carrier frequency f_0, following the Nyquist sampling theorem. This will result in higher complexity or numerous equality constraints in the following optimization problem. On the other hand, sampling the baseband signal $\mathcal{A}(|x_B^{in}(t)|)$ is more practical.*

To sample $\mathcal{A}\big(\big|x_B^{\rm in}(t)\big|\big)$, we assume its major frequency components are approximately limited within [0, $f_A^{\max}$] with $f_A^{\max}=\kappa' K\Delta_f$. κ' is the non-linear extending coefficient larger than 1. Then, based on the Nyquist sampling theorem, we set the sampling frequency at $2K\kappa'\Delta_f$. Further, to guarantee the frequency resolution of Δ_f, we take $2K\kappa'$ samples, corresponding to a sampling interval of $t_s=T/2K\kappa'$ for a period of $T=1/\Delta_f$. Denote the $2K\kappa'$ samples of $\mathcal{A}\big(\big|x_B^{\rm in}(t)\big|\big)$ by $\{A[n]\}$ for $n=0,\cdots,2K\kappa'-1$. From (3.10), we obtain the following spectrum for $x^{\rm HPA}(t)$

$$\begin{aligned}\big\{w_k^{\rm HPA}\big\}&=\mathcal{F}\big\{x^{\rm HPA}(t)\big\}|_{f=k\Delta_f+f_0}=\mathcal{F}\big\{\mathcal{A}\big(\big|x_B^{\rm in}(t)\big|\big)x^{\rm in}(t)\big\}|_{f=k\Delta_f+f_0}\\&=\frac{1}{2\kappa'}{\rm DFT}\{A[n]\}\circledast_{2K\kappa'}\big\{w_k^{\rm in}\big\},\end{aligned}\tag{3.11}$$

with

$$A[n]=\frac{G}{[1+(\frac{Gx_B^{\rm in}(t_n)}{A_s})^{2\beta}]^{\frac{1}{2\beta}}},\tag{3.12}$$

where $A[n]=\mathcal{A}\big(x_B^{\rm in}(t_n)\big)$ with $t_n=nt_s$. $n=0,\cdots,2K\kappa'-1$.

From (3.11), we express the real part of $w_k^{\rm HPA}$ by

$$\begin{aligned}\overline{w}_k^{\rm HPA}=&\frac{1}{2K\kappa'}\sum_{k_1=0}^{K-1}\overline{w}_{k_1}^{\rm in}\sum_{n=0}^{2K\kappa'-1}A[n]\cos\left(\frac{2\pi n(k-k_1)_{2K\kappa'}}{2K\kappa'}\right)\\&-\frac{1}{2K\kappa'}\sum_{k_1=0}^{K-1}\widehat{w}_{k_1}^{\rm in}\sum_{n=0}^{2K\kappa'-1}A[n]\sin\left(\frac{2\pi n(k-k_1)_{2K\kappa'}}{2K\kappa'}\right).\end{aligned}\tag{3.13}$$

Similarly, we express the imaginary part of $w_k^{\rm HPA}$ by

$$\begin{aligned}\widehat{w}_k^{\rm HPA}=&\frac{1}{2K\kappa'}\sum_{k_1=0}^{K-1}\overline{w}_{k_1}^{\rm in}\sum_{n=0}^{2K\kappa'-1}A[n]\sin\left(\frac{2\pi n(k-k_1)_{2K\kappa'}}{2K\kappa'}\right)\\&+\frac{1}{2K\kappa'}\sum_{k_1=0}^{K-1}\widehat{w}_{k_1}^{\rm in}\sum_{n=0}^{2K\kappa'-1}A[n]\cos\left(\frac{2\pi n(k-k_1)_{2K\kappa'}}{2K\kappa'}\right).\end{aligned}\tag{3.14}$$

Assume that $x^{\rm HPA}(t)$ is then transmitted into an ideal BPF with its passband [f_0, f_0+

$(K-1)\Delta_f]$, and becomes the transmitted RF signal $x^{\text{tr}}(t)$. The transfer characteristics of this ideal BPF is given by

$$w_k^{\text{tr}} = \begin{cases} w_k^{\text{HPA}}, & k \in [0,...,K-1], \\ 0, & \text{otherwise.} \end{cases} \tag{3.15}$$

3.3.4 Rectenna model

At the receiver, the wireless signal $y(t)$ is picked up and is converted into DC via a rectenna. Based on the non-linear rectenna model introduced in Section 2.2, the generated DC current at the output of the rectenna is in proportion to [1]

$$\begin{aligned} & z_{\text{DC}}\big(\{\overline{w}_k^{\text{tr}}\}, \{\widehat{w}_k^{\text{tr}}\}\big) \\ \triangleq & k_2 R_{\text{ant}} \mathcal{E}\big\{\Re\{y(t)\}^2\big\} + k_4 R_{\text{ant}}^2 \mathcal{E}\big\{\Re\{y(t)\}^4\big\} && \text{(3.16a)} \\ = & \frac{k_2 R_{\text{ant}}}{2} \sum_{n=0}^{N-1} |w_k^{\text{tr}} h_k|^2 + \frac{3k_4 R_{\text{ant}}^2}{8} \sum_{\substack{k_0,k_1,k_2,k_3 \\ k_0+k_1=k_2+k_3}} h_{k_0} w_{k_0}^{\text{tr}} h_{k_1} w_{k_1}^{\text{tr}} h_{k_2}^* w_{k_2}^{\text{tr}^*} h_{k_3}^* w_{k_3}^{\text{tr}^*}, && \text{(3.16b)} \end{aligned}$$

with $k_2 = 0.0034$ and $k_4 = 0.3829$ [1]. (3.16a) comes from [1] and is detailed in Chapter 2.2.1, which only reserves the second[5] and the fourth order terms of the Taylor approximation of the rectenna transfer characteristics, which have been able to capture the non-linearities. (3.16b) comes from [1], and is achieved since any high-frequency harmonic components in $\Re\{y(t)\}^2$ (e.g., $h_{k_0} w_{k_0}^{\text{tr}} h_{k_1}^* w_{k_1}^{\text{tr}^*} e^{-j2\pi(k_0-k_1)\Delta f t}$ for $k_0 \neq k_1$) or $\Re\{y(t)\}^4$ (e.g., $h_{k_0} w_{k_0}^{\text{tr}} h_{k_1} w_{k_1}^{\text{tr}} h_{k_2}^* w_{k_2}^{\text{tr}^*} h_{k_3}^* w_{k_3}^{\text{tr}^*} e^{-j2\pi(k_0+k_1-K_2-k_3)\Delta f t}$ for $k_0+k_1 \neq k_2+k_3$), after taking expectations over time, equal to 0.

Given the scaling term z_{DC}, the end-to-end PTE of the WPT system (based on the

[5] If only reserving the second order Taylor expansion term, the generated power at the load R would be a linear function of the received RF signals, in which case the preferred waveform for the EH shifts from multi-carrier transmission to single-carrier transmission [1]. Considering HPA's preference for low-PAPR waveforms, there would be no trade-off on waveform design between the linear EH and the non-linear HPA, and the optimal waveform becomes single-carrier transmission regardless of HPA's non-linearity.

Preliminaries in Section 2.2) is in proportion to

$$\mathrm{PTE} \propto \frac{z_{\mathrm{DC}}^2 R}{P_{\mathrm{in,HPA}} + P_{\mathrm{DC,HPA}}}, \tag{3.17}$$

where $P_{\mathrm{in,HPA}} + P_{\mathrm{DC,HPA}}$ refers to all the power supply at the transmitter[6]. Specifically, $P_{\mathrm{in,HPA}} = \frac{1}{2}\mathcal{E}\left\{\left|x^{\mathrm{in}}(t)\right|^2\right\}$ is the signal power at the HPA input and $P_{\mathrm{in,HPA}} = \frac{2A_{\mathrm{s}}}{\pi}\mathcal{E}\left\{\left|x^{\mathrm{in}}(t)\right|\right\}$ is the DC power supply at HPA.

3.4 Optimizations

In this section, we first formulate a generalized optimization problem w.r.t. the input waveform of HPA to maximize the harvested power, subjective to the input[7] and transmit power constraints[8]. Then, for tractability, we specify and solve the generalized optimization model based on two different assumptions on the frequencies of the input waveform at HPA:

1) Model I: the input waveform at HPA has the same multi-sine frequencies as the transmit waveform within the transmit pass band.

2) Model II: the input waveform at HPA uses the frequencies out of the transmit pass band to adaptively design the input waveform that can pass the BPF after HPA in a lossless way.

[6]We use z_{DC} to represent the harvested power in the chapter because it is directly in proportion to the generated DC current at the load and thus is in proportion to the harvested power. Similarly, the PTE defined in (3.17) is in proportion to the real end-to-end PTE and will represent the end-to-end PTE in the chapter. The end-to-end PTE is put forward to highlight an appropriate operating region of the WPT system, where both a satisfying harvested energy and an efficient power transfer efficiency are achieved.

[7]The input power constraint at HPA avoids poor amplifier PE which occurs when the power of HPA's input signal gets close to or exceeds HPA's saturation power.

[8]The transmit power constraint at antennas limits the RF exposure to human beings over propagation.

3.4.1 Problem formulation

We first formulate a general form of the optimization problem to maximize the harvested power in WPT in the following

$$\max_{\{\overline{w}_k^{\text{in}}\},\,\{\widehat{w}_k^{\text{in}}\}} \quad z_{\text{DC}}\big(\{\overline{w}_k^{\text{tr}}\},\,\{\widehat{w}_k^{\text{tr}}\}\big), \tag{3.18a}$$

$$\text{s.t.} \quad \frac{1}{2}\sum_{n\in\kappa^{\text{in}}} |\overline{w}_k^{\text{in}}|^2+|\widehat{w}_k^{\text{in}}|^2 \le P_{\text{in}}^{\max}, \tag{3.18b}$$

$$\frac{1}{2}\sum_{k=0}^{K-1} |\overline{w}_k^{\text{tr}}|^2+|\widehat{w}_k^{\text{tr}}|^2 \le P_{\text{tr}}^{\max}, \tag{3.18c}$$

where $P_{\text{in}}^{\max}$ and $P_{\text{tr}}^{\max}$ are the input power constraint and the transmit power constraint respectively. Next, we optimize problem (3.18) under both models.

3.4.2 Model I: input waveform with the same frequencies as the transmit waveform

As it has been mentioned, Model I solves the optimization problem where the input waveform at HPA assumes to have the same frequencies as the transmit waveform. In this context, for tractability, we collect both the input waveform of HPA $\big(\{\overline{w}_k^{\text{in}}\},\,\{\widehat{w}_k^{\text{in}}\}\big)$ and the transmit waveform $\big(\{\overline{w}_k^{\text{tr}}\},\,\{\widehat{w}_k^{\text{tr}}\}\big)$ into optimization variables so that the objective function and the transmit power constraint are in a much simpler form. The relationship between $\big(\{\overline{w}_k^{\text{in}}\},\,\{\widehat{w}_k^{\text{in}}\}\big)$ and $\big(\{\overline{w}_k^{\text{tr}}\},\,\{\widehat{w}_k^{\text{tr}}\}\big)$ is derived in (3.13) and (3.14). Intuitively, the auxiliary variables $\big(\{\overline{w}_k^{\text{tr}}\},\,\{\widehat{w}_k^{\text{tr}}\}\big)$ enable us to handle the original high complexity in (3.18a) and (3.18c) separately. The corresponding optimization problem is written as

$$\max_{\substack{\{\overline{w}_k^{\text{in}}\},\,\{\widehat{w}_k^{\text{in}}\}\\ \{\overline{w}_k^{\text{tr}}\},\,\{\widehat{w}_k^{\text{tr}}\}}} \quad z_{\text{DC}}\big(\{\overline{w}_k^{\text{tr}}\},\,\{\widehat{w}_k^{\text{tr}}\}\big), \tag{3.19a}$$

$$\text{s.t.} \quad \frac{1}{2}\sum_{k=0}^{K-1} \overline{w}_k^{\text{in}^2}+\widehat{w}_k^{\text{in}^2} \le P_{\text{in}}^{\max}, \tag{3.19b}$$

$$\frac{1}{2}\sum_{k=0}^{K-1}\overline{w}_k^{\mathrm{tr}^2}+\widehat{w}_k^{\mathrm{tr}^2}\leq P_{\mathrm{tr}}^{\max}, \tag{3.19c}$$

$$\overline{w}_k^{\mathrm{HPA}} \text{ in (3.13)}, \tag{3.19d}$$

$$\widehat{w}_k^{\mathrm{HPA}} \text{ in (3.14)}, \tag{3.19e}$$

where the constraints in(3.19d) and(3.19e) feature high non-linearity.

Problem (3.19) maximizes a convex objective (Appendix 3.7.1), which is solved by successive convex programming (SCP). In SCP, the objective term is linearly approximated by its first-order Taylor expansion at a fixed operating point, forming a new tractable optimization problem whose optimal solution is used as a new operating point of the next iteration. The procedure is repeated until two successive solutions are close enough and can be viewed as the solution of problem (3.19). Assume $\big(\{\overline{w}_k^{\mathrm{in},(l-1)}\}, \{\widehat{w}_k^{\mathrm{in},(l-1)}\}, \{\overline{w}_k^{\mathrm{tr},(l-1)}\}, \{\widehat{w}_k^{\mathrm{tr},(l-1)}\}\big)$ are the values of the operating point at the beginning of the l^{th} iteration. Then, $z_{\mathrm{DC}}\big(\{\overline{w}_k^{\mathrm{tr}}\}, \{\widehat{w}_k^{\mathrm{tr}}\}\big)$ at the l^{th} iteration is linearly approximated as [96]

$$z_{\mathrm{DC}}^{(l)}\big(\{\overline{w}_k^{\mathrm{tr}}\}, \{\widehat{w}_k^{\mathrm{tr}}\}\big)=\sum_{k=0}^{K-1}\overline{\alpha}_k^{(l)}\overline{w}_k^{\mathrm{tr}}+\widehat{\alpha}_k^{(l)}\widehat{w}_k^{\mathrm{tr}}, \tag{3.20}$$

where $\Big(\{\overline{\alpha}_k^{(l)}\}, \{\widehat{\alpha}_k^{(l)}\}\Big)$ are the first-order Taylor coefficients at the l^{th} iteration and are shown in(3.21) and (3.22).

Correspondingly, problem (3.19) can be transformed into [97]

$$\max_{\substack{\{\overline{w}_k^{\mathrm{in}}\},\,\{\widehat{w}_k^{\mathrm{in}}\}\\ \{\overline{w}_k^{\mathrm{tr}}\},\,\{\widehat{w}_k^{\mathrm{tr}}\}}} \quad z_{\mathrm{DC}}^{(l)}(\{\overline{w}_k^{\mathrm{tr}}\}, \{\widehat{w}_k^{\mathrm{tr}}\}), \tag{3.23a}$$

$$\text{s.t.} \quad g_i^{\mathrm{I}}(\{\overline{w}_k^{\mathrm{in/tr}}\}, \{\widehat{w}_k^{\mathrm{in/tr}}\})\leq 0,\ i=\{1,\,2\}, \tag{3.23b}$$

$$g_i^{\mathrm{E}}(\{\overline{w}_k^{\mathrm{in/tr}}\}, \{\widehat{w}_k^{\mathrm{in/tr}}\})=0,\ i=\{1,\,\cdots,\,2K\}, \tag{3.23c}$$

where $g_{1/2}^{\mathrm{I}}(\{\overline{w}_k^{\mathrm{in/tr}}\}, \{\widehat{w}_k^{\mathrm{in/tr}}\})$ refers to the inequality constraint in (3.19b) and (3.19c)

$$\overline{\alpha}_k^{(l)} = k_2 R_{\text{ant}} \overline{w}_k^{\text{tr},(l-1)} |h_k|^2 + \frac{3k_4 R_{\text{ant}}}{2} \Bigg[\overline{w}_k^{\text{tr},(l-1)} |w_k^{\text{tr},(l-1)}|^2 |h_k|^4 + \sum_{k_1} 2\overline{w}_k^{\text{tr},(l-1)} |w_{k_1}^{\text{tr},(l-1)}|^2 |h_k|^2 |h_{k_1}|^2 + \sum_{\substack{k_2+k_3=2n \\ k_2 \neq k_3}} \Re\{ w_k^{\text{tr},(l-1)} w_{k_2}^{\text{tr},(l-1)^*} w_{k_3}^{\text{tr},(l-1)^*} h_k^2 h_{k_2}^* h_{k_3}^* \} + \sum_{\substack{k=-k_1+k_2+k_3 \\ n \neq k_1 \neq k_2 \neq k_3}} \Re\{ w_{k_1}^{\text{tr},(l-1)} w_{k_2}^{\text{tr},(l-1)^*} w_{k_3}^{\text{tr},(l-1)^*} h_k h_{k_1} h_{k_2}^* h_{k_3}^* \} \Bigg], \tag{3.21}$$

$$\widehat{\alpha}_k^{(l)} = k_2 R_{\text{ant}} \widehat{w}_k^{\text{tr},(l-1)} |h_k|^2 + \frac{3k_4 R_{\text{ant}}}{2} \Bigg[\widehat{w}_k^{\text{tr},(l-1)} |w_k^{\text{tr},(l-1)}|^2 |h_k|^4 + \sum_{k_1} 2\widehat{w}_k^{\text{tr},(l-1)} |w_{k_1}^{\text{tr},(l-1)}|^2 |h_k|^2 |h_{k_1}|^2 - \sum_{\substack{k_2+k_3=2n \\ k_2 \neq k_3}} \Im\{ w_k^{\text{tr},(l-1)} w_{k_2}^{\text{tr},(l-1)^*} w_{k_3}^{\text{tr},(l-1)^*} h_k^2 h_{k_2}^* h_{k_3}^* \} - \sum_{\substack{k=-k_1+k_2+k_3 \\ n \neq k_1 \neq k_2 \neq k_3}} \Im\{ w_{k_1}^{\text{tr},(l-1)} w_{k_2}^{\text{tr},(l-1)^*} w_{k_3}^{\text{tr},(l-1)^*} h_k h_{k_1} h_{k_2}^* h_{k_3}^* \} \Bigg]. \tag{3.22}$$

respectively. $g_i^{\text{E}}(\{\overline{w}_k^{\text{in/tr}}\}, \{\widehat{w}_k^{\text{in/tr}}\})$ refers to all the equality constraints in (3.19d) and (3.19e).

Problem (3.23) can be solved by sequential quadratic programming (SQP). SQP is extended from solving the KKT conditions of an arbitrary non-linear program by using the Newton-Raphson (NR) method (named by KKT-NR) [96]. To summarize, in KKT-NR, the NR method is used to solve the KKT functions, where iterative sub-programs are formulated with a closed-form solution and a fast-convergence property. SQP resembles KKT-NR, by constructing a linearly constrained quadratic problem (LCQP) that has the same result as the corresponding KKT-NR sub-program at each iteration. The LCQP sub-program at each iteration approximates the original problem at the initialized point. In this way, SQP achieves the convergence property of the KKT-NR's method [97].

Since SQP derives from the KKT-NR, it also preserves the features of the KKT-NR method, i.e., it is not a feasible point (points that satisfy the constraints) method. Con-

Algorithm 1: SCP-SQP

1. **Input**: $(\{\overline{w}_k^{\text{in}}\}, \{\widehat{w}_k^{\text{in}}\}, \{\overline{w}_k^{\text{tr}}\}, \{\widehat{w}_k^{\text{tr}}\})^{(0)}$, $\epsilon_0 > 0$, $l \leftarrow 1$
2. **Output**: $(\{\overline{w}_k^{\text{in}}\}, \{\widehat{w}_k^{\text{in}}\}, \{\overline{w}_k^{\text{tr}}\}, \{\widehat{w}_k^{\text{tr}}\})^{\star}$
3. **Repeat** until $|z_{\text{DC}}(\{\overline{w}_k^{\text{tr}}\}, \{\widehat{w}_k^{\text{tr}}\})^{(l)} - z_{\text{DC}}\big(\{\overline{w}_k^{\text{tr}}\}, \{\widehat{w}_k^{\text{tr}}\}\big)^{(l-1)}| < \epsilon_0$
   - 3.1 Compute $(\{\overline{\alpha}_k\}, \{\widehat{\alpha}_k\})^{(l)}$ using (3.21) and (3.22) at the operating point $\big(\{\overline{w}_k^{\text{tr}}\}, \{\widehat{w}_k^{\text{tr}}\}\big)^{(l-1)}$
   - 3.2 Compute $(\{\overline{w}_k^{\text{in}}\}, \{\widehat{w}_k^{\text{in}}\}, \{\overline{w}_k^{\text{tr}}\}, \{\widehat{w}_k^{\text{tr}}\})^{(l)}$ in problem (3.23) using SQP
   - 3.3 Update $(\{\overline{w}_k^{\text{in}}\}, \{\widehat{w}_k^{\text{in}}\}, \{\overline{w}_k^{\text{tr}}\}, \{\widehat{w}_k^{\text{tr}}\})^{\star}$ as the current solution
   - 3.4 Calculate $z_{\text{DC}}(\{\overline{w}_k^{\text{tr}}\}, \{\widehat{w}_k^{\text{tr}}\})^{(l)}$ and update $l \leftarrow l+1$

sequently, the results from LCQP sub-programs might not meet the constraints in the original program. This is beneficial in the sense that the initialized points can be picked more randomly. However, it also gives the probability that one of the sub-programs gives a solution far from being feasible and requires more iterations to come back. In this condition, terminating the iteration in advance might result in worse performance. This drawback makes the results susceptible to the initialized points and the functions' derivatives, especially in large-scale problems or in problems with numerous constraints. Hence, when solving problem (3.19), we handle the corresponding objective function iteratively by SCP at the first stage. In this way, we construct a simpler problem for SQP and obtain more sophisticated initialized points for SQP in each iteration of SCP. The structure is named by SCP-SQP as in Algorithm 1.

Remark 2. *The solution in Model I can also be applied to other HPA models or to more sophisticated architectures in WPT, such as when considering clipping DACs at the transmitter. First, using DFT and sampling to develop the relationship between waveforms at different stages is easy to extend to other architectures. Second, the proposed SCP-SQP algorithm is also robust to solving various non-linear programs and can be extended to multi-input multi-output (MIMO) or multi-user scenarios.*

3.4.3 Model II: input waveform utilizing out-of-band frequencies

We now utilize the out-of band frequencies at HPA's input so that after HPA, the signal $x^{\mathrm{HPA}}(t)$ can pass the BPF in a lossless way. Another benefit of this model is that under a lossless BPF scenario, the input power can be written as a function of the transmit waveform, similarly to the objective function and the transmit power constraint. Hence, compared with Model I, Model II formulates the optimization problem w.r.t. the transmit waveform only, which releases the numerous non-linear equality constraints between the input waveform and the transmit waveform. Specifically, we form the optimization problem in the following

$$\max_{\left\{\overline{w}_k^{\mathrm{tr}}\right\},\,\left\{\widehat{w}_k^{\mathrm{tr}}\right\}} \quad z_{\mathrm{DC}}\big(\left\{\overline{w}_k^{\mathrm{tr}}\right\},\,\left\{\widehat{w}_k^{\mathrm{tr}}\right\}\big), \tag{3.24a}$$

$$\text{s.t.} \quad \frac{1}{2TG^2}\int_T\Big[\big|x^{\mathrm{tr}}(t)\big|^{-2\beta}-A_s^{-2\beta}\Big]^{-\frac{1}{\beta}}dt\leq P_{\mathrm{in}}^{\max}, \tag{3.24b}$$

$$\frac{1}{2}\sum_{k=0}^{K-1}\overline{w}_k^{\mathrm{tr}^2}+\widehat{w}_k^{\mathrm{tr}^2}\leq P_{\mathrm{tr}}^{\max}, \tag{3.24c}$$

where (3.24b) is shown to be the input power constraint in Appendix 3.7.2. (3.24b) is proved convex in Appendix 3.7.3.

Problem (3.24) maximizes a convex objective function, which can be solved by SCP. Similarly to the SCP-SQP method, at the l^{th} iteration, problem (3.24) is approximated by [96]

$$\max_{\left\{\overline{w}_k^{\mathrm{tr}}\right\},\,\left\{\widehat{w}_k^{\mathrm{tr}}\right\}} \quad z_{\mathrm{DC}}^{(l)}\big(\left\{\overline{w}_k^{\mathrm{tr}}\right\},\,\left\{\widehat{w}_k^{\mathrm{tr}}\right\}\big), \tag{3.25a}$$

$$\text{s.t.} \quad \text{(3.24c)}, \quad \text{(3.24b)}. \tag{3.25b}$$

Problem (3.25) is a convex problem with a linear objective function and two non-linear convex inequality constraints. However, problem (3.25) involves a highly non-linear

inequality constraint in (3.24c), which can be efficiently solved by the IP method. The IP method uses the Barrier's method to bring the inequality constraints into the objective function equivalently and then solves the resultant program by using Gradient Descend (GD) method.

Specifically, the non-linear constraints in (3.25b), according to the Barrier's method, are omitted by reformulating problem (3.25) into [98]

$$\min_{\left\{\overline{w}_k^{\mathrm{tr}}\right\},\,\left\{\widehat{w}_k^{\mathrm{tr}}\right\}} \quad -z_{\mathrm{DC}}^{(l)}(\left\{\overline{w}_k^{\mathrm{tr}}\right\},\,\left\{\widehat{w}_k^{\mathrm{tr}}\right\})+\sum_{i=1}^{2} I_{-}(f_{c,i}(\left\{\overline{w}_k^{\mathrm{tr}}\right\},\,\left\{\widehat{w}_k^{\mathrm{tr}}\right\})), \tag{3.26}$$

where

$$I_{-}(x)=\begin{cases} 0, & x\leq 0, \\ \infty, & x>0, \end{cases} \tag{3.27a}$$

$$f_{c,1}(\left\{\overline{w}_k^{\mathrm{tr}}\right\},\,\left\{\widehat{w}_k^{\mathrm{tr}}\right\})=\frac{\int_T \left[|x^{\mathrm{tr}}(t)|^{-2\beta}-A_s^{-2\beta}\right]^{-\frac{1}{\beta}} dt}{2TG^2}-P_{\mathrm{in}}^{\max}, \tag{3.27b}$$

$$f_{c,2}(\left\{\overline{w}_k^{\mathrm{tr}}\right\},\,\left\{\widehat{w}_k^{\mathrm{tr}}\right\})=\frac{1}{2}\sum_{k=0}^{K-1} \overline{w}_k^{\mathrm{tr}^2}+\widehat{w}_k^{\mathrm{tr}^2}-P_{\mathrm{tr}}^{\max}. \tag{3.27c}$$

Further, to make problem (3.26) differentiable, $I_{-}(x)$ is approximated as [98]

$$\widehat{I}_{-}(x)=-\frac{1}{t}\log(-x), \tag{3.28}$$

where t is a parameter that sets the accuracy of the approximation. The larger the t, the closer the $\widehat{I}_{-}(x)$ is to $I_{-}(x)$.

Consequently, for a specific t, the optimization problem (3.26) becomes

$$\min_{\left\{\overline{w}_k^{\mathrm{tr}}\right\},\,\left\{\widehat{w}_k^{\mathrm{tr}}\right\}} \quad -z_{\mathrm{DC}}^{(l)}(\left\{\overline{w}_k^{\mathrm{tr}}\right\},\,\left\{\widehat{w}_k^{\mathrm{tr}}\right\})-\sum_{i=1}^{2} \frac{\log(-f_{c,i}(\left\{\overline{w}_k^{\mathrm{tr}}\right\},\,\left\{\widehat{w}_k^{\mathrm{tr}}\right\}))}{t}, \tag{3.29}$$

which can be solved by GD methods such as Newton's Method [98]. The whole algorithm,

Algorithm 2: SCP-IP

1. **Input**: $\left(\{\overline{w}_k^{\rm tr}\}, \{\widehat{w}_k^{\rm tr}\}\right)^{(0)}$,$\epsilon_0 > 0$,$l \leftarrow 1$
2. **Output**: $\left(\{\overline{w}_k^{\rm tr}\}, \{\widehat{w}_k^{\rm tr}\}\right)^{\star}$
3. **Repeat** until $|z_{\rm DC}\left(\{\overline{w}_k^{\rm tr}\}, \{\widehat{w}_k^{\rm tr}\}\right)^{(l)} - z_{\rm DC}\left(\{\overline{w}_k^{\rm tr}\}, \{\widehat{w}_k^{\rm tr}\}\right)^{(l-1)}| < \epsilon_0$
   - 3.1 Compute $(\{\overline{\alpha}_k\}, \{\widehat{\alpha}_k\})^{(l)}$ using (3.21) and (3.22) at the operating point $\left(\{\overline{w}_k^{\rm tr}\}, \{\widehat{w}_k^{\rm tr}\}\right)^{(l-1)}$ using Taylor expansion
   - 3.2 Compute $\left(\{\overline{w}_k^{\rm tr}\}, \{\widehat{w}_k^{\rm tr}\}\right)^{(l)}$ using Algorithm 3
   - 3.3 Update $\left(\{\overline{w}_k^{\rm tr}\}, \{\widehat{w}_k^{\rm tr}\}\right)^{\star} \leftarrow \left(\{\overline{w}_k^{\rm tr}\}, \{\widehat{w}_k^{\rm tr}\}\right)^{(l)}$
   - 3.4 Calculate $z_{\rm DC}(\{\overline{w}_k^{\rm tr}\}, \{\widehat{w}_k^{\rm tr}\})^{(l)}$ and update $l \leftarrow l+1$

Algorithm 3: IP

1. **Input**: $\left(\{\overline{w}_k^{\rm tr}\}, \{\widehat{w}_k^{\rm tr}\}\right)^{(B_0)} \leftarrow \left(\{\overline{w}_k^{\rm tr}\}, \{\widehat{w}_k^{\rm tr}\}\right)^{(l-1)}$, $t > 0$, $\mu_B > 0$, $\epsilon_B > 0$
2. **Output**: $\left(\{\overline{w}_k^{\rm tr}\}, \{\widehat{w}_k^{\rm tr}\}\right)^{(l)}$
3. **Repeat** until $2/t \geq \epsilon_B$
   - 3.1 Compute $\left(\{\overline{w}_k^{\rm tr}\}, \{\widehat{w}_k^{\rm tr}\}\right)$ by minimizing problem (3.29) using Newton's Method with initialized point $\left(\{\overline{w}_k^{\rm tr}\}, \{\widehat{w}_k^{\rm tr}\}\right)^{(B_0)}$
   - 3.2 Update $\left(\{\overline{w}_k^{\rm tr}\}, \{\widehat{w}_k^{\rm tr}\}\right)^{(l)} \leftarrow \left(\{\overline{w}_k^{\rm tr}\}, \{\widehat{w}_k^{\rm tr}\}\right)$;
   - 3.3 Update $t \leftarrow \mu_B t$,$\left(\{\overline{w}_k^{\rm tr}\}, \{\widehat{w}_k^{\rm tr}\}\right)^{(B_0)} \leftarrow \left(\{\overline{w}_k^{\rm tr}\}, \{\widehat{w}_k^{\rm tr}\}\right)^{(l)}$

named as SCP-IP, is summarized in Algorithm 2.

Remark 3. *One concern with Model II is that the correspondent input signal incurs unlimited bandwidth (equivalent to the output signal of a non-linear inverse HPA feeding the transmit waveform) and might be impractical from the implementation aspect. However, if the out-of-band frequency components of the input signal decay rapidly, the desired input signal can be approximated by cutting off those insignificant frequency components, as shown in Appendix 3.7.4.*

Remark 4. *From the mechanisms of SCP-SQP and SCP-IP, we can deduce the pros*

and cons of these two algorithms. For SCP-SQP, one of its limitations comes from the rapidly increasing number of variables and non-linear constraints given large K. Due to its origination from the KKT-NR method, this algorithm might be sensitive to bad performance, especially with large-scale problems or numerous constraints, and relies on the initialized points heavily. In contrast, the SCP-IP strategy is only constrained by two inequalities and formulates a convex sub-program in each iteration, which provides more robustness. However, its integral non-linear constraint makes the sub-program more time-consuming on the other hand. Unfortunately, it is hard to mathematically evaluate the complexity of the algorithms, especially for the SCP-IP in Model II where an integral inequality constraint is involved. However, numerous simulations show a polynomial time-complexity with the increase in the number of variables, as well as a linear rate of convergence for the SCP for both algorithms. As expected, the SCP-IP from Model II requires a longer time due to its non-linear inequality constraint but shows a tendency to be more efficient given a large number of variables[9].

3.5 Simulations

The power harvesting and the end-to-end PTE performance of the proposed waveforms are evaluated under a Wi-Fi-like scenario with $f_0 = 5.18$ GHz and bandwidth $B = 10$ MHz unless specified. We assume a static SISO setup in most simulations unless specified. The circuit at the transmitter is simplified into a non-linear HPA and a BPF. We set a 38 dBm transmit power, a 2 dBi receive antenna gain and a 58 dB path loss. For the simulation baseline of SSPA, set the smoothing parameter to $\beta = 4$, the saturation voltage to $A_s = 10$ dBV and the small-signal gain to $G = 1$ [10] without loss of generality.

[9]Both models and their corresponding optimizations can be extended to MISO scenarios in a straightforward way. This chapter focuses on SISO to avoid potential tedious subscripts. However, a MISO simulation is provided in Section V as a verification.

[10]It is noteworthy that optimizing for arbitrary G has minimal impact on the waveform intuition. In addition, simulating $G > 1$ is equivalent to adjusting other HPA parameters, such as saturation voltage and input power constraints, with the goal of modifying the signal's relative operating regime. Hence,

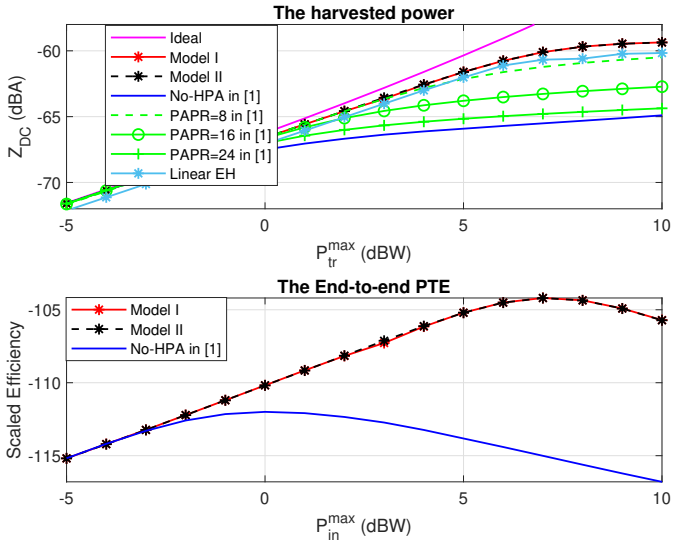

Fig. 3.3: z_{DC} with HPA's and rectenna's non-linearity and $K=8$. Ideal refers to the maximal achievable z_{DC} with an ideal HPA. Model I/II refers to the resultant waveform optimized from Model I/II considering non-linear HPA; No-HPA in [1] is to use the optimal transmit waveform from [1] directly to HPA's input, without pre-distorted to HPA's non-linearity. PAPR is to use the waveform from [1] but with PAPR constraints. 'Linear EH' refers to the optimal pre-distorted waveform that adapts to HPA's non-linearity and the WPT channel, without considering EH's linearity.

3.5.1 Frequency-flat channels

We start from frequency-flat channels to evaluate the power harvesting and end-to-end PTE performance of WPT and to uncover the waveform tendency considering both HPA's and EH's non-linearities. The frequency-flat scenario is defined as $\widetilde{h}_n=1$ for $\forall\ n$.

Fig. 3.3 plots z_{DC} (top) and the end-to-end PTE (bottom) in a frequency-flat WPT system as a function of the input/transmit power constraint ($P_{\mathrm{in}}^{\max}=P_{\mathrm{tr}}^{\max}$) using different input waveforms at the HPA, where z_{DC} of an ideal amplifier is used (the magenta line) as a benchmark. Fig. 3.3 (top) demonstrates that HPA's non-linearity significantly reduces the harvested power in WPT, especially when the transmit power increases to a level comparable with HPA's saturation power. On the other hand, the harvested power (Fig. 3.3, top) verifies the performance gain of the two end-to-end optimized waveforms

simulations in this thesis will be limited to $G=1$ with various input power budgets and saturation power in the following.

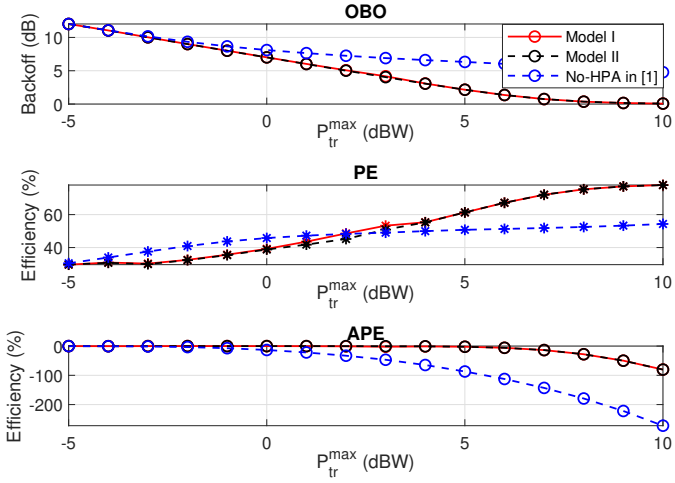

Fig. 3.4: The operating point of HPA that corresponds to Fig. 3.3. The red, black and blue curves represent the waveform from Model I, Model II and No-HPA in [1] respectively.

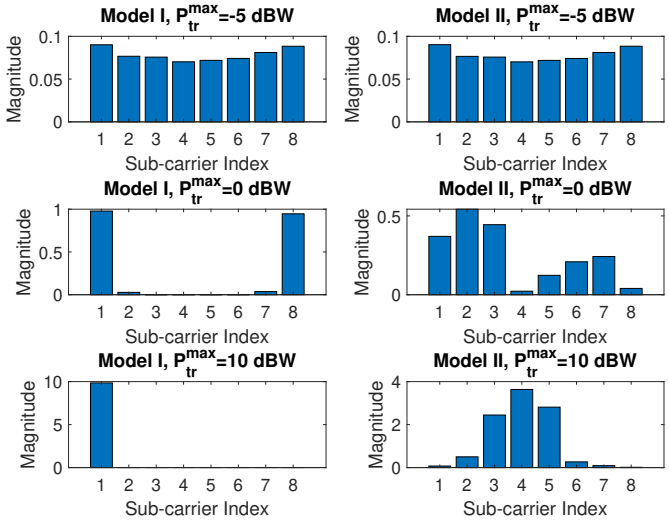

Fig. 3.5: The waveforms from the two end-to-end optimizations that correspond to Fig. 3.3, with HPA working in small signal regime, non-linear regime and saturation regime from top to the bottom.

(Model I, red, and Model II, black) over the optimal transmit waveform in [1] (the blue line) as the input of the non-linear HPA. Nevertheless, the transmit waveform with PAPR constraints (green) can compensate for HPA's non-linearity to a certain degree. As a response to Remark 3, the performance and analysis of an approximated input signal of Model II is given in Appendix 3.7.4. In addition, Fig. 3.3 (top) also plots a baseline curve whose waveform is optimized assuming a linear EH and hence is designed

to adapt to HPA's non-linearity and the WPT channel only, named as 'Linear EH'. The performance will be detailed in the following.

To gain a deeper insight into HPA's non-linear effect on the power harvesting performance and the waveform tendency, Fig. 3.3 (bottom) plots the end-to-end scaled PTE defined in (3.17). Fig. 3.4 evaluates HPA's operating points (severity of non-linearity and PE) by characterizing its OBO, PE, and APE that correspond to the simulation points in Fig. 3.3. Fig. 3.5 then plots three examples of the optimal input waveforms from Model I and Model II, respectively with HPA working in its linear, non-linear and saturation regime. Details are as follows.

In the small-signal region ($P_{\text{tr}}^{\max} < -3$ dBW, OBO > 10 dB), the HPA works in the linear regime and can be regarded as ideal, i.e. negligible power loss or out-of band frequency leakage. In this case, exploiting EH's non-linearity is crucial for enhancing the end-to-end energy harvesting performance, and hence the 'Linear EH' waveform performs the worst in Fig. 3.3 (top) as it does not account for EH's non-linearities. Also, in the small-signal regime, the waveforms obtained from Model I and Model II in Fig. 3.5 (top) overlap, both giving the maximal harvested power the same as that from the optimal transmit waveform with ideal HPA. However, in this region, the PE of HPA is low ($< 40\%$) as shown in Fig. 3.4 (middle). Increasing the input power exploits the HPA's DC power supply better, and hence gives larger PE (Fig. 3.4, middle), APE (Fig. 3.4, bottom) and also the end-to-end PTE in WPT (Fig. 3.3 bottom).

However, when the transmit power increases to over -3 dBW (OBO < 10 dB), the HPA's non-linear effect becomes non-negligible. In this non-linear region (-3 dBW $\leq P_{\text{tr}}^{\max} \leq 8$ dBW), while the harvested power still increases with the transmit power, the performance gap between different waveforms enlarges (Fig. 3.3). The waveforms from Model I and Model II give the best performance, followed by using the optimal transmit waveform with and without PAPR constraints. The reason for the performance gap is indicated in Fig. 3.4 (top), where the two end-to-end optimization waveforms provide significantly

smaller OBO, or equivalently speaking, larger output power after HPA than the No-HPA waveform in [1]. This is achieved by allocating power to fewer sub-carriers as shown in Fig. 3.5 (middle). Such an allocation exploits HPA's DC power supply better and is proved effective to compensate for HPA's non-linear degradation in Fig. 3.4 (bottom), where the HPA's APE of the proposed input waveforms of HPA (Model I and Model II) maintains the same level as the small signal regime. Consequently, we still observe an increase in the end-to-end PTE in Fig. 3.3 (bottom) for the proposed waveforms, whereas the end-to-end PTE of the No-HPA waveform starts decreasing because its high-PAPR waveform comes across severe power loss from HPA's non-linear degradation effect.

Interestingly, although in Fig. 3.3, the performance of Model I and Model II almost overlap in the non-linear region, their corresponding optimal waveforms in Fig. 3.5 (middle) are quite different from each other. Taking the point at $P_{\text{tr}}^{\max} = 0$ dBW as an example, the transmit waveform from Model I shows slightly higher PAPR than that from Model II (5.07 over 4.33) but lower transmit power (-0.01 dBW over -0.02 dBW) on the other hand. The former makes the waveform from Model I beneficial for the EH's non-linearity, while the latter indicates that the waveform from Model II passes through the HPA and BPF with less power loss, resulting in their similar power harvesting performance in the end. Such a waveform difference is attributed to their signal models. The waveform from Model II tends to have a relatively lower PAPR transmit solution because its maximal magnitude of the transmit signal, equivalent to the signal after HPA, is strictly restricted by the HPA's saturation voltage. A lower PAPR (and also the lossless BPF) makes the waveform from Model II more beneficial from the transmitter's side. In comparison, the waveform from Model I caters to the EH's non-linearity slightly better.

If further increasing the power constraint to $P_{\text{tr}}^{\max} > 8$ dBW, the HPA's saturation effect will dominate, in which condition the harvested power tends to saturate rather than increase (Fig. 3.3). In this regime, the 'Linear EH' waveform becomes promising, as the

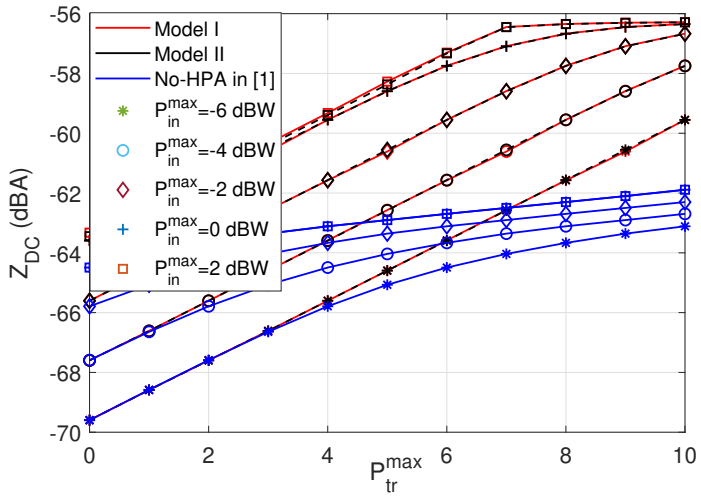

Fig. 3.6: z_{DC} of different waveforms in frequency-flat channels with different levels of the input power constraints as a function of the transmit power constraints with $K=8$.

HPA's non-linearity now plays a key role in the end-to-end energy harvesting performance. As a result, its performance surpasses all curves where only the EH's non-linearity is considered [1]. The resultant optimal input waveforms (Fig. 3.5, bottom) show a further reduction in PAPR. Despite this reduction in PAPR, Fig. 3.4 (bottom) illustrates that waveform design can no longer compensate for HPA's non-linear degradation, giving APE lower than 0. Understandably, in this region, although the harvested power (Fig. 3.3) and the HPA's PE (Fig. 3.4, middle) keep non-decreasing, the end-to-end PTE of all the waveforms drops with increasing transmit power (Fig. 3.3 bottom). This end-to-end PTE trend indicates inappropriate operating points in WPT for $P_{\mathrm{tr}}^{\max}>8$ dBW. Inspired by this, most of the following simulations are based on the operating point that gives the best overall performance in terms of both z_{DC} and the end-to-end PTE, i.e., $P_{\mathrm{tr}}^{\max}=8$ dBW for $A_s=10$ dBW and $\beta=4$.

An extension of Fig. 3.3 is shown in Fig. 3.6, where different levels of input power are compared ($P_{\mathrm{in}}^{\max}=P_{\mathrm{in}}^{\max}+\{-6,\ -4,\ -2,\ 0,\ 2\}$ dBW) in terms of the power harvesting performance and the end-to-end PTE. An indication here is that increasing the input power can compensate for HPA's non-linear degradation to some extent (Fig. 3.6). This is reasonable since larger input power gives larger transmit power at the antenna and

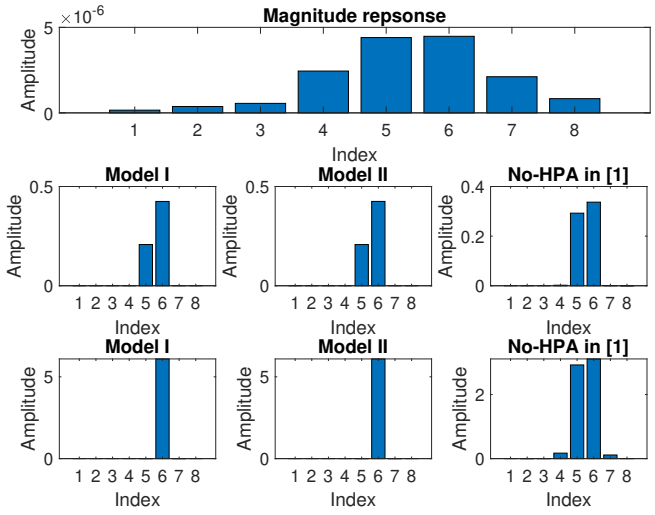

Fig. 3.7: One frequency-selective channel realization, and the corresponding optimal waveforms with $K=8$. From top to bottom, we plot the magnitude response of this channel realization, the waveform from the three models with $P_{\text{tr}}^{\max}=-5$dBW, and the waveform from the three models with $P_{\text{tr}}^{\max}=5$dBW.

therefore, larger harvested power at the receiver. However, this does not necessarily give higher end-to-end PTE since a larger input signal might suffer more severe power loss due to HPA's non-linearity.

3.5.2 Frequency-selective channels

We then evaluate the power harvesting performance of different waveforms in frequency-selective scenarios. We assume a large open space environment with an NLoS channel from model B in [99] with 18 delay taps whose power is normalized to 1. For each realization, we assume that the complex channel gain for each tap is modelled as an independent CSCG random variable, with zero mean and the variance being their normalized tap power.

As a comparison to the frequency-flat scenario, Fig. 3.7 and Fig .3.8 evaluate the waveforms' performance based on one realization of a frequency-selective channel. Fig. 3.7 (top) illustrates the magnitude response of the channel realization[11]. Fig. 3.7 (middle and

[11]We only explore the effect of CSI's magnitudes here, since the phases of channels do not affect the power harvesting performance significantly from simulations.

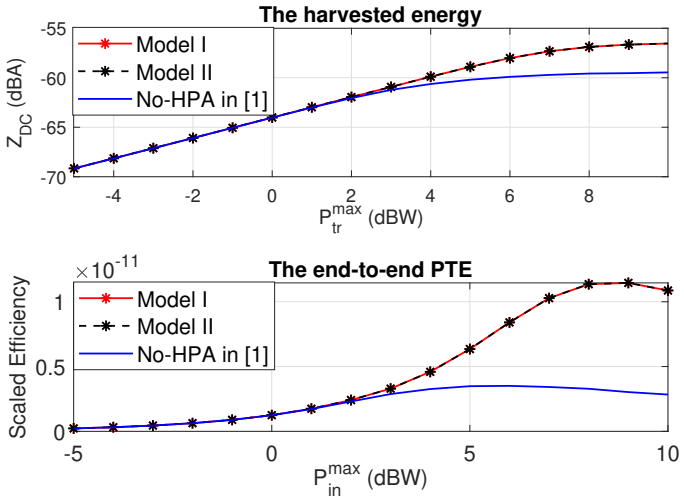

Fig. 3.8: From top to bottom, the harvested power z_{DC} and the end-to-end PTE, corresponding to Fig. 3.7.

bottom) displays the magnitude of the optimal waveforms from Model I, Model II and the No-HPA waveform in [1] in linear and non-linear region ($P_{\mathrm{in}}^{\max} = -5/5$ dBW) respectively. Fig. 3.8 plots the corresponding harvested power (top) and the end-to-end PTE (bottom).

Fig. 3.7 (middle and bottom) shows that the No-HPA waveform also features relatively lower PAPR in this frequency-selective channel realization. As a result, a smaller performance gap between the proposed waveforms and the No-HPA waveform is observed in Fig. 3.8, compared with that in Fig. 3.3. Also interestingly, with HPA's non-linearity, Fig. 3.8 (top) displays larger harvested power than that from the frequency-flat scenario in Fig. 3.3. This is reasonable since, with significant HPA's non-linearity, the proposed waveforms from Model I and Model II concentrate power on sub-carriers with the strongest channels for both frequency-flat and frequency-selective scenarios. On the other hand, the normalized frequency-selective channels offer more powerful strongest sub-carriers than the normalized frequency-flat channels. Consequently, the end-to-end PTE (Fig. 3.8, bottom) with frequency-selective channels is also significantly larger than that of the frequency-flat channels in Fig. 3.3 (bottom).

Compared with the optimal waveforms from the frequency-flat channels in Fig. 3.5, the

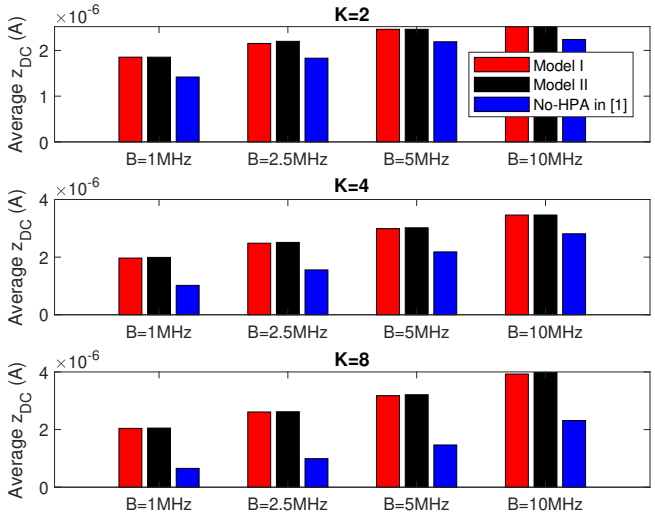

Fig. 3.9: Average z_{DC} with different bandwidth, $P_{\mathrm{in}}^{\max}=10$ dBW, $P_{\mathrm{tr}}^{\max}=8$ dBW. The red and black bars represent the waveforms from Model I and Model II respectively. The blue bar represents the No-HPA waveform in [1].

optimal waveforms from the frequency-selective channels in Fig. 3.7 do not show much difference. This is because the EH's non-linearity is preferring a lower PAPR waveform in frequency-selective scenarios, and mitigates the trade-off between the HPA's and the EH's non-linearity.

Fig. 3.9 further identifies the effect of the bandwidth on the average harvested power over hundreds of channel realizations. It demonstrates that all these three waveforms benefit from larger bandwidth, attributing to their common preference for strong channel transmission. Larger bandwidth provides more diversity between channels and thus has a larger probability of owning a more powerful strongest sub-carrier. This is highly beneficial especially when HPA's non-linearity urges single-carrier transmission. Even for the No-HPA waveform in [1] that does not consider HPA's non-linearity, transmission with larger bandwidth gives rise to lower PAPR solutions of the No-HPA waveform and mitigates its power loss through the non-linear HPA.

Although we omit MISO in the previous formulations, the models in Section III and the optimizations in Section IV can be straightforwardly extended to MISO scenarios,

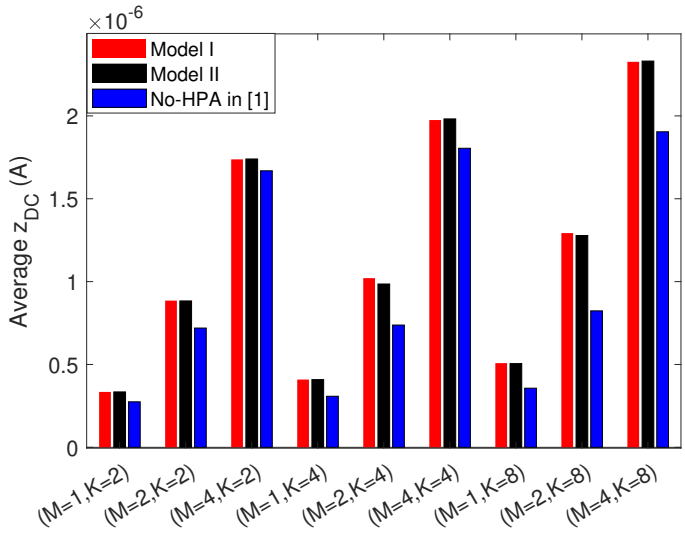

Fig. 3.10: Average z_{DC} with different numbers of antennas M and different numbers of sub-carriers N for $P_{\mathrm{In}}^{\max}=10$ dBW, $P_{\mathrm{Tr}}^{\max}=8$ dBW. The red and black bars represent the waveforms from Model I and Model II respectively. The blue bar represents the No-HPA waveform in [1].

whose average harvested power is plotted in Fig. 3.10. Fig. 3.10 shows that increasing the number of antennas benefits both the performance of Model I and Model II, since it provides more channel diversity. However, in contrast with Fig. 3.9 where the No-HPA waveform also benefits from the increased bandwidth, in Fig. 3.10, the performance gap between the No-HPA waveform and the proposed waveforms enlarges with the increasing number of antennas. This originates from the 'matched filter' solution of the No-HPA waveform in MISO, where power is allocated to each antenna proportionally to the channel strength, making the strongest antenna more vulnerable to heavier power loss from HPA. On the contrary, the waveforms from Model I and Model II can obtain a flexible trade-off between exploiting channel's diversity and reducing HPA's power loss.

Fig. 3.11 compares the average harvested power as a function of the number of sub-carriers with different saturation voltages of HPA. In [1], without HPA's non-linearity, the ideal harvested power increases proportionally to the number of sub-carriers. In contrast, in Fig. 3.11, the average harvested power shows a tendency to saturate when increasing the number of sub-carriers. This comes from a fine balance between HPA's non-linearity (favours low-PAPR transmission) and EH's non-linearity (favours relative high-PAPR

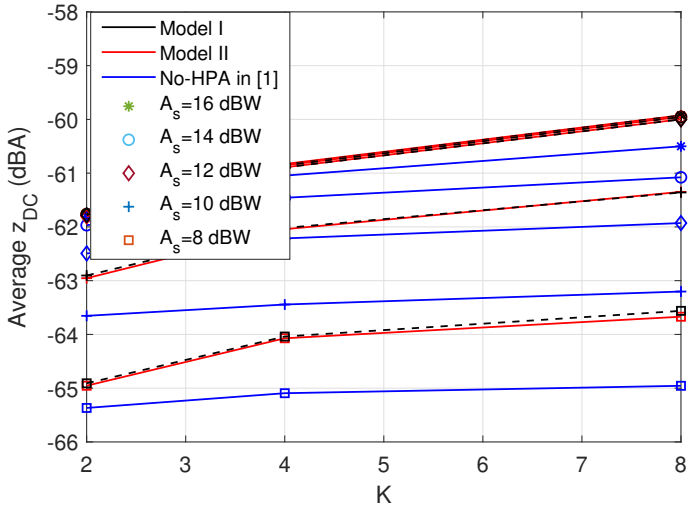

Fig. 3.11: Average z_{DC} with different numbers of sub-carriers, giving different saturation power, $P_{\mathrm{In}}^{\max}=10$, $P_{\mathrm{Tr}}^{\max}=8$ dBW.

transmission), which consequently favours only a limited number of sub-carriers for transmission. The more severe the HPA's non-linearity, the more dominant HPA's non-linear effect exerts on the input waveform design. Correspondingly, in Fig. 3.11, smaller saturation power indicates a higher non-linear operating point of HPA (smaller OBO) and thus shows a more significant saturation tendency as well as less harvested power.

3.5.3 Comparison between Model I and Model II

So far, no significant difference has been observed between the two end-to-end optimized waveforms from Model I and Model II. As an explanation, first, the waveforms from Model I and Model II converge to very similar solutions in the small-signal linear region and the saturation region. For the former, they approach the No-HPA waveform since the EH's non-linear effect dominates, while for the latter, they approach single-carrier transmission to mitigate the power loss caused by the HPA's non-linearity. Second, even within the non-linear region where the two models give different waveforms as in Fig. 3.5 (middle), the performance gap between Model I and Model II in Fig. 3.3 is still not significant. For one reason, as it has been mentioned in section 3.5.1, the waveform

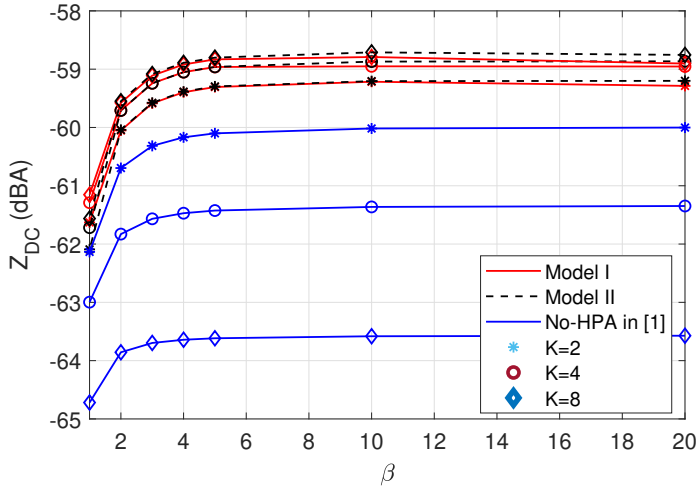

Fig. 3.12: Average z_{DC} as a function of HPA's smoothing parameter (β) given different number of sub-carriers, $P_{\mathrm{In}}^{\max}=10$ dBW, $P_{\mathrm{Tr}}^{\max}=8$ dBW, $G=1$, $A_s=10$ dBA, $B=10$ MHz.

from Model I features relatively higher PAPR and is more advantageous for the EH's non-linearity while the waveform from Model II suffers less power loss at the transmitter, finally leading to a similar end-to-end power harvesting performance between Model I and Model II. For another reason, the previous simulations are based on an HPA's smoothing parameter of $\beta=4$, which is commonly used but whose transfer characteristic experiences a sharp saturation after the linear region (Fig. 3.2). Compared with $\beta=1$, a higher smoothing parameter of $\beta=4$ decreases the performance gap between the two models because most of the signal can be regarded as working in a linear region.

Hence, to reveal the performance difference between Model I and Model II, we plot the power harvesting performance of different HPAs, characterized by different smoothing parameters in Fig. 3.12. Fig. 3.12 firstly shows that HPA with a smaller smoothing parameter produces less harvested power. This is reasonable since, from Fig. 3.2, the HPA with a smaller smoothing parameter shows higher non-linearity over the operation regime and thus suffers more severe power loss for the same input signals.

Also, Fig. 3.12 indicates that given a small smoothing parameter (i.e., $\beta=1$ where HPA suffers significant non-linearity even below the saturation voltage in Fig. 3.2), the waveform from Model I has slightly better power harvesting performance than Model

II, whereas for HPA with large smoothing parameters (i.e., $\beta = 10$ where HPA is highly linear below its saturation voltage in Fig. 3.2), the waveform from Model II outperforms slightly. Their different preferences on HPA's smoothing parameters still originate from the models. As mentioned in section 3.5.1, Model II is more advantageous in obtaining higher transmit power by generating a relatively lower PAPR waveform, which not only mitigates HPA's power loss but also makes the waveform free from the power loss from the BPF. However, with a small smoothing parameter, the high non-linearity of HPA forces both models to generate a low PAPR waveform and pass the BPF in an almost lossless way. In this case, the transmit power advantage of Model II diminishes and the PAPR advantage of Model I becomes more significant. On the contrary, when increasing the smoothing parameter, Model I is generating higher PAPR waveforms and is experiencing increasing power loss from the BPF. When the smoothing parameter becomes large enough (i.e., $\beta = 10$ for example), Model I is outperformed by Model II because its power loss from BPF becomes non-negligible.

3.6 Conclusions

This chapter investigates the optimal input waveform of HPA that maximizes the power harvesting performance in WPT, accounting for both HPA's and rectenna's non-linearities and adaptive to the CSI. Two models are proposed and solved based on whether the frequencies of the input waveform are limited by the transmit pass band or not. Simulations verify the advantages of these two optimized input waveforms, especially with highly non-linear HPAs. The proposed waveforms show that, as the HPA experiences more non-linearity, the optimal waveforms transform from high-PAPR to low-PAPR or even to single-carrier transmission. This reveals the trade-off between HPA's and rectenna's non-linearity, i.e., the former causes power loss and can be compensated by low-PAPR transmission, while the latter boosts the harvested power and is better

exploited with high-PAPR transmission. We also show that while increasing the input signal power makes use of HPA's DC power supply better and generates higher harvested power, the end-to-end PTE of the WPT system decreases when operating in HPA's highly non-linear (saturation) regime where HPA's non-linear degradation becomes more and more significant. We also compare the waveforms from the two models and show that they share very similar performance in most scenarios, but they feature different waveforms and might slightly outperform each other depending on HPA parameters.

3.7 Appendix

3.7.1 Convexity proof of the objective function in (3.19a)

The objective function in (3.19a) is easily seen to be increasing and convex w.r.t. $\mathfrak{R}\{y(t)\}^2 = \mathfrak{R}\{y(\{\overline{w}_k^{\rm tr}\}, \{\widehat{w}_k^{\rm tr}\}, t\}^2$ from (3.16a). On the other hand, if omitting t here, $\mathfrak{R}\{y(\{\overline{w}_k^{\rm tr}\}, \{\widehat{w}_k^{\rm tr}\})\}^2 \triangleq y_1(y_2(\{\overline{w}_k^{\rm tr}, \widehat{w}_k^{\rm tr}\}))$ is a composition function where

$$y_1(x) = x^2, \tag{3.30a}$$

$$y_2(\{\overline{w}_k^{\rm tr}, \widehat{w}_k^{\rm tr}\}) = \sum_{k=0}^{K-1} \Big(\overline{h}_k \cos(2\pi f_k t) - \widehat{h}_k \sin(2\pi f_k t)\Big)\overline{w}_k^{\rm tr} - \Big(\widehat{h}_k \cos(2\pi f_k t) + \overline{h}_k \sin(2\pi f_k t)\Big)\widehat{w}_k^{\rm tr} \tag{3.30b}$$

Such a composition makes $\mathfrak{R}\{y(\{\overline{w}_k^{\rm tr}\}, \{\widehat{w}_k^{\rm tr}\})\}^2$ convex w.r.t. $\{\overline{w}_k^{\rm tr}, \widehat{w}_k^{\rm tr}\}$ jointly. As a proof,

$$y_1(y_2(\theta\{\overline{w}_k^{\rm tr}, \widehat{w}_k^{\rm tr}\}_1 + (1-\theta)\{\overline{w}_k^{\rm tr}, \widehat{w}_k^{\rm tr}\}_2))$$

$$= y_1(\theta y_2(\{\overline{w}_k^{\rm tr}, \widehat{w}_k^{\rm tr}\}_1) + (1-\theta) y_2(\{\overline{w}_k^{\rm tr}, \widehat{w}_k^{\rm tr}\}_2)) \tag{3.31a}$$

$$\leq \theta y_1(y_2(\{\overline{w}_k^{\rm tr}, \widehat{w}_k^{\rm tr}\}_1)) + (1-\theta) f_1(y_2(\{\overline{w}_k^{\rm tr}, \widehat{w}_k^{\rm tr}\}_2)), \tag{3.31b}$$

which provides the convexity.

Hence, the objective z_{DC} is increasing and convex w.r.t. $\Re\{y(\{\overline{w}_k^{\mathrm{tr}}\}, \{\widehat{w}_k^{\mathrm{tr}}\})\}^2$ and $\Re\{y(\{\overline{w}_k^{\mathrm{tr}}\}, \{\widehat{w}_k^{\mathrm{tr}}\})\}^2$ is convex w.r.t. $\{\overline{w}_k^{\mathrm{tr}}, \widehat{w}_k^{\mathrm{tr}}\}$, which implies that z_{DC} is convex w.r.t. $\{\overline{w}_k^{\mathrm{tr}}, \widehat{w}_k^{\mathrm{tr}}\}$.

3.7.2 Proof of the input power constraint in (3.24b)

Firstly, we derive the inverse transfer characteristics of HPA (SSPA in (3.6)). Given the amplitude distortion function $\mathcal{A}(\cdot)$ in (3.5b) and the phase shift $\Phi(\cdot)$ in (3.5c), the inverse transfer function of HPA is characterized by $f^{-1}(\cdot)_{\mathrm{HPA}}$, composed of the inverse amplitude function $\mathcal{A}^{-1}(\cdot)$ and the inverse phase shift function $\Phi^{-1}(\cdot)$ such that

$$f_{\mathrm{HPA}}\big(f_{\mathrm{HPA}}^{-1}\big(x^{\mathrm{tr}}\big)\big) = \mathcal{A}\big(\mathcal{A}^{-1}\big(\big|x^{\mathrm{tr}}\big|\big)\big) e^{j\left(\measuredangle x^{\mathrm{tr}} + \Phi\left(|x^{\mathrm{tr}}|\right) + \Phi^{-1}\left(|x^{\mathrm{tr}}|\right)\right)} = x^{\mathrm{tr}}, \tag{3.32}$$

where $x^{\mathrm{tr}}/|x^{\mathrm{tr}}|$ is short for $x^{\mathrm{tr}}(t)/|x^{\mathrm{tr}}(t)|$, and $x^{\mathrm{tr}} = |x^{\mathrm{tr}}| e^{j\measuredangle|x^{\mathrm{tr}}|}$.

Hence, we obtain the inverse transfer characteristics of HPA

$$\mathcal{A}^{-1}\big(\big|x^{\mathrm{tr}}\big|\big) = \frac{|x^{\mathrm{tr}}|}{G}\left[1 - \left(\frac{|x^{\mathrm{tr}}|}{A_s}\right)^{2\beta}\right]^{-\frac{1}{2\beta}}, \tag{3.33}$$

$$\Phi^{-1}\big(\big|x^{\mathrm{tr}}\big|\big) = 0, \tag{3.34}$$

$$f_{\mathrm{HPA}}^{-1}\big(x^{\mathrm{tr}}\big) = \frac{x^{\mathrm{tr}}}{G}\left[1 - \left(\frac{|x^{\mathrm{tr}}|}{A_s}\right)^{2\beta}\right]^{-\frac{1}{2\beta}}. \tag{3.35}$$

Then, from Parseval's theorem (the signal power in the frequency domain equals the signal power in the time domain), combing (3.35), we have

$$\sum_{k=0}^{K-1} w_k^{\mathrm{in}^2} = \frac{1}{T}\int_T |f_{\mathrm{HPA}}^{-1}(x^{\mathrm{tr}})|^2 dt = \frac{1}{2TG^2}\int_T \left[\big|x^{\mathrm{tr}}\big|^{-2\beta} - A_s^{-2\beta}\right]^{-\frac{1}{\beta}} dt, \tag{3.36}$$

which corresponds to the constraint in (3.24b).

3.7.3 Convexity proof of the constraint in (3.24b)

Denote the constraint in (3.24b) as $f(\{\overline{w}_k^{\text{tr}}, \widehat{w}_k^{\text{tr}}\}) = h(g(\{\overline{w}_k^{\text{tr}}, \widehat{w}_k^{\text{tr}}\}))$, with $h(x) = \frac{1}{2TG^2}\int_T [x^{-\beta} - A_s^{-2\beta}]^{-\frac{1}{\beta}} dt$ and $g(\{\overline{w}_k^{\text{tr}}, \widehat{w}_k^{\text{tr}}\}) = x^{\text{tr}^2}(\{\overline{w}_k^{\text{tr}}, \widehat{w}_k^{\text{tr}}\}, t) = |\sum_k^N (\overline{w}_k^{\text{tr}} + j\widehat{w}_k^{\text{tr}}) e^{jw_k t}|^2$.

For $h(x)$, we have

$$\bigtriangledown h(x) = \frac{1}{2TG^2}\int_T \left[1 - \left(\frac{x}{A_s^2}\right)^{\beta}\right]^{-\frac{\beta+1}{\beta}} dt > 0 \tag{3.37}$$

And the second derivative

$$\bigtriangledown^2 h(x) = \frac{1}{2TG^2}\int_T \frac{\beta+1}{A_s^{2\beta}} \left[1 - \left(\frac{x}{A_s^2}\right)^{\beta}\right]^{-\frac{2\beta+1}{\beta}} x^{\beta-1} dt > 0. \tag{3.38}$$

At the same time, $g(\{\overline{w}_k^{\text{tr}}, \widehat{w}_k^{\text{tr}}\})$ can be proved convex w.r.t. $\{\overline{w}_k^{\text{tr}}, \widehat{w}_k^{\text{tr}}\}$, since again, $g(\{\overline{w}_k^{\text{tr}}, \widehat{w}_k^{\text{tr}}\})$ is a composition of a convex norm function with an affine function (Appendix A). Given increasing and convex $h(x)$, together with convex $g(\{\overline{w}_k^{\text{tr}}, \widehat{w}_k^{\text{tr}}\})$, we can see that $f(\{\overline{w}_k^{\text{tr}}, \widehat{w}_k^{\text{tr}}\})$ is convex regarding $\{\overline{w}_k^{\text{tr}}, \widehat{w}_k^{\text{tr}}\}$.

3.7.4 Approximating the input signal of Model II

Fig. 3.13 shows the spectrum of the input signal from Model II corresponding to Fig. 3.3 on the top and plots the performance of an approximated signal (Model II APPR) whose out-of band frequencies are cut off. It shows that the approximated signal achieves almost the same performance as the desired signal from the waveform 'Model II'. This can be explained by the magnitude spectrum on the top figure, where the out-of band frequency components are almost negligible. Indeed, through simulations, even if introducing more HPA non-linearities by decreasing the smoothing parameter to $\beta = 1$, the signal from 'Model II' can be perfectly approximated simply by extending the input bandwidth to

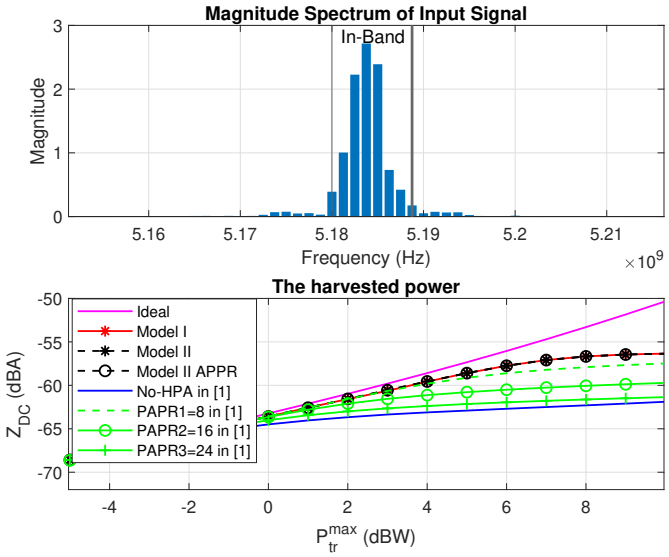

Fig. 3.13: The magnitude spectrum of the input signal from Model II (with $P_{\text{tr}}^{\max}=10$ dBW for the maximal non-linearity) (top) and the power harvesting performance corresponds to Fig. 3.3 but adding an approximated input signal of Model II whose out-off band components are cut off (bottom).

1.5 times of the transmit bandwidth.

Chapter 4

Signal Design for Dual-Functional Radar-Communication Systems

OFDM has been widely adopted in DFRC systems. However, with random CSs embedded in the DFRC waveform, the transmit signal has a random AF that affects the radar's delay-Doppler estimation performance, which has not been well explored. This chapter addresses this gap by first characterizing the outlier probability (OP) – the probability of incorrectly estimating a target's (on-grid) delay-Doppler bin – in OFDM DFRC w.r.t the CS. This subsequently motivates the OFDM DFRC waveform design problem of minimizing the OP w.r.t the CS input distribution. Conditioned on the CSs, the OP only depends on the CS magnitudes. Hence, we consider the following two schemes for the above optimization: CSs with (1) constant magnitude input distribution (PSK), and (2) variable magnitude input distribution (Gaussian). For (1), minimizing the OP reduces to the familiar power allocation design across OFDM's subcarriers and symbols, with uniform power allocation across OFDM subcarriers and a *windowed* power allocation across OFDM symbols being near-optimal. For (2), the mean and variance of the Gaussian distribution at each subcarrier is optimized, with an additional communication constraint to avoid the zero-variance solution where no CSs are carried.

We observe that subcarriers with strong communication channels feature a large variance (favour communications) while the others are characterized by a large mean (favour radar). However, the overall power allocation (i.e., the sum of the squared mean and variance) across the OFDM subcarriers and symbols is similar to (1). Simulations for (2) show that while random CS magnitudes benefit communications, they degrade radar performance, but this can be mitigated using our optimized input distribution.

4.1 Introduction

In this chapter, we consider an OFDM DFRC waveform design via input distribution optimization with the radar task being on-grid delay-Doppler bin estimation, which is of considerable practical relevance. Our contributions are summarized as follows:

(1) We start from why the OP[1] is a suitable metric for characterizing the on-grid delay-Doppler bin estimation performance of the ML estimator. We then derive an upper bound for the OP (UBOP) that is a good approximation of the OP across the whole SNR region. We show that the UBOP coincides with the signal's AF properties and is only a function of the CS magnitudes. The UBOP is adopted as the radar metric throughout the chapter.

(2) We minimize the UBOP w.r.t the input distributions of CSs with constant magnitudes (e.g. PSK), to provide intuition for radar-favoured signals. In this scheme, information is only conveyed through the CS phases, and the radar performance of the optimized solution matches that of a deterministic constant envelope signal in a pure radar system. The optimal input distribution features uniform power allocation across the OFDM subcarriers (to favour delay estimation) and a windowed power allocation across the OFDM symbols (to favour Doppler estimation). We also design signals across both the

[1]OP is defined as the probability that a wrong delay-Doppler bin is estimated. For the special case where it is known apriori that a target is present in one of the delay-Doppler bins, the OP coincides with the FAP, i.e., the 'false alarm' refers to deciding the target to any of the wrong bins after detection.

time and frequency domains because of a joint consideration of delay-Doppler estimation. This scheme is hence used as a benchmark for the case of CSs with variable magnitude input distributions.

(3) We consider the DFRC performance for input distributions of CSs with variable magnitudes, by minimizing the average UBOP (aUBOP) w.r.t the *non-zero* mean Gaussian input distribution. Deviating from the intuitive choice of a *zero-mean* Gaussian input distribution for communications, we firstly optimize a *non-zero* Gaussian input distribution for DFRC systems. A non-zero mean Gaussian gives rise to a trade-off in allocating the available power budget between the symbol mean and the symbol variance, with radar/communications favouring a less/more random input distribution through greater power allocation to the symbol mean/variance. More specifically, the simulations reveal that for subcarriers having high channel gain for communications, power is concentrated on the symbol variance in order to satisfy the communication constraints efficiently. On the other hand, for subcarriers with weak channel gains for communications, power is concentrated on the symbol means to favour radar performance. The power allocation (sum over the squared symbol means and variance) across the OFDM subcarriers, however, is similar to (2).

Organization: Section 4.2 introduces the signal and system model of a point-target mono-static SISO DFRC scenario using OFDM waveform. Then, Section 4.3 develops the ML estimator for joint delay-Doppler bin estimation, derives the OP conditioned on CS magnitudes and its tractable upper bound (UBOP). Section 4.4 considers the problem of minimizing the UBOP for PSK input distribution to shed insight into the patterns of power allocation across OFDM subcarriers and OFDM symbols that yield good radar performance. Section 4.5 extends the scope of input distributions to those symbols with variable magnitudes, by minimizing the aUBOP subject to a communication achievable rate constraint for a non-zero mean Gaussian input distribution. Section 4.6 evaluates the OP performance of the optimized input distributions from Sections 4.4 and 4.5 and

finally, Section 4.7 concludes the chapter.

4.2 Signal model

This section models a DFRC system where an OFDM transmit signal is used to simultaneously communicate with a user and sense a point target. We consider an OFDM block containing M OFDM symbols. Each OFDM symbol has K subcarriers, with an additional K_G sub-pulses of CP. We assume that a target's delay and Doppler remain unchanged over one block, and consider a mono-static radar set-up.

Let B denote the signal bandwidth, corresponding to a delay resolution of $\Delta\tau = 1/B$. We assume that the target round-trip delay is shorter than the CP duration (the maximal delay that can be estimated is $\tau_{\max} = K_G/B$). Let $T_{\text{OFDM}} = (K+K_G)/B \triangleq K_T/B$ denote the OFDM symbol duration. Hence, the radar coherent processing interval (CPI) equals MT_{OFDM}, corresponding to the Doppler resolution of $\Delta f_D = 1/(MT_{\text{OFDM}}) = B/(K_T M)$ [66].

Consider the presence of a target at a distance R and moving at velocity v w.r.t the radar. For a monostatic configuration as detailed in Section 2.3, R and v are captured on the echo signal by its time delay $\tau = 2R/c$ and Doppler frequency $f_{\text{D}} = f_c(2v/c)$, with c being the speed of light. τ and f_{D} can be represented as follows (Details in Section 2.3)

$$\tau = (n_0 + n_\epsilon)\Delta\tau, \quad n_0 \in \{0, 1, \cdots, K_G - 1\}, \tag{4.1a}$$

$$f_{\text{D}} = (v_0 + v_\epsilon)\Delta f_{\text{D}}, \quad v_0 \in \{-M/2, \cdots, 0, \cdots, (M-1)/2\}, \tag{4.1b}$$

where $n_\epsilon \in (0,1)$ and $v_\epsilon \in (-1/2, 1/2)$ are the fractional (off-grid) delay and Doppler parameters. $(n_0,\ v_0)$ denotes the target's *on-grid* delay-Doppler bin, which is the parameter of interest in this chapter.

Let $X[k,\ m]$ denote the CS at the k^{th} $(k = 0,\ \cdots,\ K-1)$ subcarrier of the m^{th} $(m =$

$0, \cdots, M-1$) symbol. After a K-point IDFT, let $x[n, m]$ ($n=0, \cdots, K-1$) denote the resulting time domain signal. After adding the CP, we obtain the following signals [65,100]

$$x_{\mathrm{CP}}[n, m]=\begin{cases} x[K-K_G+n, m], & n\in\{0, \cdots, K_G-1\}, \\ x[n-K_G, m], & n\in\{K_G, \cdots, K_T-1\}, \end{cases} \tag{4.2}$$

The analogue signal transmitted over the air is given by [100]

$$x(t)=\sum_{n,m} x_{\mathrm{CP}}[n, m]\mathrm{rect}(t-(n+K_T m)/B), \tag{4.3}$$

where we assume a rectangular basis for each sub-pulse at DAC, as in Section 2.3.

The radar return at the transceiver (after ADC) is given by [101]

$$y_{\mathrm{CP}}[n, m]=ax(t-\tau)e^{j2\pi f_{\mathrm{D}} t}|_{t=(n+K_T m)/B} \tag{4.4a}$$

$$=ax_{\mathrm{CP}}[n-n_0, m]e^{j2\pi\frac{f_{\mathrm{D}}(n+mK_T)}{B}}+w[n, m] \tag{4.4b}$$

$$=ax_{\mathrm{CP}}[n-n_0, m]e^{j2\pi\frac{f_{\mathrm{D}} n}{B}}e^{j2\pi\frac{(v_0+v_\epsilon)m}{M}}+w[n, m] \tag{4.4c}$$

$$\approx ax_{\mathrm{CP}}[n-n_0, m]e^{j2\pi\frac{(v_0+v_\epsilon)m}{M}}+w[n, m], \tag{4.4d}$$

where $a\in\mathbb{C}$ is the scattering coefficient of the target, assumed to be unchanged throughout the OFDM block. In (4.4b), the received samples after ADC lack information on the fractional n_ϵ because of the rectangular basis in (4.3). Hence, n_ϵ is often disregarded in OFDM radar and the target delay is assumed to be on-grid [92], as in Section 2.3. In (4.4d), $e^{j2\pi f_{\mathrm{D}} n/B}\approx 1$, since typically $f_{\mathrm{D}}\ll B$. Finally, $w[n, m]\sim\mathcal{CN}(0, \sigma_{\mathrm{N}}^2)$ is the AWGN. After removing the CP, we get the following expression [101]

$$y[n, m]\approx ax[n-n_0, m]e^{j2\pi\frac{(v_0+v_\epsilon)m}{M}}+w[n, m], \tag{4.5}$$

where $x[n-n_0, m]$ represents a circular shift of n_0 following (4.2). After a K-point DFT,

we get the frequency-domain signal in the following

$$Y[k,\, m] = \mu_{k,m}(\boldsymbol{\theta}_0) + W[k,\, m], \tag{4.6a}$$

$$\text{with } \mu_{k,m}(\boldsymbol{\theta}_0) := aX[k,\, m] e^{-j2\pi \frac{n_0 k}{K}} e^{j2\pi \frac{(v_0+v_\epsilon)m}{M}}, \tag{4.6b}$$

$$W[k,\, m] \sim \mathcal{CN}(0,\, \sigma_{\mathrm{N}}^2). \tag{4.6c}$$

In (4.6a)-(4.6c), $\boldsymbol{\theta}_0 \triangleq [n_0,\, v_0,\, v_\epsilon,\, A_0,\, \phi_0]^T$ denotes the true values of all of the unknown parameters in the system, with A_0 and ϕ_0 denoting the amplitude and phase of a. n_0 and v_0 are the parameters of interest, whereas the others are nuisance parameters.

4.3 Characterizing the ML estimator's OP

This section begins by formulating the ML estimator for $(n_0,\, v_0)$ over an OFDM block. We then derive the OP of this estimator. The OP is then approximated by its upper bound to yield a tractable metric that can be optimized w.r.t the CS input distribution.

4.3.1 ML estimator

From (4.6a)-(4.6c), the joint probability density function (PDF) of $Y[k,\, m]$, conditioned on the unknown parameters $\boldsymbol{\theta} \triangleq [n,\, v,\, v'_\epsilon,\, A,\, \phi]^T$, is given by [102, 103]

$$f(\mathbf{y}|\boldsymbol{\theta}) = (\pi\sigma_{\mathrm{N}}^2)^{-KM}\ e^{-\sum_{m=0}^{M-1}\sum_{k=0}^{K-1} \left|Y[k,\ m]-\mu_{k,m}(\boldsymbol{\theta})\right|^2 / \sigma_{\mathrm{N}}^2}, \tag{4.7}$$

where $\mathbf{y} \triangleq [\mathbf{y}_0^T,\, \cdots,\, \mathbf{y}_{M-1}^T]^T$ with $\mathbf{y}_m \triangleq [Y[0,\, m],\, \cdots,\, Y[K-1,\, m]]^T$. The ML estimate of $\boldsymbol{\theta}_0$, denoted by $\hat{\boldsymbol{\theta}}$, is given by [103]

$$\hat{\boldsymbol{\theta}} = \underset{\boldsymbol{\theta}}{\text{argmax}}\ \log f(\mathbf{y}|\boldsymbol{\theta}) \tag{4.8a}$$

$$=\underset{\boldsymbol{\theta}}{\text{argmax}}\ 2A\Re\Big\{e^{-j\phi}\sum_{m,k}Y[k,\,m]X[k,\,m]^*e^{j2\pi\frac{nk}{K}}e^{-j2\pi\frac{(v+v'_\epsilon)m}{M}}\Big\}$$

$$-\sum_{m,k}\big[|Y[k,\,m]|^2+|AX[k,\,m]|^2\big], \tag{4.8b}$$

Remark 5. *In* (4.8)*, estimating the off-grid parameter* v_ϵ *(embedded in* $Y[k,\ m]$*) typically involves exploiting sparsity (of targets), and is attractive because it provides "super-resolution". In this chapter, however, we restrict our focus to on-grid parameter estimation (with its well-defined resolution limits [92, 102]), as it is a relatively simpler starting point to investigate the relationship between the input distributions and sensing performance. Hence, from the following ML estimator, we treat* v_ϵ *as a nuisance parameter affecting the estimation of on-grid parameters,* $(n_0,\, v_0)$ *(neglecting* v_ϵ*), at the processor in* (4.8)*.*

In (4.8b), only the first term is a function of the target's delay-Doppler bin. Hence, the ML estimator of $(n_0,\, v_0)$ is given by (Assume the true delay-Doppler bin $(n_0,\, v_0)=(0,\, 0)$ without loss of generality [103])

$$(\hat{n},\,\hat{v})=\underset{(n,\ v)}{\text{argmax}}\ \Big|\sum_{m,\ k}Y[k,\,m]X[k,\,m]^*e^{j2\pi\frac{nk}{K}}e^{-j2\pi\frac{vm}{M}}\Big| \tag{4.9}$$

for $n\in\{0,\,\cdots,\,K_G-1\}$, $v\in\{-M/2,\,\cdots,\,M/2-1\}$.

Combining with (4.6a), the ML estimator in (4.9) is rewritten in the following expression

$$(\hat{n},\,\hat{v})=\underset{(n,\ v)}{\text{argmax}}\ \Big|\sum_{m,\ k}Ap_{k,m}e^{j2\pi\frac{nk}{K}}e^{-j2\pi\frac{vm}{M}}e^{j2\pi\frac{v_\epsilon m}{M}}+w_{\text{o}}[n,\,v]\Big| \tag{4.10a}$$

$$=\underset{(n,\ v)}{\text{argmax}}\,|\gamma_{n,v,v_\epsilon}|, \tag{4.10b}$$

where

$$p_{k,m}=|X[k,\,m]|^2, \tag{4.10c}$$

$$\gamma_{n,v,v_\epsilon}=r_{n,v,v_\epsilon}+w_{\text{o}}[n,\,v], \tag{4.10d}$$

$$r_{n,v,v_\epsilon} = \sum_{m,k} p_{k,m} e^{j2\pi\frac{nk}{K}} e^{-j2\pi\frac{vm}{M}} e^{j2\pi\frac{v_\epsilon m}{M}}, \tag{4.10e}$$

$$w_{\mathrm{o}}[n,\, v] = A^{-1} \sum_{m,\, k} W[k,\, m] X[k,\, m]^* e^{j2\pi\frac{nk}{K}} e^{-j2\pi\frac{vm}{M}}, \tag{4.10f}$$

for $n \in \{0, \cdots, K_G - 1\}$, $v \in \{-M/2, \cdots, M/2 - 1\}$.

Remark 6. *$p_{k,m}$ in (4.10c) denotes the CS power at the k^{th} OFDM subcarrier of the m^{th} OFDM symbol. γ_{n,v,v_ϵ} in* (4.10d) *represents the cross-correlation between the transmitted signals and the received distorted signals, and r_{n,v,v_ϵ} in* (4.10e) *represents the discrete AF of the transmitted signals. For r_{n,v,v_ϵ} in* (4.10e)*, the random generalization of CSs gives random $p_{k,m}$ and induces sidebobes to r_{n,v,v_ϵ}. Also, the fractional Doppler, v_ϵ, yields an M-DFT evaluated at a discrete frequency that is* not *an integer multiple of $1/M$. This induces sidelobes over all M Doppler bins to r_{n,v,v_ϵ} in general. As an illumination, Fig. 4.1 plots $|r_{n,v,v_\epsilon}|$ and $|\gamma_{n,v,v_\epsilon}|$ for: (a) BPSK input (i.e., constant magnitude CSs) and $v_\epsilon = 0$, (b) 256-QAM input (i.e., variable magnitude CSs) and $v_\epsilon = 0$, and (c) BPSK input and $v_\epsilon \neq 0$. To successfully locate $(n_0,\, v_0)$ from $|\gamma_{n,v,v_\epsilon}|$, it is desirable for the peak lobe at $|r_{0,0,v_\epsilon}|$ to be easily distinguishable from its sidelobes. Fig. 4.1b (Fig. 4.1c) show that CSs with variable magnitudes (non-zero v_ϵ) lead to AF sidelobes, which would increase the probability of incorrectly estimating $(n_0,\, v_0)$, i.e., the OP. As seen in Fig. 4.1, the sidelobe levels are a function of both the CS magnitudes and v_ϵ. Hence, the overall sidelobe level can be suppressed (and along with it the OP) through the careful design of CS input distributions (which is under our control), accounting for the effect of v_ϵ. This motivates the problem of minimizing the OP w.r.t the input distribution.*

4.3.2 ML-based radar metric

A metric that directly characterizes the ML estimator's sensing performance is the OP – the probability of incorrectly estimating $(n_0,\, v_0)$.

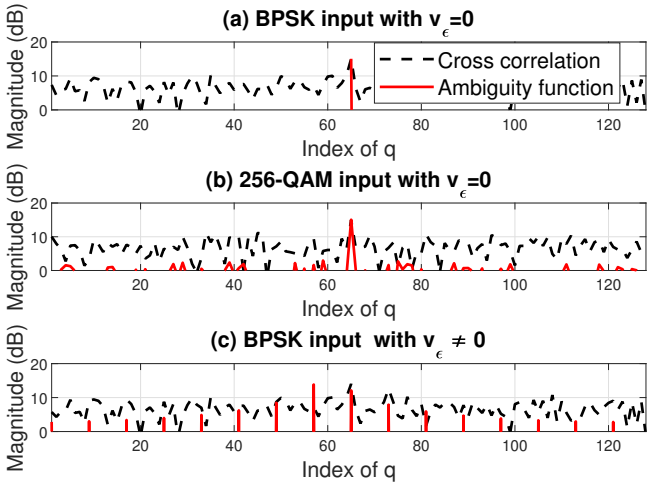

Fig. 4.1: The magnitudes of discrete AF ($|r_{n,v,v_\epsilon}|$ in (4.10e)) and the corresponding cross correlation ($|\gamma_{n,v,v_\epsilon}|$ in (4.10d) averaging over random CSs for (b) and velocities for (c)) with uniform power allocation across both OFDM subcarriers and symbols, with $K=32$, $M=16$ and $K_G=8$. The index, q, is related to delay-Doppler bin $(n,\ v)$ as follows: $q=n+(v+M/2)K_G$.

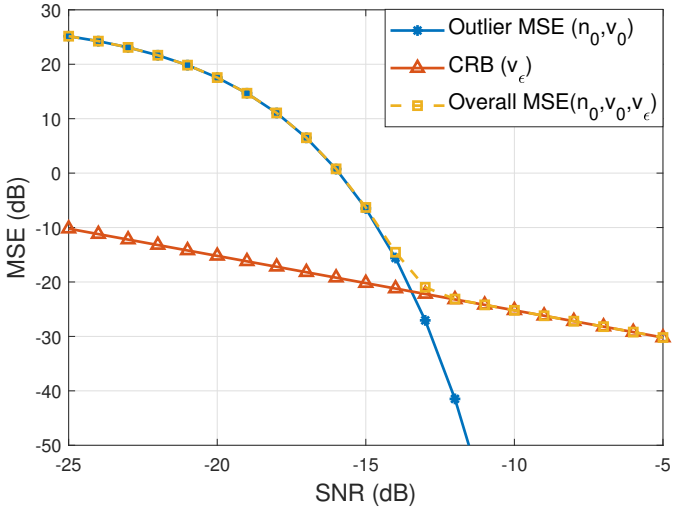

Fig. 4.2: The overall MSE, the outlier MSE and the CRB relationship for $K=32$, $K_G=8$, $M=8$.

Remark 7. *The popular CRB [103] and the well-known Ziv-Zakai bound [104] are not adopted as the radar metric. As a reason, the overall MSE of* $(n_0,\ v_0,\ v_\epsilon)$ *in* (4.8) *is composed by:* $\mathrm{MSE}(n,\ v,\ v_\epsilon)=\mathrm{MSE}(n,\ v)+\mathrm{MSE}(v_\epsilon)$. *The first term on the right-hand side,* $\mathrm{MSE}(n,\ v)$, *captures the contribution to the MSE from incorrectly estimating the delay-Doppler bin* $(n_0,\ v_0)$, *and is known as the outlier MSE. The second term captures*

the MSE w.r.t v_ϵ, conditioned on having correctly estimated the target's delay-Doppler bin (n_0, v_0), and is bounded below by the CRB. The overall $\mathrm{MSE}(n, v, v_\epsilon)$ *on the left-hand side is globally (in terms of SNR) approximated by the Ziv-Zakai bound that features high computational complexity [104]. Fig. 4.2 plots their relationship. For the on-grid estimation in our scenario, the outlier MSE should be our objective, and the outliers, from Fig. 4.2, mostly occur at the threshold SNR region* [2] *and below* [3]*. On the contrary, the overall MSE only converges to the CRB in the high SNR region when v_ϵ is also the estimation objective. Moreover, in our on-grid delay-Doppler bin estimation, the CRB is not also suitable because the parameters are discrete, breaking the regularity condition on which the CRB is defined [103]. It is also noteworthy that, while the Ziv-Zakai bound could be adjusted for discrete parameters, it results in intractable optimization formulations [104]. Hence, in this thesis, limited to the resolution issues, our focus is the outlier MSE that characterizes the on-grid estimation performance.*

To account for the arbitrariness of v_ϵ, we assume it is uniformly distributed over $(-1/2, 1/2)$, and consider the OP averaged over v_ϵ. This quantity, denoted by $\mathbb{P}_\mathrm{o}$, is the probability that the sidelobe magnitudes ($|\gamma_{n,v,v_\epsilon}|$ for $(n, v) \neq (0, 0)$) is larger than the peak lobe magnitude ($|\gamma_{0,0,v_\epsilon}|$), which can be expressed as follows [42]

$$\mathbb{P}_\mathrm{o} \triangleq \mathbb{E}_{v_\epsilon}\Big\{\mathbb{P}\Big[\bigcup_{n,v}\Big\{|\gamma_{n,v,v_\epsilon}| > |\gamma_{0,0,v_\epsilon}|\Big\}\Big]\Big\} \tag{4.11a}$$

$$\leq \mathbb{E}_{v_\epsilon}\Big\{\sum_{(n,\ v)\neq(0,\ 0)} \mathbb{P}[|\gamma_{n,v,v_\epsilon}| > |\gamma_{0,0,v_\epsilon}|]\Big\} \tag{4.11b}$$

$$\approx \mathbb{E}_{v_\epsilon}\Big\{\sum_{(n,\ v)\neq(0,\ 0)} \exp\Big\{-\frac{|r_{0,0,v_\epsilon}|}{2\sigma^2}\Big\} I_0\Big(\frac{|r_{n,v,v_\epsilon}|}{2\sigma^2}\Big)/2\Big\} \tag{4.11c}$$

$$\leq \mathbb{E}_{v_\epsilon}\Big\{\sum_{(n,\ v)\neq(0,\ 0)} \exp\Big\{-\frac{|r_{0,0,v_\epsilon}| - |r_{n,v,v_\epsilon}|}{2\sigma^2}\Big\}/2\Big\} \tag{4.11d}$$

[2] The threshold region is a typical radar phenomenon and refers to the SNR region where radar's OP/MSE decreases sharply from a saturating high value to a saturating low value, which is the region of interest.

[3] Hence, in the DFRC scenario with variable magnitude input distributions in Section 4.5.2, the average UBOP is approximated in the low SNR region.

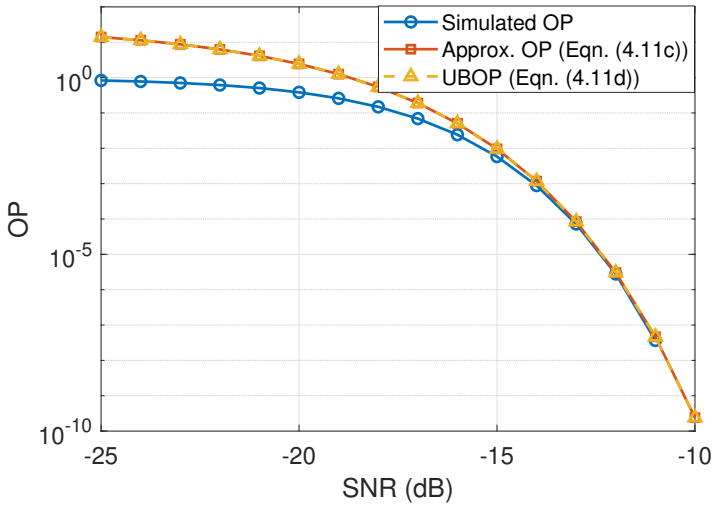

Fig. 4.3: The simulated and approximated OP for $K=32$, $K_G=8$, $M=8$.

$$\stackrel{\triangle}{=}\mathbb{P}_{\mathrm{UB}}, \tag{4.11e}$$

where $\sigma^2=\sigma_{\mathrm{N}}^2/A^2$. The inequality in (4.11b) stems from the union bound, while the upper bound in (4.11d), termed the UBOP, is more tractable for optimization w.r.t the input distribution than $\mathbb{P}_{\mathrm{o}}$. Hence, we adopt the UBOP as the radar metric from hereon. The derivation for (4.11c)-(4.11d) is provided in Appendix 4.8.1 and is shown to capture the simulated OP soundly in Fig. 4.3.

Remark 8. *The expression in* (4.11d) *captures the relationship between the UBOP and the AF [39–41]. Specifically, at low SNR,* $\sum_{(n,\ v)\neq(0,\ 0)}\exp\{-(|r_{0,0,v_\epsilon}-r_{n,v,v_\epsilon})|/2\sigma^2\}\propto \sum_{(n,\ v)\neq(0,\ 0)}-(|r_{0,0,v_\epsilon}|-|r_{n,v,v_\epsilon}|)/2\sigma^2$*, indicating that the UBOP is approximately inversely proportional to the integrated-side-to-peak-lobe-difference (ISPLD) of the AF in this regime. On the contrary, at high SNR, the maximal exponential term in* (4.11d) *dominates. Hence, the UBOP in this regime is inversely proportional to the peak-to-the-largest-side-lobe difference of the AF. The relationship with the AF further demonstrates that the OP and UBOP are sound and well-motivated metrics.*

Remark 9. *From* (4.11d) *(combining with* (4.10e)*), the UBOP is a function of the input distribution through* $p_{k,m}$*, which is only related with the CS magnitudes. This motivates*

us to consider the problem of minimizing the UBOP under two broad classes of input distributions, (i) those with constant magnitudes (e.g., PSK input distribution), and (ii) those with variable magnitudes (e.g., Gaussian input distribution), which we consider in the following sections.

4.4 Minimizing OP for constant magnitude input distributions

In this section, we minimize the UBOP ($\mathbb{P}_{\text{UB}}$ in (4.11d)) for CSs with constant magnitude input distributions, such as PSK. In this scheme, the UBOP is deterministic regardless of the random information carried by CSs' phases. Hence, waveforms with constant magnitude input distributions are able to achieve the same radar performance in DFRC as that of using deterministic OFDM waveforms in a pure radar system.

4.4.1 Problem formulation

For the special case of constant CS magnitude, the UBOP is a deterministic function of $p_{k,m}$ – i.e., the power allocation across subcarriers and OFDM symbols – and is independent of the PMV. Hence, we formulate the following optimization problem

$$\min_{\{p_{k,m}\}} \quad \mathbb{P}_{\text{UB}} \text{ in (4.11d)}, \tag{4.12a}$$

$$\text{s.t.} \quad \sum_{k,\ m} p_{k,m} \leq P^{\max}, \tag{4.12b}$$

$$p_{k,m} \geq 0,\ \forall k,\ m, \tag{4.12c}$$

where $P^{\max}$ is the transmit power constraint.

Remark 10. *In this section, our primary focus is on optimizing radar performance, while still acknowledging that information can be conveyed by phases. The communication constraint is disregarded because we implicitly assume a uniform probability mass vector over the constellation symbols, which can achieve a rate of up to* $\log_2 Q$ *bits/symbol for* $Q-PSK$*, as analyzed in Section 2.4. Hence, this scheme of constant magnitude input distributions provides a performance benchmark for the scheme of variable magnitude input distributions (Gaussian input) in Section 4.5. This part will also inspire the simplified algorithm for the Gaussian input scheme in section 4.5.3.*

For the above problem, we have the following result:

Lemma 1. *The optimal power allocation across subcarriers (*$p_{k,m}$ *across* k *for* $\forall\ m$*) to minimize* $\mathbb{P}_{\mathrm{UB}}$ *is the uniform power allocation.*

Proof. Let $p_m \triangleq \sum_k\ p_{k,m}$ denote the total power of the m^{th} OFDM symbol. The expectation over v_ϵ in (4.11d) is approximated by taking multiple samples of v_ϵ from the set $\{\epsilon_1, \cdots, \epsilon_{|\kappa|}\}$ (denoted by set κ, the larger the number of samples, the more accurate the approximation) following its uniform distribution. Hence, $\mathbb{P}_{\mathrm{UB}}$ becomes

$$
\begin{aligned}
&\mathbb{P}_{\mathrm{UB}} \\
\approx&\frac{1}{|\kappa|}\sum_{\epsilon\in\kappa}\sum_{(n,\ v)\neq(0,\ 0)}\exp\Big\{-\frac{|r_{0,0,\epsilon}|-|r_{n,v,\epsilon}|}{2\sigma^2}\Big\}\quad(\text{for large } |\kappa|) && \text{(4.13a)}\\
=&\frac{1}{|\kappa|}\sum_{\epsilon\in\kappa}\sum_{n=0,\ v\neq 0}\exp\Big\{-\frac{|r_{0,0,\epsilon}|-|r_{n,v,\epsilon}|}{2\sigma^2}\Big\}+\frac{1}{|\kappa|}\sum_{\epsilon\in\kappa}\sum_{n\neq 0}\exp\Big\{-\frac{|r_{0,0,\epsilon}|-|r_{n,v,\epsilon}|}{2\sigma^2}\Big\} && \text{(4.13b)}\\
\geq&\frac{\sum_{\epsilon\in\kappa}}{|\kappa|}\Big(\sum_{v\neq 0}\exp\Big\{-\frac{|r_{0,0,\epsilon}|-|r_{0,v,\epsilon}|}{2\sigma^2}\Big\}+\sum_{n\neq 0}\exp\Big\{-\frac{|r_{0,0,\epsilon}|}{2\sigma^2}\Big\}\Big) && \text{(4.13c)}\\
=&\frac{\mathbf{1}^T}{|\kappa|}\exp\Big\{-\frac{\mathbf{1}_{M-1}\otimes|\mathbf{r}_0|-|\mathbf{r}'|}{2\sigma^2}\Big\}+\frac{(K_G-1)M}{|\kappa|}\mathbf{1}^T\exp\Big\{-\frac{|\mathbf{r}_0|}{2\sigma^2}\Big\}\\
\triangleq&\mathbb{P}_{\mathrm{UB}}(\mathbf{r}), && \text{(4.13d)}
\end{aligned}
$$

where

$$\mathbf{r}_v = \left[r_{0,v,\epsilon_1}, \cdots, r_{0,v,\epsilon_{|\kappa|}} \right]^T \in \mathbb{C}^{|\kappa|}, \tag{4.13e}$$

$$\mathbf{r}' = \left[\mathbf{r}_1^T, \cdots, \mathbf{r}_{M-1}^T \right]^T \in \mathbb{C}^{(M-1)|\kappa|}, \tag{4.13f}$$

$$\mathbf{r} = \left[\mathbf{r}_0^T, \mathbf{r}'^T \right]^T = \mathbf{F}^{\mathrm{D}} \mathbf{p} \in \mathbb{C}^{M|\kappa|}, \tag{4.13g}$$

$$\mathbf{p} = [p_0, \cdots, p_{M-1}]^T \in \mathbb{R}^M, \tag{4.13h}$$

$$\mathbf{F}^{\mathrm{D}} = \left[\mathbf{f}^{\mathrm{D}}_{1-M/2,\epsilon_1}, \mathbf{f}^{\mathrm{D}}_{1-M/2,\epsilon_2}, \cdots, \mathbf{f}^{\mathrm{D}}_{M/2-1,\epsilon_{|\kappa|}} \right]^T \in \mathbb{C}^{M|\kappa| \times M}, \tag{4.13i}$$

$$f^{\mathrm{D}}_{v,\epsilon_l,m} = e^{-j2\pi m(v-\epsilon_l)/M},\ l = (1, \cdots, |\kappa|), \tag{4.13j}$$

where (4.13c) is achieved because $|r_{n,v,\epsilon}| \geq 0$ for $n \neq 0$ with the equality achieved if and only if $p_{k,m} = p_m/K$ since

$$r_{n,v,\epsilon} = \sum_{m,k} p_m e^{j2\pi \frac{nk}{K}} e^{-j2\pi \frac{vm}{M}} e^{j2\pi \frac{\epsilon m}{M}} / K = \sum_k e^{j2\pi \frac{nk}{K}} \sum_m p_m e^{-j2\pi \frac{vm}{M}} e^{j2\pi \frac{\epsilon m}{M}} / K = 0 \tag{4.14}$$

□

Then in (4.13c), the only variables involved are the power allocation across OFDM symbols, i.e., p_m. Hence, the optimal power allocation would have uniform power allocation across OFDM subcarriers, and we need to optimize the power allocation across OFDM symbols, i.e., p_m for $\forall m$ or equivalently $\mathbf{p}$.

With uniform (optimal) power allocation across OFDM subcarriers, the optimization problem (4.12) is simplified into

$$\min_{\mathbf{p},\, \mathbf{r}} \quad \mathbb{P}_{\mathrm{UB}}(\mathbf{r}) \text{ in (4.13d)}, \tag{4.15a}$$

$$\text{s.t.} \quad \mathbf{1}^T \mathbf{p} \leq P^{\max}, \tag{4.15b}$$

$$\mathbf{p} \succeq \mathbf{0}, \tag{4.15c}$$

$$\mathbf{r} = \mathbf{F}^{\mathrm{D}} \mathbf{p}. \tag{4.15d}$$

After obtaining the optimized power allocation across the OFDM symbols from (4.15), i.e. $\mathbf{p}$, the optimal power allocation at each OFDM symbol's sub-carrier is $p_{k,m}=p_m/K$, $\forall k$, m (from Lemma 1).

4.4.2 Low complexity optimization

Solving the non-convex problem (4.15) can be very time-consuming with a large number of OFDM symbols M, whereas in OFDM radar, M shall be large, i.e., above 512, to achieve high Doppler resolution [67]. Hence, in this section, we adopt a low-complexity alternating direction method of multipliers (ADMM) algorithm where problem (4.15) is approximately solved in an iterative manner with closed-form solutions in each round.

Considering the linear constraint in (4.15d), we adopt ADMM to iteratively update $\mathbf{p}$ and $\mathbf{r}$ until the two successive solutions get close [105]. Following the ADMM structure[4], at the l^{th} iteration, problem (4.15) is iteratively formulated as [105]

$$\mathbf{r}^{(l+1)} := \underset{\mathbf{r}}{\operatorname{argmin}} \left\{ \mathbb{P}_{\text{UB}}(\mathbf{r}) + \frac{\rho}{2} \|\mathbf{r} - \mathbf{F}^{\text{D}}\mathbf{p}^{(l)} + \mathbf{d}^{(l)}\|^2 \right\}, \tag{4.16}$$

$$\mathbf{p}^{(l+1)} := \underset{\mathbf{p}}{\operatorname{argmin}} \left\{ \mathbb{1}_{(\mathbf{1}^T\mathbf{p} \le P^{\max},\ \mathbf{p} \succeq \mathbf{0})} + \frac{\rho}{2} \|\mathbf{r}^{(l+1)} - \mathbf{F}^{\text{D}}\mathbf{p} + \mathbf{d}^{(l)}\|^2 \right\}, \tag{4.17}$$

$$\mathbf{d}^{(l+1)} := \mathbf{d}^{(l)} + \mathbf{r}^{(l+1)} - \mathbf{F}^{\text{D}}\mathbf{p}^{(l+1)}, \tag{4.18}$$

where $\mathbf{d}^{(l)}$ is the ADMM stepsize at the l^{th} iteration and ρ is the ADMM penalty coefficient.

Updating $\mathbf{r}$ *in* (4.16): To solve subproblem (4.16), we adopt SCP to approximate the exponential function in (4.16) linearly by the first-order Taylor expansion. The optimal solution of this approximated problem is then used as a new operating point of the Taylor expansion for the next SCP round. The procedure is repeated until two successive solutions are close enough.

[4]With ADMM, we obtain local optimal solutions (referred to as optimal in the following) as an approximation to the global optimal solution in this chapter, similarly to the BCD algorithm in Section 4.5.2.

$$\boldsymbol{\alpha}_v^{(l+1,t)} = \begin{cases} -\frac{\sum_{v=1}^{M-1}}{2\sigma^2|\kappa|}\exp\left\{-\frac{|\mathbf{r}_0^{(l+1,t)}|-|\mathbf{r}_v^{(l+1,t)}|}{2\sigma^2}\right\} - \frac{(K_G M-1)}{2\sigma^2|\kappa|}\exp\left\{-\frac{|\mathbf{r}_0^{(l+1,t)}|}{2\sigma^2}\right\}, & \text{for } v=0; \\ \exp\left\{-\frac{|\mathbf{r}_0^{(l+1,t)}|-|\mathbf{r}_v^{(l+1,t)}|}{2\sigma^2}\right\}/(2\sigma^2|\kappa|), & \text{otherwise.} \end{cases} \tag{4.20}$$

Consequently, assume that $\mathbf{r}^{(l+1,\ t)}$ is the optimal solution at the t^{th} iteration of SCP. Then $\mathbf{r}^{(l+1,\ t+1)}$ is updated as

$$\mathbf{r}^{(l+1,\ t+1)} = \underset{\mathbf{r}}{\operatorname{argmin}}\left\{\boldsymbol{\alpha}^{(l+1,\ t)^T}|\mathbf{r}| + \frac{\rho}{2}\|\mathbf{r}-\mathbf{F}^{\mathrm{D}}\mathbf{p}^{(l)}\|^2\right\} \tag{4.19a}$$

$$= \left(\mathbf{F}^{\mathrm{D}}\mathbf{p}^{(l)} - \boldsymbol{\theta}^{(l)} \odot \boldsymbol{\alpha}^{(l+1,\ t)}/\rho\right)^+, \tag{4.19b}$$

where $\boldsymbol{\theta}^{(l)} = \angle \mathbf{F}^{\mathrm{D}}\mathbf{p}^{(l)}$. The closed-form expression in (4.19b) is derived in Appendix 4.8.2. The first-order Taylor coefficient $\boldsymbol{\alpha}^{(l+1,\ t)} = [\boldsymbol{\alpha}_0^{(l+1,\ t)^T},\ \cdots,\ \boldsymbol{\alpha}_{M-1}^{(l+1,\ t)^T}]^T$ is expressed in (4.20).

Updating $\mathbf{p}$ *in* (4.17): Given a fixed $\mathbf{r}^{(l+1)}$, the optimal $\mathbf{p}^{(l+1)}$ can be directly solved by quadratic programming (QP) as

$$\min_{\mathbf{p}} \quad \frac{\rho}{2}\|\mathbf{r}^{(l+1)} - \mathbf{F}^{\mathrm{D}}\mathbf{p}\|^2, \tag{4.21a}$$

$$\text{s.t.} \quad \mathbf{1}^T\mathbf{p} \le P^{\max}, \tag{4.21b}$$

$$\mathbf{p} \succeq \mathbf{0}. \tag{4.21c}$$

The algorithm is summarized in Algorithm 9.

Algorithm 4: ADMM for PSK input in (4.12)

1. **Input**: $l \leftarrow 0$, $\mathbf{r}^{(0)}$, $\mathbf{p}^{(0)}$, ρ, $\epsilon_S > 0$
2. **Repeat (Solving p in** (4.15)**)**
   - 2.1 Update $\mathbf{r}^{(l+1)}$ in problem (4.16) by SCP
     - Initialize $t \leftarrow 0$; $\mathbf{r}^{(l+1,\ 0)} \leftarrow \mathbf{r}^{(l)}$
     - **while** $t \leq 10^2$
       - Compute $\boldsymbol{\alpha}^{(l+1,\ t)}$ in (4.20) at the operating point $\mathbf{r}^{(l+1,\ t)}$
       - Compute $\mathbf{r}^{(l+1,\ t+1)}$ using (4.19b)
       - $t \leftarrow t+1$; $\mathbf{r}^{(l+1)} \leftarrow \mathbf{r}^{(l+1,\ t+1)}$
     - Iteration complexity $\mathcal{O}(M^2|\kappa|)$
   - 2.2 Update $\mathbf{p}^{(l+1)}$ in (4.17) by QP (complexity $\mathcal{O}(M^3)$)
   - 2.3 $l \leftarrow l+1$; $\mathbf{p} \leftarrow \mathbf{p}^{(l+1)}$
   - 2.4 Quit if $\|\mathbf{p}^{(l+1)} - \mathbf{p}^{(l)}\| < \epsilon_S \|\mathbf{p}^{(l+1)}\|$
3. **Output**: $\mathbf{p}_{k,m} \leftarrow p_m / K$

4.5 Minimizing OP for variable magnitude input distributions (Gaussian)

This section evaluates the radar performance in OFDM DFRC with non-zero mean Gaussian input, where the magnitude of the CSs becomes a random variable obeying the Rician distribution. Consequently, we evaluate the aUBOP and then optimize the Gaussian mean and variance at each symbol's subcarriers to minimize the aUBOP. In this scheme, an achievable communication constraint is added to avoid a zero-variance optimization result where no information bits are transmitted.

4.5.1 Problem formulation

In this context, we first model the CS $X[k,\, m]$ in (4.2) as a complex non-zero mean asymmetric Gaussian variable

$$X[k,\, m]=X_{\mathrm{R}}[k,\, m]+jX_{\mathrm{I}}[k,\, m], \tag{4.22}$$

where $X_{\mathrm{R/I}}[k,\, m]\sim\mathcal{N}(\mu_{\mathrm{R/I},\, k,m},\, \sigma^2_{\mathrm{R/I},\, k,m})$.

Then, the average power (second-order moments) allocated to the real and imaginary part of the m^{th} OFDM symbol at the k^{th} subcarrier are defined as

$$\overline{p}_{\mathrm{R},k,m}=\mu^2_{\mathrm{R},k,m}+\sigma^2_{\mathrm{R},k,m}, \tag{4.23a}$$

$$\overline{p}_{\mathrm{I},k,m}=\mu^2_{\mathrm{I},k,m}+\sigma^2_{\mathrm{I},k,m}. \tag{4.23b}$$

On this basis, the AF r_{n,v,v_ϵ} in (4.11d) becomes random, making the UBOP varying. Hence, we derive the aUBOP as follows (abbreviating the expectation over $X[k,\, m]$ as X, i.e., $\mathbb{E}_X\triangleq\mathbb{E}_{X[k,\, m]}$)

$$\overline{\mathbb{P}}_{\mathrm{UB}}(\overline{\mathbf{p}},\, \boldsymbol{\sigma}) \tag{4.24a}$$

$$=\mathbb{E}_{v_\epsilon,X}\Big\{\sum_{(n,\, v)\neq(0,\, 0)}\exp\Big\{-\frac{|r_{0,0,v_\epsilon}|-|r_{n,v,v_\epsilon}|}{2\sigma^2}\Big\}/2\Big\} \tag{4.24b}$$

$$\propto\frac{1}{4\sigma^2}\sum_{(n,\, v)\neq(0,\, 0)}\mathbb{E}_{\epsilon,X}\{-|r_{0,0,\epsilon}|+|r_{n,v,\epsilon}|\} \tag{4.24c}$$

$$\leq\frac{1}{4\sigma^2}\sum_{(n,\, v)\neq(0,\, 0)}\mathbb{E}_{\epsilon}\Big\{-|\mathbb{E}_X\{r_{0,0,\epsilon}\}|+\sqrt{\mathbb{E}_X\{|r_{n,v,\epsilon}|^2\}}\Big\} \tag{4.24d}$$

$$=\frac{1}{4|\kappa|\sigma^2}\sum_{\epsilon\in\kappa}\sum_{(n,\, v)\neq(0,\, 0)}-\sqrt{\overline{\mathbf{p}}^T\mathbf{A}_\epsilon\overline{\mathbf{p}}}+g_{n,v,\epsilon}(\overline{\mathbf{p}},\, \boldsymbol{\sigma}), \tag{4.24e}$$

$$\text{with } g_{n,v,\epsilon}(\overline{\mathbf{p}},\, \boldsymbol{\sigma})=\sqrt{\overline{\mathbf{p}}^T\mathbf{A}_{n,v,\epsilon}\overline{\mathbf{p}}-2\|\overline{\mathbf{p}}-\boldsymbol{\sigma}\|^2}, \tag{4.24f}$$

$$\overline{\mathbf{p}}=\left[\overline{p}_{\mathrm{R},0,0},\, \overline{p}_{\mathrm{R},1,0},\, \cdots,\, \overline{p}_{\mathrm{I},0,0},\, \cdots,\, \overline{p}_{\mathrm{I},K-1,M-1}\right]^T, \tag{4.24g}$$

$$\boldsymbol{\sigma}=\left[\sigma_{\mathrm{R},0,0},\, \sigma_{\mathrm{R},1,0},\, \cdots,\, \sigma_{\mathrm{I},0,0},\, \cdots,\, \sigma_{\mathrm{I},K-1,M-1}\right]^T, \tag{4.24h}$$

$$\mathbf{A}_{\epsilon}=\Re\{\mathbf{f}_{0,0,\epsilon}\}\Re\{\mathbf{f}_{0,0,\epsilon}\}^T+\Im\{\mathbf{f}_{0,0,\epsilon}\}\Im\{\mathbf{f}_{0,0,\epsilon}\}^T, \tag{4.24i}$$

$$\mathbf{A}_{n,v,\epsilon}=\Re\{\mathbf{f}_{n,v,\epsilon}\}\Re\{\mathbf{f}_{n,v,\epsilon}\}^T+\Im\{\mathbf{f}_{n,v,\epsilon}\}\Im\{\mathbf{f}_{n,v,\epsilon}\}^T+2\mathbf{I}_{2KM}, \tag{4.24j}$$

$$\mathbf{f}_{n,v,\epsilon}=\mathbf{1}_2\otimes\left(\mathbf{f}^{\mathrm{D}}_{v,\ \epsilon}\otimes\mathbf{f}^{\mathrm{R}}_{n}\right)\in\mathbb{C}^{2KM}, \tag{4.24k}$$

$$f^{\mathrm{R}}_{n,k}=e^{j2\pi nk/K}, \tag{4.24l}$$

where (4.24c) assumes low SNR at the radar's receiver[5], giving $\exp\{x\}\to x+1$ for $x\to 0$ ($r_{0,0,\epsilon}\geq r_{n,v,\epsilon}$ for any $(n,\, v)$). (4.24d) is due to the concavity of the square root function. (4.24e) is achieved from Appendix 4.8.3, whose first sum term of $\mathbb{E}_{\epsilon}\{-|\mathbb{E}_X\{r_{0,0,\epsilon}\}|\}$ in (4.24d) represents the magnitude of average peak lobe, and whose second sum term of $\mathbb{E}_{\epsilon}\{-|\mathbb{E}_X\{r_{n,v,\epsilon}\}|\}$ at $(n,\, v)\neq(0,\, 0)$ in (4.24d) represents the magnitude of the average sidelobes.

Remark 11. (4.24d) *indicates that the optimization objective (aUBOP),* $\overline{\mathbb{P}}_{\mathrm{UB}}(\overline{\mathbf{p}},\, \boldsymbol{\sigma})$*, finally becomes a scaling term of the average ISPLD in low SNR, corresponding to Remark 8. Also,* (4.24e) *indicates that, without communication constraints, the optimal solution to minimize* (4.24e) *yields maximizing* $\|\overline{\mathbf{p}}-\boldsymbol{\sigma}\|$ *for an arbitrary* $\overline{\mathbf{p}}$*, i.e.,* $\sigma^2_{\mathrm{R/I},k,m}=0$ *and hence* $\overline{p}_{\mathrm{R/I},k,m}=\mu^2_{\mathrm{R/I},k,m}$*. In this context, all the power is allocated to the deterministic component of the Gaussian distributions for the radar-optimal purpose. In other words, the randomness of the CS magnitudes degrades radar's OP.*

[5] In this chapter, we only discuss the statistic approximation and the optimization in the low SNR region due to the space limit, while similar procedures can be done for the middle SNR and for the high SNR scenarios. For the middle SNR region, (4.24c) can be replaced by Taylor approximation with appropriate orders and coefficients given its finite SNR region [106]. For the high SNR region, inspired by Remark 8, the objective function might be approximated by maximizing the minimal average peak-to-side-lobe difference.

4.5.2 Optimization

We then formulate the corresponding optimization problem in DFRC using the developed metric in (4.24e). With the constraint on achievable rate, we have the optimization problem (neglecting the constant multiplier $1/(4\sigma^2)$)

$$\min_{\overline{\mathbf{p}},\, \boldsymbol{\sigma}} \quad \sum_{\epsilon\in\kappa}\sum_{(n,\ v)\neq(0,\ 0)} -\sqrt{\overline{\mathbf{p}}^T\mathbf{A}_\epsilon\overline{\mathbf{p}}}+g_{n,v,\epsilon}(\overline{\mathbf{p}},\, \boldsymbol{\sigma}), \tag{4.25a}$$

$$\text{s.t.} \quad \mathbf{1}^T\overline{\mathbf{p}}\leq P^{\max}, \tag{4.25b}$$

$$\frac{1}{2KM}\log\,\det(\mathbf{I}_{2KM}+\mathbf{C}\text{diag}\{\boldsymbol{\sigma}\})\geq R^{\text{c}}, \tag{4.25c}$$

$$\overline{\mathbf{p}}\succeq\boldsymbol{\sigma}, \tag{4.25d}$$

$$\boldsymbol{\sigma}\succeq\mathbf{0}, \tag{4.25e}$$

where (4.25c) is the average rate constraint over M OFDM symbols from Section 2.4. In (4.25c), $\mathbf{C}=2K\text{diag}\{\mathbf{1}_{2M}\otimes\mathbf{h}/(B\sigma_{\text{C}}^2)\}\in\mathbb{R}^{2KM\times 2KM}$ with the k^{th} entry of $\mathbf{h}$ being $h_k=|h_{\text{C},k}|^2$ for $k=[1,\,\cdots,\,K]$. $h_{\text{C},k}$ is the complex gain of the communication channel for the k^{th} subcarrier. σ_{C}^2 is the noise power density at the communication receiver. R^c is the minimum achievable rate constraint for communications.

For efficiency, we use the method of block coordinate descent (BCD) to solve problem (4.25). In BCD, given an initial point of $\overline{\mathbf{p}}^{(l)}/\boldsymbol{\sigma}^{(l)}$ at the l^{th} iteration, $\overline{\mathbf{p}}^{(l+1)}$ is optimized first with fixed $\boldsymbol{\sigma}^{(l)}$. Then $\boldsymbol{\sigma}^{(l+1)}$ is optimized with fixed $\overline{\mathbf{p}}^{(l+1)}$. The iteration continues until two successive solutions get close.

Updating $\overline{\mathbf{p}}$: Given $\boldsymbol{\sigma}^{(l)}$, the sub-problem for $\overline{\mathbf{p}}$ is

$$\min_{\overline{\mathbf{p}}} \quad \sum_{\epsilon\in\kappa}\sum_{(n,\ v)\neq(0,\ 0)} -\sqrt{\overline{\mathbf{p}}^T\mathbf{A}_\epsilon\overline{\mathbf{p}}}+g_{n,v,\epsilon}\Big(\overline{\mathbf{p}},\, \boldsymbol{\sigma}^{(l)}\Big), \tag{4.26a}$$

$$\text{s.t.} \quad \mathbf{1}^T\overline{\mathbf{p}}\leq P^{\max}, \tag{4.26b}$$

$$\overline{\mathbf{p}}\succeq\boldsymbol{\sigma}^{(l)}, \tag{4.26c}$$

whose objective function in (4.26a) is non-convex. As a solution, we adopt SCP similarly to Section 4.4, where the square root function in (4.26a) is approximated by its first-order Taylor expansion $\sqrt{x} \approx (x-x_0)/(2\sqrt{x_0})+\sqrt{x_0} = x/(2\sqrt{x_0})+\sqrt{x_0}/2$.

Assume $\overline{\mathbf{p}}^{(t)}$ is the operating point at the beginning of the t^{th} iteration when solving problem (4.26). Then, (4.26a) at the t^{th} iteration is linearly approximated as [96]

$$\sum_{\epsilon\in\kappa}\sum_{(n,\ v)\neq(0,\ 0)} -\sqrt{\overline{\mathbf{p}}^T\mathbf{A}_\epsilon\overline{\mathbf{p}}}+g_{n,v,\epsilon}\big(\overline{\mathbf{p}},\, \boldsymbol{\sigma}^{(l)}\big) \approx \overline{\mathbf{p}}^T\mathbf{B}^{(l,\ t)}\overline{\mathbf{p}}+\boldsymbol{\alpha}^{(l,\ t)^T}\overline{\mathbf{p}}+{\alpha_c}^{(l,\ t)}, \tag{4.27a}$$

with

$$\begin{aligned}
\mathbf{B}^{(l,\ t)} &= \sum_{\epsilon\in\kappa}\sum_{(n,\ v)\neq(0,\ 0)} \mathbf{A}_{n,v,\epsilon}/g_{n,v,\epsilon}\big(\overline{\mathbf{p}}^{(t)},\, \boldsymbol{\sigma}^{(l)}\big)/2 && (4.27b)\\
&= 2\|1\oslash\mathbf{g}^{(l,\ t)}\|^2\mathbf{I}_{2KM}+\big(\Re\{\mathbf{F}\}\oslash\mathbf{g}^{(l,\ t)}\big)\big(\Re\{\mathbf{F}\}\oslash\mathbf{g}^{(l,\ t)}\big)^T \\
&\quad +\big(\Im\{\mathbf{F}\}\oslash\mathbf{g}^{(l,\ t)}\big)\big(\Im\{\mathbf{F}\}\oslash\mathbf{g}^{(l,\ t)}\big)^T, && (4.27c)\\
\boldsymbol{\alpha}^{(l,\ t)} &= -(K_GM-1)\sum_{\epsilon\in\kappa}\mathbf{A}_\epsilon\overline{\mathbf{p}}^{(t)}/\sqrt{\mathbf{p}^{(t)^T}\mathbf{A}_\epsilon\mathbf{p}^{(t)}}-4\big(\overline{\mathbf{p}}^{(t)}-\boldsymbol{\sigma}^{(t)}\big)\|1\oslash\mathbf{g}^{(l,\ t)}\|^2, && (4.27d)\\
\mathbf{F} &= \Big[\mathbf{F}_{0,-M/2},\, \mathbf{F}_{1,-M/2},\, \cdots,\, \mathbf{F}_{K_G-1,M/2-1}\Big],\ (\text{w/o } \mathbf{F}_{0,0}) && (4.27e)\\
\mathbf{F}_{n,v} &= \Big[\mathbf{f}_{n,v,\epsilon_1},\, \cdots,\, \mathbf{f}_{n,v,\epsilon_{|\kappa|}}\Big]\in\mathbb{R}^{2KM\times|\kappa|}, && (4.27f)\\
\mathbf{g}^{(l,\ t)} &= \big[4\mathbf{q}^{(t)}+8\|\overline{\mathbf{p}}^{(t)}\|^2-8\|\overline{\mathbf{p}}^{(t)}-\boldsymbol{\sigma}^{(l)}\|^2\big]^{1/4}, && (4.27g)\\
\mathbf{q}^{(t)} &= \overline{\mathbf{p}}^{(t)^T}\Re\{\mathbf{F}\}\odot\big(\overline{\mathbf{p}}^{(t)^T}\Re\{\mathbf{F}\}\big)^*+\overline{\mathbf{p}}^{(t)^T}\Im\{\mathbf{F}\}\odot\big(\overline{\mathbf{p}}^{(t)^T}\Im\{\mathbf{F}\}\big)^*, && (4.27h)
\end{aligned}$$

where ${\alpha_c}^{(l,\ t)}$ is the Taylor constant that can be omitted.

Hence, we form the sub-problem towards solving problem (4.26) as

$$\begin{aligned}
&\min_{\overline{\mathbf{p}}} \quad \overline{\mathbf{p}}^T\mathbf{B}^{(l,\ t)}\overline{\mathbf{p}}+\boldsymbol{\alpha}^{(l,\ t)^T}\overline{\mathbf{p}}, && (4.28a)\\
&\text{s.t.} \quad (4.26\text{b})-(4.26\text{c}), && (4.28b)
\end{aligned}$$

which is a QP problem.

Updating $\boldsymbol{\sigma}$: When fixing $\overline{\mathbf{p}}$ as $\overline{\mathbf{p}}^{(l)}$, we observe that the objective function in problem (4.25) is a monotonically increasing function with $2\overline{\mathbf{p}}^{(l)^T}\boldsymbol{\sigma}-\|\boldsymbol{\sigma}\|^2$. Hence, the sub-problem for $\boldsymbol{\sigma}$ becomes

$$\min_{\boldsymbol{\sigma}} \quad 2\overline{\mathbf{p}}^{(l)^T}\boldsymbol{\sigma}-\|\boldsymbol{\sigma}\|^2, \tag{4.29a}$$

$$\text{s.t.} \quad \frac{1}{2KM}\log\det(\mathbf{I}_{2KM}+\mathbf{C}\text{diag}\{\boldsymbol{\sigma}\})\geq R^{\text{c}}, \tag{4.29b}$$

$$\overline{\mathbf{p}}^{(l)}\succeq\boldsymbol{\sigma}, \tag{4.29c}$$

$$\boldsymbol{\sigma}\succeq\mathbf{0}, \tag{4.29d}$$

which is convex. Again, for lower complexity to handle a large number of variables, we solve problem (4.29) iteratively by SCP with closed-form solutions. At the t^{th} iteration of the SCP sub-problem, the concave objective function is approximated by the first order Taylor expansion, and the sub-problem becomes [96]

$$\min_{\boldsymbol{\sigma}} \quad \boldsymbol{\beta}^{(l,\,t)^T}\boldsymbol{\sigma}, \tag{4.30a}$$

$$\text{s.t.} \quad (4.29\text{b})-(4.29\text{d}), \tag{4.30b}$$

with $\boldsymbol{\beta}^{(l,\,t)}=2\big(\overline{\mathbf{p}}^{(l)}-\boldsymbol{\sigma}^{(t)}\big)$. The closed-form solution for problem (4.30), after KKT, is given by [101]

$$\sigma_q=\begin{cases}\overline{p}_q^{(l)}, & u>\frac{2KM\beta_q^{(l,\,t)}\left(1+C_{q,q}\overline{p}_q^{(l)}\right)}{C_{q,q}};\\ 0, & 0<u<\frac{2KM\beta_q^{(l,\,t)}}{C_{q,q}};\\ \frac{u}{2KM\beta_q^{(l,\,t)}}-\frac{1}{C_{q,q}}, & \text{otherwise},\end{cases} \tag{4.31}$$

where u is the Lagrangian multiplier of constraint (4.29b), obtained by bi-section search.

The entire algorithm to solve problem (4.25) is summarized in Algorithm 5.

Algorithm 5: BCD for Gaussian input in (4.25)

1. **Input**: $l \leftarrow 0$, $\overline{\mathbf{p}}^{(0)}$, $\boldsymbol{\sigma}_R^{(0)}$, $\epsilon_S > 0$
2. **Output**: $\overline{\mathbf{p}}$, $\boldsymbol{\sigma}$
3. **Repeat**
   - 3.1 Compute $\overline{\mathbf{p}}^{(l+1)}$ in problem (4.26) using SCP
     - Initialize $t \leftarrow 0$; $\overline{\mathbf{p}}^{(l+1,\ 0)} \leftarrow \overline{\mathbf{p}}^{(l)}$
     - **while** $t \leq 10^2$
       - Compute $\mathbf{B}^{(l+1,\ t)}$ and $\boldsymbol{\alpha}^{(l+1,\ t)}$ in (4.27c)-(4.27d)
       - Compute $\overline{\mathbf{p}}^{(l+1,\ t+1)}$ using (4.28)
       - $t \leftarrow t+1$; $\overline{\mathbf{p}}^{(l+1)} \leftarrow \overline{\mathbf{p}}^{(l+1,\ t+1)}$
     - Iteration complexity: $\mathcal{O}(K^3M^3|\kappa|)$
   - 3.2 Compute $\boldsymbol{\sigma}^{(l+1)}$ in problem (4.29) using SCP
     - Initialize $t \leftarrow 0$; $\boldsymbol{\sigma}^{(l+1,\ 0)} \leftarrow \boldsymbol{\sigma}^{(l)}$
     - **while** $t \leq 10^2$
       - Compute $\boldsymbol{\beta}^{(l+1,\ t)}$ in (4.30) and $\boldsymbol{\sigma}^{(l+1,\ t+1)}$ in (4.31)
       - $t \leftarrow t+1$; $\boldsymbol{\sigma}^{(l+1)} \leftarrow \boldsymbol{\sigma}^{(l+1,\ t+1)}$
     - Iteration complexity: $\mathcal{O}(KM)$
   - 3.3 $l \leftarrow l+1$; $\overline{\mathbf{p}} \leftarrow \overline{\mathbf{p}}^{(l+1)}$; $\boldsymbol{\sigma} \leftarrow \boldsymbol{\sigma}^{(l+1)}$
   - 3.4 Quit if $|\overline{\mathbb{P}}_{\mathrm{UB}}^{(l+1)}(\overline{\mathbf{p}}, \boldsymbol{\sigma}) - \overline{\mathbb{P}}_{\mathrm{UB}}^{(l)}(\overline{\mathbf{p}}, \boldsymbol{\sigma})| < \epsilon_S$

4.5.3 Decoupling optimization

Algorithm 5 can be time-consuming given large K and M because of the large-dimensional variables and coefficients. However, inspired by the optimal power allocation in section 4.4, we give a simplified method by decoupling the optimization of Gaussian input distribution across time domain (OFDM symbols) and frequency domain (OFDM subcarriers), namely the decoupling method. Specifically, we assume that the distribution of CSs on each OFDM symbol is a scaled version of a common distribution $\overline{\mathbf{p}}_{\mathrm{K}} \in \mathbb{R}^{2K}$ and $\boldsymbol{\sigma}_{\mathrm{K}} \in \mathbb{R}^{2K}$ (accounting for the real and imaginary part). Mathematically, the final distribution of

$X[k,\, m]$ in (4.22) has the following form

$$\overline{\mathbf{p}}=\mathbf{F}_{\mathrm{M}}\overline{\mathbf{p}}_{\mathrm{K}},\ \boldsymbol{\sigma}=\mathbf{F}_{\mathrm{M}}\boldsymbol{\sigma}_{\mathrm{K}}, \tag{4.32}$$

where $\mathbf{F}_{\mathrm{M}}=\begin{bmatrix}\mathbf{p}\otimes\mathbf{I}_K & \mathbf{0}_{KM\times K}\\ \mathbf{0}_{KM\times K} & \mathbf{p}\otimes\mathbf{I}_K\end{bmatrix}\in\mathbb{R}^{2KM\times 2K}$ with $\mathbf{p}\in\mathbb{R}^M$ being the optimal power allocation across OFDM symbols in Section 4.4. Correspondingly, for the power allocation to be optimized across OFDM subcarriers, we have $\mathbf{1}^T\overline{\mathbf{p}}_{\mathrm{K}}\leq 1$ as a substitute of the power constraint and adopt the algorithm in Section 4.5.2. Consequently, compared with optimizing $\overline{\mathbf{p}}$ and $\boldsymbol{\sigma}$ of totally $4KM$ variables in section 4.5.2, after decoupling, we only need to optimize $\mathbf{p}$, $\overline{\mathbf{p}}_{\mathrm{K}}$ and $\boldsymbol{\sigma}_{\mathrm{K}}$ which are totally $M+4K$ variables.

On this basis, $\overline{\mathbb{P}}_{\mathrm{UB}}(\overline{\mathbf{p}},\, \boldsymbol{\sigma})$ in (4.24e) as a function of $\overline{\mathbf{p}}_{\mathrm{K}}$ and $\boldsymbol{\sigma}_{\mathrm{K}}$ becomes

$$\overline{\mathbb{P}}_{\mathrm{UB}}(\overline{\mathbf{p}}_{\mathrm{K}},\, \boldsymbol{\sigma}_{\mathrm{K}})=\sum_{\epsilon\in\kappa}\left[-\sqrt{\overline{\mathbf{p}}_{\mathrm{K}}{}^T\mathbf{F}_{\mathrm{M}}{}^T\mathbf{A}_{\epsilon}\mathbf{F}_{\mathrm{M}}\overline{\mathbf{p}}_{\mathrm{K}}}+\sum_{(n,\ v)\neq(0,\ 0)}g_{n,v,\epsilon}(\mathbf{F}_{\mathrm{M}}\overline{\mathbf{p}}_{\mathrm{K}},\, \mathbf{F}_{\mathrm{M}}\boldsymbol{\sigma}_{\mathrm{K}})\right] \tag{4.33a}$$

$$=A_{\mathrm{D}}^0\mathbf{1}^T\overline{\mathbf{p}}_{\mathrm{K}}+\sum_{(n,\ v)\neq(0,\ 0),\ \epsilon}g_{n,v,\epsilon}^0(\overline{\mathbf{p}}_{\mathrm{K}},\, \boldsymbol{\sigma}_{\mathrm{K}}), \tag{4.33b}$$

$$\text{with } A_{\mathrm{D}}^0=\sum_{\epsilon\in\kappa}\sqrt{\left(\mathbf{p}^T\Re\{\mathbf{f}_{0,\ \epsilon}^{\mathrm{D}}\}\right)^2+\left(\mathbf{p}^T\Im\{\mathbf{f}_{0,\ \epsilon}^{\mathrm{D}}\}\right)^2}, \tag{4.33c}$$

$$g_{n,v,\epsilon}^0(\overline{\mathbf{p}}_{\mathrm{K}},\, \boldsymbol{\sigma}_{\mathrm{K}})=\sqrt{\overline{\mathbf{p}}_K{}^T\mathbf{A}_{n,v,\epsilon}^0\overline{\mathbf{p}}_K-2\|\mathbf{p}\|^2\|\overline{\mathbf{p}}_{\mathrm{K}}-\boldsymbol{\sigma}_{\mathrm{K}}\|^2}, \tag{4.33d}$$

$$\mathbf{A}_{n,v,\epsilon}^0=\gamma_{v,\epsilon}\left[\Re\{\mathbf{f}_n^{\mathrm{R}_0}\}\Re\{\mathbf{f}_n^{\mathrm{R}_0}\}^T+\Im\{\mathbf{f}_n^{\mathrm{R}_0}\}\Im\{\mathbf{f}_n^{\mathrm{R}_0}\}^T\right]+2\|\mathbf{p}\|^2, \tag{4.33e}$$

$$\gamma_{v,\epsilon}=|\mathbf{p}^T\mathbf{f}_{v,\ \epsilon}^{\mathrm{D}}|^2,\ \mathbf{f}_n^{\mathrm{R}_0}=\mathbf{1}_2\otimes\mathbf{f}_n^{\mathrm{R}}, \tag{4.33f}$$

where (4.33b) comes from Appendix 4.8.4.

Given (4.33b), the optimal $\overline{\mathbf{p}}_{\mathrm{K}}$ and $\boldsymbol{\sigma}_{\mathrm{K}}$ using the optimal $\mathbf{p}$ from Algorithm 9 are obtained

by

$$\min_{\overline{\mathbf{p}}_{\mathrm{K}},\, \boldsymbol{\sigma}_{\mathrm{K}}} \quad \overline{\mathbb{P}}_{\mathrm{UB}}(\overline{\mathbf{p}}_{\mathrm{K}},\, \boldsymbol{\sigma}_{\mathrm{K}}) \text{ in (4.33b)}, \tag{4.34a}$$

$$\text{s.t.} \quad \mathbf{1}^T\overline{\mathbf{p}}_{\mathrm{K}} \leq 1, \tag{4.34b}$$

$$\frac{1}{2KM}\sum_{m} \log\,\det(\mathbf{I}_{2K}+p_m\mathbf{C}'\mathrm{diag}\{\boldsymbol{\sigma}_{\mathrm{K}}\}) \geq R^{\mathrm{c}}, \tag{4.34c}$$

$$\overline{\mathbf{p}}_{\mathrm{K}} \succeq \boldsymbol{\sigma}_{\mathrm{K}}, \tag{4.34d}$$

$$\boldsymbol{\sigma}_{\mathrm{K}} \succeq \mathbf{0}, \tag{4.34e}$$

where $\mathbf{C}' = 2K\mathrm{diag}\{\mathbf{1}_2 \otimes \mathbf{h}/(B\sigma^2)\} \in \mathbb{R}^{2K\times 2K}$. (4.34) can be solved in the same way as that in (4.25) in Section 4.5.2 where $\overline{\mathbf{p}}_{\mathrm{K}}$ and $\boldsymbol{\sigma}_{\mathrm{K}}$ are updated iteratively following a BCD structure, with only slight modifications on the coefficients to couple with the optimal $\mathbf{p}$. The details are:

Updating $\mathbf{p}_{\mathrm{K}}$: Then, we follow the same SCP procedure as (4.26) in Section 4.5.2 to update $\mathbf{p}_K$, with the only difference being the coefficients in (4.27c) and (4.27d) updated by

$$\mathbf{B}_0^{(l,\,t)} = 2\|\mathbf{p}\|^2\|1 \oslash \mathbf{g}_0^{(l,\,t)}\|^2\mathbf{I}_{2K} + \left(\mathbf{F}_{\mathrm{R}_0} \oslash \mathbf{g}_0^{(l,\,t)}\right)\left(\mathbf{F}_{\mathrm{R}_0} \oslash \mathbf{g}_0^{(l,\,t)}\right)^T + \left(\mathbf{F}_{\mathrm{I}_0} \oslash \mathbf{g}_0^{(l,\,t)}\right)\left(\mathbf{F}_{\mathrm{I}_0} \oslash \mathbf{g}_0^{(l,\,t)}\right)^T, \tag{4.35a}$$

$$\boldsymbol{\alpha}_0^{(l,t)} = A_D^0\mathbf{1}_{2K} - 4\|\mathbf{p}\|^2\|1 \oslash \mathbf{g}_0^{(l,\,t)}\|^2\left(\overline{\mathbf{p}}_{\mathrm{K}}^{(t)} - \boldsymbol{\sigma}_{\mathrm{K}}^{(t)}\right), \tag{4.35b}$$

with

$$\mathbf{g}_0^{(l,\,t)} = \left[4\mathbf{q}_0^{(t)} + 8\|\mathbf{p}\|^2\|\overline{\mathbf{p}}_{\mathrm{K}}^{(t)}\|^2 - 8\|\mathbf{p}\|^2\|\overline{\mathbf{p}}_{\mathrm{K}}^{(t)} - \boldsymbol{\sigma}_{\mathrm{K}}^{(l)}\|^2\right]^{1/4}, \tag{4.35c}$$

$$\mathbf{q}_0^{(t)} = \overline{\mathbf{p}}_{\mathrm{K}}^{(t)T}\left[\mathbf{F}_{\mathrm{R}_0} \odot \left(\overline{\mathbf{p}}_{\mathrm{K}}^{(t)T}\mathbf{F}_{\mathrm{R}_0}\right)^* + \mathbf{F}_{\mathrm{I}_0} \odot \left(\overline{\mathbf{p}}_{\mathrm{K}}^{(t)T}\mathbf{F}_{\mathrm{I}_0}\right)^*\right], \tag{4.35d}$$

$$\mathbf{F}_{\mathrm{R}_0/\mathrm{I}_0} = \sqrt{\boldsymbol{\gamma}} \otimes \Re/\Im\left\{\left[\mathbf{f}_0^{\mathrm{R}_0/\mathrm{I}_0},\, \cdots,\, \mathbf{f}_{K_G-1}^{\mathrm{R}_0/\mathrm{I}_0}\right]\right\}, \quad \text{removing } \left[\gamma_{0,\epsilon_1},\, \cdots,\, \gamma_{0,\epsilon_{|\kappa|}}\right] \otimes \mathbf{f}_0^{\mathrm{R}_0/\mathrm{I}_0}, \tag{4.35e}$$

$$\boldsymbol{\gamma} \triangleq \left[\gamma_{-M/2,\epsilon_1},\, \cdots,\, \gamma_{-M/2,\epsilon_{|\kappa|}},\, \cdots,\, \gamma_{M/2-1,\epsilon_{|\kappa|}}\right]. \tag{4.35f}$$

Updating $\boldsymbol{\sigma}_{\mathrm{K}}$: Each entry of $\boldsymbol{\sigma}_{\mathrm{K}}$ in (4.34c) is involved in M logdet$(\cdot)$ terms with different coefficients p_m, which requires solving an M-order polynomial function if following the same KKT procedure as when handling problem (4.29). However, the closed form solution in (4.31) for problem (4.29) comes from solving a linear function after KKT (only 1 logdet$(\cdot)$ term is involved as in (4.29b)). As a solution, we lower bound the constraint in (4.34c) by a function in the same form as (4.29b), and update the lower bound to approach the real constraint through iterations. Specifically, we have

$$\frac{1}{2KM}\sum_{m}\log\,\det(\mathbf{I}_{2K}+p_m\mathbf{C}'\mathrm{diag}\{\boldsymbol{\sigma}_{\mathrm{K}}\})\geq\mathbf{f}_1^{(t)^T}\log\,(\mathbf{I}_{2K}+\mathbf{G}\boldsymbol{\sigma}_{\mathrm{K}})+f_2^{(t)}, \tag{4.36a}$$

$$\text{with } \mathbf{f}_1^{(t)}=\frac{1}{2KM}\sum_{m}\frac{p_m\mathbf{C}'\big(\mathbf{I}_{2K}+\mathbf{G}\mathrm{diag}\big\{\boldsymbol{\sigma}_{\mathrm{K}}^{(t)}\big\}\big)}{\big(\mathbf{G}+p_m\mathbf{C}'\mathbf{G}\mathrm{diag}\big\{\boldsymbol{\sigma}_{\mathrm{K}}^{(t)}\big\}\big)}, \tag{4.36b}$$

$$f_2^{(t)}=\frac{1}{2KM}\sum_{m}\log\,\det\big(\mathbf{1}_{2K}+p_m\mathbf{C}'\mathrm{diag}\big\{\boldsymbol{\sigma}_{\mathrm{K}}^{(t)}\big\}\big)-$$
$$\mathbf{f}_1^{(t)^T}\log\big(\mathbf{1}_{2K}+\mathbf{G}\boldsymbol{\sigma}_{\mathrm{K}}^{(t)}\big), \tag{4.36c}$$

$$\mathbf{G}=\max\{\mathbf{p}\}\mathbf{C}', \tag{4.36d}$$

whose inequality comes from $\log(1+c_1x)\geq c_2\log(1+c_3x)+c_4$ with $c_2=c_1(1+c_3x_0)/(c_3+c_1c_3x_0)$ and $c_4=\log(1+c_1x_0)-c_2\log(1+c_3x_0)$ (by making the Talyor approximation of $\log(1+c_1x)$ w.r.t the term $\log(1+c_3x)$, i.e., $\log(1+c_1x)=\log(1+c_1/c_3(e^t-1))|_{t=\log(1+c_3x)}$). Specifically, in (4.36a), each diagonal entry in $\log(\mathbf{I}_{2K}+p_m\mathbf{C}'\mathrm{diag}\{\boldsymbol{\sigma}_{\mathrm{K}}\})$ for $\forall\ m$ is approximated at the point $\log(\mathbf{I}_{2K}+\mathbf{G}\boldsymbol{\sigma}_{\mathrm{K}})$, combining the M logdet$(\cdot)$ terms in (4.34c) into one logdet$(\cdot)$ term. This will give (4.34) the same format as in (4.29) in terms of the communication rate constraint. As a result, the closed-form solution for updating $\boldsymbol{\sigma}_{\mathrm{K}}$ in (4.31) can be adopted directly with only coefficient modifications.

The entire decoupling method is summarized in algorithm 6.

Algorithm 6: Decoupling Algorithm

1. **Input**: $l \leftarrow 0$, $\overline{\mathbf{p}}_{\mathrm{K}}^{(0)}$, $\boldsymbol{\sigma}_{\mathrm{K}}^{(0)}$, $\epsilon_S > 0$
2. **Output**: $\overline{\mathbf{p}}$, $\boldsymbol{\sigma}$
   - 2.1 Obtain $\mathbf{p}$ by Algorithm 9; complexity $\mathcal{O}(M^2 \max\{M, |\kappa|\})$
   - 2.2 Obtain $\overline{\mathbf{p}}_{\mathrm{K}}$, $\boldsymbol{\sigma}_{\mathrm{K}}$ by Algorithm 5, with updated coefficients in (4.35) and $P^{\max} = 1$; complexity $\mathcal{O}(K^3)$
   - 2.3 Update $\overline{\mathbf{p}} \leftarrow \mathbf{F}_{\mathrm{M}} \overline{\mathbf{p}}_{\mathrm{K}}$, $\boldsymbol{\sigma} \leftarrow \mathbf{F}_{\mathrm{M}} \boldsymbol{\sigma}_{\mathrm{K}}$

4.6 Simulations

This section investigates the radar performance of the OFDM DFRC waveform optimized w.r.t our proposed metrics - UBOP for PSK input distribution and aUBOP for Gaussian input distribution. For comparison, we also consider OFDM DFRC waveforms optimized w.r.t two widely used radar metrics, the CRB [56,60] and the RMI [107,108]. Simulations are performed based on the 802.11p standard (wireless access in vehicular environments) following a similar setup as in [67]. Specifically, for practical vehicular applications, we conduct the simulations within the 24 GHz Industrial, Scientific, and Medical frequency bands, with the effective isotropic radiated power limited below 30 dBm and a bandwidth of 90.909 MHz. Most radar channel parameters are the same as the communication channel parameters since they experience the same physical channel model. In most simulations, we select $K = 1024$, $K_G = 256$ and $M = 512$, which gives a range resolution of 1.67m and a velocity resolution of 2.14m/s. To fit a practical vehicle scenario, we set the maximal relative velocity of 55.6m/s (equivalent to 200km/h). The range (velocity) of the target is chosen uniformly within the maximum values that can be unambiguously estimated (213m for the range to avoid ambiguity [6] and 55.6m/s for velocity). For simplification, we assume a mono-static point-target scenario for radar and assume a static communication user. Besides, we assume a noise power density of -208dBW/Hz at both communications and radar receivers, with a communication path loss of 108 dB

[6] The corresponds to the maximal range whose echoes do not break the CP duration.

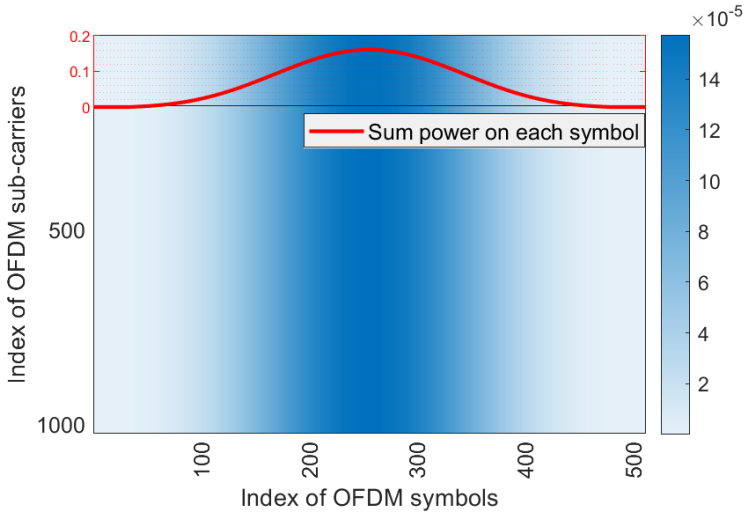

Fig. 4.4: The grey-scale map of the proposed optimal OFDM waveform for $K = 1024$, $K_G = 256$, $M = 512$ at $P^{\max} = -15$ dBW (a low SNR region), with the red curve illuminating the total power (sum over subcarriers) at each OFDM symbol.

and an average radar path loss of 130 dB (target at 106.7 m) for optimization. At the target, assume an average cross section power loss of -10dBm^2 [67]. For the Gaussian input, the communication channel is an NLOS model with 18 taps from Model B in [109].

4.6.1 OFDM with PSK input distribution (constant magnitude)

This section investigates the radar performance and characteristics of an OFDM DFRC waveform optimized w.r.t UBOP for PSK input. As it has been mentioned in Section 4.4, the PSK input distribution is intended to shed insight into the characteristics of an OFDM signal well-suited for on-grid delay-Doppler bin estimation, and hence the communication rate constraint is not explicitly enforced.

First, Fig. 4.4 sheds light on an OFDM DFRC waveform optimized to minimize the UBOP metric for PSK input distribution at $P^{\max} = -15$ dBW (a low SNR region). Fig. 4.4 demonstrates an interesting observation that, the optimal power allocation has uniform power allocation across subcarriers, as proved in Section 4.4. However, in the

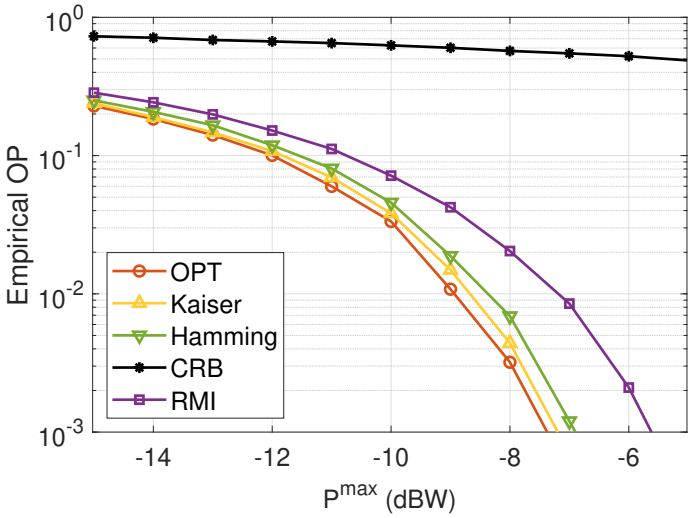

Fig. 4.5: The empirical OP of delay-Doppler estimation between the proposed metric (OPT), RMI, CRB and two windowed power allocation (Hamming and Kaiser) across the OFDM symbols, with BPSK input for $K=1024$, $K_G=256$, $M=512$. The worst SNR (the farthest range bin) at the radar's receiver and the SNR at the communication's receiver respectively range from -51 dB to -41 dB and from 1.4 dB to 16.4 dB respectively.

time domain, the power allocation shapes like a window (similar to Hamming or Kaiser in the low SNR), as illuminated by the red curve in Fig. 4.4, which plots the sum power on each OFDM symbol in the time domain. This is reasonable from the perspective of windowing to handle the problem of leakage frequencies giving fractional v_ϵ. With a low receive SNR, all the sidelobes arising from the frequency leakage might lead to outlier (*Remark* 6 and *Remark* 8), in which case a window with high dynamic delay (such as Hamming and Kaiser) is beneficial since those dissimilar frequency components that are not aligned to the desired frequency can all be suppressed satisfyingly [110]. In contrast, given a high receive SNR, the outlier mainly originates from the aligned highest sidelobe around the peak lobe, in which occasion the optimal window turns back to uniform power allocation across OFDM symbols since the rectangular window provides higher sensitivity. The windowing shift tendency from low SNR to high SNR is consistent with *Remark* 8.

Given the optimal waveform intuition from Fig. 4.4, Fig. 4.5 compares the empirical OP between OFDM waveforms optimized w.r.t UBOP (red, 'OPT'), RMI (purple) and CRB (black) as a function of the transmit power. Two windowed power allocation strategies

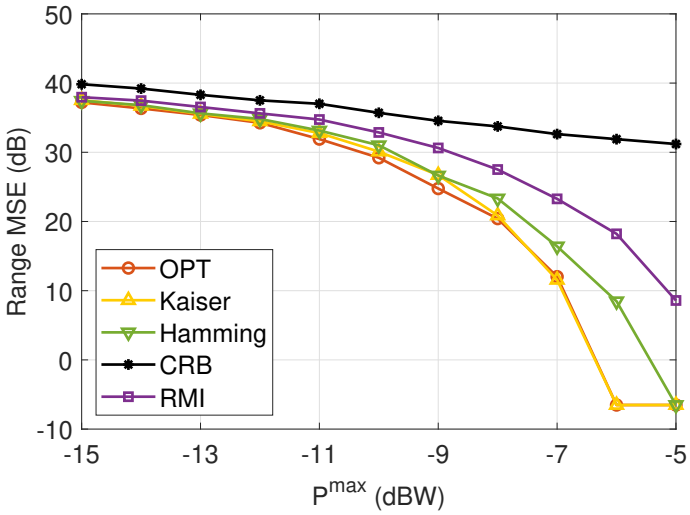

Fig. 4.6: The empirical range MSE, corresponding to Fig. 4.5.

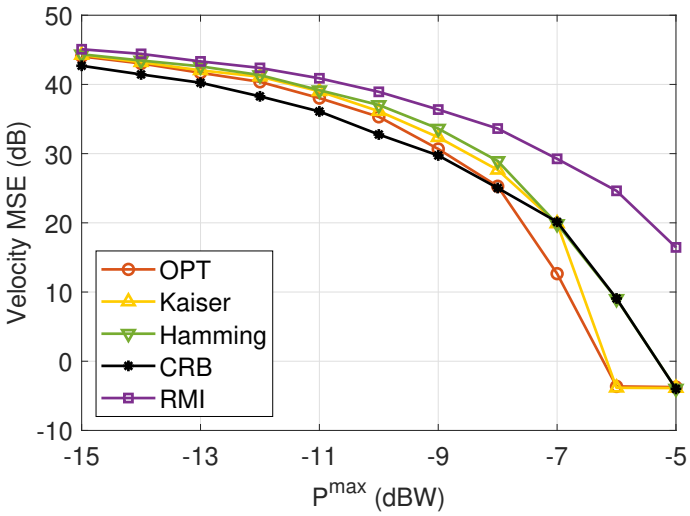

Fig. 4.7: The empirical velocity MSE, corresponding to Fig. 4.5.

are also introduced as an optimization-free strategy inspired by the optimal 'OPT' in Fig. 4.4, where uniform power allocation is adopted across subcarriers and a window (green for the 'Hamming' window and yellow for the 'Kaiser' window) is added for power allocation across symbols. Besides the OP, we also plot the MSE of the range-velocity (delay-Doppler) estimation in Fig. 4.6 and Fig. 4.7, to provide more insight into the characteristics of different power allocation strategies.

Fig. 4.5 demonstrates that our proposed power allocation 'OPT' achieves the best OP, followed by the two windowed power allocation strategies, 'Kaiser' and 'Hamming', and

then 'RMI' and 'CRB'. The optimality of the 'OPT' power allocation originates from a thorough consideration of a joint delay-Doppler bin estimation, especially the frequency leakage problem as it has been analyzed. Using Hamming and Kaiser windows achieves sub-optimal performance in Fig. 4.5 since these two windows both help suppress the side-lobes in the low SNR. Also noteworthy, between 'RMI' and 'CRB', 'RMI' shows relatively better performance on delay estimation in Fig. 4.6, because its optimal power allocation gives uniform spectrum density (the same as the optimal power allocation across subcarriers) [7], which is coincident with the waveform preference for delay estimation. In contrast, 'CRB' achieves relatively better Doppler MSE (even exceeds that of the 'OPT' power allocation in low SNR) in Fig. 4.7, because the 'CRB' [8] power allocation obtains very reliable Doppler estimation from the first and the last subcarriers by concentrating the power upon them. However, this results in very poor delay estimation performance on the other hand.

4.6.2 OFDM with Gaussian input distribution (variable magnitude)

In this section, we evaluate the OP performance given Gaussian input distribution (simulated as 256-QAM). In this part, since there is no closed-form expression for the average RMI and CRB with communication constraints, we substitute these two metrics with their sub-optimal solutions[9]. In this section, we first verify the effectiveness of the proposed aUBOP metric by comparing its radar performance with other metrics given a fixed communication constraint (Fig. 4.8 and Fig. 4.9). Later, we focus on the R-C trade-off from the aspect of the R-C region in Fig. 4.10, the randomness trade-off in Fig. 4.11 and the optimal waveform tendency in Fig. 4.12.

[7] Given a pure radar system, the RMI metric intuitively benefits the received power.

[8] The CRB intuitively maximizes the effective bandwidth, whose optimal power allocation naturally concentrates on the edge frequencies [56].

[9] Specifically, we first decide the minimal power that is required by the Gaussian variance to satisfy the communication constraint. The rest power of 'RMI' and 'CRB' are then allocated to their Gaussian mean for the benefit of radar, following their criterion to maximize the 'RMI' and minimize the 'CRB'.

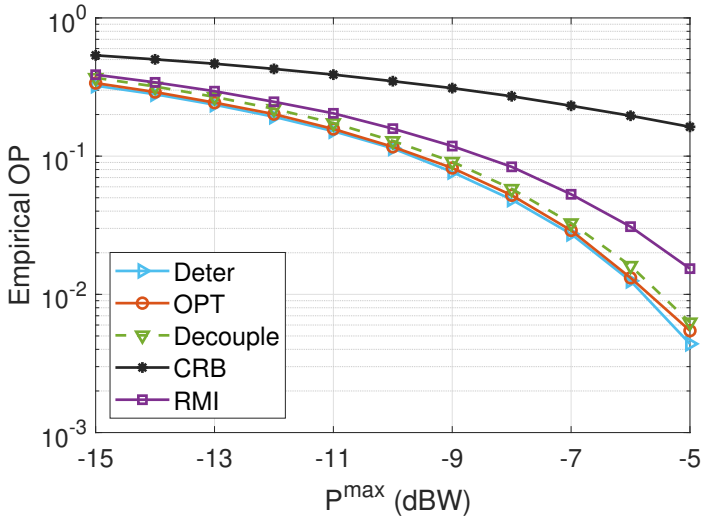

Fig. 4.8: The empirical OP given $R^c = 2.12$ bits/s/Hz with $K = 32$, $K_G = 8$, $M = 16$. The red curve refers to the optimal input distribution proposed in Algorithm 5, shortened as 'OPT'. The green curve refers to the simplified decoupling method in Algorithm 6, shortened as 'Decouple'. The cyan curve is the radar benchmark from the optimal PSK signal in Section 4.4, shortened as 'Deter'. Similarly, the purple curve refers to the 'RMI' metric and the black curve refers to the 'CRB' metric.

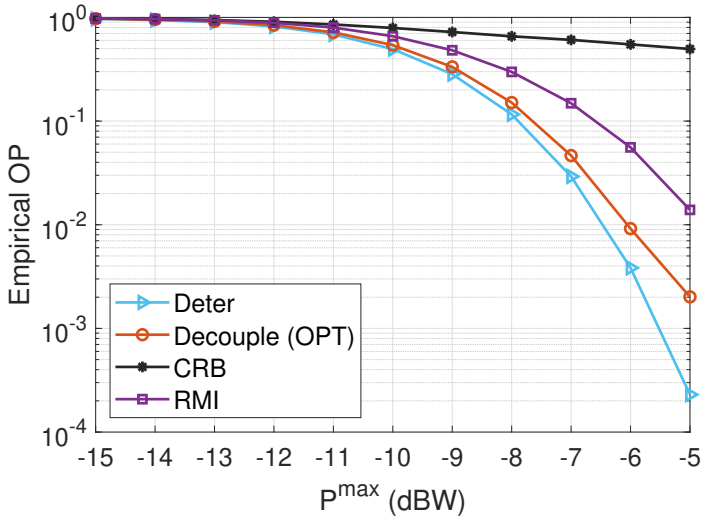

Fig. 4.9: The empirical OP with Gaussian input, $K = 1024$, $K_G = 256$, and $M = 512$.

Fig. 4.8 simulates the radar performance with a smaller number of OFDM subcarriers and symbols to first compare the proposed two inputs, the 'OPT' (red) in Algorithm 5 and the 'Decouple' (green) in Algorithm 6, together with the sub-optimal 'RMI' (purple) and 'CRB' (black) solutions. We also plot the optimal 'PSK' input as a benchmark ('Deter', cyan) to show the effect of the variable magnitudes of Gaussian CSs. Firstly, by

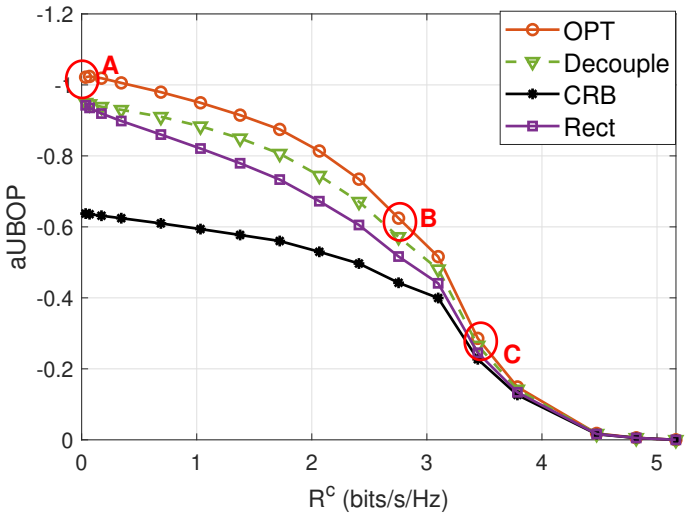

Fig. 4.10: The R-C region trade-off in OFDM DFRC for $P^{\max}=0$ dBW, $K=32$, $K_G=8$ and $M=16$.

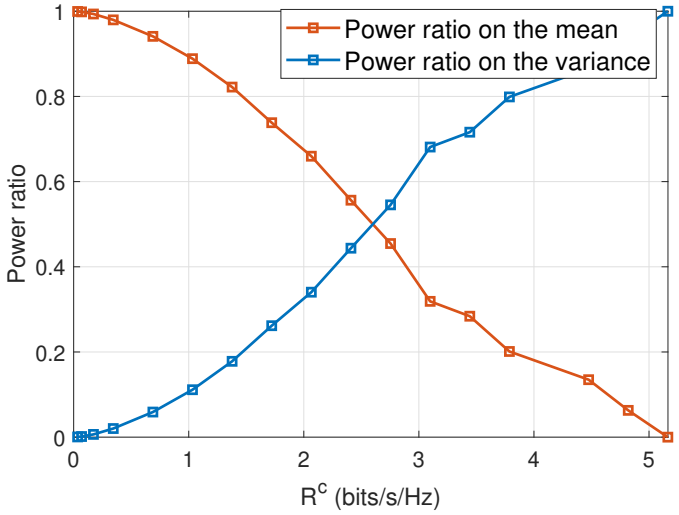

Fig. 4.11: The power ratio of the squared symbol means (deterministic components) and the symbol variance (random components) corresponding to the 'OPT' input distribution (red) in Fig. 4.10.

comparing with the 'Deter' input, Fig. 4.8 shows that variable magnitudes degrade the radar performance. Then, when comparing between the four Gaussian inputs, Fig. 4.8 verifies that our proposed 'OPT' input achieves the best overall performance, followed by the 'Decouple' input which has a close OP performance but with much lower complexity. To further verify the efficiency of the 'Decouple' input, we also plot in Fig. 4.9 with a normal OFDM set-up of 1024 subcarriers and 512 symbols, where the 'Decouple' input

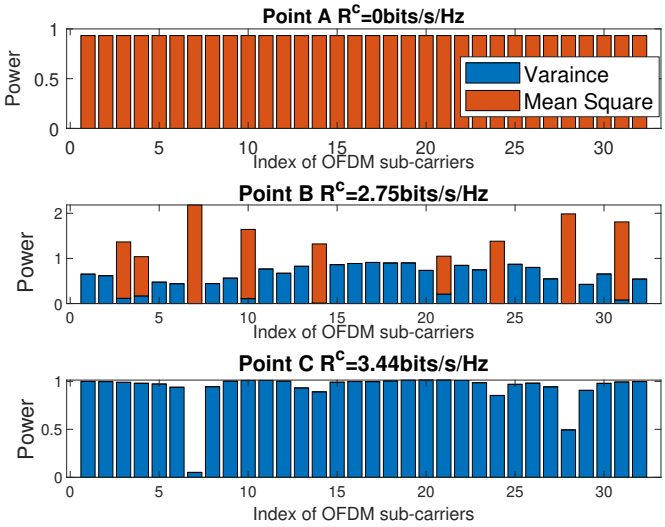

Fig. 4.12: Examples of the mean power (red) and the variance power (blue) at each subcarrier (sum over OFDM symbols) in one channel realization for the 'OPT' input distribution at points 'A', 'B' and 'C' in Fig. 4.10. The sum of the mean power (red) and the variance power (blue) is the total power at the subcarrier.

still outperforms the 'RMI' input and the 'CRB' input significantly.

Next, we illuminate the R-C trade-off in OFDM DFRC from different aspects. First, Fig. 4.10 depicts the average R-C region over 300 channel realizations. It again shows that our proposed metrics achieve a larger R-C region than the other metrics, with the optimal being 'OPT', closely followed by the simplified 'Decouple' method. The 'CRB' is the worst since it does not fit our scenario of on-grid parameter estimation (as in Remark 7).

Given the R-C region in Fig. 4.10, Fig. 4.11 depicts the power ratio of the symbol means against the symbol variance corresponding to the 'OPT' input distribution in Fig. 4.10. It shows that, with stricter constraints on the achievable rate, the power budget is shifting from the symbol means to the symbol variance. This illuminates the R-C trade-off from the perspective of statistics, i.e., the deterministic-random trade-off, with the former being favoured by radar and the latter being favoured by communications.

Finally, Fig. 4.12 sheds light on a general trend in the power allocation strategy in the spectrum domain, taking examples at points 'A' (no communication constraint), 'B' (a relatively strict communication constraint) and 'C' (the strictest achievable com-

munication constraint in the channel realization) in Fig. 4.10, from the top to the bottom. From 'A' to 'C', giving increasing achievable rate constraints, the total power is transferred from symbol means (red) to symbol variance (blue), which is coincident with the deterministic-random trade-off in Fig. 4.11. Specifically, 'A' emphasizes that the best radar performance is achieved by uniform power allocation across the subcarriers to the symbol mean, and 'C' is the input distribution that achieves the highest communication rate for the selected channel realization (hence whose power is all allocated to the symbol variance in a water-filling way). 'C' shows that subcarriers 17, 19, etc, have strong channel gains for communications and hence are allocated more power on their variances, whereas subcarriers 7, 28 have weak channel gains for communications on the contrary. Interestingly, if comparing 'B' with 'C' then, we observe a tendency that, subcarriers with strong communication channel gains (e.g., 17, 19, etc) tend to have large variances to satisfy the achievable rate constraint in a power-efficient way, with the rest power budget allocated to the symbol means prior to the remaining subcarriers (e.g., 7, 28). This roughly guarantees a relatively uniform power allocation across OFDM subcarriers, and is similar to the power allocation strategy for the constant magnitude input distribution (PSK).

4.7 Conclusions

This paper investigates the optimal input distributions of random CSs in OFDM DFRC. We introduce the OP as the radar metric in OFDM DFRC and show its appropriateness through analysis and simulations. The OP is then upper-bounded for optimization tractability and is a function of the magnitude of CSs, which inspires us to consider two classes of CS input distributions, (1) constant magnitude input distribution (i.e., PSK), and (2) variable magnitude input distribution (i.e., non-zero mean Gaussian). The OP is optimized under both scenarios, and low-complexity algorithms with closed-form solutions are proposed. Interestingly, through analysis and simulations, we show that for

both scenarios, the optimized power allocation features a uniform power allocation across OFDM subcarriers and a windowed power allocation across OFDM symbols. For (2), the optimized input distribution exhibits a randomness trade-off, i.e., a higher achievable rate constraint for communications forces a transfer of the available power budget from the symbol means (to favour radar) to the symbol variance (to favour communications). More specifically, for subcarriers having high channel gain for communications, power is concentrated on the symbol variance in order to satisfy the communication constraints efficiently. On the other hand, for subcarriers with weak channel gains for communications, power is concentrated on the symbol means to favour radar performance.

4.8 Appendix

4.8.1 Derivation of the OP in (4.11b)

The probability of $\mathbb{P}[|\gamma_{n,v,\epsilon}|>|\gamma_{0,0,\epsilon}|]$ in (4.11b) is derived based on [111]. Given a pair of complex Gaussian random variables $[\gamma_{0,0,\epsilon},\gamma_{n,v,\epsilon}]$ with the mean $[r_{0,0,\epsilon},r_{n,v,\epsilon}]$, we have

$$\mathbb{P}[A_{n,v,\epsilon}]=\mathbb{P}[|\gamma_{n,v,\epsilon}|>|\gamma_{0,0,\epsilon}|]=\mathbb{P}\big[|\gamma_{0,0,\epsilon}|^2-|\gamma_{n,v,\epsilon}|^2<0\big] \tag{4.37a}$$

$$\approx Q\{\nu_1(n,\,v),\nu_2(n,\,v)\}-\frac{1}{2}I_0(\nu_1(n,\,v)\nu_2(n,\,v))\exp\big\{-\big(\nu_1(n,\,v)^2+\nu_2(n,\,v)^2\big)/2\big\} \tag{4.37b}$$

$$=Q\{\nu_1(n,\,v),\nu_2(n,\,v)\}-\frac{1}{2}\exp\left\{-\frac{|r_{0,0,\epsilon}|}{2\sigma^2}\right\}I_0\left(\frac{|r_{n,v,\epsilon}|}{2\sigma^2}\right) \tag{4.37c}$$

$$\approx\frac{1}{2}\exp\big\{-\frac{|r_{0,0,\epsilon}|}{2\sigma^2}\big\}I_0\big(\frac{|r_{n,v,\epsilon}|}{2\sigma^2}\big), \tag{4.37d}$$

$$\text{with } \nu_1(n,\,v)=\sqrt{(r_{0,0,\epsilon}-R_{n,v,\epsilon}^{1/2})/(2\sigma^2)}, \tag{4.37e}$$

$$\nu_2(n,\,v)=\sqrt{(r_{0,0,\epsilon}+R_{n,v,\epsilon}^{1/2})/(2\sigma^2)}, \tag{4.37f}$$

$$R_{n,v,\epsilon}=|r_{0,0,\epsilon}|^2-|r_{n,v,\epsilon}|^2, \tag{4.37g}$$

where (4.37b) comes from [111], and (4.37d) is a further simplification adopting Marcum-Q lower bound from [112].

The Bessel function involved in (4.37d) will introduce high complexity when being used for optimization in the following. Hence, we upper bound (4.37d) as

$$\mathbb{P}[A_{n,v,\epsilon}] \approx \frac{1}{2}\exp\Big\{-\frac{r_{0,0,\epsilon}}{2\sigma^2}\Big\} I_0\bigg(\frac{|r_{n,v,\epsilon}|}{2\sigma^2}\bigg) = \frac{1}{2}\exp\Big\{-\frac{r_{0,0,\epsilon}}{2\sigma^2}\Big\} \sum_{p=0}^{\infty} \frac{1}{p!p!}\bigg(\frac{|r_{n,v,\epsilon}|}{4\sigma^2}\bigg)^{2p} \tag{4.38a}$$

$$\leq \frac{1}{2}\exp\big\{-\frac{r_{0,0,\epsilon}}{2\sigma^2}\big\}\big[\sum_{p=0}^{\infty}\frac{1}{p!}\bigg(\frac{|r_{n,v,\epsilon}|}{4\sigma^2}\bigg)^{p}\big]^2 = \frac{1}{2}\exp\big\{-\frac{r_{0,0,\epsilon}-|r_{n,v,\epsilon}|}{2\sigma^2}\big\}, \tag{4.38b}$$

where the inequality in (4.38b) comes from $\sum_k a_k^2 \leq (\sum_k a_k)^2$ for $a_k \geq 0\ \forall k$, and (4.38b) comes from the Taylor expansion of exponential functions.

4.8.2 Proof of the closed-form solution for (4.19b)

For $\mathbf{r}^{(l+1,\ t+1)} = \text{argmin}\Big\{\boldsymbol{\alpha}^{(l+1,\ t)^T}\mathbf{r}^{|\cdot|} + \frac{\rho}{2}\|\mathbf{r}-\mathbf{F}^{\text{D}}\mathbf{p}^{(l)}\|^2\Big\}$, we have

$$\boldsymbol{\alpha}^{(l+1,\ t)^T}\mathbf{r}^{|\cdot|} + \frac{\rho}{2}\|\mathbf{r}-\boldsymbol{\beta}^{(l)}\|^2 = \sum_q \alpha_q^{(l+1,\ t)}|r_q| + \frac{\rho}{2}|r_q-\beta_q^{(l)}|^2 \tag{4.39a}$$

$$= \sum_q \alpha_v^{(l+1,\ t)}\sqrt{\Re\{r_q\}^2+\Im\{r_q\}^2} + \frac{\rho}{2}\big(\Re\{r_q\}^2+\Im\{r_q\}^2\big)$$

$$-\rho\big(\Re\{r_q\}\Re\big\{\beta_q^{(l)}\big\}+\Im\{r_q\}\Im\big\{\beta_q^{(l)}\big\}\big)+\frac{\rho}{2}|\beta_q^{(l)}|^2 \tag{4.39b}$$

$$\geq \sum_q \frac{\rho}{2}|r_q|^2 + \big(\alpha_q^{(l)}-\rho|\beta_q^{(l)}|\big)|r_q| + \frac{\rho}{2}|\beta_q^{(l)}|^2, \tag{4.39c}$$

where $\boldsymbol{\beta}^{(l)} = \mathbf{F}^{\text{D}}\mathbf{p}^{(l)}$. (4.39c) applies the Cauchy-Schwarz inequality and reaches the minimal if and only if $\Re\{r_q\}/\Im\{r_q\} = \Re\Big\{\beta_q^{(l)}\Big\}/\Im\Big\{\beta_q^{(l)}\Big\}$. Hence, the minimal value of (4.39c) is achieved by $\big[\mathbf{F}^{\text{D}}\mathbf{p}^{(l)} - \angle\big(\mathbf{F}^{\text{D}}\mathbf{p}^{(l)}\big)\odot\boldsymbol{\alpha}^{(l)}/\rho\big]^+$.

4.8.3 Proof of (4.24e)

For (4.24d), we have for the first term (peak lobe related)

$$\mathbb{E}_{X[k,\ m]}\{r_{0,0,\epsilon}\}=\sum_{k,\ m}\mathbb{E}_{X[k,\ m]}\{p_{k,\ m}\exp\{j2\pi mv_\epsilon/M\}\} \tag{4.40}$$

$$=\sum_{k,\ m}\overline{p}_{k,\ m}\exp\{j2\pi mv_\epsilon/M\}. \tag{4.41}$$

Then, we take expectation over v_ϵ by sampling, similarly to the solution in Section 4.4, which results in

$$\mathbb{E}_\epsilon\{|\mathbb{E}_X\{r_{0,0,\epsilon}\}|\}=\frac{1}{|\kappa|}\sum_{v_\epsilon}|\sum_{k,\ m}\overline{p}_{k,\ m}\exp\{j2\pi mv_\epsilon/M\}|=\frac{1}{|\kappa|}\sum_{v_\epsilon}\sqrt{\overline{\mathbf{p}}^T\mathbf{A}_\epsilon\overline{\mathbf{p}}}, \tag{4.42}$$

with $\mathbf{A}_\epsilon$ in (4.24i).

For $(n,\ v)\neq(0,\ 0)$ in (4.24d), we first take average over $X[k,\ m]$ (denote $f^{\mathrm{D}}_{v,\epsilon,m}f^{\mathrm{R}}_{n,k}$ by $F^{(n,v,\epsilon)}_{k,m}$) and obtain

$$\mathbb{E}_X\big\{|r_{n,v,\epsilon}|^2\big\}=\mathbb{E}_X\Big\{|\sum_{k,\ m}p_{k,\ m}F^{(n,v,\epsilon)}_{k,m}|^2\Big\}$$

$$=\sum_{k_1,\ m_1,\ k_2,\ m_2}\mathbb{E}_X\Big\{p_{k_1,m_1}F^{(n,v,\epsilon)}_{k_1,m_1}p_{k_2,m_2}F^{(n,v,\epsilon)^*}_{k_2,\ m_2}\Big\}+\sum_{k,\ m}\mathbb{E}_X\big\{|p_{k,m}|^2\big\} \tag{4.43a}$$

$$=\sum_{k_1,\ m_1,\ k_2,\ m_2}\mathbb{E}_X\{p_{k_1,m_1}\}\mathbb{E}_X\{p_{k_2,m_2}\}F^{(n,v,\epsilon)}_{k_1,m_1}F^{(n,v,\epsilon)^*}_{k_2,m_2}$$

$$-\sum_{k,\ m}\big[\mathbb{E}_X\{p_{k,m}\}\mathbb{E}_X\{p_{k,m}\}-\mathbb{E}_X\big\{|p_{k,m}|^2\big\}\big] \tag{4.43b}$$

$$=\sum_{k_1,\ m_1,k_2,\ m_2}\overline{p}_{k_1,m_1}\overline{p}_{k_2,m_2}F^{(n,v,\epsilon)}_{k_1,m_1}F^{(n,v,\epsilon)^*}_{k_2,m_2}-\sum_{k,\ m}\overline{p}^2_{k,m}+\sum_{k,\ m}Q_{k,m} \tag{4.43c}$$

$$=\Big(\Re\Big\{\mathbf{f}^{(n,v,\epsilon)^T}\Big\}\overline{\mathbf{p}}\Big)^2+\Big(\Im\Big\{\mathbf{f}^{(n,v,\epsilon)^T}\Big\}\overline{\mathbf{p}}\Big)^2+2\sum_{k,\ m}\big[{\overline{p}_{\mathrm{R},k,m}}^2+{\overline{p}_{\mathrm{I},k,m}}^2-{\mu_{\mathrm{R},k,m}}^4-{\mu_{\mathrm{I},k,m}}^4\big] \tag{4.43d}$$

$$=\overline{\mathbf{p}}^T\mathbf{A}_{n,v,\epsilon}\overline{\mathbf{p}}-2\|\overline{\mathbf{p}}-\boldsymbol{\sigma}\|^2, \tag{4.43e}$$

with $\mathbf{A}_{n,v,\epsilon}$ in (4.24j), and where (4.43c) is achieved since

$$\begin{aligned} Q_{k,\ m} &= \mathbb{E}_{X[k,\ m]}\big\{|p_{k,m}|^2\big\} = 3\overline{p}_{k,m}^2 - 2({\mu_{\mathrm{R},k,m}}^4 + {\mu_{\mathrm{I},k,m}}^4) - 4\overline{p}_{\mathrm{R},k,m}\overline{p}_{\mathrm{I},k,m} \\ &= \overline{p}_{k,m}^2 + 2\big[{\overline{p}_{\mathrm{R},k,m}}^2 + {\overline{p}_{\mathrm{I},k,m}}^2 - {\mu_{\mathrm{R},k,m}}^4 - {\mu_{\mathrm{I},k,m}}^4\big]. \end{aligned} \tag{4.44a}$$

4.8.4 Proof of (4.33b) in the decoupling method

For the first term in (4.33a), we have

$$\begin{aligned} &\sum_{\epsilon\in\kappa}\sqrt{\overline{\mathbf{p}}_{\mathrm{K}}{}^T\mathbf{F}_{\mathrm{M}}{}^T\mathbf{A}_\epsilon\mathbf{F}_{\mathrm{M}}\overline{\mathbf{p}}_{\mathrm{K}}} \\ =&\sum_{\epsilon\in\kappa}\sqrt{\overline{\mathbf{p}}_{\mathrm{K}}{}^T\mathbf{F}_{\mathrm{M}}{}^T\Big[\Re\{\mathbf{f}_{0,0,\epsilon}\}\Re\{\mathbf{f}_{0,0,\epsilon}\}^T + \Im\{\mathbf{f}_{0,0,\epsilon}\}\Im\{\mathbf{f}_{0,0,\epsilon}\}^T\Big]\mathbf{F}_{\mathrm{M}}\overline{\mathbf{p}}_{\mathrm{K}}} \qquad (4.45a) \\ =&\sum_{\epsilon\in\kappa}\sqrt{\big(\mathbf{p}^T\Re\big\{\mathbf{f}_{0,\ \epsilon}^{\mathrm{D}}\big\}\big)^2 + \big(\mathbf{p}^T\Im\big\{\mathbf{f}_{0,\ \epsilon}^{\mathrm{D}}\big\}\big)^2}\mathbf{1}^T\overline{\mathbf{p}}_{\mathrm{K}} = A_0^{\mathrm{D}}\mathbf{1}^T\overline{\mathbf{p}}_{\mathrm{K}}, \qquad (4.45b) \end{aligned}$$

where (4.45b) comes from

$$\begin{aligned} &\mathbf{F}_{\mathrm{M}}{}^T\Re\{\mathbf{f}_{0,0,\epsilon}\}\Re\{\mathbf{f}_{0,0,\epsilon}\}^T\mathbf{F}_{\mathrm{M}} \\ =&\begin{bmatrix}\big(\mathbf{p}^T\otimes\mathbf{I}_K\big)\big(\Re\big\{\mathbf{f}_{0,\ \epsilon}^{\mathrm{D}}\big\}\otimes\mathbf{f}_0^{\mathrm{R}}\big)\\ \big(\mathbf{p}^T\otimes\mathbf{I}_K\big)\big(\Re\big\{\mathbf{f}_{0,\ \epsilon}^{\mathrm{D}}\big\}\otimes\mathbf{f}_0^{\mathrm{R}}\big)\end{bmatrix}\begin{bmatrix}\big(\mathbf{p}^T\otimes\mathbf{I}_K\big)\big(\Re\big\{\mathbf{f}_{0,\ \epsilon}^{\mathrm{D}}\big\}\otimes\mathbf{f}_0^{\mathrm{R}}\big)\\ \big(\mathbf{p}^T\otimes\mathbf{I}_K\big)\big(\Re\big\{\mathbf{f}_{0,\ \epsilon}^{\mathrm{D}}\big\}\otimes\mathbf{f}_0^{\mathrm{R}}\big)\end{bmatrix}^T \qquad (4.45c) \\ =&\big(\mathbf{p}^T\Re\big\{\mathbf{f}_{0,\ \epsilon}^{\mathrm{D}}\big\}\big)^2\mathbf{1}_{2K\times 2K}. \qquad (4.45d) \end{aligned}$$

For the second term in (4.33a), we have

$$\begin{aligned} &\mathbf{A}_{n,v,\epsilon}^0 = \mathbf{F}_{\mathrm{M}}{}^T\mathbf{A}_{n,v,\epsilon}\mathbf{F}_{\mathrm{M}} \\ =&\mathbf{F}_{\mathrm{M}}^T\Big[\Re\{\mathbf{f}_{n,v,\epsilon}\}\Re\{\mathbf{f}_{n,v,\epsilon}\}^T + \Im\{\mathbf{f}_{n,v,\epsilon}\}\Im\{\mathbf{f}_{n,v,\epsilon}\}^T + 2\mathbf{I}_{2KM}\Big]\mathbf{F}_{\mathrm{M}} \qquad (4.46a) \\ =&|\gamma_{v,\epsilon}|^2\Big[\Re\big\{\mathbf{f}_n^{\mathrm{R}_0}\big\}\Re\big\{\mathbf{f}_n^{\mathrm{R}_0}\big\}^T + \Im\big\{\mathbf{f}_n^{\mathrm{R}_0}\big\}\Im\big\{\mathbf{f}_n^{\mathrm{R}_0}\big\}^T\Big] + 2\|\mathbf{p}\|^2, \qquad (4.46b) \end{aligned}$$

where $\gamma_{v,\epsilon} = |\mathbf{p}^T \mathbf{f}^{\mathrm{D}}_{v,\ \epsilon}|^2$ and $\mathbf{f}^{\mathrm{R}_0}_n = \mathbf{1}_2 \otimes \mathbf{f}^{\mathrm{R}}_n \in \mathbb{C}^{2K}$.

Chapter 5

Signal Design for Multi-Functional Integrated Sensing, Communications and Powering Systems

The wireless domain is witnessing a flourishing of integrated systems, e.g. (a) ISAC, and (b) WIPT, due to their potential to use resources (spectrum, power) judiciously. Inspired by this trend, we investigate ISCAP, through the design of a wideband OFDM signal to power a sensor while simultaneously performing target-sensing and communications. To characterize the ISCAP performance region, we assume symbols with non-zero mean asymmetric Gaussian input distribution, and optimize its mean and variance at each subcarrier to maximize the harvested power, subject to constraints on the achievable rate (communications) and the average side-to-peak-lobe difference (sensing). The resulting input distribution, through simulations, achieves a larger performance region than that of (i) a symmetric complex Gaussian input distribution with identical mean and variance for the real and imaginary parts, (ii) a CSCG input distribution, and (iii) the superposed power-splitting communication and sensing signal (the coexisting solution). In particular, the optimized input distribution balances the three functions by exhibiting the following

features: (a) symbols in subcarriers with strong communication channels have high variance to satisfy the rate constraint, while the other symbols are dominated by the mean, forming a relatively uniform sum of mean and variance across subcarriers for sensing; (b) with looser communication and sensing constraints, large absolute means appear on subcarriers with stronger powering channels for higher harvested power. As a final note, the results highlight the great potential of the co-designed ISCAP system for further efficiency enhancement.

5.1 Introduction

Future wireless networks are expected to feature billions of devices carrying out tasks like sensing, communications and computing. This calls for better spectrum utilization to accommodate more users and services, as well as a sustainable energizing technique [63, 82, 83]. For the former, ISAC using a common transmit signal has been widely investigated [57, 79–81]. For the latter, thanks to the consistent decrease in the power consumption of wireless devices [84], WIPT has been regarded as a promising technique to provide sustainable powering, by generating power from the communicating RF signals.

In this chapter, we aim to enhance spectrum efficiency further by implementing sensing, communications, and powering with a unified wideband signal, namely the ISCAP system. Our previous chapters have built a strong foundation for investigating the ISCAP system. Specifically, this chapter extends the multi-sine waveform exploration in WPT in Chapter 3 to OFDM signals with non-linear rectenna, while leaving the HPA's non-linearity as a future work in ISCAP. Also, the wideband insights in DFRC in Chapter 4 inspire the radar metric in OFDM ISCAP and motivate us to optimize a non-zero mean Gaussian input distribution to explore the performance boundaries of the proposed ISCAP system. Moreover, deviating from the Gaussian input distribution in Chapter 4, in this chapter, an asymmetry between the real and imaginary part of the

Gaussian distribution is particularly highlighted, due to the WPT functionality inspired by Chapter 3. Our contributions are summarized as follows:

1. We set up a wideband ISCAP system, where an OFDM signal is transmitted to power a sensor, communicate with an information decoder and sense a point target simultaneously. To evaluate the system performance region, we develop the metric of each function – respectively the average integrated-side-to-peak-lobe-difference (aISPLD) for sensing[1], the achievable rate for communications, and the harvested power for powering – accounting for CS randomness. For the power metric in particular, we follow the non-linear EH model in [1] and derive the average harvested power of CP OFDM (CP-OFDM) where the power contribution from the OFDM CP part is particularly involved[2].

2. Based on the metrics of the three functions, we construct an optimization problem w.r.t the symbol mean and symbol variance of each OFDM subcarrier to maximize the harvested power with constraints on achievable rate and aISPLD. The optimization problem is solved by using ADMM. During each ADMM iteration, we first solve the total allocated power at each subcarrier (the sum of the mean and variance) by using SCP, after which we determine the allocation of power over the mean and variance at each subcarrier by utilizing the parametric successive convex approximation (PSCA).

3. Through simulations, we verify the performance region gain of the proposed input distribution in ISCAP over the co-designed symmetric/zero-mean input distribution as well as the PS input signals in a coexisting scenario. We also gain insight into the fundamental trade-offs between the three functions on input distribution, which can

[1]The aISPLD is proposed as a scaling term of the UBOP in Chapter 4.

[2]Different from [113] which reconstructs the OFDM CP by superposing rectangular pulses for better power harvesting, this chapter accounts for the traditional CP construction (circular-shift of the data part) and evaluates the impact of the CS input distribution on the harvested power from the CP part, which is emitted in [93] where only the data part is considered. Hence, the chapter will not encounter degraded communication performance arising from the interference from the additional rectangular pulses in CP as in [113].

be summarized as follows: a) powering prefers allocating power to the symbol mean with asymmetric real and imaginary part in proportional to the corresponding's powering channel, sensing prefers allocating power to the symbol mean uniformly across subcarriers, and communication requires allocating power to the symbol variance in proportion to communication channels' strength of its subcarrier; b) In a general ISCAP set-up with communication and sensing constraints, a part of subcarriers has a high variance for achievable rate (and usually a low mean) while the remaining subcarriers are dominated by the mean, forming a relatively uniform power allocation across subcarriers for the aISPLD constraint. Given looser constraints on achievable rate and aISPLD, the optimal input distribution shifts to a power-favouring distribution with asymmetric mean allocation adaptive to the powering channels.

Organization: Section 5.2 models a SISO OFDM ISCAP system with a point target, where the signal at each stage is mathematically expressed. The metrics for powering, sensing and communications are also expressed based on an asymmetric non-zero mean Gaussian input. Then, Section 5.3 optimizes the mean and the variance of the input distribution across subcarriers, by maximizing the harvested power constraining on the achievable rate and the aISPLD. Section 5.3 provides simulation results and Section 5.5 draws the conclusion.

5.2 System and signal models

This section begins by modelling the ISCAP system and the transmit OFDM signal, as shown in Fig. 5.1. We then identify performance metrics for each function, namely, the harvested power per OFDM symbol at the EH in Section 5.2.2, the aISPLD (representing the average OP) for range-velocity estimation at the sensing transceiver in Section 5.2.3, and the achievable rate per OFDM symbol at the communication receiver in Section 5.2.4.

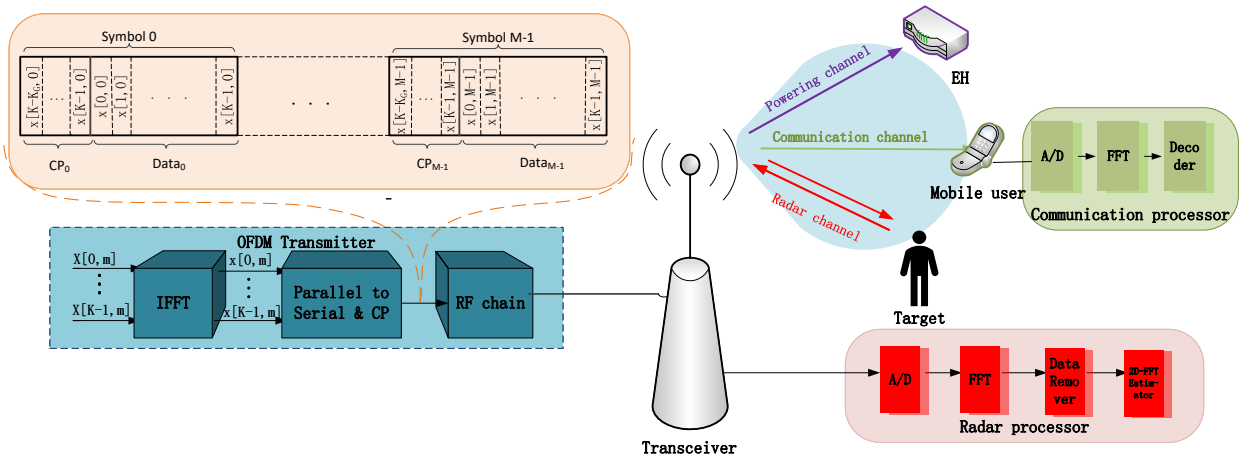

Fig. 5.1: System and OFDM Signal Model for ISCAP.

5.2.1 Transmit signal

Without loss of generality, we consider a SISO ISCAP system as shown in Fig. 5.1, with a multi-functional transmitter and separated receivers for sensing, communications and powering, among which the sensing receiver is co-located with the transmitter. Besides the block model of the ISCAP system, Fig. 5.1 also depicts the OFDM symbol model at the transmitter, where M OFDM symbols with K orthogonal subcarriers and K_G CP sub-pulses for each OFDM symbol are used.

The CS at the k^{th} ($k=0, \cdots, K-1$) sub-carrier of the m^{th} ($m=0, \cdots, M-1$) OFDM symbol can be expressed as

$$X[k, m]=X^{\text{R}}[k, m]+jX^{\text{I}}[k, m], \tag{5.1}$$

where $X^{\text{R}}[k, m] \sim \mathcal{N}(\mu_k^{\text{R}}, \sigma_k^{\text{R}^2})$ and $X^{\text{I}}[k, m] \sim \mathcal{N}(\mu_k^{\text{I}}, \sigma_k^{\text{I}^2})$ (assume the same input distribution spectrum across OFDM symbols). Hence, the average power on the real and imaginary part of the k^{th} subcarrier is given as

$$p_k^{\text{R}} \triangleq \mathbb{E}_{X^{\text{R}}[k, m]}\left\{X^{\text{R}}[k, m]^2\right\}=\mu_k^{\text{R}^2}+\sigma_k^{\text{R}^2}, \forall\, m, \tag{5.2a}$$

$$p_k^{\text{I}} \triangleq \mathbb{E}_{X^{\text{I}}[k, m]}\left\{X^{\text{I}}[k, m]^2\right\}=\mu_k^{\text{I}^2}+\sigma_k^{\text{I}^2}, \forall\, m. \tag{5.2b}$$

After IDFT, we obtain the time domain signal $x[n,\, m]$ ($n=0,\, \cdots,\, K-1$), namely the n^{th} sub-pulse of the m^{th} symbol. $x[n,\, m]$, after adding the CP, becomes [87, 100]

$$x_{\text{CP}}[n,\, m]=x[\langle n-K_G\rangle_K,\, m],\, n=0,\, \cdots,\, K_{\text{T}}-1, \tag{5.3}$$

where $K_{\text{T}}=K_G+K$.

Then, the baseband analogue signal is written as (from Section 2.1 [87])

$$x(t)=\sum_{m=0}^{M-1}\sum_{n=0}^{K_{\text{T}}-1} x_{\text{CP}}[n,\, m]\text{sinc}[Bt-(n+mK_{\text{T}})]\triangleq\sum_{q=0}^{K_{\text{T}}M-1} x_{\text{CP}}[q]\text{sinc}[Bt-q], \tag{5.4}$$

with $q=mK_{\text{T}}+n$, $x_{\text{CP}}[q]=x_{\text{CP}}[n,\, m]$ and B is the bandwidth of the OFDM signal.

After up-converting, we express the transmit signal by [87]

$$x_{\text{RF}}(t)=\sum_{m=0}^{M-1}\sum_{n=0}^{K_{\text{T}}-1} x_{\text{CP}}[n,\, m]\text{sinc}[Bt-(n+mK_{\text{T}})]e^{j2\pi f_c t}, \tag{5.5}$$

where f_c is the central frequency.

For future analysis, we define the following vectors

$$\text{Symbol mean vector: } \boldsymbol{\mu}\triangleq\left[\mu_0^{\text{R}},\, \mu_1^{\text{R}},\, \cdots,\, \mu_{K-1}^{\text{R}},\, \mu_0^{\text{I}},\, \cdots,\, \mu_{K-1}^{\text{I}}\right]^T, \tag{5.6a}$$

$$\text{Symbol variance vector: } \boldsymbol{\sigma}\triangleq\left[\sigma_0^{\text{R}^2},\, \sigma_1^{\text{R}^2},\, \cdots,\, \sigma_{K-1}^{\text{R}\ 2},\, \sigma_0^{\text{I}^2},\, \cdots,\, \sigma_{K-1}^{\text{I}\ 2}\right]^T, \tag{5.6b}$$

$$\text{Symbol power vector: } \mathbf{p}\triangleq\left[p_0^{\text{R}},\, p_1^{\text{R}},\, \cdots,\, p_{K-1}^{\text{R}},\, p_0^{\text{I}},\, \cdots,\, p_{K-1}^{\text{I}}\right]^T \tag{5.6c}$$

$$\text{Symbol mean matrix: } \mathbf{U}\triangleq\boldsymbol{\mu}\boldsymbol{\mu}^T \tag{5.6d}$$

$$\text{Power allocation matrix: } \mathbf{P}\triangleq\mathbf{U}+\text{diag}(\boldsymbol{\sigma}), \tag{5.6e}$$

where $\mathbf{U}$ and $\mathbf{P}$ are defined for Section 5.3. In Section 5.3, we will optimize w.r.t $\mathbf{U}$ and $\mathbf{P}$ to decide $\boldsymbol{\mu}$ and $\boldsymbol{\sigma}$.

5.2.2 Metric for powering

This section models the received signal at the EH, and derives the corresponding scaling term of the harvested power as the powering metric.

Assume that the signal is transmitted over a multipath channel with L paths, where the gain and delay of the l^{th} ($1 \leq l \leq L$) tap are respectively a_l and τ_l. The real received signal at EH is [1]

$$y_{\text{RF}}(t) = \Re\left\{\sum_{l=1}^{L} a_l x_{\text{RF}}(t-\tau_l) + w(t)\right\}, \tag{5.7}$$

where $w(t) \sim \mathcal{CN}(0, \sigma_{\text{n}_\text{P}}^2)$ is the AWGN at EH.

At EH, the impinging signal $y_{\text{RF}}(t)$ is converted into direct current via a rectenna circuit for power harvesting. We model the non-linear rectenna referring to Section 2.2, whose output harvested power is proved in proportion to a scaling term z_{DC}. The scaling term z_{DC} is then extended in [93] to wideband OFDM signals as a function of CS input distribution, which is written as [1, 93]

$$z_{\text{DC}} = \mathbb{E}_x\left\{\mathcal{E}\left[k_2 y_{\text{RF}}(t)^2 + k_4 y_{\text{RF}}(t)^4\right]\right\} \tag{5.8a}$$

$$= \sum_{m=0}^{M-1} \sum_{n=0}^{K_{\text{T}}-1} \frac{k_2}{M} \mathbb{E}_x\left\{|y[n, m]|^2\right\} + \sum_{m=0}^{M-1} \sum_{n=0}^{K_{\text{T}}-1} \frac{3k_4}{4M} \left(\mathbb{E}_x\left\{|y[n, m]|^4\right\} + \mathbb{E}_x\left\{|\widetilde{y}[n, m]|^4\right\}\right), \tag{5.8b}$$

where $k_2 = 0.024$ and $k_4 = 19.145$ [1]. In (5.8b), denote $y(t)$ as the complex baseband signal of $y_{\text{RF}}(t)$ [93] . Then, $y[n, m]$ and $\widetilde{y}[n, m]$ are the samples of $y(t)$ taken at times $t = (K_{\text{T}} m + n)/B$ and $(2K_{\text{T}} m + 2n + 1)/2B$, which collectively form a sequence of samples capturing the power of $y(t)$ (based on the sampling theorem and Parseval's theorem [34]). In this sense, the operation in (5.8b) to simplify (5.8a) is different from the simplification for multi-sine waves in Chapter 3 where we take integrals on the continuous signal power. Herein, the method fits more to the practical OFDM structure in (5.5). However, it is

noteworthy that [93] does not account for the harvested power attributed by the CP part of OFDM signals when expressing (5.8b) as a function of the input distribution, which we address in the following.

If sampling at $t=(K_{\mathrm{T}}m+n)/B$, $y[n,\,m]$ is given by [87]

$$y[n,\,m]=y((K_{\mathrm{T}}m+n)/B) \tag{5.9a}$$

$$=\sum_{l}a_l\sum_{q}x_{\mathrm{CP}}[q]\mathrm{sinc}[K_{\mathrm{T}}m+n-q-l]+w[n,\,m] \tag{5.9b}$$

$$=\sum_{l}a_l x_{\mathrm{CP}}[K_{\mathrm{T}}m+n-l]+w[n,\,m] \tag{5.9c}$$

$$=\sum_{l}a_l x_{\mathrm{CP}}[n-l,\,m]+w[n,\,m], \tag{5.9d}$$

where $x_{\mathrm{CP}}[n-l,\,m]=x_{\mathrm{CP}}[K_{\mathrm{T}}+n-l,\,m-1]$ for $n<l$. $w[n,\,m]$ is the sampled noise at $y[n,\,m]$.

Similarly, if sampling at $t=(2K_{\mathrm{T}}m+2n+1)/2B$, $\widetilde{y}[n,\,m]$ is given by [93]

$$\widetilde{y}[n,\,m]=y((2K_{\mathrm{T}}m+2n+1)/2B) \tag{5.10a}$$

$$=\sum_{l}a_l\sum_{q}x_{\mathrm{CP}}[q]\mathrm{sinc}\left[\frac{2K_{\mathrm{T}}m+2n+1}{2}-q-\tau_l\right]+w[n,\,m] \tag{5.10b}$$

$$=\sum_{j}x_{\mathrm{CP}}[K_{\mathrm{T}}m+n-j]\sum_{l}a_l\mathrm{sinc}\left[j+\frac{1}{2}-l\right]+w[n,\,m]\quad(j=K_{\mathrm{T}}m+n-q) \tag{5.10c}$$

$$\triangleq\sum_{j}\widetilde{a}_j x_{\mathrm{CP}}[n-j,\,m]+\widetilde{w}[n,\,m], \tag{5.10d}$$

$$\text{where } \widetilde{a}_j=\begin{cases}\sum_l a_l\mathrm{sinc}\left[j+\frac{1}{2}-l\right], & 0\le j\le L-1;\\ 0\ (\text{approximate}), & j>L,\end{cases} \tag{5.10e}$$

where $\widetilde{w}[n,\,m]$ is the sampled noise at $\widetilde{y}[n,\,m]$.

Remark 12. *$\widetilde{y}[n,\,m]$ in* (5.10d) *is similar to $y[n,\,m]$ in* (5.9d)*, with a_l substituted by $\widetilde{a}_l$.*

Hence, most of the future analysis related with $y[n,\, m]$ can be adopted to $\widetilde{y}[n,\, m]$ directly after changing the coefficient.

Given any m, the expression of $y[n,\, m]$ in (5.9d) (or $\widetilde{y}[n,\, m]$ in (5.10d)) are classified into two parts: (i) the CP duration for $0 \leq n \leq K_G - 1$ over which the received sub-pulses involves interaction between the m^{th} OFDM symbol and the $(m-1)^{\text{th}}$ OFDM symbol; (ii) the data duration for $K_G \leq n \leq K_{\text{T}} - 1$ where there is no inter-symbol interference. Hence, the final harvested power in (5.8b) also needs consideration from these two parts.

In the following, we first consider the sub-pulses' power over the m^{th} data duration ($K_G \leq n \leq K_{\text{T}} - 1$) and then move to the sub-pulses' power over the m^{th} CP duration ($0 \leq n \leq K_G - 1$). For future analysis, we define the vector that collects the m^{th} transmit OFDM symbol in the frequency domain as

$$\mathbf{x}_m \triangleq [X[0,\, m],\, \cdots,\, X[K-1,\, m]]^T,\, m = 0,\, \cdots,\, M-1, \tag{5.11a}$$

$$\overline{\mathbf{x}}_m \triangleq \left[\Re\{\mathbf{x}_m\}^T,\, \Im\{\mathbf{x}_m\}^T\right]^T. \tag{5.11b}$$

Furthermore, from (5.9d) and (5.10d), we define the complex gain of the frequency-domain powering channel as

$$\mathbf{H}_{\text{P}} \triangleq \text{diag}([h_{\text{P},\,0},\, \cdots,\, h_{\text{P},\,\text{K}-1}]),\, \text{with}\, h_{\text{P},\,k} = \text{IDFT}\{a_l\}_{(k)}; \tag{5.12a}$$

$$\widetilde{\mathbf{H}}_{\text{P}} \triangleq \text{diag}\left(\left[\widetilde{h}_{\text{P},\,0},\, \cdots,\, \widetilde{h}_{\text{P},\,\text{K}-1}\right]\right),\, \text{with}\, \widetilde{h}_{\text{P},\,k} = \text{IDFT}\{\widetilde{a}_l\}_{(k)}. \tag{5.12b}$$

Power of data duration: Starting from the data duration ($K_G \leq n \leq K_{\text{T}} - 1$), take $y[n,\, m]$ as an example first. $y[n,\, m]$ (for $K_G \leq n \leq K_{\text{T}} - 1$) can be re-expressed as

$$y[n,\, m] = \text{IDFT}\{\mathbf{H}_{\text{P}}\mathbf{x}_m\}_{(n)} + w[n,\, m] = \mathbf{a}_n^{\text{R}\,T}\overline{\mathbf{x}}_m + j\mathbf{a}_n^{\text{I}\,T}\overline{\mathbf{x}}_m + w[n,\, m], \tag{5.13a}$$

$$\text{with}\, \mathbf{a}_n^{\text{R}} = [\Re\{\mathbf{f}_n\mathbf{H}_{\text{P}}\},\, -\Im\{\mathbf{f}_n\mathbf{H}_{\text{P}}\}]^T, \tag{5.13b}$$

$$\mathbf{a}_n^{\text{I}} = [\Im\{\mathbf{f}_n\mathbf{H}_{\text{P}}\},\, \Re\{\mathbf{f}_n\mathbf{H}_{\text{P}}\}]^T, \tag{5.13c}$$

$$\mathbf{f}_n = \left[1,\, e^{j\frac{2\pi n}{K}},\, ...,\, e^{j\frac{2\pi n(K-1)}{K}}\right] \text{ (the } n^{\text{th}} \text{ row of the IDFT matrix).} \tag{5.13d}$$

Similarly, for $\widetilde{y}[n,\, m]$, we have

$$\widetilde{y}[n,\, m] = \widetilde{\mathbf{a}}_n^{\mathrm{R}\,T}\overline{\mathbf{x}}_m + j\widetilde{\mathbf{a}}_n^{\mathrm{I}\,T}\overline{\mathbf{x}}_m + \widetilde{w}[n,\, m], \tag{5.14a}$$

$$\text{with } \widetilde{\mathbf{a}}_n^{\mathrm{R}} = \left[\Re\left\{\mathbf{f}_n\widetilde{\mathbf{H}}_{\mathrm{P}}\right\},\, -\Im\left\{\mathbf{f}_n\widetilde{\mathbf{H}}_{\mathrm{P}}\right\}\right]^T, \tag{5.14b}$$

$$\widetilde{\mathbf{a}}_n^{\mathrm{I}} = \left[\Im\left\{\mathbf{f}_n\widetilde{\mathbf{H}}_{\mathrm{P}}\right\},\, \Re\left\{\mathbf{f}_n\widetilde{\mathbf{H}}_{\mathrm{P}}\right\}\right]^T. \tag{5.14c}$$

On this basis, the second-order and the fourth-order expectations of $y[n,\, m]$ in (5.8b), i.e., $\mathbb{E}\{|y[n,\, m]|^2\}$ and $\mathbb{E}\{|y[n,\, m]|^4\}$, are given in (5.15a) and (5.15b) respectively (Details in Appendix 5.6.1). Following the same way, we also give the fourth-order expectations of $\widetilde{y}[n,\, m]$, i.e., $\mathbb{E}\{|\widetilde{y}[n,\, m]|^4\}$, in (5.15c) (Details in Appendix 5.6.1).

$$\mathbb{E}\left\{|y[n,\, m]|^2\right\} = \mathrm{Tr}(\mathbf{A}_n\mathbf{P}) + \sigma_{\mathrm{nP}}^2 \triangleq z_{\mathrm{DC},\,n}^{\mathrm{data},\,2}(\mathbf{P},\, \mathbf{U}), \tag{5.15a}$$

$$\begin{aligned}\mathbb{E}\left\{|y[n,\, m]|^4\right\} &= \mathrm{Tr}^2(\mathbf{A}_n\mathbf{P}) + 6\sigma_{\mathrm{nP}}^2\,\mathrm{Tr}(\mathbf{A}_n\mathbf{P}) + 2\mathrm{Tr}(\mathbf{A}_n\mathbf{P}\mathbf{A}_n\mathbf{P}) - 2\mathrm{Tr}(\mathbf{A}_n\mathbf{U}\mathbf{A}_n\mathbf{U}) + 3\sigma_{\mathrm{nP}}^4 \\ &\triangleq z_{\mathrm{DC},\,n}^{\mathrm{data},\,4}(\mathbf{P},\, \mathbf{U}),\end{aligned} \tag{5.15b}$$

$$\begin{aligned}\mathbb{E}\left\{|\widetilde{y}[n,\, m]|^4\right\} &= \mathrm{Tr}^2\left(\widetilde{\mathbf{A}}_n\mathbf{P}\right) + 6\sigma_{\mathrm{nP}}^2\,\mathrm{Tr}(\mathbf{A}_n\mathbf{P}) + 2\mathrm{Tr}\left(\widetilde{\mathbf{A}}_n\mathbf{P}\widetilde{\mathbf{A}}_n\mathbf{P}\right) - 2\mathrm{Tr}\left(\widetilde{\mathbf{A}}_n\mathbf{U}\widetilde{\mathbf{A}}_n\mathbf{U}\right) + 3\sigma_{\mathrm{nP}}^4 \\ &\triangleq \widetilde{z}_{\mathrm{DC},\,n}^{\mathrm{data},\,4}(\mathbf{P},\, \mathbf{U}),\end{aligned} \tag{5.15c}$$

$$\text{with } \mathbf{A}_n = \mathbf{a}_n^{\mathrm{R}}\mathbf{a}_n^{\mathrm{R}\,T} + \mathbf{a}_n^{\mathrm{I}}\mathbf{a}_n^{\mathrm{I}\,T}, \tag{5.15d}$$

$$\widetilde{\mathbf{A}}_n = \widetilde{\mathbf{a}}_n^{\mathrm{R}}\widetilde{\mathbf{a}}_n^{\mathrm{R}\,T} + \widetilde{\mathbf{a}}_n^{\mathrm{I}}\widetilde{\mathbf{a}}_n^{\mathrm{I}\,T}. \tag{5.15e}$$

Power of CP duration: Based on (5.9d), $y[n,\, m]$ (for $0 \leq n \leq K_G - 1$) can be re-written as

$$y[n,\, m] = \sum_{l=0}^{n} a_l x_{\mathrm{CP}}[n-l,\, m] + \sum_{l=n+1}^{K_G-1} a_l x_{\mathrm{CP}}[K_{\mathrm{T}}+n-l,\, m-1] + w[n,\, m] \tag{5.16a}$$

$$= \sum_{l=0}^{n} a_l x[K-K_G+n-l,\, m] + \sum_{l=n+1}^{K_G-1} a_l x[K+n-l,\, m-1] + w[n,\, m] \tag{5.16b}$$

$$= \sum_{p=K-K_G}^{K-K_G+n} a_{K-K_G+n-p} x[p,\, m] + \sum_{p=K-K_G+n+1}^{K-1} a_{K+n-p} x[p,\, m-1] + w[n,\, m]$$

$$= \mathbf{b}_{1,\, n}{}^{T} \mathbf{x}_m + \mathbf{b}_{2,\, n}{}^{T} \mathbf{x}_{m-1} + w[n,\, m], \tag{5.16c}$$

$$= \mathbf{b}^{\mathrm{R}}_{1,\, n}{}^{T} \overline{\mathbf{x}}_m + \mathbf{b}^{\mathrm{R}}_{2,\, n}{}^{T} \overline{\mathbf{x}}_{m-1} + j\Big(\mathbf{b}^{\mathrm{I}}_{1,\, n}{}^{T} \overline{\mathbf{x}}_m + \mathbf{b}^{\mathrm{I}}_{2,\, n}{}^{T} \overline{\mathbf{x}}_{m-1}\Big) + w[n,\, m], \tag{5.16d}$$

with $\mathbf{b}_{i,\, n} = \mathrm{DFT}\{\mathbf{a}_{\mathrm{CP}i,\, n}\}$, for $i = 1,\, 2$, (5.16e)

$$a_{\mathrm{CP1},\, n,\, k} = \begin{cases} a_{K-K_G+n-k}, & K-K_G \le k \le K-K_G+n, \\ 0, & \text{otherwise}, \end{cases} \tag{5.16f}$$

$$a_{\mathrm{CP2},\, n,\, k} = \begin{cases} a_{K+n-k}, & K-K_G+n-1 \le k \le K-1, \\ 0, & \text{otherwise}, \end{cases} \tag{5.16g}$$

$$\mathbf{b}^{\mathrm{R}}_{i,\, n} = \big[\Re\{\mathbf{b}_{i,\, n}{}^{T}\},\, -\Im\{\mathbf{b}_{i,\, n}{}^{T}\}\big]^{T}, \tag{5.16h}$$

$$\mathbf{b}^{\mathrm{I}}_{i,\, n} = \big[\Im\{\mathbf{b}_{i,\, n}{}^{T}\},\, \Re\{\mathbf{b}_{i,\, n}{}^{T}\}\big]^{T}. \tag{5.16i}$$

Similarly, $\widetilde{y}[n,\, m]$ $(0 \le n \le K_G - 1)$ can be re-written as

$$\widetilde{y}[n,\, m] = \widetilde{\mathbf{b}}^{\mathrm{R}}_{1,\, n}{}^{T} \overline{\mathbf{x}}_m + \widetilde{\mathbf{b}}^{\mathrm{R}}_{2,\, n}{}^{T} \overline{\mathbf{x}}_{m-1} + j\Big(\widetilde{\mathbf{b}}^{\mathrm{I}}_{1,\, n}{}^{T} \overline{\mathbf{x}}_m + \widetilde{\mathbf{b}}^{\mathrm{I}}_{2,\, n}{}^{T} \overline{\mathbf{x}}_{m-1}\Big) + \widetilde{w}[n,\, m], \tag{5.17a}$$

where the corresponding expressions for $\widetilde{\mathbf{b}}^{\mathrm{R}}_{i,\, n}$ and $\widetilde{\mathbf{b}}^{\mathrm{I}}_{i,\, n}$ $(i = 1,\, 2)$ are obtained by replacing a_l with $\widetilde{a}_l$ respectively in (5.16e)-(5.16i).

Consequently, the second-order and the fourth-order expectations of the CP duration sub-pulses are (Details in Appendix 5.6.2)

$$\mathbb{E}\big\{|y[n,\, m]|^2\big\} = \mathrm{Tr}(\mathbf{B}_n \mathbf{P} + 2\mathbf{D}_n \mathbf{U}) + \sigma^2_{\mathrm{n_P}} \triangleq z^{\mathrm{CP},\, 2}_{\mathrm{DC},\, n}(\mathbf{P},\, \mathbf{U}), \tag{5.18a}$$

$$\begin{aligned} \mathbb{E}\big\{|y[n,\, m]|^4\big\} = {} & \mathrm{Tr}^2(\mathbf{B}_n \mathbf{P} + 2\mathbf{D}_n \mathbf{U}) + 6\sigma^2_{\mathrm{n_P}}\, \mathrm{Tr}(\mathbf{B}_n \mathbf{P} + 2\mathbf{D}_n \mathbf{U}) + 2\mathrm{Tr}(\mathbf{B}_{1,\, n} \mathbf{P} \mathbf{B}_{1,\, n} \mathbf{P} + \mathbf{B}_{2,\, n} \mathbf{P} \mathbf{B}_{2,\, n} \mathbf{P}) \\ & + 4\mathrm{Tr}\big(\mathbf{D}_n \mathbf{P} \mathbf{D}_n^T \mathbf{P} + \mathbf{D}_n \mathbf{U} \mathbf{D}_n \mathbf{U} + \mathbf{B}_{1,\, n} \mathbf{U} \mathbf{B}_{2,\, n} \mathbf{U} + \mathbf{B}_{1,\, n} \mathbf{P} \mathbf{D}_n \mathbf{U} + \mathbf{B}_{2,\, n} \mathbf{P} \mathbf{D}_n^T \mathbf{U}\big) \\ & + 4\mathrm{Tr}\big(\mathbf{B}_{1,\, n} \mathbf{U} \mathbf{D}_n^T \mathbf{P} + \mathbf{B}_{2,\, n} \mathbf{U} \mathbf{D}_n \mathbf{P}\big) - 2\mathrm{Tr}\big(\mathbf{E}_n \mathbf{U} \mathbf{E}_n^T \mathbf{U}\big) + 3\sigma^4_{\mathrm{n_P}} \\ \triangleq {} & z^{\mathrm{CP},\, 4}_{\mathrm{DC},\, n}(\mathbf{P},\, \mathbf{U}), \end{aligned} \tag{5.18b}$$

$$\begin{aligned}\mathbb{E}\left\{|\widetilde{y}[n,\,m]|^4\right\}=&\mathrm{Tr}^2\left(\widetilde{\mathbf{B}}_n\mathbf{P}+2\widetilde{\mathbf{D}}_n\mathbf{U}\right)+6\sigma_{\mathrm{n_P}}^2\mathrm{Tr}\left(\widetilde{\mathbf{B}}_n\mathbf{P}+2\widetilde{\mathbf{D}}_n\mathbf{U}\right)+2\mathrm{Tr}\left(\widetilde{\mathbf{B}}_{1,\,n}\mathbf{P}\widetilde{\mathbf{B}}_{1,\,n}\mathbf{P}+\widetilde{\mathbf{B}}_{2,\,n}\mathbf{P}\widetilde{\mathbf{B}}_{2,\,n}\mathbf{P}\right)\\&+4\mathrm{Tr}\left(\widetilde{\mathbf{D}}_n\mathbf{P}\widetilde{\mathbf{D}}_n^T\mathbf{P}+\widetilde{\mathbf{D}}_n\mathbf{U}\widetilde{\mathbf{D}}_n\mathbf{U}+\widetilde{\mathbf{B}}_{1,\,n}\mathbf{U}\widetilde{\mathbf{B}}_{2,\,n}\mathbf{U}+\widetilde{\mathbf{B}}_{1,\,n}\mathbf{P}\widetilde{\mathbf{D}}_n\mathbf{U}+\widetilde{\mathbf{B}}_{2,\,n}\mathbf{P}\widetilde{\mathbf{D}}_n^T\mathbf{U}\right)\\&+4\mathrm{Tr}\left(\widetilde{\mathbf{B}}_{1,\,n}\mathbf{U}\widetilde{\mathbf{D}}_n^T\mathbf{P}+\widetilde{\mathbf{B}}_{2,\,n}\mathbf{U}\widetilde{\mathbf{D}}_n\mathbf{P}\right)-2\mathrm{Tr}\left(\widetilde{\mathbf{E}}_n\mathbf{U}\widetilde{\mathbf{E}}_n^T\mathbf{U}\right)+3\sigma_{\mathrm{n_P}}^4\\\triangleq&\widetilde{z}_{\mathrm{DC},\,n}^{\mathrm{CP},\,4}(\mathbf{P},\,\mathbf{U}),\end{aligned}\tag{5.18c}$$

$$\text{with }\mathbf{B}_n=\mathbf{B}_{1,\,n}+\mathbf{B}_{2,\,n},\ \widetilde{\mathbf{B}}_n=\widetilde{\mathbf{B}}_{1,\,n}+\widetilde{\mathbf{B}}_{2,\,n},\tag{5.18d}$$

$$\mathbf{B}_{i,\,n}=\mathbf{b}_{i,\,n}^{\mathrm{R}}\mathbf{b}_{i,\,n}^{\mathrm{R}\,T}+\mathbf{b}_{i,\,n}^{\mathrm{I}}\mathbf{b}_{i,\,n}^{\mathrm{I}\,T},\text{ for }i=1,\,2,\tag{5.18e}$$

$$\widetilde{\mathbf{B}}_{i,\,n}=\widetilde{\mathbf{b}}_{i,\,n}^{\mathrm{R}}\widetilde{\mathbf{b}}_{i,\,n}^{\mathrm{R}\,T}+\widetilde{\mathbf{b}}_{i,\,n}^{\mathrm{I}}\widetilde{\mathbf{b}}_{i,\,n}^{\mathrm{I}\,T},\text{ for }i=1,\,2,\tag{5.18f}$$

$$\mathbf{D}_n=\mathbf{b}_{1,\,n}^{\mathrm{R}}\mathbf{b}_{2,\,n}^{\mathrm{R}\,T}+\mathbf{b}_{1,\,n}^{\mathrm{I}}\mathbf{b}_{2,\,n}^{\mathrm{I}\,T},\ \widetilde{\mathbf{D}}_n=\widetilde{\mathbf{b}}_{1,\,n}^{\mathrm{R}}\widetilde{\mathbf{b}}_{2,\,n}^{\mathrm{R}\,T}+\widetilde{\mathbf{b}}_{1,\,n}^{\mathrm{I}}\widetilde{\mathbf{b}}_{2,\,n}^{\mathrm{I}\,T}\tag{5.18g}$$

$$\mathbf{E}_n=\mathbf{B}_{1,\,n}+\mathbf{D}_n+\mathbf{B}_{2,\,n}^T+\mathbf{D}_n^T,\ \widetilde{\mathbf{E}}_n=\widetilde{\mathbf{B}}_{1,\,n}+\widetilde{\mathbf{D}}_n+\widetilde{\mathbf{B}}_{2,\,n}^T+\widetilde{\mathbf{D}}_n^T.\tag{5.18h}$$

Total power: After re-organization, the scaling term of the generated power of the m^{th} OFDM symbol as a function of the input distribution is given as

$$\begin{aligned}z_{\mathrm{DC}}(\mathbf{P},\,\mathbf{U})=&\sum_{n=0}^{K_G-1}k_2z_{\mathrm{DC},\,n}^{\mathrm{CP},\,2}(\mathbf{P},\,\mathbf{U})+\frac{3k_4}{4}\left(z_{\mathrm{DC},\,n}^{\mathrm{CP},\,4}(\mathbf{P},\,\mathbf{U})+\widetilde{z}_{\mathrm{DC},\,n}^{\mathrm{CP},\,4}(\mathbf{P},\,\mathbf{U})\right)\\&+\sum_{n=K_G}^{K_{\mathrm{T}}-1}k_2z_{\mathrm{DC},\,n}^{\mathrm{data},\,2}(\mathbf{P},\,\mathbf{U})+\frac{3k_4}{4}\left(z_{\mathrm{DC},\,n}^{\mathrm{data},\,4}(\mathbf{P},\,\mathbf{U})+\widetilde{z}_{\mathrm{DC},\,n}^{\mathrm{data},\,4}(\mathbf{P},\,\mathbf{U})\right).\end{aligned}\tag{5.19}$$

5.2.3 Metric for sensing

In terms of sensing, we consider a point-target sensing scenario aiming at the range-velocity bin estimation. The sensing's performance is guaranteed by restricting its aISPLD of the AF. Moreover, according to Chapter 4, the aISPLD is shown to be in proportion to the upper bound of the average OP, i.e., the probability of incorrectly estimating the target's range-velocity bin using the ML estimator in OFDM ISAC systems in low SNR.

On this basis, we express our sensing metric, $\overline{\mathrm{UB}}_{\mathrm{OP}}$ as in [101] in the following

$$\overline{\mathrm{UB}}_{\mathrm{OP}}(\mathbf{p},\,\boldsymbol{\mu})=-M(K_GM-1)\mathbf{1}^T\mathbf{p}+\sum_{(r,\,v)\neq(0,\,0)}\sqrt{g_{r,v}(\mathbf{p})+g_2(\boldsymbol{\mu})}, \tag{5.20a}$$

$$\text{with } g_{r,v}(\mathbf{p})=M^2\delta(v)|\big(\mathbf{1}_2^T\otimes\mathbf{f}_n\big)\mathbf{p}|^2+2M\|\mathbf{p}\|^2, \tag{5.20b}$$

$$g_2(\boldsymbol{\mu})=-2M\sum_{k=0}^{2K-1}|\mu_k|^4, \tag{5.20c}$$

where $(r,\,v)$ represents the range-velocity bin candidate for the OFDM ISAC system, with $r=0,\,\cdots,\,K_G-1$ and $v=-M/2,\,\cdots,\,M/2-1$. Assuming a target at $(r,\,v)=(0,\,0)$, the first sum term in (5.20a) represents the average peak lobe at $(r,\,v)=(0,\,0)$ and the second sum term in (5.20a) represents the upper bound of the average sum of side lobes where $(r,\,v)\neq(0,\,0)$.

Remark 13. *Given a transmit power constraint, i.e., a fixed* $\mathbf{1}^T\mathbf{p}$*, the aISPLD metric in* (5.20) *is minimized by maximizing the symbol mean at each OFDM subcarrier, i.e.,* $\boldsymbol{\mu}=\mathbf{p}$*, while the optimal* $\mathbf{p}$ *is to be uniform across OFDM sub-carriers from Chapter 4.*

Similar to the powering metric expression in (5.19), we re-formulate the sensing metric $\overline{\mathrm{UB}}_{\mathrm{OP}}(\mathbf{p},\,\boldsymbol{\mu})$ in (5.20) as a function of $\mathbf{P}$ and $\mathbf{U}$

$$\widetilde{\mathrm{UB}}_{\mathrm{OP}}(\mathbf{P},\,\mathbf{U})=-M(K_GM-1)\mathrm{Tr}(\mathbf{P})+\sum_{(r,\,v)\neq(0,\,0)}\sqrt{\widetilde{g}_{r,v}(\mathbf{P})+\widetilde{g}_2(\mathbf{U})}, \tag{5.21a}$$

$$\text{with } \widetilde{g}_{r,v}(\mathbf{P})=\big(\mathbf{f}_{r,v}^{\mathrm{R}}\mathrm{diag}(\mathbf{P})\big)^2+\big(\mathbf{f}_{r,v}^{\mathrm{I}}\mathrm{diag}(\mathbf{P})\big)^2+2M\|\mathrm{diag}(\mathbf{P})\|^2, \tag{5.21b}$$

$$\widetilde{g}_2(\mathbf{U})=-2M\|\mathrm{diag}(\mathbf{U})\|^2, \tag{5.21c}$$

$$\mathbf{f}_{r,v}^{\mathrm{R/I}}=M\delta(v)\mathfrak{R}/\mathfrak{I}\big\{\mathbf{1}_2^T\otimes\mathbf{f}_n\big\}. \tag{5.21d}$$

5.2.4 Metric for communication

For the communication system, the complex received signal at the k^{th} subcarrier is [87]

$$Y_{\text{C}}[k,\, m]{=}h_{\text{C},\, k}X[k,\, m]{+}w_{\text{C}}[k,\, m], \tag{5.22}$$

where $h_{\text{C},\, k}$ is the complex gain of the communication channel of the k^{th} OFDM subcarrier. $w_{\text{C}}[k,\, m]$ is the AWGN at the communication receiver with its noise power spectrum density being σ_{nC}^2.

Given that the variance of the real and imaginary part of $X[k,\, m]$ are ${\sigma_k^{\text{R}}}^2$ and ${\sigma_k^{\text{I}}}^2$ respectively, the average communication achievable rate in OFDM can be written as (from Section 2.4 [93])

$$R\big(\{\sigma_k^{\text{R}},\, \sigma_k^{\text{I}}\}\big){=}\frac{1}{2KM}\sum_{k,\, m}\Big[\log\left(1{+}\frac{2K|h_{\text{C},\, k}|^2{\sigma_k^{\text{R}}}^2}{B\sigma_{\text{nC}}^2}\right){+}\log\left(1{+}\frac{2K|h_{\text{C},\, k}|^2{\sigma_k^{\text{I}}}^2}{B\sigma_{\text{nC}}^2}\right)\Big]. \tag{5.23}$$

(5.23) can be re-formulated in the following vector form

$$R(\boldsymbol{\sigma}){=}\frac{1}{2K}\log\,\det[\mathbf{I}_{2K}{+}\mathbf{C}_1\text{diag}(\boldsymbol{\sigma})], \tag{5.24a}$$

$$\text{with } \mathbf{C}_1{=}\text{diag}\Big(\big[\mathbf{c}_1^T,\, \mathbf{c}_1^T\big]^T\Big) \text{ for } c_{1,\, k}{=}\frac{2K|h_{\text{C},\, k}|^2}{B\sigma_{\text{nC}}^2}. \tag{5.24b}$$

5.3 Optimal OFDM waveform design

In this section, we formulate the problem to optimize the performance region of the ISCAP system, i.e., to maximize the harvested power per symbol given constraints on the transmit power, the achievable rate (communication) and the aISPLD (sensing). The formulated problem is non-convex, where we propose an ADMM-based algorithm

to obtain a local optimal solution.

5.3.1 Problem formulation

The optimization problem that maximizes the harvested power per symbol given achievable rate constraint and the aISPLD constraint is formulated as

$$\max_{\mathbf{P},\,\mathbf{U},\,\boldsymbol{\sigma}} \quad z_{\mathrm{DC}}(\mathbf{P},\,\mathbf{U}) \text{ in (5.19)}, \tag{5.25a}$$

$$\text{s.t.} \quad \mathrm{Tr}(\mathbf{P}) \leq P_{\max}, \tag{5.25b}$$

$$R(\boldsymbol{\sigma}) \geq C_{\min}, \tag{5.25c}$$

$$\widetilde{\mathrm{UB}}_{\mathrm{FAP}}(\mathbf{P},\,\mathbf{U}) \leq S_{\max}, \tag{5.25d}$$

$$\mathbf{U} \geq 0, \tag{5.25e}$$

$$\mathrm{rank}(\mathbf{U}) = 1, \tag{5.25f}$$

$$\boldsymbol{\sigma} \succeq 0, \tag{5.25g}$$

$$\mathbf{P} = \mathbf{U} + \mathrm{diag}(\boldsymbol{\sigma}), \tag{5.25h}$$

where $P_{\max}$ in (5.25b) is the transmit power constraint at the transmitter, $C_{\min}$ in (5.25c) is the minimum rate constraint for communication, and $S_{\max}$ in (5.25d) is the maximal aISPLD constraint for sensing. Constraint (5.25e) and (5.25f) ensure a solution for $\mathbf{U} = \boldsymbol{\mu}\boldsymbol{\mu}^T$. (5.25g) ensures positive covariance and (5.25h) establishes the relationship between the variables as defined in (5.6d)-(5.6e).

5.3.2 Problem optimization

The rank 1 constraint in problem (5.25) is relaxed first during the optimization and is handled at the final stage by Gaussian randomization [114]. On this basis, we solve the remaining optimization problem following an ADMM structure [105].

The ADMM structure of problem (5.25), relaxing the rank 1 constraint in (5.25f) is expressed as [105]

$$\min_{\mathbf{P},\,\mathbf{U},\,\boldsymbol{\sigma}} \quad -z_{\mathrm{DC}}(\mathbf{P},\,\mathbf{U})+f_{\mathrm{I},\,\mathbf{P},\mathbf{U}}(\mathbf{P},\,\mathbf{U})+f_{\mathrm{I},\,\boldsymbol{\sigma},\,\mathbf{U}}(\boldsymbol{\sigma},\,\mathbf{U}), \tag{5.26a}$$

$$\text{s.t.} \quad \mathbf{U}+\mathrm{diag}(\boldsymbol{\sigma})-\mathbf{P}=\mathbf{0}, \tag{5.26b}$$

where $f_{\mathrm{I},\,\mathbf{P},\,\mathbf{U}}(\mathbf{P},\,\mathbf{U})$ is the indicator function of $\mathbf{P}$ and $\mathbf{U}$ corresponding to the constraint in (5.25b) and (5.25d), and $f_{\mathrm{I},\,\boldsymbol{\sigma},\,\mathbf{U}}(\boldsymbol{\sigma},\,\mathbf{U})$ is the indicator function of $\boldsymbol{\sigma}$ and $\mathbf{U}$ corresponding to the constraints in (5.25c), (5.25d), (5.25e) and (5.25g), i.e.,

$$f_{\mathrm{I},\,\mathbf{P},\,\mathbf{U}}(\mathbf{P},\,\mathbf{U}) \triangleq f_{\mathrm{I}}(\mathrm{Tr}(\mathbf{P})\leq P_{\max})+f_{\mathrm{I}}\Big(\widetilde{\mathrm{UB}}_{\mathrm{FAP}}(\mathbf{P},\,\mathbf{U})\leq S_{\max}\Big), \tag{5.27}$$

$$f_{\mathrm{I},\,\boldsymbol{\sigma},\,\mathbf{U}}(\boldsymbol{\sigma},\,\mathbf{U}) \triangleq f_{\mathrm{I}}(R(\boldsymbol{\sigma})\geq C_{\min})+f_{\mathrm{I}}\Big(\widetilde{\mathrm{UB}}_{\mathrm{FAP}}(\mathbf{P},\,\mathbf{U})\leq S_{\max}\Big)+f_{\mathrm{I}}(\mathbf{U}\geq 0)+f_{\mathrm{I}}(\boldsymbol{\sigma}\succeq 0). \tag{5.28}$$

Following the ADMM structure in problem (5.26), the variables of $\mathbf{P}$, $\mathbf{U}$ and $\boldsymbol{\sigma}$ at the l^{th} ADMM iteration are successively updated by [105]

$$\mathbf{P}^{(l+1)} := \mathrm{argmin}\Big\{-z_{\mathrm{DC}}\big(\mathbf{P},\,\mathbf{U}^{(l)}\big)+f_{\mathrm{I},\,\mathbf{P},\mathbf{U}}\big(\mathbf{P},\mathbf{U}^{(l)}\big)+\tfrac{\rho}{2}\|\mathbf{U}^{(l)}-\mathbf{P}+\mathrm{diag}\big(\boldsymbol{\sigma}^{(l)}\big)-\mathbf{V}^{(l)}\|^2\Big\}, \tag{5.29}$$

$$\big\{\mathbf{U}^{(l+1)},\,\boldsymbol{\sigma}^{(l+1)}\big\} := \mathrm{argmin}\Big\{-z_{\mathrm{DC}}\big(\mathbf{P}^{(l+1)},\,\mathbf{U}\big)+f_{\mathrm{I},\,\boldsymbol{\sigma},\,\mathbf{U}}(\boldsymbol{\sigma},\,\mathbf{U})+\tfrac{\rho}{2}\|-\mathbf{P}^{(l+1)}+\mathbf{U}+\mathrm{diag}(\boldsymbol{\sigma})-\mathbf{V}^{(l)}\|^2\Big\}, \tag{5.30}$$

$$\mathbf{V}^{(l+1)} := \mathbf{V}^{(l)}+\mathbf{P}^{(l+1)}-\mathbf{U}^{(l+1)}-\mathrm{diag}\big(\boldsymbol{\sigma}^{(l+1)}\big), \tag{5.31}$$

where $\mathbf{V}^{(l)}$ is the alternating direction at the l^{th} iteration and ρ is the updating step-size in ADMM.

Next, we solve the sub-problems in (5.29) and (5.30) respectively to update the variables $\mathbf{P}$, $\mathbf{U}$ and $\boldsymbol{\sigma}$.

Updating $\mathbf{P}^{(l+1)}$: The sub-problem to solve (5.29) is

$$\min_{\mathbf{P}} \quad -z_{\mathrm{DC}}\big(\mathbf{P},\,\mathbf{U}^{(l)}\big)+\frac{\rho}{2}\|-\mathbf{P}+\mathbf{U}^{(l)}+\mathrm{diag}\big(\boldsymbol{\sigma}^{(l)}\big)-\mathbf{V}^{(l)}\|^2 \tag{5.32a}$$

$$\begin{aligned}\mathbf{G}^{(t)}=&\textstyle\sum_{n=K_G}^{K'-1}k_2\mathbf{A}_n^T+\frac{3k_4}{4}\left[2\mathrm{Tr}\left(\mathbf{A}_n\mathbf{P}^{(t)}\right)\mathbf{A}_n^T+6\sigma_{\mathrm{nP}}^2\mathbf{A}_n^T+4\mathbf{A}_n\mathbf{P}^{(t)}\mathbf{A}_n+2\mathrm{Tr}\left(\widetilde{\mathbf{A}}_n\mathbf{P}^{(t)}\right)\widetilde{\mathbf{A}}_n^T+6\sigma_{\mathrm{nP}}^2\widetilde{\mathbf{A}}_n^T+4\widetilde{\mathbf{A}}_n\mathbf{P}^{(t)}\widetilde{\mathbf{A}}_n\right]\\&+\textstyle\sum_{n=0}^{K_G-1}k_2\mathbf{B}_n^T+\frac{3k_4}{4}\left[2\mathrm{Tr}\left(\mathbf{B}_n\mathbf{P}^{(t)}+2\mathbf{D}_n\mathbf{U}^{(l)}\right)\mathbf{B}_n^T+6\sigma_{\mathrm{nP}}^2\mathbf{B}_n^T+2\mathrm{Tr}\left(\widetilde{\mathbf{B}}_n\mathbf{P}^{(t)}+2\widetilde{\mathbf{D}}_n\mathbf{U}^{(l)}\right)\widetilde{\mathbf{B}}_n^T+6\sigma_{\mathrm{nP}}^2\widetilde{\mathbf{B}}_n^T\right]\\&+\textstyle\sum_{n=0}^{K_G-1}3k_4\left[\mathbf{B}_{1,\ n}\left(\mathbf{P}^{(t)}\mathbf{B}_{1,\ n}+\mathbf{U}^{(l)}\mathbf{D}_n^T\right)+\mathbf{D}_n^T\left(\mathbf{P}^{(t)}\mathbf{D}_n+\mathbf{U}^{(l)}\mathbf{B}_{2,\ n}\right)+\mathbf{D}_n\left(\mathbf{P}^{(t)}\mathbf{D}_n^T+\mathbf{U}^{(l)}\mathbf{B}_{1,\ n}\right)+\mathbf{B}_{2,\ n}\left(\mathbf{P}^{(t)}\mathbf{B}_{2,\ n}+\mathbf{U}^{(l)}\mathbf{D}_n\right)\right]\\&+\textstyle\sum_{n=0}^{K_G-1}3k_4\left[\widetilde{\mathbf{B}}_{1,\ n}\left(\mathbf{P}^{(t)}\widetilde{\mathbf{B}}_{1,\ n}+\mathbf{U}^{(l)}\widetilde{\mathbf{D}}_n^T\right)+\widetilde{\mathbf{D}}_n^T\left(\mathbf{P}^{(t)}\widetilde{\mathbf{D}}_n+\mathbf{U}^{(l)}\widetilde{\mathbf{B}}_{2,\ n}\right)+\widetilde{\mathbf{D}}_n\left(\mathbf{P}^{(t)}\widetilde{\mathbf{D}}_n^T+\mathbf{U}^{(l)}\widetilde{\mathbf{B}}_{1,\ n}\right)+\widetilde{\mathbf{B}}_{2,\ n}\left(\mathbf{P}^{(t)}\widetilde{\mathbf{B}}_{2,\ n}+\mathbf{U}^{(l)}\widetilde{\mathbf{D}}_n\right)\right].\end{aligned}\tag{5.34}$$

$$\text{s.t.}\quad \mathrm{Tr}(\mathbf{P})\leq P_{\max},\tag{5.32b}$$

$$\widetilde{\mathrm{UB}}_{\mathrm{FAP}}\left(\mathbf{P},\,\mathbf{U}^{(l)}\right)\leq S_{\max},\tag{5.32c}$$

which is non-convex due to the objective $-z_{\mathrm{DC}}\left(\mathbf{P},\,\mathbf{U}^{(l)}\right)$ and the constraint (5.32b). However, $-z_{\mathrm{DC}}\left(\mathbf{P},\,\mathbf{U}^{(l)}\right)$ in the objective function is concave w.r.t. $\mathbf{P}$, and can be handled by using SCP. In SCP, the concave part of the objective function is successively substituted by a linear Taylor approximation operating at the point which is the local optimal of the previous round. Specifically, suppose $\mathbf{P}^{(t)}$ is the optimal point at the t^{th} SCP iteration, then, at the $(t+1)^{\mathrm{th}}$ iteration, $-z_{\mathrm{DC}}(\mathbf{P},\mathbf{U}^{(l)})$ in the objective function is substituted by [96]

$${z_{\mathrm{DC}}}^{(t+1)}\left(\mathbf{P},\,\mathbf{U}^{(l)}\right)={z_{\mathrm{DC},\ 0}}^{(t)}\left(\mathbf{P}^{(t)},\,\mathbf{U}^{(l)}\right)+\mathrm{Tr}\left(\mathbf{G}^{(t)^T}\mathbf{P}\right),\tag{5.33}$$

where $\mathbf{G}^{(t)}$ is the first-order Taylor coefficient, expressed in (5.34). ${z_{\mathrm{DC},\ 0}}^{(t)}\left(\mathbf{P}^{(t)},\,\mathbf{U}^{(l)}\right)$ is the Taylor constant to be omitted.

Similarly, the non-linear constraint in (5.32c) is also approximated by its linear upper bound in each iteration of SCP. Since the concavity of (5.32c) comes from the square root function, we approximate the square root function by using Taylor expansion

$$\widetilde{\mathrm{UB}}_{\mathrm{FAP}}\left(\mathbf{P},\,\mathbf{U}^{(l)}\right)\leq -M(K_GM-1)\mathrm{Tr}(\mathbf{P})+\sum_{(r,\ v)\neq(0,\ 0)}\frac{2\left(\widetilde{g}_{r,v}\left(\mathbf{P}^{(t)}\right)+\widetilde{g}_2\left(\mathbf{U}^{(l)}\right)\right)}{\alpha_{r,v}^{(l,t)}}+\tag{5.35a}$$

$$\sum_{(r,\ v)\neq(0,\ 0)}\frac{\left[\widetilde{g}_{r,v}(\mathbf{P})+\widetilde{g}_2\left(\mathbf{U}^{(l)}\right)-\widetilde{g}_{r,v}\left(\mathbf{P}^{(t)}\right)-\widetilde{g}_2\left(\mathbf{U}^{(l)}\right)\right]}{\alpha_{r,v}^{(l,t)}}\tag{5.35b}$$

$$= \alpha^{(l,t)} - M(K_G M - 1)\mathrm{Tr}(\mathbf{P}) + \sum_{(r,\ v)\neq(0,\ 0)} \frac{\widetilde{g}_{r,v}(\mathbf{P})}{\alpha_{r,v}^{(l,t)}} \tag{5.35c}$$

$$\triangleq \widetilde{\mathrm{UB}}_{\mathrm{FAP}}^{(t)}(\mathbf{P}), \tag{5.35d}$$

$$\text{with } \alpha_{r,v}^{(l,t)} = 2\sqrt{\widetilde{g}_{r,v}(\mathbf{P}^{(t)}) + \widetilde{g}_2(\mathbf{U}^{(l)})},$$

$$\alpha^{(l,t)} = \sum_{(r,\ v)\neq(0,\ 0)} \frac{\widetilde{g}_{r,v}\big(\mathbf{P}^{(t)}\big) + 2\widetilde{g}_2\big(\mathbf{U}^{(l)}\big)}{\alpha_{r,v}^{(l,t)}}. \tag{5.35e}$$

Hence, combing (5.33) and (5.35), the sub-problem to solve problem (5.32) becomes

$$\min_{\mathbf{P}} \quad -\mathrm{Tr}\Big(\mathbf{G}^{(t)^T}\mathbf{P}\Big) + \frac{\rho}{2}\|\mathbf{P} - \mathbf{U}^{(l)} - \mathrm{diag}\big(\boldsymbol{\sigma}^{(l)}\big) + \mathbf{V}^{(l)}\|^2,$$

$$\text{s.t.} \quad \mathrm{Tr}(\mathbf{P}) \leq P_{\max}, \tag{5.36a}$$

$$\widetilde{\mathrm{UB}}_{\mathrm{FAP}}^{(t)}(\mathbf{P}) \leq S_{\max}, \tag{5.36b}$$

which is a convex Quadratic Constrained Quadratic Programming (QCQP) problem, whose Lagrangian is given by

$$L(\mathbf{P},\, u_1,\, u_2) = -\sum_n \mathrm{Tr}\Big(\mathbf{G}^{(t)^T}\mathbf{P}\Big) + \frac{\rho}{2}\|\mathbf{P} - \mathbf{U}^{(l)} - \mathrm{diag}\big(\boldsymbol{\sigma}^{(l)}\big) + \mathbf{V}^{(l)}\|^2$$
$$+ u_1(\mathrm{Tr}(\mathbf{P}) - P_{\max}) + u_2\Big(\widetilde{\mathrm{UB}}_{\mathrm{FAP}}^{(t)}(\mathbf{P}) - S_{\max}\Big), \tag{5.37}$$

where u_1 and u_2 are the non-negative Lagrange multipliers.

Taking the first-order derivative and combining (5.35a), we have

$$\frac{\partial L(\mathbf{P},\, u_1,\, u_2)}{\partial \mathbf{P}} = -\mathbf{G}^{(t)} + \rho\big(\mathbf{P} - \mathbf{U}^{(l)} - \mathrm{diag}\big(\boldsymbol{\sigma}^{(l)}\big) + \mathbf{V}^{(l)}\big) + [u_1 - u_2 M(K_G M - 1)]\mathbf{I}_{2K} +$$
$$u_2 \mathrm{diag}\left\{ \sum_{(r,\ v)\neq(0,\ 0)} \left[\frac{2\mathbf{F}_{r,v}^{\mathrm{R}}}{\alpha_{r,v}^{(l,t)}} + \frac{2\mathbf{F}_{r,v}^{\mathrm{I}}}{\alpha_{r,v}^{(l,t)}} + \frac{4M}{\alpha_{r,v}^{(l,t)}}\mathbf{I}_{2K} \right] \mathrm{diag}(\mathbf{P}) \right\}, \tag{5.38}$$

where $\mathbf{F}_{r,v}^{\mathrm{R}} = \mathbf{f}_{r,v}^{\mathrm{R}\ T}\mathbf{f}_{r,v}^{\mathrm{R}}$ and $\mathbf{F}_{r,v}^{\mathrm{I}} = \mathbf{f}_{r,v}^{\mathrm{I}\ T}\mathbf{f}_{r,v}^{\mathrm{I}}$.

$$\frac{\partial L}{\partial \mathbf{p}}=\underbrace{\left\{\rho\mathbf{I}_{2K}+u_2\sum_{r,v}\frac{2}{\alpha_{r,v}^{(l,t)}}\left[\mathbf{F}_{r,v}^{\mathrm{R}}+\mathbf{F}_{r,v}^{\mathrm{I}}+2M\mathbf{I}_{2K}\right]\right\}}_{\mathbf{Q}^{(t)}(u_2)}\mathbf{p}+u_1\underbrace{-u_2M(K_GM-1)-\mathbf{g}^{(t)}+\rho\left(-\boldsymbol{\mu}^{(l)}-\boldsymbol{\sigma}^{(l)}+\mathbf{v}^{(l)}\right)}_{\mathbf{q}^{(t)}(u_2)}. \tag{5.41}$$

Equating (5.38) to $\mathbf{0}$, we observe that, for the non-diagonal elements of $\mathbf{P}$, the stationary point is irrelevant with the multipliers u_1 and u_2, and can be directly calculated as

$$P_{k,j}=\frac{1}{\rho}G_{k,j}^{(t)}+U_{k,j}^{(l)}-V_{k,j}^{(l)},\ \ (j\neq k). \tag{5.39}$$

For the diagonal elements of $\mathbf{P}$, (5.38) can be re-organized into (5.41) where $\mathbf{p}=\mathrm{diag}(\mathbf{P})$, $\mathbf{g}^{(t)}=\mathrm{diag}\left(\mathbf{G}^{(t)}\right)$, $\boldsymbol{\mu}^{(t)}=\mathrm{diag}\left(\mathbf{U}^{(t)}\right)$ and $\mathbf{v}^{(t)}=\mathrm{diag}\left(\mathbf{V}^{(t)}\right)$. After being setting into $\mathbf{0}$, (5.41) gives the result as

$$P_{k,k}=p_k=\left(\begin{bmatrix}\mathbf{Q}^{(t)}(u_2) & \mathbf{1}\\ \mathbf{1} & 0\end{bmatrix}^{-1}\begin{bmatrix}-\mathbf{q}^{(t)}(u_2)\\ P_{\max}\end{bmatrix}\right)_k, \tag{5.40}$$

where $k=0,\ \cdots,\ 2K-1$. u_2 is obtained by bi-section search. $\mathbf{Q}^{(t)}(u_2)$ and $\mathbf{q}^{(t)}(u_2)$ are shown in (5.41).

The algorithm to solve sub-problem (5.29) is summarized in algorithm 7.

Updating $\mathbf{U}^{(l+1)}$ and $\boldsymbol{\sigma}^{(l+1)}$

Similarly, the sub-problem of (5.30) is

$$\min_{\mathbf{U},\boldsymbol{\sigma}}\quad -z_{\mathrm{DC}}\left(\mathbf{P}^{(l+1)},\mathbf{U}\right)+\frac{\rho}{2}\|-\mathbf{P}^{(l+1)}+\mathbf{U}+\mathrm{diag}(\boldsymbol{\sigma})-\mathbf{V}^{(l)}\|^2, \tag{5.42a}$$

$$\text{s.t.}\quad \mathbf{U}\succeq\mathbf{0}, \tag{5.42b}$$

$$\boldsymbol{\sigma}\succeq\mathbf{0}, \tag{5.42c}$$

$$R(\boldsymbol{\sigma})\geq C_{\min}, \tag{5.42d}$$

Algorithm 7: SCP for $\mathbf{P}^{(l+1)}$

Input: $t \leftarrow 0$, $\mathbf{P}^{(l+1,\ 0)}$, ϵ_0, $u_{2_{\mathrm{L}}}$, $u_{2_{\mathrm{U}}}$

Output: $\mathbf{P}^{(l+1)}$

Repeat

1. Compute $\mathbf{G}^{(t)}$ from (5.34), $\alpha_{r,v}^{(l,t)}$ and $\alpha^{(l,t)}$ from (5.35e) at the operating point $\mathbf{P}^{(l+1,\ t)}$

2. Find u_2 by bi-section search:

   2.1 $u_2 \leftarrow 0$, $\mathbf{P}(0)$ from (5.39) and (5.40)

   2.2 **If** $\widetilde{\mathrm{UB}}_{\mathrm{FAP}}^{(t)}(\mathbf{P}(u_2)) > S_{\max}$

   $\mathbf{P}^{(l+1,\ t+1)} \leftarrow \mathbf{P}(u_2)$

   else

   $\mathbf{P}^{(l+1,\ t+1)} \leftarrow \mathbf{P}(u_2)$

   while $|\widetilde{\mathrm{UB}}_{\mathrm{FAP}}^{(t)}(\mathbf{P}(u_2)) - S_{\max}| > \epsilon_0$

   $u_2 = (u_{2_{\mathrm{L}}} + u_{2_{\mathrm{U}}})/2$

   calculate $\mathbf{P}(u_2)$ from (5.39) and (5.40)

   If $\widetilde{\mathrm{UB}}_{\mathrm{FAP}}^{(t)}(\mathbf{P}(u_2)) < S_{\max}$

   $u_{2_{\mathrm{U}}} = u_2$

   elseif $\widetilde{\mathrm{UB}}_{\mathrm{FAP}}^{(t)}(\mathbf{P}(u_2)) > S_{\max}$

   $u_{2_{\mathrm{L}}} = u_2$

   end

   end

   end

3. Compute $\mathbf{P}^{(l+1,\ t+1)}$ combining (5.39) and (5.40)

4. $t \leftarrow t+1$; $\mathbf{P}^{(l+1)} \leftarrow \mathbf{P}^{(l+1,\ t+1)}$

5. Quit if $\|\mathbf{P}^{(l+1,\ t+1)} - \mathbf{P}^{(l+1,\ t)}\| < \epsilon_0 \|\mathbf{P}^{(l+1,\ t+1)}\|$

$$\widetilde{\mathrm{UB}}_{\mathrm{FAP}}(\mathbf{P}^{(l+1)}, \mathbf{U}) \leq S_{\max}, \tag{5.42e}$$

whose concave part in the objective function in (5.42a) is still substituted by a linear approximation by using SCP. Specifically, at the t^{th} SCP iteration, $-z_{\mathrm{DC}}\big(\mathbf{P}^{(l+1)}, \mathbf{U}\big)$ in

$$\begin{aligned}\mathbf{J}^{(t)}=&\textstyle\sum_{k=0}^{K_G-1}2k_2\mathbf{D}_n^T+3k_4\Big[\mathrm{Tr}\big(\mathbf{B}_n\mathbf{P}^{(l+1)}+2\mathbf{D}_n\mathbf{U}^{(t)}\big)\mathbf{D}_n^T+\mathrm{Tr}\big(\widetilde{\mathbf{B}}_n\mathbf{P}^{(l+1)}+2\widetilde{\mathbf{D}}_n\mathbf{U}^{(t)}\big)\mathbf{D}_n^T+3\sigma_{\mathrm{n_P}}^2\mathbf{D}_n^T+3\sigma_{\mathrm{n_P}}^2\widetilde{\mathbf{D}}_n^T\Big]\\&+\textstyle\sum_{k=0}^{K_G-1}3k_4\Big[2\mathbf{D}_n^T\mathbf{U}^{(t)}\mathbf{D}_n^T+\mathbf{B}_{1,\ n}\mathbf{U}^{(t)}\mathbf{B}_{2,\ n}+\mathbf{B}_{2,\ n}\mathbf{U}^{(t)}\mathbf{B}_{1,\ n}+\mathbf{D}_n^T\mathbf{P}^{(l+1)}\mathbf{B}_{1,\ n}+\mathbf{D}_n\mathbf{P}^{(l+1)}\mathbf{B}_{2,\ n}\Big]\\&+\textstyle\sum_{k=0}^{K_G-1}3k_4\Big[\mathbf{B}_{1,\ n}\mathbf{P}^{(l+1)}\mathbf{D}_n+\mathbf{B}_{2,\ n}\mathbf{P}^{(l+1)}\mathbf{D}_n^T+\widetilde{\mathbf{B}}_{1,\ n}\mathbf{P}^{(l+1)}\widetilde{\mathbf{D}}_n+\widetilde{\mathbf{B}}_{2,\ n}\mathbf{P}^{(l+1)}\widetilde{\mathbf{D}}_n^T\Big]\\&+\textstyle\sum_{k=0}^{K_G-1}3k_4\Big[2\widetilde{\mathbf{D}}_n^T\mathbf{U}^{(t)}\widetilde{\mathbf{D}}_n^T+\widetilde{\mathbf{B}}_{1,\ n}\mathbf{U}^{(t)}\widetilde{\mathbf{B}}_{2,\ n}+\widetilde{\mathbf{B}}_{2,\ n}\mathbf{U}^{(t)}\widetilde{\mathbf{B}}_{1,\ n}+\widetilde{\mathbf{D}}_n^T\mathbf{P}^{(l+1)}\widetilde{\mathbf{B}}_{1,\ n}+\widetilde{\mathbf{D}}_n\mathbf{P}^{(l+1)}\widetilde{\mathbf{B}}_{2,\ n}\Big].\end{aligned}\quad(5.44)$$

(5.42a) becomes [96]

$$\begin{aligned}z_{\mathrm{DC}}{}^{(t)}(\mathbf{U})=&z_{\mathrm{DC},\ 0}{}^{(t)}+\mathrm{Tr}\Big(\mathbf{J}^{(t)^T}\mathbf{U}\Big)-\sum_{n=K_G}^{K'-1}2\mathrm{Tr}(\mathbf{A}_n\mathbf{U}\mathbf{A}_n\mathbf{U})-\\&\sum_{n=0}^{K_G-1}2\Big[\mathrm{Tr}(\mathbf{E}_n\mathbf{U}\mathbf{E}_n\mathbf{U})+\mathrm{Tr}\Big(\widetilde{\mathbf{E}}_n\mathbf{U}\widetilde{\mathbf{E}}_n\mathbf{U}\Big)\Big],\end{aligned}\quad(5.43)$$

where $\mathbf{J}^{(t)}$ is given in (5.44). $z_{\mathrm{DC},\ 0}{}^{(t)}$ is the Taylor constant to be omitted. Note that $\mathbf{A}_n$ is positive semi-definite from the definition and $\mathbf{E}_n/\widetilde{\mathbf{E}}_n$ are positive semi-definite as proved in Appendix 5.6.2.

The constraint in (5.42e) is a decrease function w.r.t. $\|\mathrm{diag}(\mathbf{U})\|^2$, and can be equivalently transformed into

$$\|\mathrm{diag}(\mathbf{U})\|^2\geq r^{(l)},\quad(5.45)$$

where $r^{(l)}$ can be found by bisection search such that $\sum_{(r,\ v)\neq(0,\ 0)}-\mathrm{Tr}(\mathbf{P})+\sqrt{\widetilde{g}_{r,v}(\mathbf{P})-2r^{(l)}}=S_{\max}$.

(5.45) is still a concave non-linear constraint, but can be handled by introducing a parametric vector $\mathbf{v}$ and utilizing the inequality

$$\|\mathrm{diag}(\mathbf{U})\|^2\geq\frac{\big(\mathbf{v}^T\|\mathrm{diag}(\mathbf{U})\|\big)^2}{\|\mathbf{v}\|^2},\quad(5.46)$$

which holds if and only if $\mathrm{diag}\{\mathbf{U}\}_k/v_k=c$ (c constant) for $\forall k$. Hence, the constraint in (5.45) can be substituted by (5.46), taking $\mathbf{v}$ as the diagonal elements of the optimal $\mathbf{U}$ from the previous round in each SCP iteration. The algorithm that introduces auxiliary

Algorithm 8: SCP-PSCA for $\left(\mathbf{U}^{(l+1)}, \boldsymbol{\sigma}^{(l+1)}\right)$

1. **Input**: $t \leftarrow 0$, $\left(\mathbf{U}^{(l,\,0)}, \boldsymbol{\sigma}^{(l,\,0)}\right)$, ϵ_0
2. **Output**: $\left(\mathbf{U}^{(l+1)}, \boldsymbol{\sigma}^{(l+1)}\right)$
3. **Repeat**
   - 3.1 Compute $\mathbf{J}^{(t)}$ from (5.44) at $\left(\mathbf{U}^{(l,t)}, \boldsymbol{\sigma}^{(l,t)}\right)$;
   - 3.2 Compute $\mathbf{v}^{(t)} = \mathrm{diag}\left(\mathbf{U}^{(t)}\right)$
   - 3.3 Compute $\left(\mathbf{U}^{(l,t)}, \boldsymbol{\sigma}^{(l,t)}\right)$ in problem (5.47) using cvx
   - 3.4 $t \leftarrow t+1$; $\left(\mathbf{U}^{(l+1)}, \boldsymbol{\sigma}^{(l+1)}\right) \leftarrow \left(\mathbf{U}^{(l+1,\,t+1)}, \boldsymbol{\sigma}^{(l+1,\,t+1)}\right)$
   - 3.5 Quit if $\|\mathbf{U}^{(l+1,\,t+1)} - \mathbf{U}^{(l+1,\,t)}\| < \epsilon_0 \|\mathbf{U}^{(l+1,\,t+1)}\|$

variables to form an achievable convex upper bound is named PSCA [115].

Combining with (5.46), at the t^{th} iteration, we have [115]

$$\min_{\mathbf{U},\,\boldsymbol{\sigma}} \quad z_{\mathrm{DC}}{}^{(t)}(\mathbf{U}) + \frac{\rho}{2}\|-\mathbf{P}^{(l+1)} + \mathbf{U} + \mathrm{diag}(\boldsymbol{\sigma}) - \mathbf{V}^{(l)}\|^2 \tag{5.47a}$$

$$\text{s.t.} \quad \frac{\mathbf{v}^{(t)^T}\mathrm{diag}(\mathbf{U})}{\sqrt{\|\mathbf{v}^{(t)}\|^2}} \geq \sqrt{r^{(l)}}, \tag{5.47b}$$

$$(5.42\text{b}),\ (5.42\text{c}),\ \text{and}\ (5.42\text{d}), \tag{5.47c}$$

where $\mathbf{v}^{(t)} = \mathrm{diag}\left(\mathbf{U}^{(t)}\right)$ and which is a convex programming that can be solved by cvx.

The algorithm to solve sub-problem (5.30) is summarized in algorithm 8. The whole algorithm is summarized in Algorithm 9.

5.4 Simulation results

In this section, we simulate the performance of the ISCAP system and evaluate its C-P region (maximal harvested power as a function of the achievable rate constraint, for a

Algorithm 9: ADMM

1. **Input**: $l \leftarrow 0$, $k \leftarrow 0$, $\mathbf{P}^{(0)}$, $\mathbf{U}^{(0)}$, $\boldsymbol{\sigma}^{(0)}$, $\epsilon_S > 0$, $\rho > 0$
2. **Output**: $\mathbf{p}^\star$, $\boldsymbol{\mu}^\star$, $\boldsymbol{\sigma}^\star$

2.1 **While** $k < 20$

While $\|\mathbf{P}^{(l+1)} - \mathbf{P}^{(l+1)}\| < \epsilon_0 \|\mathbf{P}^{(l+1)}\|$

Update $\mathbf{P}^{(l+1)}$ by Algorithm 7

Update $\left(\mathbf{U}^{(l+1)}, \boldsymbol{\sigma}^{(l+1)}\right)$ by Algorithm 8

Update $\mathbf{V}^{(l+1)}$ in (5.31)

$l \leftarrow l+1$

end

end

2.2 Obtain $\boldsymbol{\mu}^\star$ from $\mathbf{U}^\star$ using Gaussian randomization [114]

2.3 $p_k^\star \leftarrow {\mu_k^\star}^2 + \sigma_k^\star, \quad k = (0, \cdots, 2K-1)$

fixed aISPLD[3] constraint) and its S-P region (maximal harvested power as a function of the aISPLD constraint, for a fixed achievable rate constraint).

Throughout the simulations, the performance of the ISCAP system is evaluated under a Wi-Fi like scenario with $f_0 = 5.18$ GHz. For simplification, we assume a signal antenna at the transceiver, communication receiver and the energy harvester. We also consider a point-target mono-static radar scenario, and a static communication user and energy harvester. At the transmitter, assume an OFDM signal with bandwidth $B = 30$ MHz, $K = 8$ sub-carriers, $K_G = 4$ CP pulses and 40 dBm transmit power. The communication channel is an NLoS model from Model B in [109], with a 108 dB path-loss (around 1 km), -110 dBW noise power, and a 0 dB communication SNR over simulations. The powering channel is similarly simulated as the communication channel but with a 58 dB path-loss (around 10 m), with a -108 dBW noise power. For the sensing function, we assume an average -20 dB radar receiver SNR at over simulations.

[3]The aISPLD constraint is normalized when plotting the simulations

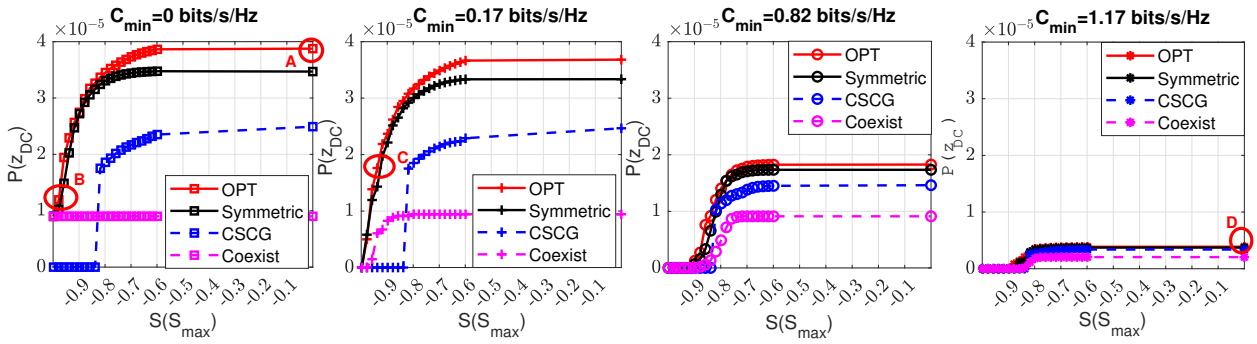

Fig. 5.2: The average S-P region given different achievable rate constraints ($C_{\min}=0$, 0.12, 0.47, 0.82, 1.17 bits/s/Hz from left to right). 'OPT' (red) refers to the optimized asymmetric complex Gaussian input distribution from Section 5.3. 'Symmetric' (black) refers to the optimized symmetric complex Gaussian input distribution. 'CSCG' (blue) refers to the optimized CSCG input distribution. 'Coexist' (magenta) refers to the non-co-design signal superposed by the optimal communication and sensing signals through PS. $P(Z_{\mathrm{DC}})=0$ means that the exerted rate and aISPLD constraints are not feasible at this point.

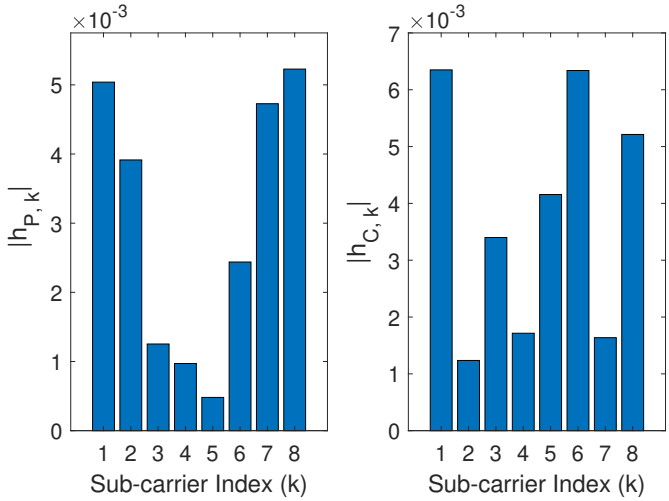

Fig. 5.3: Left: Magnitude response of one powering channel realization; Right: Magnitude response of one communications channel realization.

5.4.1 S-P region

Fig. 5.2 plots the average S-P region over 300 channel realizations, given different constraints on the communication achievable rate. We compare three co-design input distributions; namely, the asymmetric complex Gaussian from Section 5.3 (red curve with

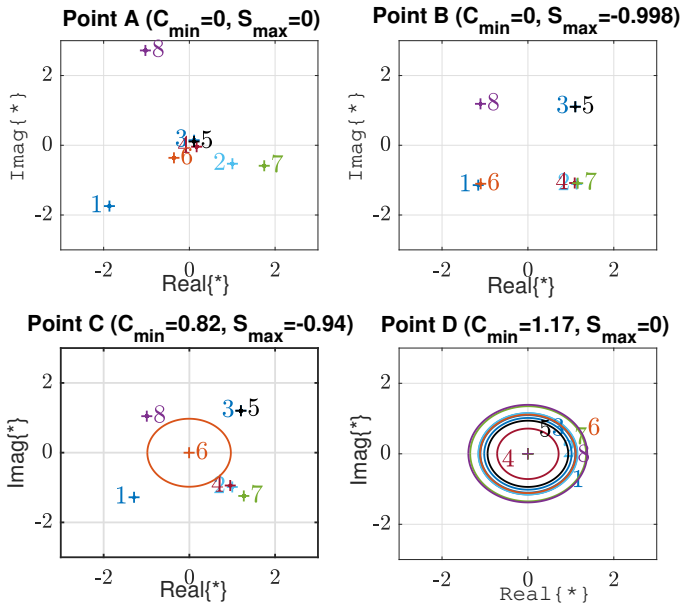

Fig. 5.4: For the channel realizations in Fig. 5.3, the 'OPT' input distribution corresponding to points A, B, C, and D in Fig. 5.2. For each sub-carrier (numbered 1 through 8), its complex Gaussian distribution is represented by an ellipse whose center is the mean, and whose width and height correspond to the variance of the real and imaginary parts, respectively.

legend 'OPT'), the symmetric complex Gaussian (black curve with legend 'Symmetric'), the CSCG (blue curve with legend 'CSCG')[4], and the coexisting PS input distribution (magenta curve with legend 'Coexist'[5]). Figs. 5.3 and 5.4 are companion figures to Fig. 5.2. Specifically, Fig. 5.4 plots the 'OPT' input distributions corresponding to points 'A', 'B', 'C' and 'D' in Fig. 5.2 for channel realizations given by Fig. 5.3. The insights from this collection of figures are as follows:

- Point 'A' in Fig. 5.2 refers to the scenario without achievable rate and aISPLD constraints, i.e., a pure powering system. From the corresponding plot in Fig. 5.4, we observe that all the power is allocated to the symbol means of the sub-carrier,

[4]The optimal 'Symmetric' input and the optimal 'CSCG' input are also achieved from the optimization problem in section 5.3. For the optimal 'Symmetric' input, we substitute $\mu_k^{\mathrm{I}}=\mu_k^{\mathrm{R}}$, $\sigma_k^{\mathrm{I}}=\sigma_k^{\mathrm{R}}$ in problem (5.25) and only needs to optimize $2K$ variables rather than $4K$. Similarly, for the optimal 'CSCG' input, we only need to optimize $\sigma_k^{\mathrm{I}}=\sigma_k^{\mathrm{R}}$ with $\mu_k^{\mathrm{I}}=\mu_k^{\mathrm{R}}=0$.

[5]The 'Coexist' input satisfies the same transmit power constraint as the three co-design inputs. In particular, the variance of the 'Coexist' input is decided by the communication function (the variance that satisfies the achievable rate with minimal power) and the mean of the 'Coexist' input is the optimal sensing input using the remaining power.

proportional to the strength of the powering channel in Fig. 5.3. For instance, sub-carriers 8 and 1 have the two strongest powering channels (large values of $|h_{P,k}|$) and hence, the largest amount of power allocated to them (i.e., farthest from the origin). Furthermore, the optimal symbol means of the real and imaginary parts are unequal, in line with the asymmetric complex Gaussian distribution, highlighting the powering system's performance dependence on having different real and imaginary parts of the symbol mean adaptive to the powering channels, as it has mentioned in footnote. Finally, we see from Fig. 5.2 that for fixed achievable rate and aISPLD constraints, the asymmetric complex Gaussian input distribution leads to higher harvested power than the other three symmetric input distributions.

- From 'A' to 'B', a stricter aISPLD constraint is imposed (from $S_{\max} = 0$ to $S_{\max} = -0.998$, with the lowest achievable aISPLD being $S_{\max} = -1$). However, like 'A', there is no achievable rate constraint. Hence, 'B' corresponds to an input distribution designed for *integrated sensing and power transfer*. The resulting 'OPT' input distribution still allocates all of the available transmit power to the symbol means, but with a more uniform power allocation across OFDM sub-carriers. This is because the lowest value of the aISPLD metric in (5.20) is achieved when the OFDM symbols have the same magnitudes across OFDM sub-carriers (from Chapter 4), so that the best AF for sensing is achieved. Indeed, Fig. 5.2 shows that the lowest value of aISPLD can be achieved by both asymmetric ('OPT') and symmetric ('Symmetric') inputs – the non-zero power $P(z_{\mathrm{DC}})$ starts from the same value of $S(S_{\max})$ axis in Fig. 5.2 (they share the same feasible region of the sensing and communication constraints). The takeaway is that, while the complex mean is the essential component for sensing's performance, the sensing's performance is not affected by either having identical or different values for the real and imaginary parts of the mean, as long as the total power allocation to the complex symbol mean is fixed, which is in sharp contrast with the powering system's preference as it has been mentioned.

- From 'B' to 'C', the aISPLD is looser (from -0.998 to $=-0.94$), but the achievable rate constraint, $C_{\min}$, is tighter (from 0 to 0.82 bits/s/Hz)[6]. Since the sensing and communications constraints are non-trivial, 'C' corresponds to an input distribution designed for ISCAP. Compared with 'B', the 'OPT' input distribution of 'C' still shows a tendency for uniform power allocation across OFDM sub-carriers to satisfy the aISPLD constraint, except that at sub-carrier 6 (owning the strongest communication channel in Fig. 5.3), the allocated power is shifted from the mean to the variance in order to satisfy the achievable rate constraint efficiently.

- From 'C' to 'D', the aISPLD is further loosened (to $S_{\max}=0$ the same as 'A'), whereas the achievable rate constraint is further tightened (to 1.17 bits/s/Hz). Thus, point 'D' corresponds to an input distribution designed for WIPT. Due to the large value of $C_{\min}$, the available power is allocated solely to the symbol variance of each sub-carrier, largely in proportion to the strength of the communication channel. For instance, sub-carriers 1 and 6 have the two strongest communication channels (large values of $|h_{C,k}|$) and hence, the largest amount of power allocated to them (i.e., larger ellipses). Once the achievable rate constraint is satisfied, the remaining power is distributed to sub-carriers with strong powering channels (e.g., sub-carrier 7, which also has a large ellipse). In contrast, sub-carriers with weak communications and powering channels (e.g., sub-carrier 4) have no power allocated to them.

To summarize, Fig. 5.2 demonstrates that our proposed non-zero mean asymmetric 'OPT' distribution achieves the largest S-P region, followed by the 'Symmetric' and the 'CSCG' input distributions. In particular, due to its asymmetric input, the gap between the 'OPT' and other S-P regions enlarges as the achievable rate and/or aISPLD constraint is loosened. Generally, the three co-design inputs (especially the 'OPT' and the 'Symmetric') outperform the 'Coexist' for any achievable rate constraint. The comparison between the different points in Fig. 5.2 indicates the following two general trade-offs

[6]The highest achievable rate for the channel in Fig. 5.3 is 1.23 bits/s/Hz.

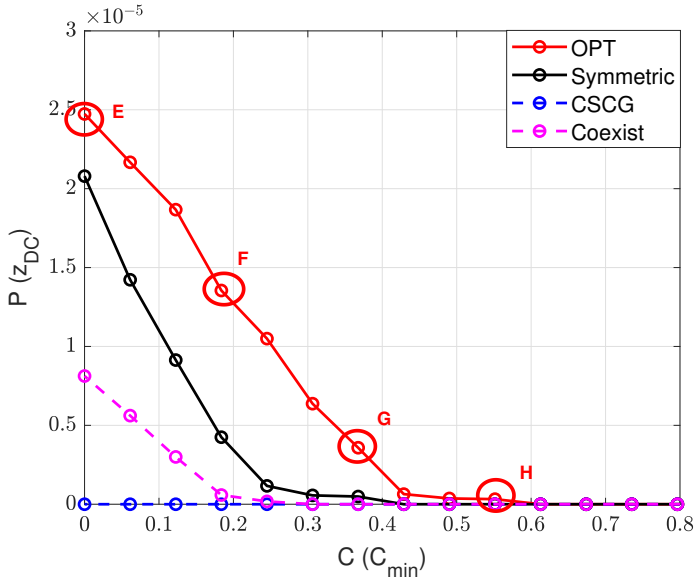

Fig. 5.5: The average C-P region given $S_{\max} = -0.948$, comparing the 'OPT', 'Symmetric', 'CSCG' and 'Coexist' inputs.

between the three functions in the ISCAP system:

1) the trade-off between power allocation to the symbols mean and variance – the former is beneficial for sensing and powering (especially with frequency-flat channels) while the latter is essential for communications;

2) for power allocation to the symbol mean in particular, powering prefers an allocation that is asymmetric and proportional to the strength of powering channel, while sensing favors uniform and symmetric power allocation.

5.4.2 C-P region

For further verification, we plot the average C-P region of the ISCAP system in Fig. 5.5 given a fixed non-trivial aISPLD constraint of $S_{\max} = -0.948$. Similarly, four optimal input distributions on the C-P region, 'E', 'F', 'G' and 'H' are plotted in Fig. 5.6, corresponding to the same channel realizations in Fig. 5.3. The takeaways are concluded as:

- Fig. 5.5 reveals a smaller performance gap between different inputs given stricter

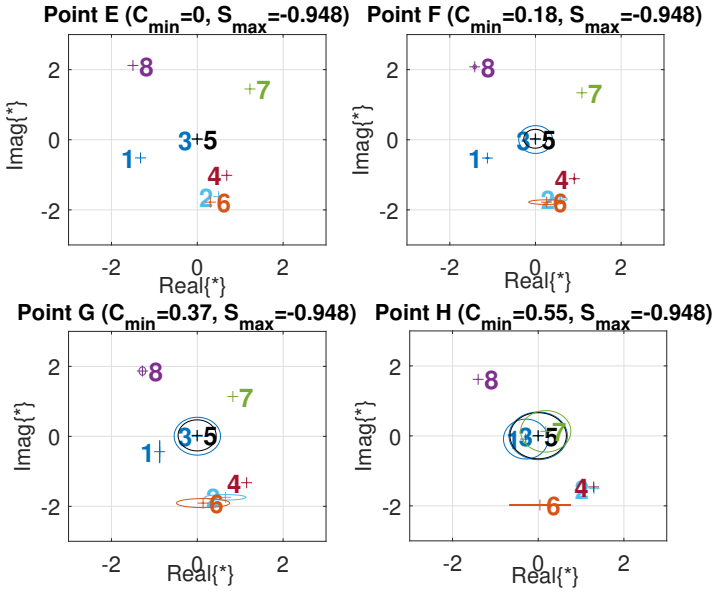

Fig. 5.6: The 'OPT' input constellation of points E, F, G and H in Fig. 5.5 corresponds to the channel realizations in Fig. 5.3.

constraints on the achievable rate, since they all converge to a CSCG input (i.e., $C_{\min} \geq 0.55$ bits/s/Hz) for the best communications. On the other hand, given loose achievable rate constraints, the 'OPT' input outperforms the other inputs significantly because of its flexibility to have asymmetric inputs catering to the preference of powering, i.e., the constellations for 'E', 'F', 'G' and 'H' have different values for the real and imaginary parts at the symbol means and variances (e.g., sub-carrier 6 with a horizontal ellipse centering around $(0, -2)$). In terms of the power allocation tendency, from 'E' to 'H' in Fig. 5.6, we observe that increasing achievable rate constraints ($C_{\min} = \{0, 0.18, 0.37, 0.55\}$ bits/s/Hz) forces more power allocated to the symbol variance, prior to the sub-carriers with strong communication channels (sub-carrier 6 for example).

- Comparing 'E' in Fig. 5.6 with 'B' in Fig. 5.4 (both exerted no communication constraint and corresponding to the integrated sensing and power transfer), all of their power is allocated to the symbol means. However, 'E' is less uniform than B because of looser aISPLD constraints ($S_{\max} = -0.948$ for 'E' over $S_{\max} = -0.998$ for 'B'), and is more adaptive to powering channels by allocating more power to

sub-carriers 1, 7 and 8 (the strongest powering channels). The relatively strict aISPLD of 'E' indicates that good sensing can also be achieved even with a relatively dispersive power allocation if the power is mainly allocated to the mean of the Gaussian input. On the contrary, when comparing 'E' and 'H', given the additional communication constraint at 'H', the total power assigned to each sub-carrier at 'H' has to be more uniform than 'E' to satisfy the same aISPLD constraint.

To sum up, Fig. 5.5 again highlights the performance gain of the co-design inputs, especially the proposed 'OPT' input compared with the 'Coexist' input. In addition, with both constraints on achievable rate and aISPLD, part of the sub-carriers are mainly allocated power to the symbol variance while the others are mainly allocated power to the symbol mean, forming a relatively uniform power allocation across sub-carriers dependent on the strictness of the aISPLD constraint. Once satisfying the communication and sensing constraints, as much power as possible is allocated to the symbol mean of the sub-carries with strong powering channels, i.e., sub-carriers 1 and 8. Such an input tendency, interacted by all three functions, is hard to obtain by a simple PS input, hence highlighting the significance of input signal co-design in ISCAP.

The overall S-C-P region of the 'OPT' input corresponding to the channels in Fig. 5.3 is given in Fig. 5.7 for more details. Understandably, looser communication/sensing constraints give the flexibility to generate more energy.

5.5 Conclusions

This chapter investigates an ISCAP system, where a wideband OFDM signal is used to simultaneously serve the functions of sensing, communications, and powering. The performance of each function is evaluated given an OFDM signal with Gaussian CSs, whose input distribution across subcarriers is optimized to maximize the harvested power

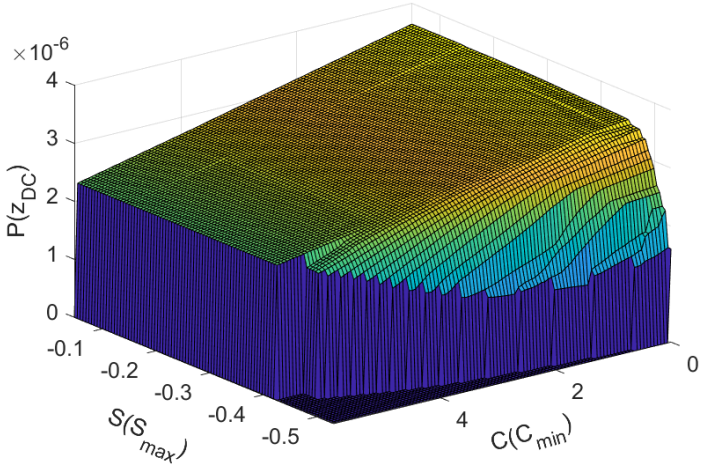

Fig. 5.7: S-C-P region of the 'OPT' input with 30 dBm transmit power.

while satisfying the communication and sensing constraints. Simulations first verify the performance gain of the ISCAP system using the proposed input distribution over the PS signals in a co-existing scenario, i.e., a larger harvested power with the same communication and sensing constraints. Further simulations and analysis reveal how the optimal input distribution trades off between the three functions: a) Firstly, powering favors asymmetric power allocation according to the powering channels, sensing allocates power uniformly to the symbol mean of each subcarrier, and communications allocates power to the symbol variance of subcarriers following a water-filling way; b) Secondly, in a general ISCAP set-up with both communication and sensing constraints, part of the subcarriers have a high symbol variance for the achievable rate while the rest subcarriers have high symbol mean, forming a relatively uniform power allocation across subcarriers to meet the aISPLD constraints. Given a looser aISPLD constraint, the input spectrum can become more powering-beneficial by allocating power asymmetrically to the symbol mean of subcarriers, adaptive to the powering channel.

5.6 Appendix

5.6.1 Proof of (5.15a) - (5.15c)

For the second-order statistics in the OFDM data duration in (5.15a), we have

$$\begin{aligned}\mathbb{E}\{|y[n,\,m]|^2\}=&\mathbb{E}\Big\{\overline{\mathbf{x}}_m^T\mathbf{A}_n^{\mathrm{R}}\overline{\mathbf{x}}_m+2w_R[n,\,m]\mathbf{a}_n^{\mathrm{R}\,T}\overline{\mathbf{x}}_m+\overline{\mathbf{x}}_m^T\mathbf{A}_n^{\mathrm{I}}\overline{\mathbf{x}}_m+2w_{\mathrm{I}}[n,\,m]\mathbf{a}_n^{\mathrm{I}\,T}\overline{\mathbf{x}}_m+|w[n,\,m]|^2\Big\}\\ =&\mathbb{E}\{\overline{\mathbf{x}}_m^T\mathbf{A}_n\overline{\mathbf{x}}_m\}=\mathrm{Tr}(\mathbf{A}_n\mathbf{P})+\sigma_{\mathrm{nP}}^2,\end{aligned}\tag{5.48a}$$

where $\mathbf{A}_n^{\mathrm{R/I}}=\mathbf{a}_n^{\mathrm{R/I}}\mathbf{a}_n^{\mathrm{R/I}\,T}$ is positive semi-definite.

For the fourth-order statistics in (5.15b), define $w_{\mathrm{R/I}}[n,\,m]$ as the real/imaginary part of noise $w[n,\,m]$ respectively, and we have

$$\begin{aligned}\mathbb{E}\{|y[n,\,m]|^4\}=&\mathbb{E}\{\overline{\mathbf{x}}_m^T\mathbf{A}_n^{\mathrm{R}}\overline{\mathbf{x}}_m\overline{\mathbf{x}}_m^T\mathbf{A}_n^{\mathrm{R}}\overline{\mathbf{x}}_m+4w_{\mathrm{R}}^2[n,\,m]\overline{\mathbf{x}}_m^T\mathbf{A}_n^{\mathrm{R}}\overline{\mathbf{x}}_m+2|w[n,\,m]|^2\overline{\mathbf{x}}_m^T\big(\mathbf{A}_n^{\mathrm{R}}+\mathbf{A}_n^{\mathrm{I}}\big)\overline{\mathbf{x}}_m\}+\\ &\mathbb{E}\{\overline{\mathbf{x}}_m^T\mathbf{A}_n^{\mathrm{I}}\overline{\mathbf{x}}_m\overline{\mathbf{x}}_m^T\mathbf{A}_n^{\mathrm{I}}\overline{\mathbf{x}}_m+4w_{\mathrm{I}}^2[n,\,m]\overline{\mathbf{x}}_m^T\mathbf{A}_n^{\mathrm{I}}\overline{\mathbf{x}}_m+2\overline{\mathbf{x}}_m^T\mathbf{A}_n^{\mathrm{R}}\overline{\mathbf{x}}_m\overline{\mathbf{x}}_m^T\mathbf{A}_n^{\mathrm{I}}\overline{\mathbf{x}}_m\}+\\ &\mathbb{E}\{2w_{\mathrm{R}}^2[n,\,m]w_{\mathrm{I}}^2[n,\,m]+w_{\mathrm{R}}^4[n,\,m]+w_{\mathrm{I}}^4[n,\,m]\}\qquad(5.49a)\\ =&\mathbb{E}\Big\{\big(\overline{\mathbf{x}}_m^T\mathbf{A}_n\overline{\mathbf{x}}_m\big)^2\Big\}+6\sigma_{\mathrm{nP}}^2\mathbb{E}\{\overline{\mathbf{x}}_m^T\mathbf{A}_n\overline{\mathbf{x}}_m\}+3\sigma_{\mathrm{nP}}^4\qquad(5.49b)\\ =&\mathrm{Tr}^2(\mathbf{A}_n\mathbf{P})+6\sigma_{\mathrm{nP}}^2\,\mathrm{Tr}(\mathbf{A}_n\mathbf{P})+2\mathrm{Tr}(\mathbf{A}_n\mathbf{P}\mathbf{A}_n\mathbf{P})-2\mathrm{Tr}(\mathbf{A}_n\mathbf{U}\mathbf{A}_n\mathbf{U})+3\sigma_{\mathrm{nP}}^4,\\ &\qquad(5.49c)\end{aligned}$$

with $\mathbf{A}_n=\mathbf{A}_n^{\mathrm{R}}+\mathbf{A}_n^{\mathrm{I}}$ and where (5.49c) is achieved by

$$\begin{aligned}\mathbb{E}\Big\{\big(\overline{\mathbf{x}}_m^T\mathbf{A}_n\overline{\mathbf{x}}_m\big)^2\Big\}=&\mathbb{E}^2\{\overline{\mathbf{x}}_m^T\mathbf{A}_n\overline{\mathbf{x}}_m\}+\mathrm{Var}\{\overline{\mathbf{x}}_m^T\mathbf{A}_n\overline{\mathbf{x}}_m\}\qquad(5.50a)\\ =&\mathrm{Tr}^2(\mathbf{A}_n\mathbf{P})+2\mathrm{Tr}(\mathbf{A}_n\boldsymbol{\sigma}\mathbf{A}_n\boldsymbol{\sigma})+4\boldsymbol{\mu}^T\mathbf{A}_n\boldsymbol{\sigma}\mathbf{A}_n\boldsymbol{\mu}\qquad(5.50b)\\ =&\mathrm{Tr}^2(\mathbf{A}_n\mathbf{P})+2\mathrm{Tr}(\mathbf{A}_n\mathbf{P}\mathbf{A}_n\mathbf{P})-2\mathrm{Tr}(\mathbf{A}_n\mathbf{U}\mathbf{A}_n\mathbf{U}),\qquad(5.50c)\end{aligned}$$

where $\mathrm{Var}\{*\}$ is the variance function.

5.6.2 Proof of (5.18a) - (5.18c)

For the second-order statistics in the CP duration, we have

$$\mathbb{E}\{|y[n,\,m]|^2\}=\mathbb{E}\left\{\left(\mathbf{b}^{\mathrm{R}}_{1,\,n}{}^{T}\overline{\mathbf{x}}_m+\mathbf{b}^{\mathrm{R}}_{2,\,n}{}^{T}\overline{\mathbf{x}}_{m-1}\right)^2+\left(\mathbf{b}^{\mathrm{I}}_{1,\,n}{}^{T}\overline{\mathbf{x}}_m+\mathbf{b}^{\mathrm{I}}_{2,\,n}{}^{T}\overline{\mathbf{x}}_{m-1}\right)^2\right\}+\sigma^2_{\mathrm{n_P}} \tag{5.51a}$$

$$=\mathbb{E}\{\overline{\mathbf{x}}^T_m\mathbf{B}_{1,\,n}\overline{\mathbf{x}}_m+\overline{\mathbf{x}}^T_{m-1}\mathbf{B}_{2,\,n}\overline{\mathbf{x}}_{m-1}+2\overline{\mathbf{x}}^T_m\mathbf{D}_n\overline{\mathbf{x}}_{m-1}\}+\sigma^2_{\mathrm{n_P}} \tag{5.51b}$$

$$=\mathrm{Tr}(\mathbf{B}_n\mathbf{P})+2\mathrm{Tr}(\mathbf{D}_n\mathbf{U})+\sigma^2_{\mathrm{n_P}}, \tag{5.51c}$$

where $\mathbf{B}_n=\mathbf{B}_{1,\,n}+\mathbf{B}_{2,\,n}\in\mathbb{R}^{2K\times 2K}$ with $\mathbf{B}_{1/2,\,n}=\mathbf{b}^{\mathrm{R}}_{1/2,\,n}\mathbf{b}^{\mathrm{R}}_{1/2,\,n}{}^{T}+\mathbf{b}^{\mathrm{I}}_{1/2,\,n}\mathbf{b}^{\mathrm{I}}_{1/2,\,n}{}^{T}\in\mathbb{R}^{2K\times 2K}$ $\mathbf{D}_n=\mathbf{b}^{\mathrm{R}}_{1,\,n}\mathbf{b}^{\mathrm{R}}_{2,\,n}{}^{T}+\mathbf{b}^{\mathrm{I}}_{1,\,n}\mathbf{b}^{\mathrm{I}}_{2,\,n}{}^{T}\in\mathbb{R}^{2K\times 2K}$.

For the fourth-order term of CP, re-organize $y[n,\,m]$ in (5.16) as

$$y[n,\,m]=\mathbf{b}^{\mathrm{R}}_n{}^{T}\mathbf{v}+\mathbf{b}^{\mathrm{I}}_n{}^{T}\mathbf{v}+w[n,\,m], \tag{5.52a}$$

$$\text{with }\mathbf{v}=[\overline{\mathbf{x}}_m{}^{T},\,\overline{\mathbf{x}}_{m-1}{}^{T}]^T,\ \mathbf{b}^{\mathrm{R/I}}_n{}^{T}=[\mathbf{b}^{\mathrm{R/I}}_{1,\,n}{}^{T},\,\mathbf{b}^{\mathrm{R/I}}_{2,\,n}{}^{T}]^T, \tag{5.52b}$$

which, following (5.49b) and (5.50c), gives

$$\mathbb{E}\{|y[n,\,m]|^4\}=\mathbb{E}\left\{\left[\mathbf{v}^T\mathbf{B}'_n\mathbf{v}\right]^2\right\}+6\sigma^2_{\mathrm{n_P}}\mathbb{E}\{\mathbf{v}^T\mathbf{B}'_n\mathbf{v}\}+3\sigma^4_{\mathrm{n_P}}, \tag{5.53a}$$

$$\text{and }\mathbb{E}\{[\mathbf{v}^T\mathbf{B}'_n\mathbf{v}]^2\}=\mathbb{E}\{\mathbf{v}^T\mathbf{B}'_n\mathbf{v}\}^2+\mathrm{Var}\{\mathbf{v}^T\mathbf{B}'_n\mathbf{v}\} \tag{5.53b}$$

$$=\mathbb{E}\{\mathbf{v}^T\mathbf{B}'_n\mathbf{v}\}^2+2\mathrm{Tr}\big(\mathbf{B}'_n\overline{\mathbf{\Sigma}}\mathbf{B}'_n\overline{\mathbf{\Sigma}}\big)+4\overline{\boldsymbol{\mu}}^T\mathbf{B}'_n\overline{\mathbf{\Sigma}}\mathbf{B}'_n\overline{\boldsymbol{\mu}} \tag{5.53c}$$

$$=[\mathrm{Tr}(\mathbf{B}_n\mathbf{P})+2\mathrm{Tr}(\mathbf{D}_n\mathbf{U})]^2+2\mathrm{Tr}\big(\mathbf{B}'_n\overline{\mathbf{P}}\mathbf{B}'_n\overline{\mathbf{P}}\big)-2\mathrm{Tr}\big(\mathbf{B}'_n\overline{\mathbf{U}}\mathbf{B}'_n\overline{\mathbf{U}}\big), \tag{5.53d}$$

$$\text{with }\overline{\boldsymbol{\mu}}=\big[\boldsymbol{\mu}^T,\,\boldsymbol{\mu}^T\big]^T,\ \overline{\mathbf{\Sigma}}=\mathrm{diag}\Big\{\big[\boldsymbol{\sigma}^T,\,\boldsymbol{\sigma}^T\big]^T\Big\},\ \overline{\mathbf{U}}=\overline{\boldsymbol{\mu}}\overline{\boldsymbol{\mu}}^T,\ \overline{\mathbf{P}}=\overline{\mathbf{U}}+\overline{\mathbf{\Sigma}}, \tag{5.53e}$$

$$\mathbf{B}'_n=\mathbf{b}^{\mathrm{R}}_n\mathbf{b}^{\mathrm{R}}_n{}^{T}+\mathbf{b}^{\mathrm{I}}_n\mathbf{b}^{\mathrm{I}}_n{}^{T}=\begin{bmatrix}\mathbf{B}_{1,\,n} & \mathbf{D}_n\\ \mathbf{D}^T_n & \mathbf{B}_{2,\,n}\end{bmatrix}. \tag{5.53f}$$

If expanding the second and third term in (5.53d) as a function of $\mathbf{U}$ and $\mathbf{P}$, we have

$$\mathrm{Tr}\big(\mathbf{B}'_n\overline{\mathbf{P}}\mathbf{B}'_n\overline{\mathbf{P}}\big)=\mathrm{Tr}\left(\begin{bmatrix}\mathbf{B}_{1,\,n} & \mathbf{D}_n\\ \mathbf{D}_n^T & \mathbf{B}_{2,\,n}\end{bmatrix}\begin{bmatrix}\mathbf{P} & \mathbf{U}\\ \mathbf{U} & \mathbf{P}\end{bmatrix}\begin{bmatrix}\mathbf{B}_{1,\,n} & \mathbf{D}_n\\ \mathbf{D}_n^T & \mathbf{B}_{2,\,n}\end{bmatrix}\begin{bmatrix}\mathbf{P} & \mathbf{U}\\ \mathbf{U} & \mathbf{P}\end{bmatrix}\right) \tag{5.54a}$$

$$=\mathrm{Tr}\left(\begin{bmatrix}\mathbf{B}_{1,\,n}\mathbf{P}+\mathbf{D}_n\mathbf{U} & \mathbf{B}_{1,\,n}\mathbf{U}+\mathbf{D}_n\mathbf{P}\\ \mathbf{D}_n^T\mathbf{P}+\mathbf{B}_{2,\,n}\mathbf{U} & \mathbf{D}_n^T\mathbf{U}+\mathbf{B}_{2,\,n}\mathbf{P}\end{bmatrix}^2\right) \tag{5.54b}$$

$$=\mathrm{Tr}\big(\mathbf{B}_{1,\,n}\mathbf{P}\mathbf{B}_{1,\,n}\mathbf{P}+2\mathbf{D}_n\mathbf{P}\mathbf{D}_n^T\mathbf{P}+\mathbf{B}_{2,\,n}\mathbf{P}\mathbf{B}_{2,\,n}\mathbf{P}\big)+$$

$$2\mathrm{Tr}(\mathbf{D}_n\mathbf{U}\mathbf{D}_n\mathbf{U}+\mathbf{B}_{1,\,n}\mathbf{U}\mathbf{B}_{2,\,n}\mathbf{U})+2\mathrm{Tr}(\mathbf{B}_{1,\,n}\mathbf{P}\mathbf{D}_n\mathbf{U}) \tag{5.54c}$$

$$+2\mathrm{Tr}\big(\mathbf{B}_{2,\,n}\mathbf{P}\mathbf{D}_n^T\mathbf{U}\big)+2\mathrm{Tr}\big(\mathbf{B}_{1,\,n}\mathbf{U}\mathbf{D}_n^T\mathbf{P}\big)+2\mathrm{Tr}(\mathbf{B}_{2,\,n}\mathbf{U}\mathbf{D}_n\mathbf{P}), \tag{5.54d}$$

and

$$\mathrm{Tr}\big(\mathbf{B}'_n\overline{\mathbf{U}}\mathbf{B}'_n\overline{\mathbf{U}}\big)=\mathrm{Tr}\left(\begin{bmatrix}\mathbf{B}_{1,\,n} & \mathbf{D}_n\\ \mathbf{D}_n^T & \mathbf{B}_{2,\,n}\end{bmatrix}\begin{bmatrix}\mathbf{U} & \mathbf{U}\\ \mathbf{U} & \mathbf{U}\end{bmatrix}\begin{bmatrix}\mathbf{B}_{1,\,n} & \mathbf{D}_n\\ \mathbf{D}_n^T & \mathbf{B}_{2,\,n}\end{bmatrix}\begin{bmatrix}\mathbf{U} & \mathbf{U}\\ \mathbf{U} & \mathbf{U}\end{bmatrix}\right) \tag{5.55a}$$

$$=\mathrm{Tr}\left(\begin{bmatrix}\mathbf{E}_{1,\,n}\mathbf{U}\mathbf{E}_{1,\,n}^T & \mathbf{E}_{1,\,n}\mathbf{U}\mathbf{E}_{2,\,n}\\ \mathbf{E}_{2,\,n}^T\mathbf{U}\mathbf{E}_{1,\,n}^T & \mathbf{E}_{2,\,n}^T\mathbf{U}\mathbf{E}_{2,\,n}\end{bmatrix}\begin{bmatrix}\mathbf{U} & \mathbf{U}\\ \mathbf{U} & \mathbf{U}\end{bmatrix}\right) \tag{5.55b}$$

$$=\mathrm{Tr}\big(\mathbf{E}_n\mathbf{U}\mathbf{E}_n^T\mathbf{U}\big), \tag{5.55c}$$

where $\mathbf{E}_n=\mathbf{E}_{1,\,n}+\mathbf{E}_{2,\,n}^T=\big(\mathbf{b}_{1,\,n}^{\mathrm{R}}+\mathbf{b}_{2,\,n}^{\mathrm{R}}\big)\big(\mathbf{b}_{1,\,n}^{\mathrm{R}}+\mathbf{b}_{2,\,n}^{\mathrm{R}}\big)^T+\big(\mathbf{b}_{1,\,n}^{\mathrm{I}}+\mathbf{b}_{2,\,n}^{\mathrm{I}}\big)\big(\mathbf{b}_{1,\,n}^{\mathrm{I}}+\mathbf{b}_{2,\,n}^{\mathrm{I}}\big)^T$ is positive semi-definite with $\mathbf{E}_{1,\,n}=\mathbf{B}_{1,\,n}+\mathbf{D}_n$ and $\mathbf{E}_{2,\,n}=\mathbf{B}_{2,\,n}+\mathbf{D}_n$.

Chapter 6

Conclusions

6.1 Conclusions

The thesis explores the wideband signal design for various wireless systems with practical considerations, including WPT with non-linear HPA, DFRC system with on-grid parameter estimation, and upgrade the integration to a multi-functional ISCAP system where communications, sensing and WPT are performed simultaneously. Specifically,

Firstly, in Chapter 3, we investigate signal preferences in a WPT system with non-linear considerations on its transmitters (e.g., HPA) and receivers (e.g., rectenna). We show that the energy harvesting performance of WPT can be maximized through proper waveform design, exploiting rectenna's non-linearity benefits and suppressing HPA's non-linearity degradation. Moreover, the optimal waveform exhibits a significant trade-off between HPA's and rectenna's non-linearities, with the former preferring low PAPR signals and the latter featuring high PAPR signals.

Secondly, in Chapter 4, we exploit the optimal input distribution for DFRC systems with practical system considerations. We characterize the on-grid range-velocity estimator of the OFDM radar system for input distribution design, whose optimal solution shows the

fundamental deterministic-random trade-off between radar and communications. More specifically, we show that for PSK input with constant magnitude input distribution, the optimal power allocation is uniform across OFDM sub-carriers and windowing across OFDM symbols adaptive to the SNR. For Gaussian input with varying magnitude input distribution, a similar power allocation strategy to the PSK scheme is advised, additionally with power allocation to symbol variance for sub-carriers with strong communication channels and to symbol mean for sub-carriers with weak communication channels.

Finally, in Chapter 5, we expand the scope of wireless integration by investigating an ISCAP system to perform communications, sensing and WPT simultaneously using a common signal. Our simulations show that through the signal co-design enabled by ISCAP, the overall performance region outperforms that of coexisting systems significantly, and we show that when integrating with multiple functionalities, it is beneficial to assume a non-zero mean asymmetric complex Gaussian distribution, which provides greater flexibility in input distribution design to meet different functionality requirements.

6.2 Future directions

With the development of IoT, multi-function is becoming a significant feature of future wireless networks, because the integration between different functionalities can enhance spectrum efficiency significantly. Deviating from our thesis, the future directions of wideband waveform design for integrated systems can be classified into two lines:

1. The first line is to examine and improve the waveform design of the existing integrated systems with deeper and more practical considerations, by (a) investigating and mitigating the conflicted differences between different functionalities, such as the random-deterministic trade-off in Chapter 4 which has been overlooked in early ISAC literature; and (b) by accounting for the system's practical limits that origi-

nate from the hardware non-linearities or resource limitations, such as the non-linear HPA considered in Chapter 3 and the on-grid estimation in Chapter 4. For example:

- Involving the analysis of HPA non-linearities in the integrated systems (i.e., ISAC and ISCAP) to explore its effect on the wideband signal's input distribution as in Chapter 3, i.e., either the random-deterministic trade-off is exaggerated or diminished with non-linearities.
- Exploring the random-deterministic trade-off between radar/WPT and communications with multiple antennas in ISCAP.
- Investigating whether there is a signal trade-off for integrated sensing and powering (ISAP) in IoT with practical system considerations, as sensing and WPT share more preferences, e.g., determinism and wideband (high PAPR) signals.

2. The second line of future direction is to exploit similarities of different functionalities, such as the origination of ISAC/WIPT systems where scientists exploited the spectrum and platform similarities at the beginning. There are two ways to realize the similarity exploitation, (a) a novel integration of different functionalities similar to Chapter 5, (b) an upgrade of existing integration with detailed protocol designs under different scenarios. For example,

   - Involving localization functionality with the communications and sensing functionalities, considering the similarities between communication channel estimations, sensing and localization which all describe the environment. In this sense, localization (likewise communications and sensing) can provide prior information for the other two functionalities, reducing their resource requirement or enhancing performance. For example, information from localization helps communications to identify its channel estimation correctness and to decide the beamformer better to enhance achievable rate or security.
   - Exploiting the existing ISAC protocol further about balancing the resources (i.e., time) between the different phases in an ISAC protocol. Specifically, a

general ISAC protocol might have two main phases, the first phase performs blind radar scanning and communication channel estimation and the second phase exploits the first phase's priori information for precise radar tracking and communication transmission. The time resource should be carefully allocated between the first and second phases, trading off between more precise prior information and a longer duration of task execution.

- Exploiting overlooked similarities between the two functionalities in ISAC design. For example, in the first phase of the abovementioned protocol, what would be the best pilot design for sensing and communication channel estimation, when they both have no prior knowledge of the environment? A key question to be addressed is to which extent the optimal pilot design for one functionality compromises the other, i.e., whether there is an inherent trade-off, or if it is possible to design a pilot that simultaneously optimizes both functionalities.

References

[1] B. Clerckx and E. Bayguzina, "Waveform design for wireless power transfer," *IEEE Transactions on Signal Processing*, vol. 64, no. 23, pp. 6313–6328, 2016.

[2] E. Mustafa, J. Shuja, A. I. Jehangiri, S. Din, F. Rehman, S. Mustafa, T. Maqsood, A. N. Khan *et al.*, "Joint wireless power transfer and task offloading in mobile edge computing: a survey," *Cluster Computing*, pp. 1–20, 2021.

[3] G. K. Ijemaru, K. L.-M. Ang, and J. K. Seng, "Mobile collectors for opportunistic internet of things in smart city environment with wireless power transfer," *Electronics*, vol. 10, no. 6, p. 697, 2021.

[4] Y.-H. Suh and K. Chang, "A high-efficiency dual-frequency rectenna for 2.45-and 5.8-GHz wireless power transmission," *IEEE Transactions on Microwave Theory and Techniques*, vol. 50, no. 7, pp. 1784–1789, 2002.

[5] J.-P. Curty, N. Joehl, F. Krummenacher, C. Dehollain, and M. J. Declercq, "A model for /spl mu/-power rectifier analysis and design," *IEEE Transactions on Circuits and Systems I: Regular Papers*, vol. 52, no. 12, pp. 2771–2779, 2005.

[6] B. Clerckx, K. Huang, L. R. Varshney, S. Ulukus, and M.-S. Alouini, "Wireless power transfer for future networks: Signal processing, machine learning, computing, and sensing," *IEEE Journal of Selected Topics in Signal Processing*, vol. 15, no. 5, pp. 1060–1094, 2021.

[7] B. Clerckx, A. Costanzo, A. Georgiadis, and N. B. Carvalho, "Toward 1G mobile power networks: RF, signal, and system designs to make smart objects autonomous," *IEEE Microwave Magazine*, vol. 19, no. 6, pp. 69–82, 2018.

[8] R. Dickinson and W. C. Brown, "Radiated microwave power transmission system efficiency measurements," Jet Propulsion Lab., California Inst. of Tech. Pasadena, CA, United States, Tech. Rep. JPL-TM-33-727, Sep 1975.

[9] Z. Feng, B. Clerckx, and Y. Zhao, "Waveform and beamforming design for intelligent reflecting surface aided wireless power transfer: Single-user and multi-user solutions," *IEEE Transactions on Wireless Communications*, vol. 21, no. 7, pp. 5346–5361, 2022.

[10] A. Collado and A. Georgiadis, "Improving wireless power transmission efficiency using chaotic waveforms," in *2012 IEEE/MTT-S International Microwave Symposium Digest*. IEEE, 2012, pp. 1–3.

[11] A. Boaventura, D. Belo, R. Fernandes, A. Collado, A. Georgiadis, and N. B. Carvalho, "Boosting the efficiency: Unconventional waveform design for efficient wireless power transfer," *IEEE Microwave Magazine*, vol. 16, no. 3, pp. 87–96, 2015.

[12] M. S. Trotter, J. D. Griffin, and G. D. Durgin, "Power-optimized waveforms for improving the range and reliability of RFID systems," in *2009 IEEE International Conference on RFID*. IEEE, 2009, pp. 80–87.

[13] B. Clerckx and E. Bayguzina, "Low-complexity adaptive multisine waveform design for wireless power transfer," *IEEE Antennas and Wireless Propagation Letters*, vol. 16, pp. 2207–2210, 2017.

[14] Kim, Junghoon and Clerckx, Bruno and Mitcheson, Paul D, "Signal and system design for wireless power transfer: Prototype, experiment and validation," *IEEE Transactions on Wireless Communications*, vol. 19, no. 11, pp. 7453–7469, 2020.

[15] J. Kim, B. Clerckx, and P. D. Mitcheson, "Signal and system design for wireless power transfer: Prototype, experiment and validation," *IEEE Transactions on Wireless Communications*, vol. 19, no. 11, pp. 7453–7469, 2020.

[16] H. Yang and B. Clerckx, "Large-scale multiantenna multisine wireless power transfer," *IEEE Transactions on Signal Processing*, vol. 65, no. 21, pp. 5812–5827, 2017.

[17] S. Shen and B. Clerckx, "Beamforming optimization for MIMO wireless power transfer with nonlinear energy harvesting: RF combining versus DC combining," *IEEE Transactions on wireless communications*, vol. 20, no. 1, pp. 199–213, 2020.

[18] Shen, Shanpu and Clerckx, Bruno, "Joint waveform and beamforming optimization for MIMO wireless power transfer," *IEEE Transactions on Communications*, 2021.

[19] Y. Huang and B. Clerckx, "Waveform design for wireless power transfer with limited feedback," *IEEE Transactions on Wireless Communications*, vol. 17, no. 1, pp. 415–429, 2017.

[20] S. Abeywickrama, R. Zhang, and C. Yuen, "Refined nonlinear rectenna modeling and optimal waveform design for multi-user multi-antenna wireless power transfer," *IEEE Journal of Selected Topics in Signal Processing*, vol. 15, no. 5, pp. 1198–1210, 2021.

[21] K.-W. Kim, H.-S. Lee, and J.-W. Lee, "Opportunistic waveform scheduling for wireless power transfer with multiple devices," *IEEE Transactions on Wireless Communications*, vol. 19, no. 9, pp. 5651–5665, 2020.

[22] Kim, Kyeong-Won and Lee, Hyun-Suk and Lee, Jang-Won, "Waveform design for fair wireless power transfer with multiple energy harvesting devices," *IEEE Journal on Selected Areas in Communications*, vol. 37, no. 1, pp. 34–47, 2018.

[23] L. R. Varshney, "Transporting information and energy simultaneously," in *2008 IEEE international symposium on information theory*. IEEE, 2008, pp. 1612–1616.

[24] B. Clerckx, R. Zhang, R. Schober, D. W. K. Ng, D. I. Kim, and H. V. Poor, "Fundamentals of wireless information and power transfer: From RF energy harvester models to signal and system designs," *IEEE journal on selected areas in communications*, vol. 37, no. 1, pp. 4–33, 2018.

[25] H. Son and B. Clerckx, "Joint beamforming design for multi-user wireless information and power transfer," *IEEE Transactions on Wireless Communications*, vol. 13, no. 11, pp. 6397–6409, 2014.

[26] Q. Shi, W. Xu, J. Wu, E. Song, and Y. Wang, "Secure beamforming for MIMO broadcasting with wireless information and power transfer," *IEEE Transactions on Wireless Communications*, vol. 14, no. 5, pp. 2841–2853, 2015.

[27] B. Clerckx, Z. B. Zawawi, and K. Huang, "Wirelessly powered backscatter communications: Waveform design and SNR-energy tradeoff," *IEEE Transactions on Communications*, vol. 21, no. 10, pp. 2234–2237, 2017.

[28] B. Clerckx, "Wireless information and power transfer: Nonlinearity, waveform design, and rate-energy tradeoff," *IEEE Transactions on Signal Processing*, vol. 66, no. 4, pp. 847–862, 2017.

[29] J. Park and B. Clerckx, "Joint wireless information and energy transfer in a K-user MIMO interference channel," *IEEE Transactions on wireless communications*, vol. 13, no. 10, pp. 5781–5796, 2014.

[30] A. A. Nasir, X. Zhou, S. Durrani, and R. A. Kennedy, "Relaying protocols for wireless energy harvesting and information processing," *IEEE Transactions on wireless communications*, vol. 12, no. 7, pp. 3622–3636, 2013.

[31] B. Clerckx, A. Costanzo, A. Georgiadis, and N. B. Carvalho, "Toward 1G mobile power networks: RF, signal, and system designs to make smart objects autonomous," *IEEE Microwave Magazine*, vol. 19, no. 6, pp. 69–82, 2018.

[32] P. Mukherjee, S. Lajnef, and I. Krikidis, "MIMO SWIPT systems with power amplifier nonlinearities and memory effects," *IEEE Wireless Communications Letters*, vol. 9, no. 12, pp. 2187–2191, 2020.

[33] "Novel Frequency-Splitting SWIPT for Overcoming Amplifier Nonlinearity, author=Jang, Hyeon Ho and Choi, Kae Won and Kim, Dong In," *IEEE Wireless Communications Letters*, vol. 9, no. 6, pp. 826–829, 2020.

[34] I. Krikidis, "Information-energy capacity region for SWIPT systems with power amplifier nonlinearity," in *2020 IEEE International Symposium on Information Theory (ISIT)*. IEEE, 2020, pp. 3067–3072.

[35] J. J. Park, J. H. Moon, H. H. Jang, and D. I. Kim, "Performance Analysis of Power Amplifier Nonlinearity on Multi-Tone SWIPT," *IEEE Wireless Communications Letters*, vol. 10, no. 4, pp. 765–769, 2020.

[36] L. Chen, X. Wu, X. Wang, W. Qi, X. Hong, J. Shi, J. Hu, and K. Yang, "Performance Tradeoff Analysis of Hybrid Signaling SWIPT Systems with Nonlinear Power Amplifiers," *Electronics*, vol. 10, no. 11, p. 1364, 2021.

[37] N. Khalfet and I. Krikidis, "Information energy capacity region for swipt systems over rayleigh-fading channels," *IEEE Transactions on Communications*, pp. 1–1, 2022.

[38] N. Ayir, T. Riihonen, M. Allén, and M. F. T. Fierro, "Waveforms and end-to-end efficiency in RF wireless power transfer using digital radio transmitter," *IEEE Transactions on Microwave Theory and Techniques*, vol. 69, no. 3, pp. 1917–1931, 2021.

[39] E. Fishler, A. Haimovich, R. Blum, L. Cimini, D. Chizhik, and R. Valenzuela, "Spatial diversity in radars—models and detection performance," *IEEE Transactions on Signal Processing*, vol. 54, no. 3, pp. 823–838, 2006.

[40] F. D. S. Moulin, C. Wiame, L. Vandendorpe, and C. Oestges, "Joint performance metrics for integrated sensing and communication systems in automotive scenarios," *arXiv preprint arXiv:2208.12790*, 2022.

[41] P. Chen, C. Qi, L. Wu, and X. Wang, "Waveform design for kalman filter-based target scattering coefficient estimation in adaptive radar system," *IEEE transactions on Vehicular Technology*, vol. 67, no. 12, pp. 11 805–11 817, 2018.

[42] F. Athley, "Threshold region performance of maximum likelihood direction of arrival estimators," *IEEE Transactions on Signal Processing*, vol. 53, no. 4, pp. 1359–1373, 2005.

[43] S. Sen and A. Nehorai, "Adaptive design of OFDM radar signal with improved wideband ambiguity function," *IEEE Transactions on Signal Processing*, vol. 58, no. 2, pp. 928–933, 2009.

[44] G. Lellouch, A. K. Mishra, and M. Inggs, "Design of OFDM radar pulses using genetic algorithm based techniques," *IEEE Transactions on Aerospace and Electronic Systems*, vol. 52, no. 4, pp. 1953–1966, 2016.

[45] C. B. Barneto, T. Riihonen, S. D. Liyanaarachchi, M. Heino, N. González-Prelcic, and M. Valkama, "Beamformer design and optimization for full-duplex joint communication and sensing at mm-waves," *arXiv preprint arXiv:2109.05932*, 2021.

[46] O. Dizdar, A. Kaushik, B. Clerckx, and C. Masouros, "Rate-Splitting Multiple Access for Joint Radar-Communications with Low-Resolution DACs," in *2021 IEEE International Conference on Communications Workshops (ICC Workshops)*, 2021, pp. 1–6.

[47] L. Yin and B. Clerckx, "Rate-splitting multiple access for dual-functional radar-communication satellite systems," in *2022 IEEE Wireless Communications and Networking Conference (WCNC)*, 2022, pp. 1–6.

[48] A. Aubry, V. Carotenuto, A. De Maio, A. Farina, and L. Pallotta, "Optimization theory-based radar waveform design for spectrally dense environments," *IEEE Aerospace and Electronic Systems Magazine*, vol. 31, no. 12, pp. 14–25, 2016.

[49] S. Sen and A. Nehorai, "Adaptive OFDM radar for target detection in multipath scenarios," *IEEE Transactions on Signal Processing*, vol. 59, no. 1, pp. 78–90, 2011.

[50] A. Evers and J. A. Jackson, "Analysis of an LTE waveform for radar applications," in *2014 IEEE Radar Conference*. IEEE, 2014, pp. 0200–0205.

[51] X. Shao, C. You, W. Ma, X. Chen, and R. Zhang, "Target sensing with intelligent reflecting surface: Architecture and performance," *IEEE journal on selected areas in communications*, vol. 40, no. 7, pp. 2070–2084, 2022.

[52] S. Lu, F. Liu, and L. Hanzo, "The Degrees-of-Freedom in Monostatic ISAC Channels: NLoS Exploitation Vs. Reduction," *IEEE transactions on Vehicular Technology*, pp. 1–6, 2022.

[53] M. Bell, "Information theory and radar waveform design," *IEEE transactions on information theory*, vol. 39, no. 5, pp. 1578–1597, 1993.

[54] Y. Liu, G. Liao, J. Xu, Z. Yang, and Y. Zhang, "Adaptive OFDM integrated radar and communications waveform design based on information theory," *IEEE Transactions on Communications*, vol. 21, no. 10, pp. 2174–2177, 2017.

[55] A. Dogandzic and A. Nehorai, "Cramer-Rao bounds for estimating range, velocity, and direction with an active array," *IEEE Transactions on Signal Processing*, vol. 49, no. 6, pp. 1122–1137, 2001.

[56] S. D. Liyanaarachchi, T. Riihonen, C. B. Barneto, and M. Valkama, "Optimized waveforms for 5G–6G communication with sensing: Theory, simulations and experiments," *IEEE Transactions on wireless communications*, vol. 20, no. 12, pp. 8301–8315, 2021.

[57] B. Paul, A. R. Chiriyath, and D. W. Bliss, "Survey of RF communications and sensing convergence research," *IEEE Access*, vol. 5, pp. 252–270, 2016.

[58] F. Liu, C. Masouros, A. P. Petropulu, H. Griffiths, and L. Hanzo, "Joint radar and communication design: Applications, state-of-the-art, and the road ahead," *IEEE Transactions on Communications*, vol. 68, no. 6, pp. 3834–3862, 2020.

[59] F. Liu, Y. Cui, C. Masouros, J. Xu, T. X. Han, Y. C. Eldar, and S. Buzzi, "Integrated Sensing and Communications: Toward Dual-Functional Wireless Networks for 6G and Beyond," *IEEE journal on selected areas in communications*, vol. 40, no. 6, pp. 1728–1767, 2022.

[60] A. Liu, Z. Huang, M. Li, Y. Wan, W. Li, T. X. Han, C. Liu, R. Du, D. K. P. Tan, J. Lu, Y. Shen, F. Colone, and K. Chetty, "A survey on fundamental limits of integrated sensing and communication," *IEEE Communications Surveys & Tutorials*, vol. 24, no. 2, pp. 994–1034, 2022.

[61] B. Donnet and I. Longstaff, "Combining MIMO radar with OFDM communications," in *2006 European radar conference*. IEEE, 2006, pp. 37–40.

[62] D. Garmatyuk, J. Schuerger, Y. Morton, K. Binns, M. Durbin, and J. Kimani, "Feasibility study of a multi-carrier dual-use imaging radar and communication system," in *2007 European Microwave Conference*. IEEE, 2007, pp. 1473–1476.

[63] C. B. Barneto, T. Riihonen, M. Turunen, L. Anttila, M. Fleischer, K. Stadius, J. Ryynänen, and M. Valkama, "Full-duplex OFDM radar with LTE and 5G NR waveforms: Challenges, solutions, and measurements," *IEEE Transactions on Microwave Theory and Techniques*, vol. 67, no. 10, pp. 4042–4054, 2019.

[64] C. Xu, B. Clerckx, and J. Zhang, "Multi-antenna joint radar and communications: Precoder optimization and weighted sum-rate vs probing power tradeoff," *IEEE Access*, vol. 8, pp. 173 974–173 982, 2020.

[65] T. Hwang, C. Yang, G. Wu, S. Li, and G. Y. Li, "OFDM and its wireless applications: A survey," *IEEE transactions on Vehicular Technology*, vol. 58, no. 4, pp. 1673–1694, 2008.

[66] C. Sturm, T. Zwick, and W. Wiesbeck, "An OFDM system concept for joint radar and communications operations," in *VTC Spring 2009-IEEE 69th Vehicular Technology Conference*. IEEE, 2009, pp. 1–5.

[67] C. Sturm and W. Wiesbeck, "Waveform design and signal processing aspects for fusion of wireless communications and radar sensing," *Proceedings of the IEEE*, vol. 99, no. 7, pp. 1236–1259, 2011.

[68] C. Baquero Barneto, T. Riihonen, M. Turunen, L. Anttila, M. Fleischer, K. Stadius, J. Ryynänen, and M. Valkama, "Full-Duplex OFDM Radar With LTE and 5G NR Waveforms: Challenges, Solutions, and Measurements," *IEEE Transactions on Microwave Theory and Techniques*, vol. 67, no. 10, pp. 4042–4054, 2019.

[69] C. R. Berger, B. Demissie, J. Heckenbach, P. Willett, and S. Zhou, "Signal processing for passive radar using OFDM waveforms," *IEEE Journal of Selected Topics in Signal Processing*, vol. 4, no. 1, pp. 226–238, 2010.

[70] L. Hu, Z. Du, and G. Xue, "Radar-communication integration based on ofdm signal," in *2014 IEEE international conference on signal processing, communications and computing (ICSPCC)*. IEEE, 2014, pp. 442–445.

[71] D. Garmatyuk, P. Giza, N. Condict, and S. Mudaliar, "Randomized OFDM waveforms for simultaneous radar operation and asynchronous covert communications," in *2018 IEEE Radar Conference (RadarConf18)*, 2018, pp. 0975–0980.

[72] M. I. Skolnik, *Radar handbook*. McGraw-Hill Education, 2008.

[73] X. Tian and Z. Song, "On radar and communication integrated system using OFDM signal," in *2017 IEEE Radar Conference (RadarConf)*. IEEE, 2017, pp. 0318–0323.

[74] S. Aditya, O. Dizdar, B. Clerckx, and X. Li, "Sensing using coded communications signals," *IEEE Open Journal of the Communications Society*, vol. 4, pp. 134–152, 2023.

[75] N. Levanon and E. Mozeson, *Radar signals*. John Wiley & Sons, 2004.

[76] V. Karimi, R. Mohseni, and S. Samadi, "Adaptive OFDM waveform design for cognitive radar in signal-dependent clutter," *IEEE Systems Journal*, vol. 14, no. 3, pp. 3630–3640, 2019.

[77] Y. Xiong, F. Liu, Y. Cui, W. Yuan, T. X. Han, and G. Caire, "On the fundamental tradeoff of integrated sensing and communications under gaussian channels," *IEEE transactions on information theory*, 2023.

[78] F. Liu, Y. Xiong, K. Wan, T. X. Han, and G. Caire, "Deterministic-random tradeoff of integrated sensing and communications in gaussian channels: A rate-distortion perspective," in *2023 IEEE International Symposium on Information Theory (ISIT)*. IEEE, 2023, pp. 2326–2331.

[79] H. Wymeersch, D. Shrestha, C. M. de Lima, V. Yajnanarayana, B. Richerzhagen, M. F. Keskin, K. Schindhelm, A. Ramirez, A. Wolfgang, M. F. de Guzman *et al.*, "Integration of Communication and Sensing in 6G: a Joint Industrial and Academic Perspective," *arXiv preprint arXiv:2106.13023*, 2021.

[80] W. Yuan, Z. Wei, S. Li, J. Yuan, and D. W. K. Ng, "Integrated sensing and communication-assisted orthogonal time frequency space transmission for vehicular networks," *arXiv preprint arXiv:2105.03125*, 2021.

[81] S. Aditya, O. Dizdar, B. Clerckx, and X. Li, "Sensing using coded communications signals," *IEEE Open Journal of the Communications Society*, vol. 4, pp. 134–152, 2023.

[82] B. Paul, A. R. Chiriyath, and D. W. Bliss, "Survey of RF communications and sensing convergence research," *IEEE Access*, vol. 5, pp. 252–270, 2017.

[83] K. Wu and L. Han, "Joint wireless communication and radar sensing systems - state of the art and future prospects," *Iet Microwaves Antennas & Propagation*, vol. 7, no. 11, pp. 876–885, 2013.

[84] J. Koomey, S. Berard, M. Sanchez, and H. Wong, "Implications of historical trends in the electrical efficiency of computing," *IEEE Annals of the History of Computing*, vol. 33, no. 3, pp. 46–54, 2010.

[85] Y. Chen, H. Hua, and J. Xu, "ISAC Meets SWIPT: Multi-functional Wireless Systems Integrating Sensing, Communication, and Powering," *arXiv preprint arXiv:2211.10605*, 2022.

[86] X. Li, X. Yi, Z. Zhou, K. Han, Z. Han, and Y. Gong, "Multi-user beamforming design for integrating sensing, communications, and power transfer," in *2023 IEEE Wireless Communications and Networking Conference (WCNC)*, 2023, pp. 1–6.

[87] D. Tse and P. Viswanath, *Fundamentals of wireless communication*. Cambridge university press, 2005.

[88] C. Rapp, "Effects of HPA-nonlinearity on a 4-DPSK/OFDM-signal for a digital sound broadcasting signal," *ESASP*, vol. 332, pp. 179–184, 1991.

[89] H. Ochiai, "An analysis of band-limited communication systems from amplifier efficiency and distortion perspective," *IEEE Transactions on Communications*, vol. 61, no. 4, pp. 1460–1472, 2013.

[90] P. Kryszkiewicz, "Amplifier-coupled tone reservation for minimization of OFDM nonlinear distortion," *IEEE Transactions on Vehicular Technology*, vol. 67, no. 5, pp. 4316–4324, 2018.

[91] M. Goutay, F. A. Aoudia, J. Hoydis, and J.-M. Gorce, "End-to-end learning of OFDM waveforms with PAPR and ACLR constraints," in *2021 IEEE Globecom Workshops (GC Wkshps)*. IEEE, 2021, pp. 1–6.

[92] S. Mercier, S. Bidon, D. Roque, and C. Enderli, "Comparison of correlation-based ofdm radar receivers," *IEEE Transactions on Aerospace and Electronic Systems*, vol. 56, no. 6, pp. 4796–4813, 2020.

[93] M. Varasteh, B. Rassouli, and B. Clerckx, "SWIPT signaling over frequency-selective channels with a nonlinear energy harvester: Non-zero mean and asymmetric inputs," *IEEE Transactions on Communications*, vol. 67, no. 10, pp. 7195–7210, 2019.

[94] N. Varnica, X. Ma, and A. Kavcic, "Capacity of power constrained memoryless AWGN channels with fixed input constellations," in *Global Telecommunications Conference, 2002. GLOBECOM '02. IEEE*, vol. 2, 2002, pp. 1339–1343 vol.2.

[95] Z. Fu, L. Anttila, M. Abdelaziz, M. Valkama, and A. M. Wyglinski, "Frequency-selective digital predistortion for unwanted emission reduction," *IEEE Transactions on Communications*, vol. 63, no. 1, pp. 254–267, 2014.

[96] J. Nocedal and S. J. Wright, *Numerical optimization*. Springer, 1999.

[97] P. T. Boggs and J. W. Tolle, "Sequential quadratic programming," *Acta numerica*, vol. 4, pp. 1–51, 1995.

[98] S. Boyd, S. P. Boyd, and L. Vandenberghe, *Convex optimization*. Cambridge university press, 2004.

[99] E. N. Committee *et al.*, "Channel models for HIPER-LAN/2 in different indoor scenarios," *ETSI EP BRAN 3ERI085B*, 1998.

[100] Y.-P. Lin and S.-M. Phoong, "OFDM transmitters: analog representation and DFT-based implementation," *IEEE Transactions on Signal Processing*, vol. 51, no. 9, pp. 2450–2453, 2003.

[101] Y. Zhang, S. Aditya, and B. Clerckx, "Input Distribution Optimization in OFDM Dual-Function Radar-Communication Systems," *arXiv preprint arXiv:2305.06635*, 2023.

[102] C. Sturm, E. Pancera, T. Zwick, and W. Wiesbeck, "A novel approach to OFDM radar processing," in *2009 IEEE Radar Conference*. IEEE, 2009, pp. 1–4.

[103] S. M. Kay, *Fundamentals of statistical signal processing: estimation theory*. Prentice-Hall, Inc., 1993.

[104] A. Weiss and E. Weinstein, "Fundamental limitations in passive time delay estimation–part i: Narrow-band systems," *IEEE Transactions on Acoustics, Speech, and Signal Processing*, vol. 31, no. 2, pp. 472–486, 1983.

[105] D. P. Bertsekas, *Constrained optimization and Lagrange multiplier methods*. Academic press, 2014.

[106] W. Fraser, "A survey of methods of computing minimax and near-minimax polynomial approximations for functions of a single independent variable," *Journal of the ACM (JACM)*, vol. 12, no. 3, pp. 295–314, 1965.

[107] M. Bica, K.-W. Huang, V. Koivunen, and U. Mitra, "Mutual information based radar waveform design for joint radar and cellular communication systems," in *2016 IEEE International Conference on Acoustics, Speech and Signal Processing (ICASSP)*. IEEE, 2016, pp. 3671–3675.

[108] C. Shi, F. Wang, M. Sellathurai, J. Zhou, and S. Salous, "Power minimization-based robust OFDM radar waveform design for radar and communication systems

in coexistence," *IEEE Transactions on Signal Processing*, vol. 66, no. 5, pp. 1316–1330, 2017.

[109] P. S. J. Medbo, "Channel Models for HIPERLAN/2 in Different Indoor Scenarios," *3ERI085B, ETSI EP BRAN*, March,1998.

[110] J. W. Adams, "A new optimal window (signal processing)," *IEEE Transactions on Signal Processing*, vol. 39, no. 8, pp. 1753–1769, 1991.

[111] K. H. Biyari and W. C. Lindsey, "Statistical distributions of hermitian quadratic forms in complex gaussian variables," *IEEE transactions on information theory*, vol. 39, no. 3, pp. 1076–1082, 1993.

[112] A. Annamalai and C. Tellambura, "A simple exponential integral representation of the generalized Marcum Q-function QM (a, b) for real-order M with applications," in *MILCOM 2008 - 2008 IEEE Military Communications Conference*, 2008, pp. 1–7.

[113] H. Kassab, F. Rottenberg, T. Feuillen, C. Wiame, and J. Louveaux, "Superposition of rectangular power pulses and cp-ofdm signal for swipt," *EURASIP Journal on Wireless Communications and Networking*, vol. 2022, no. 1, pp. 1–26, 2022.

[114] Z.-Q. Luo, W.-K. Ma, A. M.-C. So, Y. Ye, and S. Zhang, "Semidefinite relaxation of quadratic optimization problems," vol. 27, no. 3, pp. 20–34, 2010.

[115] A. Beck, A. Ben-Tal, and L. Tetruashvili, "A sequential parametric convex approximation method with applications to nonconvex truss topology design problems," *Journal of Global Optimization*, vol. 47, pp. 29–51, 2010.